University of
Stavanger

**Faculty of Science and Technology**

# MASTER'S THESIS

| | |
|---|---|
| **Study program / Specialization:**<br>Industrial Economics, Risk Management and Planning<br>/ Project Management | Spring semester, 2011<br>Open access |
| **Writer:**<br>Kim A. Øvstebø | …………………………………………<br>**(Writer's signature)** |

**Faculty supervisor:** Merete Vadla Madland

**External supervisor(s):** Merete Vadla Madland
Reidar Inge Korsnes

**Title of thesis:**

A mechanical study of the sulphate effect on chalk

**Credits (ECTS):** 30

**Key words:**
- Water weakening of chalk
- High porosity chalk
- Aging
- Triaxial compressive tests
- Creep tests
- Brazilian tests
- Temperature effect
- Sulphate effect
- Failure envelope

**Pages:** 146

**+ enclosure:** 46

Stavanger, June 15th 2011

# A mechanical study of sulphate effect on chalk

**Master Thesis by**

**Kim A. Øvstebø**

**Spring 2011**

University of Stavanger
Faculty of Science and Technology
Department of Petroleum Engineering

# Abstract

The main objective of this thesis was to investigate any possible effects of sulphate on the mechanical strength of chalk. Related to this, the following sub-objectives can be listed: Investigating temperature effect on chalk's mechanical strength, obtaining estimates of chalk's failure envelope (in a *q-p'* plot) at different testing conditions and with different brines, and estimate the cohesion ($S_0$) and friction angle ($\varphi$) of the chalk.

High porosity outcrop chalk from Liège was tested experimentally in two different cell types, and by performing four different types of tests at two different temperature conditions. Hydrostatic, deviatoric and creep tests were carried out in triaxial test cells, while Brazilian tests were performed in a Brazilian test cell. By the use of a heating jacket mounted onto the triaxial cells, and a heating element connected to the front cover of the Brazilian cell, it was possible to perform high temperature tests at 130 °C. About half of the tests were carried out at ambient temperature, so that also the temperature effect could be studied. The testing brine used in the work with this thesis was mainly synthetic seawater without sulphate (SSW–($SO_4^{2-}$)). Due to close co-operation with a student working on a corresponding, parallel master thesis, results from identical tests carried out by the use of synthetic seawater (SSW) as testing brine were also provided. This gave the opportunity to study any possible sulphate effects on the mechanical strength of chalk.

A total of 57 chalk cores, with an average porosity of 39.57%, were saturated with testing brine before testing. All cores tested at high temperature were also aged in an aging cell at 130 °C for three weeks prior to testing. Results from Brazilian, deviatoric (with varying degree of radial support) and hydrostatic tests at different testing conditions could be presented in Mohr diagrams where mechanical parameters could be determined, and also in *q-p'* plots where estimated failure envelopes (consisting of shear failure line and end cap line, at which shear failure and pore collapse is the dominating failure mechanisms, respectively) could be compared. Estimated mechanical parameters were also determined from the shear failure line in the *q-p'* diagram, and showed a good match with the values obtained from the Mohr circle plots.

Experimental results showed that chalk tested at 130 °C was weaker when sulphate was present in the pore fluid, both when regarding shear failure and pore collapse. On average, at high temperature testing yield points and Young's moduli values were a factor approx. 1.3 higher for tests where sulphate was *not* present. At ambient temperature, no clear sulphate effect was observed. In fact, if any trend could be noticed at all, it would be that chalk experienced a higher resistance against shear failure when sulphate was present in the fluid. When comparing temperature conditions for all tests run with the use of SSW as testing brine, it was found that yield points and elasticity moduli values for ambient temperature tests were on average a factor 1.5 higher than for high temperature tests. Thus, sulphate seems to have a weakening effect on chalk at high temperature, while no clear trend is seen at ambient temperature. In the absence of sulphate, there did not seem to be any clear temperature effect.

High temperature (130 °C) creep test results showed that deformation was to a large extent dependant on the presence of sulphate in the continuously flooded fluid. Measured in terms of axial strain, the deformation obtained from flooding synthetic seawater (SSW) was at a certain creep time (≈ 32,000 minutes) a factor 1.62 higher than what was observed when SSW–($SO_4^{2-}$) was flooded. In addition, it was observed that when sulphate was introduced to the pore fluid during creep, this generated a significantly increasing deformation. The opposite was observed when sulphate was removed, typically indicated by the creep strain-creep time curve flattening out. The "introduction" and "removing" of sulphate was simply obtained by changing flooding brine between SSW and SSW–($SO_4^{2-}$).

Chemical analyses of water samples of the effluent water during creep showed large additional production of calcium (from the chalk) and extensive losses of magnesium from the aqueous solution. The latter observation is most likely a result of precipitation of magnesium bearing minerals. Indications of sulphate precipitation as anhydrite ($CaSO_4$), probably, were also seen, as well as it seemed that the immediate reaction of introduced sulphate ions was dependent on the previous flooding fluid(s) and possible actions they would cause inside the chalk.

# Acknowledgements

With this I would like to show my gratitude for help and support of all kinds received from both members of the "Chalk Group", fellow students, family and friends during the work with my Master Thesis.

First of all, I want to say that I am very thankful for getting the opportunity to work together with so many proficient persons in such a great environment. After the work with my Bachelor Thesis in 2009 on this very exciting and interesting research programme, I was always prepared to come back for my Master Thesis. Special thanks are addressed to Associate Professor Merete Vadla Madland for again giving me this opportunity and caring about my work, even though I in reality "belonged" to the Department of Industrial Economics, Risk Management and Planning at the University of Stavanger.

I would also like to address special thanks to Ph.D. Reidar Inge Korsnes who once again was my very supportive, skilful and helpful supervisor. From my experiences related my Bachelor Thesis I knew already how helpful and understanding he would be throughout all stages of this work, and that he would really care about my work. All the enthusiastic conversations about the research and other common interests have been of great importance to me. He was always receptive to questions. From the time he was my supervisor in 2009 I knew that I could not have had a better supervisor – and this impression is maintained.

Senior engineer Kim André Vorland is also thanked for his enthusiasm and help at the rock mechanics laboratory. He was always available when help was needed.

Thanks to all fellow students at the laboratory for socializing and many interesting discussions.

Andreas Davidsen, especially, for the exceptionally good cooperation throughout the whole work, from the very first experimental work and to the very end of the writing phase. He has been my invaluable collaborator through five years of studies, and through several long days at the laboratory he has always been motivating and helpful.

Finally, I would like to thank my family and friends for many inspiring conversations about my Master Thesis during times with frustration and lack of motivation. My parents especially.

Again, thanks to all!

Kim André Øvstebø, Stavanger 2011

# Table of contents

# 1 Introduction

Carbonate rocks have been an important type of reservoir rocks for several years, and worldwide, when regarding oil and gas production. A survey covering hundreds of the largest hydrocarbon fields all over the world was reviewed (in 1985), with the result that approximately 60% of all recoverable oil were held in carbonate reservoirs (Roehl & Choquette, 1985). More recent investigations support this value, and a market analysis performed by Schlumberger in 2007 also propose that more than 40% of the worldwide gas reserves are found in carbonates (Schlumberger Market Analysis, 2007). Carbonate rocks which constitute hydrocarbon reservoirs consist mainly (90%) of the sedimentary rocks dolostone and limestone (Reeder, 1983). Chalk is a soft, white, porous and very fine-grained sedimentary rock of the type limestone. Chalk has maintained its biogenic origin, and consists therefore principally of the mineral calcite ($CaCO_3$) (Roehl & Choquette, 1985).

Chalk is found as an important reservoir rock for many oil and gas fields in the southern part of the North Sea. In the Central Graben on the Norwegian sector, more precisely, large volumes of petroleum are entrapped in Upper Cretaceous to Lower Tertiary hydrocarbon-bearing strata, and held in both oil and gas fields. The “Greater Ekofisk area” is a common term for this area, where the first discovery (which happened to be the largest) was made in 1969. Ekofisk and Valhall are two of the largest fields in this area, which today includes seven major oil fields mainly constituted by chalk (D’Heur, 1986).

It has been experienced that the chalk reservoirs in this area are quite unusual, and specific problems have been associated with both exploration, development and production of these fields (Needham & Jacobs, 1995). In some areas the reservoir thickness ranges up to several hundred metres, but 3,000 metres is commonly used when describing the reservoir depth. Typical porosities for the mentioned chalk reservoirs are 20-35%, which are generally quite high for rocks buried at these depths. But in some local areas within these fields, the porosity even approaches 50%, which is nothing but extraordinary. Most of the chalk reservoirs within this southernmost part of the North Sea are low-permeable as the permeability does not exceed 5 mD, while typical reservoir temperatures lie in the range 90-130 °C (D’Heur, 1986; Roehl & Choquette, 1985).

One of the fields where extensive challenges have been experienced is the Ekofisk field; an overpressured, naturally fractured high porosity chalk reservoir (Sylte et al., 1999) with an initial temperature of 130 °C. Production of this field was started in 1971, by primary drive mechanisms (pressure depletion) such as oil expansion and reservoir compaction. In 1987, after the primary production declined, a full field seawater injection was started of two reasons. First of all to displace the oil in the reservoir and hence increase the oil recovery. But another reason was to generate a pressure support within the reservoir, as observations from late 1984 had showed that compaction of the chalk reservoir occurred as a result of increased effective stress during production (due to pore pressure depletion). With respect to the oil recovery, the seawater injection was considered a success as it doubled the recovery from 24% to 48% (Sulak et al., 1990). However, the reservoir compaction unexpectedly continued and has even caused sea-bed subsidence through the years. This compaction phenomenon is commonly referred to as *water weakening of chalk* (Austad et al., 2008).

Ever since this sea-bed subsidence was discovered oil companies have had extra costs related to safety upgrades (among others), and platform evacuations caused by waves and high sea levels have been experienced more frequently. Thus, a growing interest of finding the cause of this water weakening effect has arised, especially among the oil companies, to be able to reduce the extent of negative consequences. In addition, the compaction caused by water weakening may also result in an extra oil production, so the attempt to reveal the backgrounds for this phenomenon is interesting for several reasons. Hence, research activity has been extensively executed on chalk behaviour and mechanical properties of chalk in general, since the sea bed subsidence was detected.

DaSilva et al. (1985) suggested that mechanical properties of chalk, typically regarding chalk's strength, were in the main dependent on porosity and silica content within the chalk. From further research it has been stated that the primarily compaction of the chalk reservoir was a result of conventional pressure depletion, and deformation due to pore collapse (Johnson & Rhett, 1986). The water weakening effect has been expressed to be the main mechanism from the early 1990's (Sylte et al., 1999). This latter understanding has focused research activities more and more towards the fluid (water) saturation of the chalk.

Risnes (2001) and Risnes et al. (2003) presented experimental results from laboratory studies on high porosity outcrop chalk. When considering chalk strength, it was shown that chalk is strongest in dry condition ("saturated with air"), and that the chalk's strength was reduced for saturated fluids in the following order: oil/glycol, methanol, water. In other words, water was the fluid with the largest weakening effect. Through the years, many different mechanisms have been suggested in attempts to explain and describe the water weakening effect. Such mechanisms may be divided into physical, physico-chemical and chemical effects.

One of the main weakening mechanisms when regarding physical effects has traditionally been capillary forces. Capillary forces occur at grain (solid particle) surfaces but work between two fluids having dissimilar compositions – a wetting phase (typically water) and a non-wetting phase (oil or gas). However, many scientists did not believe that capillary forces could be the main mechanism of the observed compaction, and seeked other explanations. This lead to growing discussions of rapid, chemical reactions occurring at the grain contacts. In connection with this, important experimental work was performed by Risnes et al. (2003) and Risnes et al. (2005), where it was demonstrated that the strength of oil saturated chalk was more or less equal to the strength of glycol saturated chalk – despite the fact that glycol is fully miscible with water and oil is not. In other words; When glycol was used as saturation fluid, there would be no capillary forces present to keep the chalk's strength at the same level as for oil saturated chalk. These observations contributed to the theory that the possible capillary effects on chalk weakening probably play a minor role.

Instead of discussing pure physical effects, Risnes et al. (2005) rather considered some physico-chemical effects to be the main mechanisms of water weakening. Mechanisms like repulsive and van der Waals attractive forces, as well as electrical surface charge, were investigated. Nevertheless, it was concluded that none of those mechanisms would be strong enough to cause the observed weakening of chalk.

Chemical effects have been given more and more attention the last years, and some of the proposed chemical processes have been grain-to-grain dissolution, precipitation, substitution and intergranular pressure solution (IPS). Among others, Korsnes (2007) studied the possible substitution process, which is described in terms of ions (like magnesium, $Mg^{2+}$) in aqueous solution substituting calcium ions in chalk. Such a reaction would typically occur when chalk is exposed to (seawater like) brines at high temperatures – equivalent to the case when seawater is injected into a chalk reservoir. Chemically, this is indicated by an increase in calcium ($Ca^{+}$) concentration in the brine, and decrease in other ion concentration(s). A theory connected to this idea was that the presence of sulphate ($SO_4^{2-}$) in the pore-filling brine would contribute to a larger scale of magnesium-calcium substitution. On the other hand, more recent studies carried out by Madland et al. (2009) clearly showed that sulphate is not a necessary component in the saturation or flooding fluid to obtain a considerable chemical deformation. By exposing chalk to $MgCl_2$ brine they observed deformation even large enough to be compared with deformation caused by sulphate containing synthetic seawater (SSW). Madland et al. (2009) also demonstrated by calculations that the calcium amount in the chalk accessible for substitution was a lot less than the amounts observed in the produced effluent water during flooding. Hence, the understanding is that chalk compaction cannot be a result of substitution solely.

Dissolution and precipitation processes suggested to occur when chalk gets in contact with water has also been extensively investigated. Hiorth et al. (2008) showed that several minerals are supersaturated when seawater is flooded through chalk at 130 °C. When such minerals precipitate, ion components are removed from the aqueous solution. This causes disturbance in the equilibrium, and solid material – typically calcite – will dissolve in an attempt to re-establish the state of equilibrium. One of the minerals that are suggested to be supersaturated is the sulphate containing anhydrite ($CaSO_4$), and the effect of sulphate on mechanical strength of chalk in general has been investigated extensively. Among others by Heggheim et al. (2004), Strand et al. (2005), Korsnes et al. (2006b), Madland et al. (2009), Hiorth et al. (2010) and Megawati et al. (2011). In addition to the theory of precipitation, sulphate is also believed to adsorb onto chalk's surface at specific conditions (Megawati et al. 2011). For some conditions it is claimed that presence of sulphate weakens the chalk significantly, while others have shown that sulphate is not at all needed to obtain large scale deformation.

To sum up, there are many different theories suggested to be the main effect on water weakening of chalk. Chalk is a highly complicated material, and there are probably still several unexposed secrets left to be revealed. Even though thorough research activity is continuously in progress, the main mechanisms of the water weakening of chalk are not yet entirely understood.

In the work with this thesis, one of the main objectives was to study any possible effect of sulphate on the mechanical strength of chalk, in combination with investigating whether any temperature effects could be observed. This was made possible by co-operating and comparing test results with experimental work carried out for a parallel master thesis (Davidsen, 2011). For the great basis of comparison all results from both studies will be presented and treated in this thesis. Four different types of experimental tests were executed to obtain comprehensive and comparable test results. This included hydrostatic tests, deviatoric tests at several different radial stresses, Brazilian tests and creep tests. Results from the three first types could be treated to obtain so-called "failure envelopes" in *q-p'* diagrams. An exceptionally good experimental method to study chemical aspects of water weakening of chalk, is to analyse water samples of the effluent water during creep testing. For being able to study any sulphate effect, two different test brines were used; synthetic seawater (SSW) and synthetic seawater without sulphate (SSW–($SO_4^{2-}$)). Since the only difference between them was the presence of sulphate, any observed differenced experienced for similar testing conditions could probably be related to the sulphate presence. Temperature effect could be studied by performing tests at two different temperature conditions; ambient temperature and high temperature (130 °C).

# 2 Theory

## 2.1 Carbonate rocks

### 2.1.1 Carbonate rocks in general

Carbonate rocks are a type of sedimentary rocks which consists mainly of carbonate minerals. Sedimentary rocks like this may be deposited as chemical precipitates, biogenic sediments or as clastic sediments (Bjørlykke, 1989). Chemical precipitates will in this case be solid carbonate deposits (or salts) composed by anionic complexes of $(CO_3)^{2-}$ and divalent metallic cations like $Ca^{2+}$, $Mg^{2+}$, $Fe^{2+}$, $Ba^{2+}$ and $Cu^{2+}$, typically. By "biogenic" it is meant that the sediment is constituted of deposits of living beings (Ahr, 2008), while a "clastic" sediment means that it is made of eroded debris of other (carbonate) rocks (Link, 2001). Usually, carbonate sediments are generated in shallow, warm oceans. Due to the different depositional methods, carbonate sediments are composed of particles with a large variance of sizes, shapes and mineralogy mixed together. One of the results of this mixture is that the void spaces in between the particles are often large, yielding a high porosity (Lucia, 1999).

Internal bonds within the $CO_3^{2-}$ structure are stronger than the ionic bonding between the carbonate groups and the different cations. In other words, the amount of energy needed to break the salt molecules into two ions is less than what is needed to break down the carbonate groups. Under the right physical and chemical circumstances the cation part of the carbonate salt (i.e. $Ca^{2+}$ ions) may be substituted. Korsnes et al. (2006a, b) and Korsnes et al. (2008) discussed this substitution process in terms of $Mg^{2+}$ ions dissolved in (pore) water replacing $Ca^{2+}$ ions on intergranular contacts.

Carbonates can be divided into groups based on their crystal lattice structure or the internal arrangement of atoms, and each such group has its own recognizable crystal system. The most common carbonate minerals crystallize in the hexagonal system and hence belong to the "hexagonal group". Among the members of this group, *calcite* ($CaCO_3$) and *dolomite* ($Ca,Mg(CO_3)_2$) are the two most common. *Aragonite* ($CaCO_3$) is another common carbonate mineral which actually has the same composition as calcite – i.e. they are polymorphs of calcium carbonate – but belongs to another group as it crystallizes in the orthorhombic system (Ahr, 2008).

Within the mentioned groups, it is the arrangement of atoms that distinguish the minerals from each other. For instance, dolomite can typically form from calcite if $Mg^{2+}$-bearing water gets in touch with the latter and a chemical replacement process of calcium and magnesium ions occurs. This process is called dolomitization and its chemical equation is presented in Eq. 2.1:

$$2CaCO_3 + Mg^{2+} \rightleftarrows Ca,Mg(CO_3)_2 + Ca^{2+} \qquad \text{(Eq. 2.1)}$$

The equation can also be read the opposite direction than described above, making it a dedolomitization (or calcitization) process where calcite is the resulting mineral. Which direction this reaction will move depends both on the $Ca^{2+}$-$Mg^{2+}$ ratio and the salinity of the ion bearing water (Selley, 1998; Roehl & Choquette, 1985). Both the calcium and the magnesium ion are divalent, but the latter is of a smaller size. This causes a change in the dolomite lattice and results in a loss of rotational symmetry (Ahr, 2008).

Of all naturally occurring carbonates the sedimentary rocks *limestone* and *dolostone* make up as much as almost 90% (Reeder, 1983). And in fact, when dealing with hydrocarbon reservoirs of carbonate rocks worldwide those are distributed more or less half-and-half between limestone and dolostone (Zenger et al., 1980). Further, these rock types mainly consist of the mentioned minerals; pure limestone contains more than 90% of pure calcite and pure dolostone consists of 90% or more dolomite (Bissell & Chilingar, 1967). The third mentioned mineral, Aragonite, is quite common in modern oceans but rather rare to spot in ancient rock records (Ahr, 2008). The reason is that it is unstable in the subsurface and is easily being converted to the hexagonal isomorph, i.e. calcite. As a matter of fact, this polymorphic reaction yields an increase in bulk volume of 8%, resulting in a noticeable loss of porosity (North, 1985).

Carbonate reservoirs have for many years contributed significantly to the production of oil and gas worldwide. A survey of the world's largest fields known in 1967 was conducted by Halbouty et al. (1970). A review of the statistics, reproduced by Roehl & Choquette (1985), presented that 44% of these "giant" fields produced either substantially or entirely from carbonate reservoirs. This proportion is comparable to results from more up-to-date studies, like the U.S. Geological Survey (USGS) presented by Ahlbrandt et al. (2005). They suggested that approximately 2/5 (≈ 40%) of the investigated fields consisted purely or partly of carbonate lithology. When focusing on oil fields, the review by Roehl & Choquette (1985) suggested that around 61% of recoverable oil in giant fields is found in carbonate reservoirs. A more recent market analysis performed by Schlumberger in 2007 agreed with these reviews, claiming that "more than 60% of the world's oil and 40% of the world's gas reserves are held in carbonates" (Schlumberger Market Analysis, 2007).

### 2.1.2 Chalk in general

*Chalk* is a soft, white, porous and very fine-grained sedimentary rock of the type limestone which has maintained its biogenic origin (Roehl & Choquette, 1985). Often, chalks are referred to as either *pure* or *impure*, based on their content of calcite ($CaCO_3$). Chalks which (almost) exclusively consist of calcium carbonate are classified as pure, while impure chalks also can contain other minerals such as dolomite, silica and clay.

Principally, pure chalks are built up of both whole and fragmentary parts of skeletons, produced by single-celled marine planktonic algae known as coccolithophorids. The skeletons are built up of calcite tablets or platelets of typical order of magnitude of 0.5-2.5 μm across, which are arranged in rosettes (or rings) called coccoliths. These coccolith rings have diameters which typically lies within the range of 3-15 μm (Røgen & Fabricius, 2002), and up to 20 such rings grouped together and overlapped can form spherical shaped coccospheres. Typical size of a coccosphere may be 30 μm across. They are held together by organic tissue, but easily disintegrated to coccoliths and further to calcite platelets during sediment burial. (Glennie, 1998). Hence, complete coccospheres are rarely found in chalks, but complete coccolith rings are quite common. Such a ring, in addition to other greater and smaller fragmentary parts and grains, are all perceptible on the highly magnified SEM (Scanning Electron Microscope) picture of Liège outcrop chalk in Fig. 2.1. Especially due to all the small particles, the surface area of chalk is quite large; around 2 $m^2/g$ (Røgen & Fabricius, 2002).

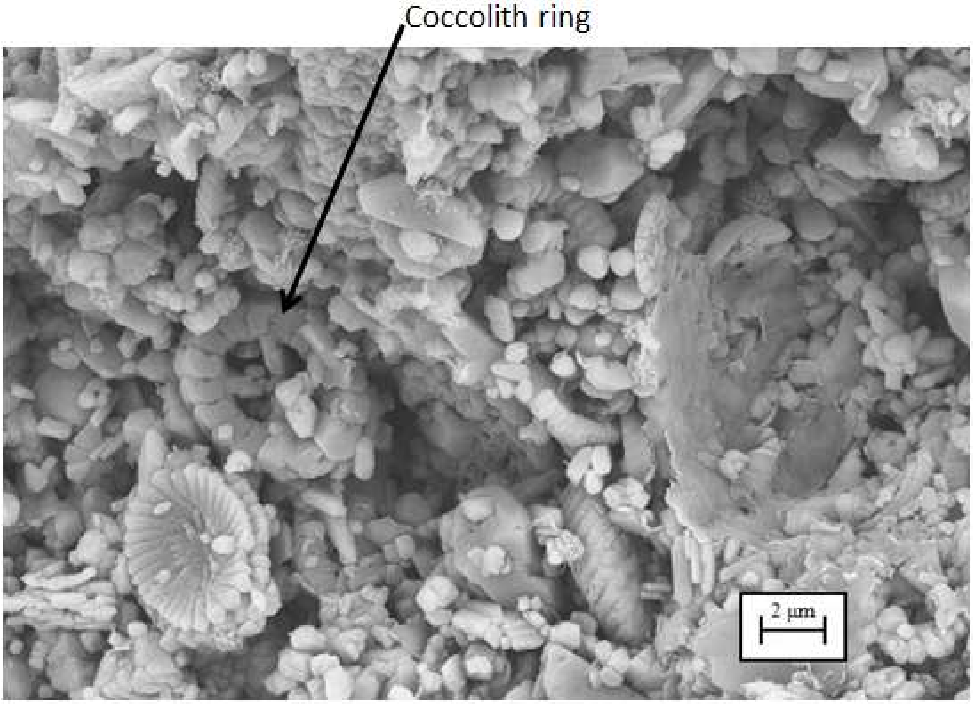

Figure 2.1: *SEM picture – magnified 12,460 times – of outcrop chalk from Liège, where coccolith rings are shown together with other fragmentary parts and grains of very different sizes.*

Pure and highly porous chalks consist of a mixture of whole coccolith rings and fragments and grains of quite different sizes. Due to this, chalk materials often have a rather open structure. Some pore spaces even may be notably greater than the sizes of the single grains. This is one of the reasons why chalks often hold high porosity, but on the other hand also some of the reason why highly porous chalks often have as low permeabilities as in the range of 1-5 mD (Scholle, 1977). The latter is explained by the fact that the smallness of the grains makes the pore throats very narrow. Large sizes of pore bodies compared to the surrounding grains also make the chalk highly susceptible to pore collapse, as prospective movement of small fragments or grains may fill the voids and even block passages between larger fragments (Risnes, 2001; Strand et al., 2006; Madland, 2005)

Studies of chalks often involve strength and mechanical properties. Mechanically, highly porous chalks behave as frictional materials. They usually fail in a shear failure mode but as already mentioned; due to the open structure, pore collapse should also be considered as a possible failure mechanism. In addition to the porosity, the content of silica is also an important factor when considering the strength of chalks (DaSilva et al., 1985). Typical parameter values for chalks that are classified as “weak”, are porosity higher than 35% and silica content less than 7% (Risnes, 2001).

### 2.1.3 Chalk as a reservoir rock in the North Sea

For many oil and gas fields in the southern part of the North Sea, chalk is found as an important reservoir rock – both on the Norwegian and the Danish sector. On the Norwegian sector Ekofisk, Eldfisk and Valhall can be mentioned as some of the largest and most important fields. Typical reservoir depths are 3,000 metres, and for most chalk reservoirs in the North Sea the temperature is in the range of 90-130 °C. Porosity within chalk reservoirs in this area typically lies between 20-35%, which is quite high, but in some of the mentioned fields the porosity sometimes even approaches 50% (D'Heur, 1986; Roehl & Choquette, 1985). Such values are tremendously high, especially for rocks at depths of 3,000 metres. Usually, diagenetic processes would have reduced the porosity considerably. Evaluations performed by Scholle (1977) suggest that chalk fields in the North Sea, at burial depths of 2,000-3,000 metres, should have porosities in the order of 10%. However, in these mentioned reservoirs high porosities have been preserved. The prevention and limitation of compaction and diagenetic processes are probably due to early invasion of hydrocarbons as well as generated overpressures (Risnes, 2001).

It is expected that pore fluids have played an important role when regarding conservation of porosity; both connate fluids (which are mainly brines derived from seawater) and migrated fluids (petroleum, in the main). Permeability barriers may hinder pore fluids from escaping, and as overburden stress increases with time the pore pressure can build up beyond the regular hydrostatic level. In over-pressured situations like this, more of the overburden stress will be balanced by the pore fluids. The intergranular stress will therefore be lower than in normally pressured rocks, and the physical drive towards pressure solution and generation of pore-filling cement will be reduced. (For explanation about the stress term, please see Paragraph *2.3.1 Stress (σ)*).

In addition, hydrocarbon fluids have (probably) invaded the pores both early and efficiently, and have expelled the initial brines to a large degree. In fact, in some parts of the oil-wet North Sea chalk, the water saturation (due to irreplaceable water) is less than 10%. As a result of this, less chalk needs to be dissolved for the pore water to be saturated with it. And as the water gets fully saturated the porosity reduction along with the diagenetic processes will gradually cease (Scholle, 1975; 1977).

## 2.2 Porosity (*Φ*)

As seen chalk is a composite material, which makes it inhomogeneous on a microscopic scale. This is also the case for rocks in general, and means that rock materials cannot be treated as homogeneous, solid materials. As a matter of fact rocks' behaviour, for instance their elasticity (see Chapter *2.3 Rock mechanics – Elasticity*), depends to a considerable extent on the non-solid part of the material (Fjær et al., 2008). In other words, the degree of void space in between the solid particles is important, and also the content (fluid) and its parameters; physical, such as density and pressure, as well as chemical, e.g. ionic composition and pH.

Materials that are composite in a way that creates void space in between solid particles, are called porous materials. Based on an object consisting of such a material the term *porosity* can be defined. If the total volume (bulk volume) of an object is called $V_b$, the volume of solid material (matrix volume) is called $V_m$ and the volume of void space (pore volume) is called $V_p$, the total volume can be expressed this way:

$$V_b = V_m + V_p \qquad \text{(Eq. 2.2)}$$

Chalk is a good example of a porous material, and chalk cores are often used for experimental work. In Fig. 2.2 a fluid saturated chalk core is used as an example to present the relation between the three mentioned volumes. The rightmost figure clearly shows the relationship between the fluid ($V_p$) and the solid ($V_m$) volumes which constitute the bulk volume.

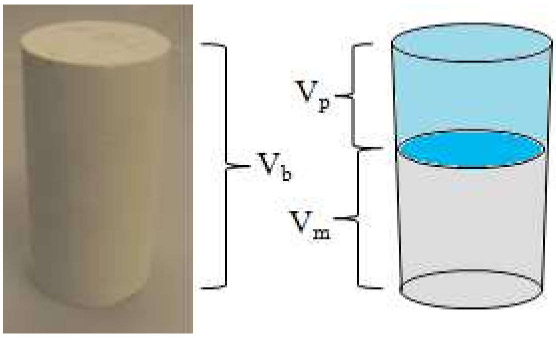

Figure 2.2: *The relationship between matrix volume* ($V_m$) *and volume of free fluid in the pores* ($V_p$)*, which together constitute the bulk volume* ($V_b$)*, for a fluid saturated (chalk) core.*

In cases where the object is a cylindrical core, the bulk volume can be expressed by this formula:

$$V_b = \frac{\pi \cdot D^2 \cdot L}{4} \qquad \text{(Eq. 2.3)}$$

where

D: Diameter of the core
L: Length of the core

By saturating the core with a fluid, and weighing the core both in totally dry and totally saturated condition, the pore volume can be found. The weight of the fluid will be equal to the difference between the two weight values, and by dividing on the fluid's density the volume of the void space can be calculated:

$$V_p = \frac{W_s - W_d}{\rho_f} \qquad \text{(Eq. 2.4)}$$

where

$W_s$: Weight in saturated condition
$W_d$: Weight in dry condition
$\rho_f$: Density of the saturating fluid

When both the bulk and the pore volume are known, the porosity ($\Phi$) of the object can be defined as the proportion between them. (See Eq. 2.5). Porosity is a dimensionless quantity, but by multiplying the value by 100 it can be given as a percentage.

$$\Phi = \frac{V_p}{V_b} \qquad \text{(Eq. 2.5)}$$

The term *porosity* can be divided into three more specific concepts, namely *total*, *effective* and *non-effective* porosity. These are the engineering considerations which tell more precisely how an object (e.g. a reservoir) can contain a fluid (Link, 1987). Furthermore, pores can be divided into three different morphological types – *catenary pores*, *cul-de-sac* (or *dead-end*) *pores* and *closed pores* – where the two first ones contribute to effective porosity and closed pores constitute the non-effective porosity (Selley, 1998). Fig. 2.3 shows an overview of the mentioned classifications.

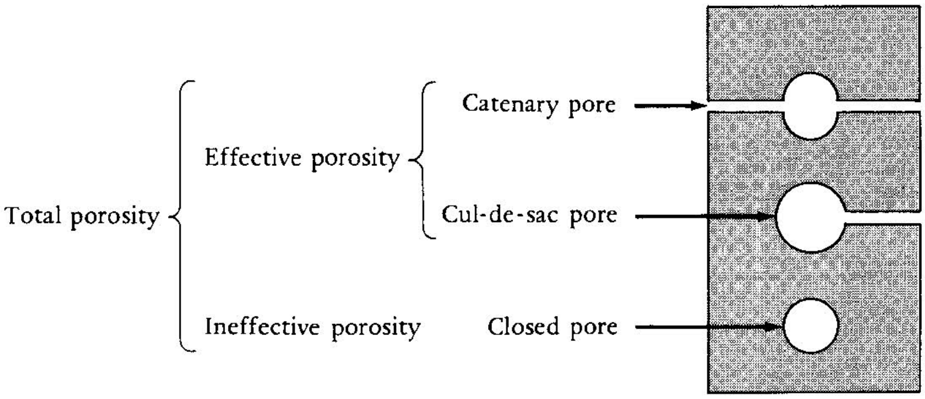

Figure 2.3: *Overview and illustration of the pore type classification and to which concept of porosity each of them belong. (From Selley (1998)).*

Some pores are totally isolated in between the material's solid particles, and therefore have no connection or communication with other pores. Such closed pores will for instance not contribute to the pore volume found by using the mentioned method and formulas, as they will not be filled with the saturating fluid. Instead, the volume of isolated pores will make up a part of the matrix volume. Fluids which are already contained in such a void cannot be removed from the object. This can for example be the case when producing from a reservoir rock, where fluids in closed pores are non-producible and often called "fixed fluids".

Effective porosity only comprises the pores which are interconnected to other pores, so that the contained fluid can be replaced and produced. As shown, both the so-called catenary and cul-de-sac pores are effective pores in this regard. Catenary pores have communication with other pores through more than one throat passage – there are “chains” of passages in between them. Cul-de-sac pores are also called dead-ends, as they are only connected to another pore through one throat passage. Regarding hydrocarbon production, natural or artificial water drive can flush out hydrocarbons from catenary pores but will not affect cul-de-sac pores. However, the latter type will be filled with fluid during saturation, and hence contributes to the effective porosity measure (Selley, 1998).

When regarding petroleum activities effective porosity is the most interesting, as it gives the fraction of void space filled with *recoverable* (producible) fluids. Non-effective porosity, on the other hand, concerns the closed pores from which fluids cannot be produced, while the total amount of void space inside the bulk volume – including both the effective and non-effective – constitutes the so-called total porosity. Usually, the effective porosity lies somewhere in the range of 40-75% of the total porosity, except in unconsolidated sediments (North, 1985).

During the work with this thesis, the explained method and calculations have been used for deciding porosity of chalk cores. As the saturating fluid will not fill the closed pores, it should be noted that it is the *effective* porosity which is found.

## 2.3 Rock mechanics – Elasticity

*Please note that the theory – both text and figures – presented in this part (Chapter* 2.3 Rock mechanics – Elasticity*) is mainly based on Fjær et al. (2008) unless otherwise is stated.*

Elasticity can be defined as the ability that a material has to resist deformation when being exposed to forces, and also to recover from deformation afterwards. Such forces can arise from pressure, stretching, bending and/or twisting. In theory, all materials are elastic to a certain extent, and within the term of rock mechanics elasticity is an important phenomenon. There is often a linear ratio between the exerted forces and the resulting deformations. In fact, in cases where the exerted forces are changed just slightly, the response always seems to be linear. Hence, all discussions on elasticity include the theory of linear elasticity.

The theory of elasticity comprises primarily the concepts of *stress* and *strain*, which will be presented and defined in the following.

### 2.3.1 Stress ($\sigma$)

**Stress ($\sigma$) in general**

Just like pressure, the term *stress* ($\sigma$) is defined as the force ($F$) acting on a (cross-section) area ($A$):

$$\sigma = \frac{F}{A} \qquad \text{(Eq. 2.6)}$$

In the work with this thesis stress is an important parameter and the variables will be presented with their SI units, i.e. Newton [N] and square metre [$m^2$] for force and area, respectively. Equivalent to pressure this gives a stress unit of [$N/m^2$], which is commonly referred to as Pascal [Pa]. The sign of the stress is defined by convention. In rock mechanics the stresses that are dealt with are (almost) exclusively compressive. Hence, traditionally the sign convention within rock mechanics establishes that compressive stresses are positive, while tensile stresses are negative. Since it is a matter of convention it is important that there is consistency in the use of signs, so that possible misunderstandings will be avoided.

The concept of stress will here be linked to the case where a piston is placed on top of a chalk core. The piston acts on the core with a certain force, and in fact any cross-section of the core is being exposed to this force. Fig. 2.4 shows this principle with a similar example, namely a weight put on top of a pillar.

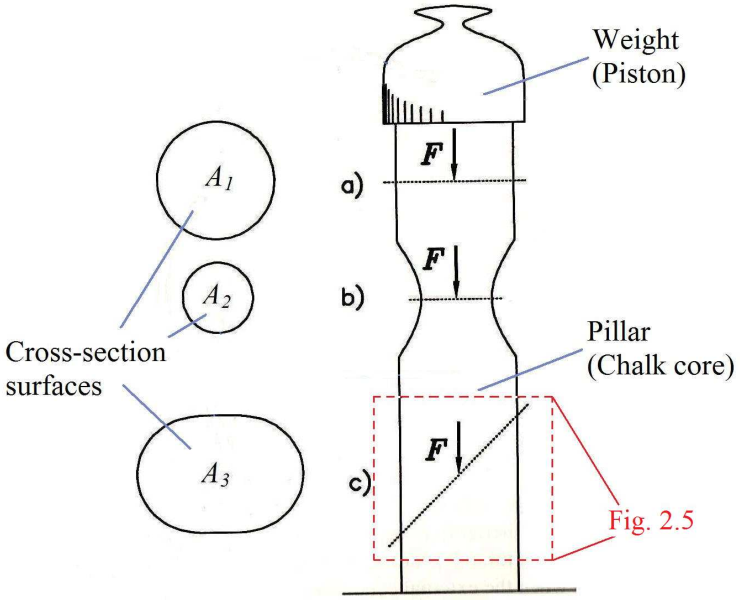

Figure 2.4: *Illustration of area dependence on stress, as a force is acting on different cross-section areas. Smaller area results in a higher stress. (See Eq. 2.6).*

Newton's third law of motion states that for every action (or force) in nature, there is always an equal and opposite directed reaction (force). In accordance with this law, the pillar in Fig. 2.4 reacts with a force of equal size as the external force from the weight, but in the contrary direction. Given that the pillar is placed on a horizontal plane, gravitational force ($F$) from the weight will work vertically and hence orthogonal to any horizontal cross-section. Both cross-section a) and b) in Fig. 2.4 are horizontal, but their areas – $A_1$ and $A_2$, respectively – are different. Cross-section area $A_1$ at position a) is the bigger one, and hence the stress will be lower at this point, but the magnitude of the force $F$ is the same in both positions. In experimental work where test objects (e.g. chalk cores) are exposed to external forces, it is of importance that the cross-section area does not vary along the length of the object. In the specific case with this thesis, this could be checked by measuring the diameter at different positions of the cylindrical cores.

### Normal stress ($\sigma$) and shear stress ($\tau$)

However, the direction of the force is not necessarily always perpendicular to the cross-section or the surface, as exemplified in position c) in Fig. 2.4. The orientation of surface $A_3$ makes it necessary to decompose the force ($F$) into two components, where one is *perpendicular* (normal) to the surface ($F_n$) and the other one is parallel to it ($F_p$). This decomposition of force $F$ is presented in Fig. 2.5:

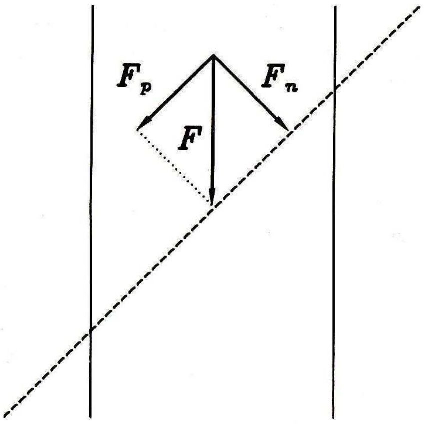

Figure 2.5: *Decomposition of a force* F *into two components; one normal (*$F_n$*) and one parallel (*$F_p$*) to the cross-section area.*

Decomposing the force into two components also result in two different expressions of stress; *normal stress* ($\sigma$) and *shear stress* ($\tau$) which are connected to the normal and the parallel force, respectively. Equations for the two types of stresses can be presented with Eq. 2.6 as a basis:

$$\sigma = \frac{F_n}{A} \qquad \text{(Eq. 2.7)}$$

and

$$\tau = \frac{F_p}{A} \qquad \text{(Eq. 2.8)}$$

where the cross-section area $A$ represents any surface exposed to the decomposed force $F$.

Even along one given surface area the force may vary. Any surface can be divided into an infinite number of sections ($\Delta A$), each of them exposed to an infinitely small portion of the total force ($\Delta F$). In some cases the *local stress* at a certain point $P$ on the surface is of interest. As the force $\Delta F$ may differ from one subsection to another, only the specific section $i$ containing this point $P$ should be considered at a time. Eq. 2.9 shows that the stress at point $P$ can be defined as the limit value of $\Delta F_i/\Delta A_i$ when $\Delta A_i$ goes to zero:

$$\sigma = \lim_{\Delta \mathrm{A_i} \to 0} \frac{\Delta F_i}{\Delta A_i} \qquad \text{(Eq. 2.9)}$$

As Eq. 2.9 defines the *local stress* at a certain point within a cross-section, it can be stated that Eq. 2.6 rather gives the *average stress* at the cross-section.

### Total stress ($\sigma$) and effective stress ($\sigma$’)

When regarding porous materials, it is important to distinguish between the two terms of *total* and *effective stress*. Because, when a force acts on a surface area of a porous object (e.g. a chalk core) the object as a whole is exposed to a so-called *total stress* ($\sigma$). This external stress is in equilibrium with the internal stress, consisting of the pressure inside the pores ($p_p$) and the intergranular stress ($\sigma'$), and the latter is commonly referred to as *effective stress*. The balance between these three mentioned parameters is shown in Fig. 2.6 and Eq. 2.10:

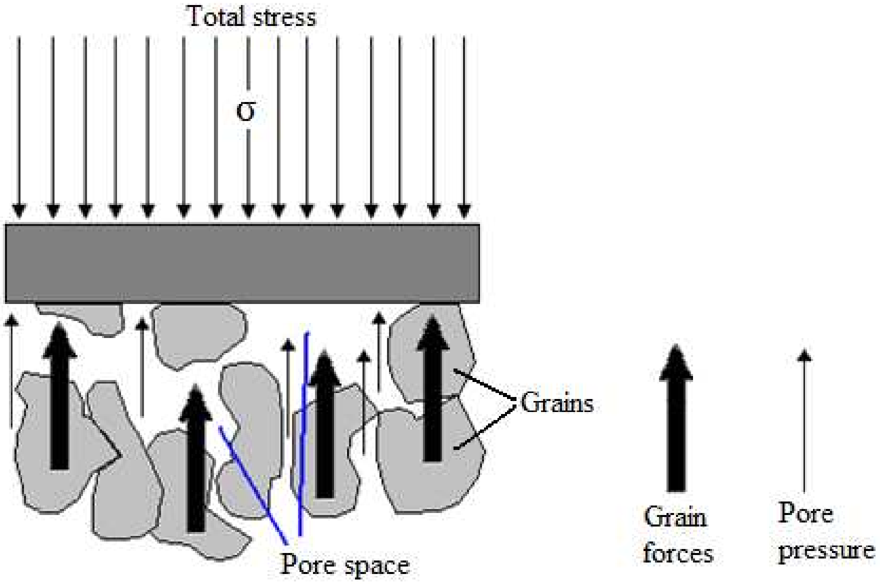

Figure 2.6: *Illustration of total and effective stress on a porous material. (Inspired by Finsnes (2004)).*

Total stress = Effective stress + Pore pressure

$$\sigma = \sigma' + p_p \tag{Eq. 2.10}$$

Karl von Terzaghi turned this relation into a mathematical definition of effective stress:

$$\sigma' = \sigma - p_p \tag{Eq. 2.11}$$

From this equation it is clearly shown that a higher pore pressure will reduce the effective stress on the grains, as a larger part of the external stress will be balanced by the pore fluid. Terzaghi's equation can further be derived to also include a scaling factor in the pore pressure term which is called Biot's constant ($\alpha$):

$$\sigma' = \sigma - (\alpha \cdot p_p) \tag{Eq. 2.12}$$

This constant is limited to the range $\Phi < \alpha \leq 1$, where $\Phi$ is the porosity of the object/material. High porosity materials, as well as weak and unconsolidated materials, will have high values of $\alpha$, i.e. close to 1.

### Principal stresses ($\sigma_3 \leq \sigma_2 \leq \sigma_1$)

To be able to give a complete description of the stress state at a certain point within an object, it is needed to identify the stresses related to surfaces oriented in three orthogonal directions. Three-dimensionally (x-, y- and z-direction), three stresses will be related to each surface. For example, a surface which is normal to the x-axis will have the following stresses related to it; a normal stress ($\sigma_x$), a shear stress related to a force in y-direction ($\tau_{xy}$) and a shear stress related to a force in the z-direction ($\tau_{xz}$). Only one shear stress will be associated with the surface physically. But the shear stress orientation must, however, be identified – most practical by identifying both the y- and z-components. Similar identifications can be done for surfaces normal to the y- and the z-axis.

Based on Fig. 2.5 both forces and stresses were decomposed when considering a cross-section through a sample which was not perpendicular to the direction of the load. For simplification, a two-dimensional figure was used, and will also here be used to define the *principal stresses* – illustrated in the xy-plane.

Consider a surface which is oriented normal to a general direction $\theta$ in the xy-plane. The normal ($\sigma$) and the shear ($\tau$) stresses at this surface are illustrated in Fig. 2.7, where the hypotenuse represents the surface of a triangle at rest – i.e. no net forces act on it.

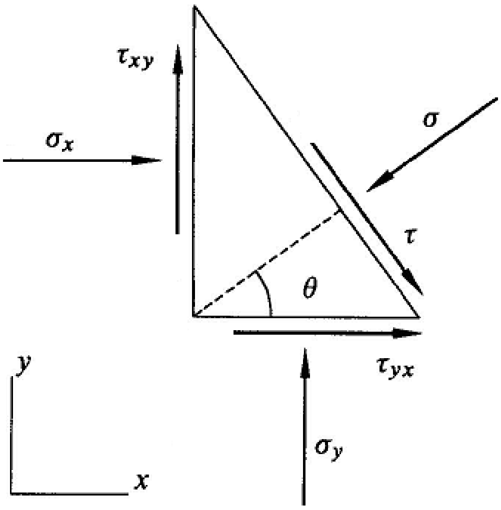

Figure 2.7: *Force equilibrium on a triangle at rest, where the hypotenuse represents a surface oriented perpendicular to a general direction* θ *in the xy-plane. The arrows show the direction of the forces acting on the triangle, assuming that all the stress components are positive (compressive).*

By cancelling out forces, the following equations can be listed for the normal and the shear stress, respectively:

$$\sigma = \sigma_x \cdot \cos^2(\theta) + \sigma_y \cdot \sin^2(\theta) + 2 \cdot \tau_{xy} \cdot \sin(\theta) \cdot \cos(\theta) \qquad \text{(Eq. 2.13)}$$

$$= \frac{1}{2} \cdot (\sigma_x + \sigma_y) + \frac{1}{2} \cdot (\sigma_x - \sigma_y) \cdot \cos(2\theta) + \tau_{xy} \cdot \sin(2\theta) \qquad \text{(Eq. 2.14)}$$

$$\tau = \sigma_y \cdot \sin(\theta) \cdot \cos(\theta) - \sigma_x \cdot \cos(\theta) \cdot \sin(\theta) + \tau_{xy} \cdot \cos(\theta) \cdot \cos(\theta) - \tau_{yx} \cdot \sin(\theta) \cdot \sin(\theta) \quad \text{(Eq. 2.15)}$$

$$= \frac{1}{2} \cdot (\sigma_y - \sigma_x) \cdot \sin(2\theta) + \tau_{xy} \cdot \cos(2\theta) \qquad \text{(Eq. 2.16)}$$

From the latter equation it is possible to get $\tau = 0$ by choosing an orientation $\theta$ so that:

$$\tan(2\theta) = \frac{2 \cdot \tau_{xy}}{\sigma_x - \sigma_y} \qquad \text{(Eq. 2.17)}$$

There are two different solutions of $\theta$ ($\theta_1$ and $\theta_2$) corresponding to two different directions for which the shear stress is non-existing. These two directions are known as the principal axes of stress and are orthogonal. The corresponding normal stresses ($\sigma_1$ and $\sigma_2$) are called the *principal stresses* and can be presented mathematically by introducing Eq. 2.17 into Eq. 2.14:

$$\sigma_1 = \frac{1}{2} \cdot \left(\sigma_x + \sigma_y\right) + \sqrt{\tau_{xy}^2 + \frac{1}{4} \cdot \left(\sigma_x - \sigma_y\right)^2} \qquad \text{(Eq. 2.18)}$$

$$\sigma_2 = \frac{1}{2} \cdot \left(\sigma_x + \sigma_y\right) - \sqrt{\tau_{xy}^2 + \frac{1}{4} \cdot \left(\sigma_x - \sigma_y\right)^2} \qquad \text{(Eq. 2.19)}$$

Usually, the solutions of the two principal stresses are chosen so that $\sigma_1 \geq \sigma_2$. Hence, the principal stress in direction $\theta_1$, which defines a principal axis, is larger than the principal stress in the other direction ($\theta_2$) which identifies a principal axis.

Further, principal stresses can also be defined in **three dimensions** as test samples often are exposed to stresses in all directions. The notation is conveniently chosen so that $\sigma_1 \geq \sigma_2 \geq \sigma_3$, where $\sigma_1$ still is the so-called *maximum principal stress*. But now, the *minimum principal stress* is denoted by $\sigma_3$, and $\sigma_2$ is here the symbol for an *intermediate principal stress*.

The deduction of principal stresses in three dimensions is naturally more complicated than what has been shown here for 2D. But, for objects that have a cylindrical geometry both the intermediate and the minimum principal stress will be equal, typically. The reason of this is that they will both be acting radially towards the object, generated by the same confining (surrounding) pressure. Since all the tested samples in the work with this thesis are of cylindrical shape, the deductions in 3D will therefore not be carried out here. Instead, the relation $\sigma_2 = \sigma_3$ is set up, and only $\sigma_1$ and $\sigma_3$ will be used in this thesis.

### Mohr's stress circle

First, consider the basic theory about principal axes in two dimensions again.

The coordinate system can be reoriented so that the x-axis and the first principal axis are parallel, while also the y-axis is parallel with the other principal axis. Based on Eq. 2.14 and Eq. 2.16 the normal and the shear stress in a general direction $\theta$ relative to the x-axis can then be determined by:

$$\sigma = \frac{1}{2} \cdot (\sigma_1 + \sigma_2) + \frac{1}{2} \cdot (\sigma_1 - \sigma_2) \cdot \cos(2\theta) \qquad \text{(Eq. 2.20)}$$

$$\tau = -\frac{1}{2} \cdot (\sigma_1 - \sigma_2) \cdot \sin(2\theta) \qquad \text{(Eq. 2.21)}$$

In a $\tau$-$\sigma$ diagram corresponding values of these two parameters can be plotted. The plot will have the shape of a circle as illustrated in Fig. 2.8, with its centre on the $\sigma$-axis and having a radius equal to $(\sigma_1 - \sigma_2)/2$. Such a circle is called a *Mohr circle*.

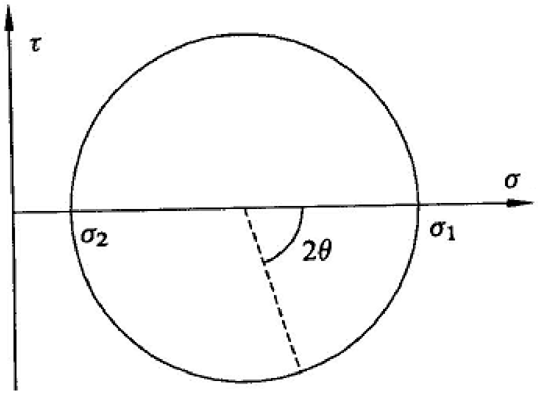

Figure 2.8: *Basic illustration of the Mohr circle, showing how it connects the principal stresses (here:* $\sigma_1$ *and* $\sigma_2$*).*

Similar to the theory of the principal stresses, the construction of Mohr circles in **three dimensions** is also considerably more complicated than in 2D. But since the testing of cylindrical samples provides the opportunity to set $\sigma_2 = \sigma_3$ the basic theory shown here will be applicable, with $\sigma_1$ as the maximum principal stress and $\sigma_3$ as the minimum.

Mohr circles are commonly used as tools when analyzing rock failure mechanisms, and form the basis of the failure related Mohr-Coulomb criterion. (See Paragraph *2.3.6 Mohr-Coulomb criterion*).

## 2.3.2 Strain (ε)

When regarding deformation in mechanics and physics, the term *strain* (ε) is usually used as a measure. Deformation of an object (or a "body") typically occurs when it is exposed to external forces. To get an understanding of deformation and strain a sample can be considered, and especially the position of a specific particle (or point) within the sample. The initial position of the particle can be denoted by x, y, z, as shown in Fig. 2.9:

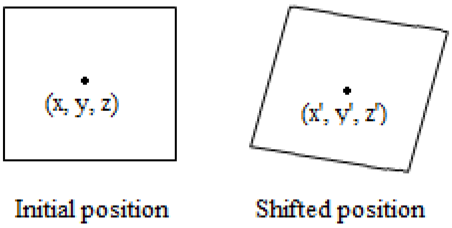

Figure 2.9: *Illustration of deformation of a sample (or a "body"), after being exposed to external forces.*

After external forces have acted on the body, the position of the specific particle has been shifted from its initial. The shift in x-, y- and z-direction can be denoted by the quantities *u*, *v* and *w*, respectively. These quantities can be referred to as the displacement of the particle. It is important that the signs of the displacements (*u*, *v* and *w*) are consistent with the signs of the stresses, defined in Paragraph *2.3.1 Stress (σ)*. The displacements are considered positive when directed in the negative direction of the axes. Thus, the shifted (new) position of the particle will have the coordinates (x', y', z'), mathematically represented by:

$$x' = x - u \tag{Eq. 2.22}$$

$$y' = y - v \tag{Eq. 2.23}$$

$$z' = z - w \tag{Eq. 2.24}$$

In some cases the displacements $u$, $v$ and $w$ are equal for each and every particle within a body. Then, the displacement is simply a translation of a rigid body. But if the positions of the particles within a body instead are changed relatively to each other so that the new positions cannot be obtained simply by a rigid translation of it, the body is said to be strained.

Fig. 2.10 shows an example of such a strained body, where a cylindrical shaped core (e.g. chalk core) has been strained due to external forces $F_x$ and $F_y$. This example shows the experience from the two types of tests performed in the work with this thesis – hydrostatic tests and deviatoric tests. The figure illustrates the case where a (chalk) core is exposed to forces in all directions. Due to the core's cylindrical shape all forces in the horizontal plane will be equal, $F_y$. When the (axial) forces in the x-direction ($F_x$) are equal to $F_y$ the core is loaded hydrostatically, while in the case where $F_x$ deviates from $F_y$ the core experience a deviatoric load. The latter type of test is typically performed by keeping the surrounding force in the y-direction constant while the axial force in x-direction is increased to a higher level.

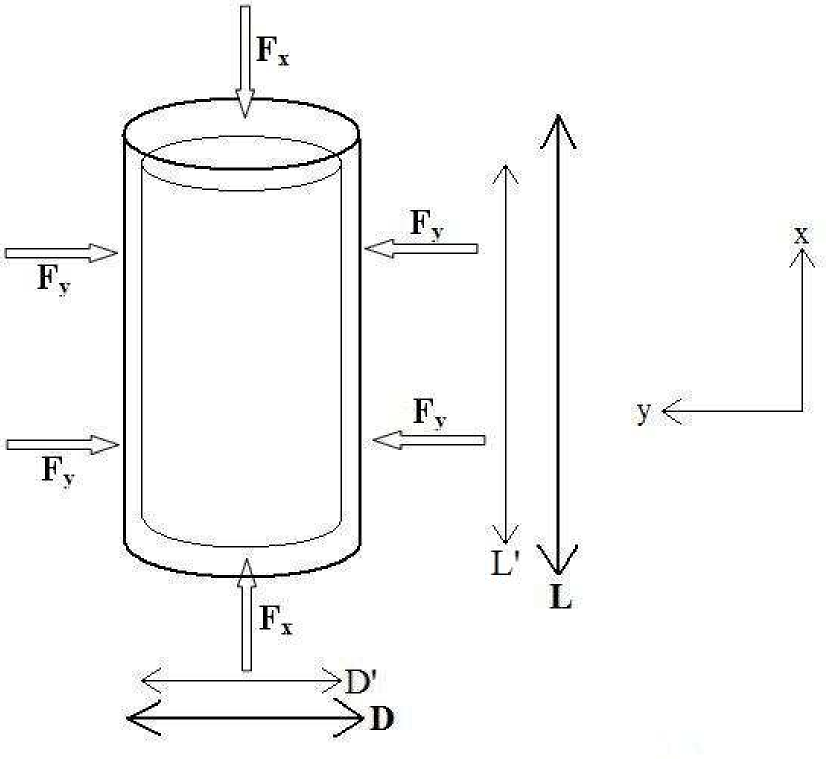

Figure 2.10: *Deformation on a cylindrical object (e.g. chalk core) caused by* hydrostatic *compression. (*D*: Diameter.* F*: Force.* L*: Length). (From Øvstebø (2009)).*

Strain ($\varepsilon$) can be defined as the deformation relative to the original length – both in the same direction. Therefore, there must be defined one equation in each direction of deformation. Considering Fig. 2.10 the strain in the x-direction is defined by

$$\varepsilon_x = \frac{\Delta L}{L} = \frac{L - L'}{L} \qquad \text{(Eq. 2.25)}$$

while the strain in the y-direction is given by

$$\varepsilon_y = \frac{\Delta D}{D} = \frac{D - D'}{D} \qquad \text{(Eq. 2.26)}$$

where

$\varepsilon_x$: Strain in the x-direction. (“Axial” strain).
$\varepsilon_y$: Strain in the y-direction.
*L & D*: Length and diameter, respectively, prior to compression.
*L’ & D’*: Length and diameter, respectively, after compression.

The quantity of strain, often called *elongation*, is dimensionless, and usually given as a percentage. A necessary remark about the term *deformation* is that it has to be understood as a *change in the normal shape*. This means that a “deformed length” can either be longer or shorter than the initial length. Through a hydrostatic compression all lengths in a body will get shorter than initially. On the other hand, the case of so-called uniaxial compression is different. A simple sketch to present the latter is shown in Fig. 2.11:

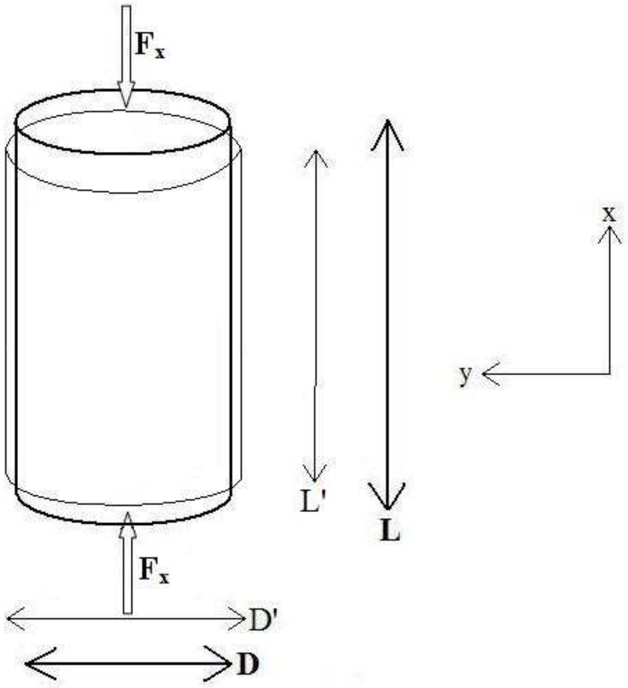

Figure 2.11: *Deformation on a cylindrical object (e.g. chalk core) caused by* uniaxial *compression. (*D*: Diameter.* F*: Force.* L*: Length).*

During a uniaxial load, where forces only are exerted in one direction (*here:* axial, x-direction) and there exists no force or pressure support in any other direction, the compression in the force direction will result in an expansion in another (the y-) direction.

No matter what type of load a sample is being exposed to, it will deform in more than one direction, (except in the case of uniaxial strain tests where the specific purpose is to maintain strain in one direction only). Hence, it can be of interest to measure the total (summed) deformation of the sample, known as *volumetric strain* ($\varepsilon_{vol}$). For instance when calculating the bulk modulus ($K$) – an elasticity modulus – the volumetric strain is one of two parameters. Eq. 2.18 shows this standard formula for calculating $\varepsilon_{vol}$:

$$\varepsilon_{vol} = \frac{\Delta V}{V} = \varepsilon_x + \varepsilon_y + \varepsilon_z \qquad \text{(Eq. 2.27)}$$

where $\varepsilon_x$, $\varepsilon_y$ *and* $\varepsilon_z$ *are* the strains in the x- (*here:* “Axial” strain), y- and z-direction, respectively. The cores that have been tested in this work have been cylindrical, and in these cases the volumetric strain is made up of an axial ($\varepsilon_x$) and a radial ($\varepsilon_r$) strain:

$$\varepsilon_{vol} = \varepsilon_x + (2 \cdot \varepsilon_r) \qquad \text{(Eq. 2.28)}$$

There was not used equipment for measuring this radial deformation in the work with this thesis. However, by assuming that the tested object has an isotropic behaviour – i.e. that the physical properties are the same in all directions – it can also be assumed that the axial and the radial strain are (approximately) equal during hydrostatic loading. Thus, the volumetric strain can be presented as being dependent on axial strain only:

$$\varepsilon_{vol} = \varepsilon_x + (2 \cdot \varepsilon_x) = 3 \cdot \varepsilon_x \qquad \text{(Eq. 2.29)}$$

### 2.3.3 Bulk modulus (*K*-modulus)

The *bulk modulus*, often referred to as the *K-modulus*, is an important elasticity modulus when regarding *hydrostatic* conditions, and belongs to the theory of linear elasticity. This means that there are linear relationships between applied stresses and the resulting strains. When an object is exposed to the same stress (force) in the three orthogonal directions it is said to be hydrostatically compressed, and $K$ is understood as a measure of the object’s ability to resist this compression. The hydrostatic compression will cause deformation in all directions, and the ratio of hydrostatic stress ($\sigma_h$) relative to the volumetric strain ($\varepsilon_{vol}$) presents the definition of the bulk modulus:

$$K = \frac{\sigma_h}{\varepsilon_{vol}} \qquad \text{(Eq. 2.30)}$$

The dimension of the bulk modulus will be the same as for stress, since the strain is dimensionless. The value of strain is typically very small compared to the hydrostatic stress, which makes the K-modulus large. In those cases, if the value of stress is given in

MegaPascal [MPa], the bulk modulus is often given in GigaPascal [GPa]. The hydrostatic stress is the same in both the x-, y- and z-direction:

$$\sigma_h = \sigma_x = \sigma_y = \sigma_z \quad \text{(Eq. 2.31)}$$

and the volumetric strain is shown in Eq. 2.29 to be three times the axial strain. Then, with the mentioned assumption of isotropy, the bulk modulus can be presented like this:

$$K = \frac{\sigma_h}{3 \cdot \varepsilon_x} = \frac{(\sigma_h / \varepsilon_x)}{3} \quad \text{(Eq. 2.32)}$$

As will be shown in Paragraph *2.5.1 Standard triaxial compression test* hydrostatic (axial) stress ($\sigma_h = \sigma_x$) can be plotted versus axial strain ($\varepsilon_x$) for a hydrostatic loading. The plotted curve will be straight with a slope equal to $\sigma_x/\varepsilon_x$. Thus, the bulk modulus can easily be calculated by dividing the slope value by 3. (See Eq. 2.32).

In the plots presented in this thesis, the axial strain values on the x-axis will be given as percentages, so the slope must me multiplied by 100 to get the correct value of *K*. In addition, to get the *K* value in GPa the value must be divided by 1,000. When the slope value is *a* from the general linear equation:

$$y = a \cdot x + b \quad \text{(Eq. 2.33)}$$

the equation for calculating bulk modulus from the plot will then be:

$$K\,[\text{GPa}] = \frac{a\,[\text{MPa}]}{3} \cdot \frac{100}{1000} = \frac{a\,[\text{MPa}]}{30} \quad \text{(Eq. 2.34)}$$

If the x-axis consisted of volumetric strain instead, the *K*-modulus could be obtained by dividing the slope by 10. But it should be noticed that far from all materials behave isotropically, so the results from using this assumption will not be entirely comparable with standard calculations from using Eq. 2.30. But as an approximation it is a good and easy method, and the different results from using this same method with the assumption can of course be compared with each other.

### 2.3.4 Young's modulus (*E*-modulus)

Another elasticity parameter is the *Young's modulus*, also called *E-modulus*. It differs from the *K*-modulus by concerning another type of load, namely the *uniaxial* (or deviatoric). Fig. 2.11 shows the typical deformation of a test core that has been loaded uniaxially. But, similar to *K*, Young's modulus is also included in the term of linear elasticity. With basis in this theory, the following equation can be written for the linear relationship between axial stress ($\sigma_x$) and axial strain ($\varepsilon_x$) under a uniaxial load:

$$\varepsilon_x = \frac{1}{E} \cdot \sigma_x \quad \text{(Eq. 2.35)}$$

which also is known as Hooke's law, and where $E$ is the symbol for Young's modulus.

Young's modulus can be defined as a sample's (material's) resistance against uniaxial compression (caused by uniaxial stress), and can be considered as a measure of the material's stiffness. Transforming Hooke's law gives the equation for calculating $E$:

$$E = \frac{\sigma_x}{\varepsilon_x} \qquad \text{(Eq. 2.36)}$$

which, equivalent to the case for $K$, tells that this elasticity modulus can be found directly from an axial stress versus axial strain plot for a uniaxial (or deviatoric) loading. Also equivalent to the bulk modulus; if $a$ is the slope from the linear curve, $\sigma_x$ is given in MPa and $\varepsilon_x$ is a small number (as in most cases) given as a fraction instead of percentage, the $E$-modulus can be calculated in GPa by multiplying Eq. 2.27 by 100 and dividing by 1,000:

$$E\,[\text{GPa}] = a\,[\text{MPa}] \cdot \frac{100}{1000} = \frac{a\,[\text{MPa}]}{10} \qquad \text{(Eq. 2.37)}$$

## 2.3.5 Failure mechanisms

If an object of rock material is exposed to stresses of sufficient size it will eventually go into failure. When failure occurs, the rock changes shape permanently, internal bondings in the material break and the object may even fall apart. In addition, the material loses ability to carry loads (additional) loads, and will deform at a higher rate than before failure for the same increase in loads.

The process of rock failure is very complex and still not entirely understood. Instead of derivations from laws of physics the theory of rock failure is therefore rather based on (mathematical) descriptions of observed behaviour obtained from experimental work. When testing a sample of a certain bulk it should be noticed that the concept of rock failure is connected to the condition of the solid framework. In other words, the failure-causing stresses are the *effective* stresses working on the framework, or the external stress minus the amount of stress carried by the pore fluid.

A term which is commonly used together with failure is *strength*, as this is determined by the stress level at which a rock typically fails. Rock strength is not a uniquely defined parameter and will therefore only be "meaningful" when the stress geometry (i.e. the type of test in a laboratory setting) is specified.

Two of the most important tests used for measuring rock strength are the *uniaxial* and the *triaxial* test. A uniaxial test is performed at zero confining stress, and is therefore also called unconfined compression test. For a cylindrical shaped core the stress will only be applied in the axial direction, and there will be no radial stress. Triaxial tests are on the other hand carried out with a non-zero confining stress. Hence the test sample will be exposed to stresses in all directions. These principles are shown back in Fig. 2.10 and Fig. 2.11.

In the following, three failure mechanisms will be presented briefly. An object which is in tension and exposed to excessive tensile stress, may eventually go into *tensile failure*. Compressed objects will fail in other ways. In both uniaxial and triaxial tests the most common failure mechanism is *shear failure*, caused by excessive shear stress. A third failure mechanism, which is usually observed in highly porous materials where the grain skeleton forms a quite open structure – such as chalks – is *pore collapse*. This is also known as compaction failure, and may occur under excessive hydrostatic stress. These three mechanisms of failure are sketched in Fig. 2.12:

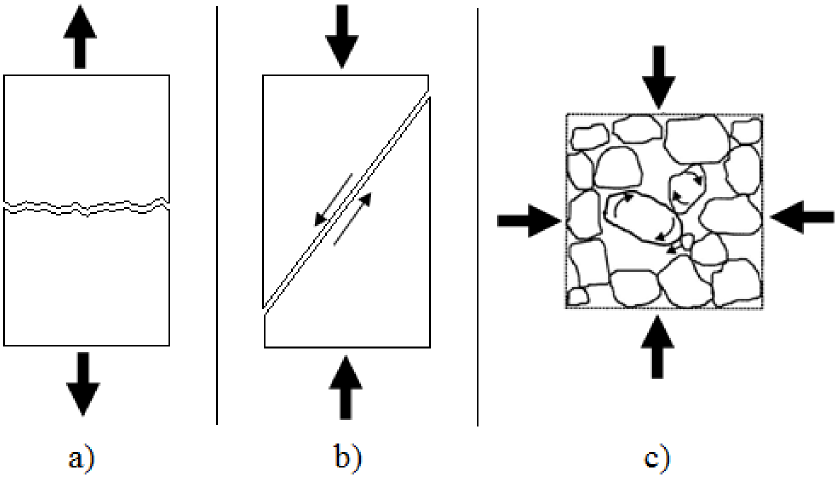

Figure 2.12: *Sketches of typical fracture planes in the cases of* a*) tensile failure and* b*) shear failure, and reorientation of grains when experiencing* c*) compaction failure due to pore collapse. (Inspired by Fjær et al. (2008)).*

## Tensile failure

When the effective tensile stress across some plane in a sample exceeds the critical limit of the material, tensile failure will occur. The critical limit is called the tensile strength ($T_0$) of the material, having the same dimension as stress, and this is a characteristic property of the rock material. For most sedimentary rocks the tensile strength is fairly low. As sketched in Fig. 2.12 *a)*, a sample suffering tensile failure will typically split along one (or very few) fracture plane(s) oriented normal to the direction of the tensile stress. It is common that such failure planes arise from pre-existing cracks in the material oriented the mentioned way.

## Shear failure

When the shear stress along some plane in a sample is increased to a sufficiently high level, shear failure will occur. The fracture plane will typically form like shown in Fig. 2.12 *b)* and due to a fault zone developing along this plane the two parts will move relative to each other in a frictional process. The failure mode for materials that undergo uniaxial (unconfined compression) loading or triaxial loading with low effective radial support will typically be shear failure. $\tau_{max}$ is the symbol of the critical shear stress at which shear failure will occur.

## Pore collapse (compaction failure)

As in the case of chalk, some materials have a quite open internal structure and therefore also a high porosity. During compression, typically under (pure) hydrostatic loading and especially when there is a certain radial support, grains may break from each other and/or loosen from the structure. These loose particles can be pushed, twisted and reorganized so that they fill the larger voids, resulting in a closer packing of the material. Fig. 2.12 *c)* shows an illustration of these changes, where the sample as a whole will experience compaction.

Special for chalk is that the grains may be of considerable different sizes, where some of the smaller grains can be pushed directly into the pore space after being loosened from the structure. On the other hand, in for instance sandstones, the pore sizes are typically of the same order of magnitude as the size of the grains. In such cases, the pore collapse will rather consist of reorientation of grains to better fill the voids. However, even though compaction failure as a whole is considered to be a matter of pore collapse, this type of failure actually also arise from excessive *shear* forces acting through grains and grain contacts locally. Hence, pore collapse (compaction failure) might as well be regarded as shear failure which is distributed within the material.

### 2.3.6 Mohr-Coulomb criterion

A test sample that suffers from shear failure will experience a fracture which splits the sample into two separated bodies. If the sample is still exposed to stress, there will be a relative movement between these two bodies which is counteracted by a frictional force. Such frictional forces are dependent on the force normal to the contact plane between the two bodies. A reasonable assumption can then be stated, saying that the critical shear stress ($\tau_{max}$) depends on the effective normal stress ($\sigma'$) acting over the failure plane. This assumption is called Mohr's hypothesis and can be presented by the relationship in Eq. 2.38:

$$|\tau_{\max}| = f(\sigma') \qquad \text{(Eq. 2.38)}$$

From this definition failure criteria can be deduced, at which the intermediate principal stress has no effect. Hence, pure shear failures are only dependent on the minimum ($\sigma_3'$) and the maximum ($\sigma_1'$) principal stresses, (given by their effective values).

One of the most frequently used criteria is the *Mohr-Coulomb criterion*. Based on Eq. 2.38 and by assuming that $f(\sigma')$ is a linear function of $\sigma'$, the following relationship can be set up:

$$|\tau| = S_0 + \mu \cdot \sigma' \qquad \text{(Eq. 2.39)}$$

where $S_0$ is the inherent shear strength – commonly called *cohesion* – of the material, and $\mu$ is the *coefficient of internal friction*. The constant factor $\mu$ is a parameter contributing to determine the frictional force on the failure plane when shear failure has already occurred. In contrast to this, the cohesion ($S_0$) says something about the state of the material at the moment the failure is initiated. It can be said that motion along the failure plane before failure is initiated – i.e. when the plane is still intact – is resisted by the internal cohesive force of the material. To be able to achieve failure at all this resistivity must be defeated, and cohesion ($S_0$) can be defined as this internal strength. Or in other words; cohesion is equal to the weakest force able to initiate failure, in cases where there is no normal stress present to generate friction ($\sigma' = 0$) (Jaeger, 2007).

Fig. 2.13 illustrates the Mohr-Coulomb criterion where a Mohr circle touches the failure line and where $\varphi$ is the *angle of internal friction* (or simply *friction angle*), having the following relation to the material's coefficient of internal friction ($\mu$):

$$\tan(\varphi) = \mu \qquad \text{(Eq. 2.40)}$$

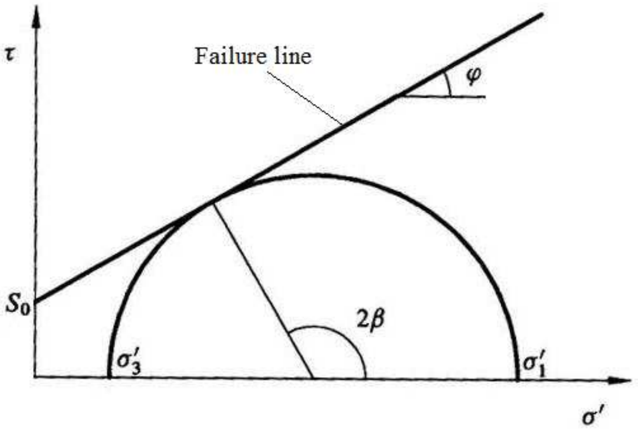

Figure 2.13: *The Mohr-Coulomb criterion illustrated in a τ-σ' diagram, showing the relation between a Mohr circle, its connected minimum* ($\sigma_3$) *and maximum* ($\sigma_1$) *principal stress, the failure line, the cohesion* ($S_0$) *and the friction angle* ($\varphi$)*.*

In the *τ-σ'* diagram the linear Mohr-Coulomb failure line represents the material's critical combination of shear and normal stress for failure to happen. Most materials have a certain shear strength (cohesion), and the failure line will not go below this shear stress value in the diagram. The exception is cohesion-less materials, for which the failure line will go through the origin. If the Mohr circle for a sample of a certain material at certain conditions does not reach up to the failure line, this means that failure will not be initiated along any plane within the sample. An increase in loads onto the sample, and hence also effective stresses, will make the Mohr circle expand and eventually touch the failure line. At the stress conditions where the failure line becomes a tangent to the circle, the failure criterion is fulfilled for some plane(s) within the sample, and failure will occur.

Fig. 2.13 also illustrates that the intermediate effective stress has no effect on the Mohr-Coulomb criterion. Hence, this criterion is characterized as being two-dimensional. But as long as the tested samples are cylindrical and all "lateral" stresses are equal, the test conditions may also be considered as 2D. In other words, the minimum and intermediate effective stresses are equal, and there will be no conflict between test results and the criterion.

Graphically, the friction angle ($\varphi$) is the angle between the horizontal $\sigma'$-axis and the failure line, and hence determines the slope of the latter. The cohesion ($S_0$) is determined by the point where the failure line intersects the vertical $\tau$-axis, i.e. it is equal to the shear stress when there is no effective normal stress present ($\sigma' = 0$). Another parameter which is introduced in the figure is the angle $2\beta$ which defines the position of the point where the failure line is the tangent to the Mohr circle. The stress values at this point are of interest since this specific combination of $\tau$ and $\sigma'$ will initiate failure in the material. They can be expressed mathematically by the following equations:

$$|\tau| = \frac{1}{2} \cdot (\sigma_1' - \sigma_3') \cdot \sin(2\beta) \qquad \text{(Eq. 2.41)}$$

$$\sigma' = \frac{1}{2}\cdot(\sigma_1' + \sigma_3') + \frac{1}{2}\cdot(\sigma_1' - \sigma_3')\cdot\cos(2\beta) \quad \text{(Eq. 2.42)}$$

Some of the parameters that are shown graphically in a $\tau$-$\sigma$' diagram in Fig. 2.13, are also shown in a cylindrical test sample setting in Fig. 2.14.

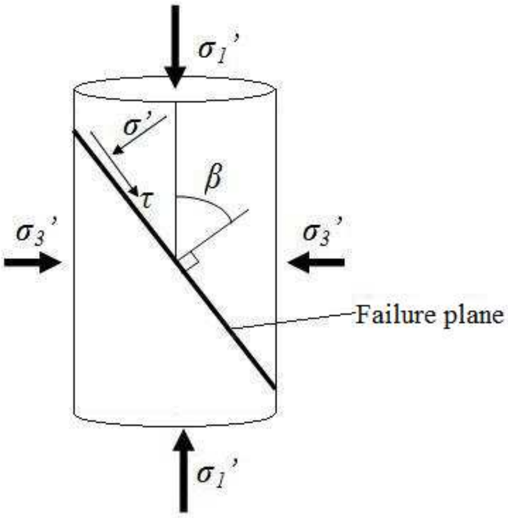

Figure 2.14: *Illustration of the relations of some parameters to a cylindrical shaped sample; principal stresses* ($\sigma_3$' *and* $\sigma_1$'), *a shear failure plane, the stresses* ($\tau$ *and* $\sigma$') *acting on the plane and the orientation* ($\beta$) *of it.*

This figure shows how the different stresses are associated with a cylindrical shaped sample and its (possible) shear failure plane. But it also illustrates how $\beta$ is connected to the orientation of the failure plane, as this parameter represents the angle for which the Mohr-Coulomb failure criterion is fulfilled. The orientation (failure) angle ($\beta$) and the friction angle ($\varphi$) are related to each other by this simple equation:

$$\beta = \frac{\pi}{4} + \frac{\varphi}{2} = 45^o + \frac{\varphi[^o]}{2} \quad \text{(Eq. 2.43)}$$

Since $\varphi$ is a constant value in the Mohr-Coulomb criterion, this will be the only parameter affecting $\beta$.

In the case of uniaxial compression there will only be a load in one (the axial) direction. This axial load generates the maximum effective stress ($\sigma_1$') and since there is no radial support $\sigma_3$' can be set equal to zero. Materials have a certain strength to resist uniaxial compression, denoted by $C_0$, but at increased load the material will eventually go into failure. The maximum effective stress ($\sigma_1$') at the moment of failure is equal to the mentioned strength ($C_0$), which can be given by this mathematical expression:

$$C_0 = 2\cdot S_0\cdot\frac{\cos(\varphi)}{1-\sin(\varphi)} = 2\cdot S_0\cdot\tan(\beta) \quad \text{(Eq. 2.44)}$$

when the failure mechanism is *shear failure*.

The uniaxial compression strength is dependent on the cohesion ($S_0$) and the friction angle ($\varphi$), but by using the relationship in Eq. 2.43 the latter can be replaced by the failure angle ($\beta$). Finally, the Mohr-Coulomb criterion can be expressed with principal stresses in the following equation:

$$\sigma_1' = C_0 + \sigma_3' \cdot \tan^2(\beta) = 2 \cdot S_0 \cdot \tan(\beta) + \sigma_3' \cdot \tan^2(\beta) \qquad \text{(Eq. 2.45)}$$

## 2.3.7 *q-p'* plot

Mechanical properties of rocks can typically be determined by performing several triaxial compression tests at different confining pressures, generating radial support to varying extents. Stress-strain diagrams will provide studies with elastic properties and data associated with failure (or yield). (Please see Paragraphs *2.5.1 Standard triaxial compression test* and *2.5.3 Yield*). Such failure data (failure/yield points) may be given in pairs with their corresponding confining stresses and displayed graphically in different types of diagrams. One of these diagram types has already been presented, namely the *τ-σ'* plot. But another very common way of displaying strength data is by using the *q-p' plot*. At least within soil mechanics *q-p'* plots are standard for plotting of failure surfaces, but this trend is increasing in rock mechanics too.

The two parameters which constitute this kind of plot are the *generalized shear stress* (*q*) and the *mean effective stress* ($\bar{\sigma}'$), usually denoted by *p'*. Based on the different effective stresses on a test sample, these two parameters can be computed from the following equations:

$$q = \frac{1}{\sqrt{2}} \cdot \sqrt{(\sigma_1' - \sigma_2')^2 + (\sigma_2' - \sigma_3')^2 + (\sigma_1' - \sigma_3')^2} \qquad \text{(Eq. 2.46)}$$

$$p' = \bar{\sigma}' = \frac{1}{3} \cdot (\sigma_1' + \sigma_2' + \sigma_3') \qquad \text{(Eq. 2.47)}$$

both of them having the same dimensions as stress, naturally.

Since the two radial stresses in a standard triaxial compression test on a cylindrical sample are the same, it is common to set $\sigma_2' = \sigma_3'$. (Due to cylindrical geometry they are both generated from the same confining pressure). Thus, the two equations above can be simplified to the equations shown below:

$$q = \sigma_1' - \sigma_3' \qquad \text{(Eq. 2.48)}$$

$$p' = \frac{\sigma_1' + 2 \cdot \sigma_3'}{3} \qquad \text{(Eq. 2.49)}$$

When performing a specific test, its stress path can be traced as a line in the *q-p'* plot. With increased loads the sample will eventually go into failure (or yield), and in the *q-p'* diagram this is illustrated by the stress path crossing the curve itself, or the *failure envelope*. This way, the *q-p'* plot can be drawn by the strength results of several triaxial tests on the same material.

Each test will generate one pair of strength values, and hence one pair of *q-p'* values to form a single point on the curve. When a number of tests have been performed providing the diagram with an adequate amount of plotting points, the failure envelope of the material can be drawn.

This failure envelope bounds the elastic region in the *q-p'* plot, i.e. stress conditions within the envelope have not reached failure and thus not caused any permanent deformation to the material. As seen in Fig. 2.15 the envelope consists of two main parts, namely the linear *shear failure line* for lower values of *p'* before transition to the *end cap* part for higher *p'* values.

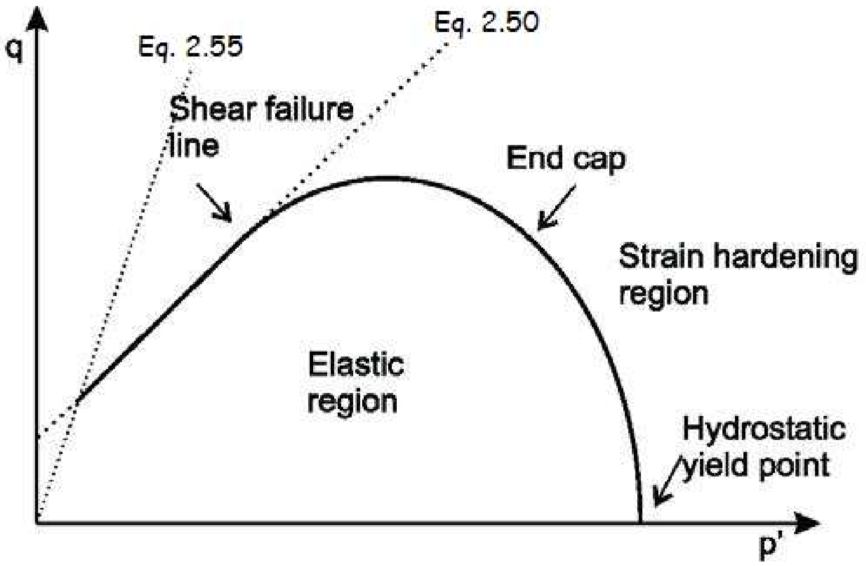

Figure 2.15: *A typical* q-p' *plot, showing the parts of the failure envelope and how it bounds the elastic region. (From Madland (2005); Korsnes (2007)).*

The different parts of the failure envelope typically tell which failure mechanism will be dominant for different stress combinations. (See Paragraph *2.3.5 Failure mechanisms*). A compression test performed on a sample by uniaxial (unconfined compression) loading or triaxial loading with low effective radial support, will typically end with shear failure. The results from such a test will create a *q-p'* plotting point on the linear shear failure line. As also described in the paragraph regarding failure mechanisms, tests performed at higher confining pressure (higher values of $\sigma_3'$) typically experience compaction failure, or pore collapse. Hence, this is the dominant failure mechanism on the end cap part of the failure envelope. It can also be mentioned that the envelope can be drawn all the way down to the *p'*-axis left of the shear failure line by a *tensile failure line*. Results from tensile tests will land on this line, naturally. However, this is not discussed any further here since the tests that are carried out in this work are (almost) exclusively compression tests.

By involving cohesion ($S_0$) and friction angle ($\varphi$) a mathematical relation between the Mohr-Coulomb criterion and the shear failure line in the *q-p'* plot can be presented. This part of the failure envelope can be defined by the following relation (Risnes et al., 1998):

$$q = \frac{6 \cdot \sin(\varphi)}{3 - \sin(\varphi)} \cdot p' + \frac{6 \cdot S_0 \cdot \cos(\varphi)}{3 - \sin(\varphi)} \qquad \text{(Eq. 2.50)}$$

This is equivalent to the basic equation for a linear relationship:

$$y = a \cdot x + b \tag{Eq. 2.51}$$

where *y* and *x* represent the two variables *q* and *p'*, respectively, and where the factor:

$$a = \frac{6 \cdot \sin(\varphi)}{3 - \sin(\varphi)} \tag{Eq. 2.52}$$

corresponds to the slope of the shear failure line, while the term:

$$b = \frac{6 \cdot S_0 \cdot \cos(\varphi)}{3 - \sin(\varphi)} \tag{Eq. 2.53}$$

corresponds to the point where the failure line would intersect the *q*-axis. By transforming the two latter equations it is possible to determine both the friction angle and the cohesion from the *q-p'* plot – if the shear failure line is already known or estimated (e.g. by linear regression, as will be done in this present work). The friction angle value typically lies within the range of (0°, 90°). For these values, and based on Eq. 2.52 and Eq. 2.53, the following correlations can be put up:

- A steeper shear failure line (*higher a*) correlates to a *higher friction angle* ($\varphi$).
- A higher intersection point with the *q*-axis (*higher b*) correlates to a *higher cohesion value* ($S_0$).

When comparing failure envelope curves, as will be done in Chapter *5 Discussion*, these two clues can be useful for quick (but not detailed) interpretations of the mechanical parameters $S_0$ and $\varphi$, and hence also $\beta$ and $\mu$.

As observed in Fig. 2.15 the shear failure line is not traced all the way back to the *q*-axis, but is rather "cut off" by another broken linear line through the origin. This dotted line determines the minimum value of the shear failure line, and is based on connecting Eq. 2.48 and Eq. 2.49 (for calculating *q* and *p'*, respectively) by eliminating the term for maximum effective stress ($\sigma_1'$). The procedure is shown below, resulting in the equation for the broken linear line:

$$q = \sigma_1' - \sigma_3' \Rightarrow \qquad \sigma_1' = q + \sigma_3' \tag{Eq. 2.54}$$

$$p' = \frac{\sigma_1' + 2 \cdot \sigma_3'}{3} = \frac{(q + \sigma_3') + 2 \cdot \sigma_3'}{3} \Rightarrow \qquad q = 3 \cdot p' - \sigma_3' \tag{Eq. 2.55}$$

During a compression test, the lowest applicable value for the radial (minimum) effective stress is zero. In such a case, Eq. 2.55 becomes the linear line through the origin with the slope 3:1, which determines the lower end point of the shear failure line.

In the presentations within this thesis, shear failure lines will be calculated by the use of linear regression of plotting points, while second order polynomial regression is used for estimating the end cap parts of the failure envelopes.

## 2.4 Chemical aspects of water weakening

Through the last decade there has been comprehensive research on probable effects which aqueous chemistry may have on the mechanical strength of chalk. Among others, it has been observed that chalk in contact with seawater at high temperature (typically 130 °C) is considerably weaker than when it is exposed to distilled water. At least when creep and hydrostatic yield strength is regarded. Several different types of brines have been tested through the years, and common for most of them has been that typical physical parameters like density and viscosity are quite similar. (Madland et al., 2011). Hence, the chemical aspect of the water weakening effect has been given a lot of attention, and different theories have been suggested based on chemical nature. Some of the most widespread theories is here presented in the following subsections.

### 2.4.1 Dissolution

Even though chalk grain sizes may vary, they are generally very small. As a result of this, and the construction of chalks, pore fluids will be in contact with a very large surface area of solid particles. This makes fluid-rock interactions within the chalk highly possible. The type of chalk used in this experimental work, referred to as Liège outcrop chalk, has been studied with respect to this. Among others by Megawati et al. (2011), who found the specific surface area to be as high as 4.2 $m^2/g$.

The solubility of a compound determines to which extent it will dissolve into liquid phase under certain conditions. Based on this phenomenon, all chemical compounds have a solubility product constant ($K_{sp}$), mathematically defined by the product of the concentrations of produced ions divided by the product of the reactant concentrations (Sienko & Plane, 1974). A mineral's solubility is dependent on temperature in the matter that the solubility usually increases with increasing temperature.

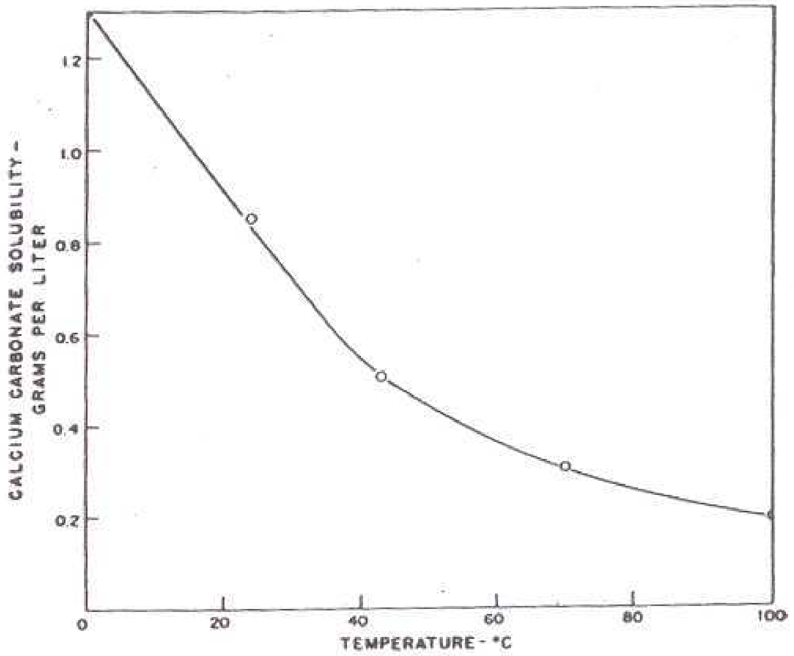

Figure 2.16: *The temperature effect on solubility of $CaCO_3$ in pure water, at a $CO_2$ pressure of 0.987 atm. (From Miller (1952)).*

The observation made for chalk, on the other hand, deviates from this general "rule", as increasing temperature will *not* result in increased rates of chemical dissolving reactions. Thus, chalk can be considered a famous "exception that proves the rule". This is an important and characteristic property of chalk which of course has to be taken into account when studying this material. Fig. 2.16 is shown as an illustration of this phenomenon, presenting results from an investigation of temperature effects on the solubility of chalk.

*NB! Please note that the following is not entirely relevant for the work with this thesis, as neither CO2 gas nor pH is considered. However, some simple chemical equations which in general consider dissolution/precipitation are listed and described and presented here as supplementary information about this subject.*

Carbon dioxide gas is soluble in water to a certain extent, depending on parameters such as temperature, partial pressure of $CO_2$ ($P_{CO2}$) and ionic strength of the water. This reaction affects the *dissolution* of chalk, as dissolved carbon dioxide ($CO_2(aq)$) generates weak carbonic acid:

$$CO_2(aq) \ + \ H_2O(l) \ \rightleftarrows \ [H_2CO_3] \ \rightleftarrows \ H^+ \ + \ HCO_3^- \qquad \text{(Eq. 2.56)}$$

Dissolution of chalk is, namely, dependent on the pH of the pore filling fluid. Under alkaline and neutral conditions chalk's solubility is almost negligible, which means that only very small amounts of solid chalk will dissolve into liquid. For chalk in contact with distilled water, with a pH value equal to 7 (ideally), the solubility product is about $K_{sp} = 3.8 \cdot 10^{-9}$. In more acidic solutions, where the amounts of protons ($H^+$) are higher, more chalk will dissolve (Madland, 2005). The following equation shows this reaction:

$$CO_3^{2-} \ + \ H^+ \ \rightleftarrows \ HCO_3^- \qquad \text{(Eq. 2.57)}$$

where carbonate ions from solid chalk ($CaCO_3(s)$) are transformed to bicarbonate. As the latter is formed, a scarcity of carbonate ions in the solution will arise. More calcium carbonate will therefore be dissolved to reach equilibrium, and this process can occur as long as there exists free protons ($H^+$) in the solution. Based on the mentioned reactions, the dissolution process of chalk in its entirety can be presented by this reaction balance:

$$CaCO_3(s) \ + \ CO_2(aq) \ + \ H_2O(l) \ \rightleftarrows \ Ca^{2+} \ + \ 2HCO_3^- \qquad \text{(Eq. 2.58)}$$

where solid chalk and dissolved carbon dioxide gas react with water to form bicarbonates. Calcium ions are bi-products. As mentioned, the solubility of $CO_2(aq)$ depends on some specific parameters – and if the partial pressure is constant while the temperature decreases the solubility of $CO_2(aq)$ actually increases (Madland, 2005). Hence, Le Chatelier's principle states that temperature reduction will force the reaction in Eq. 2.58 towards the right, and contribute to more dissolution of chalk.

### 2.4.2 Precipitation

The reaction balance in Eq. 2.58 may also be regarded from right to left, i.e. as a *precipitation* reaction. Consider an aqueous solution which is in equilibrium with solid calcium carbonate ($CaCO_3(s)$) and dissolved carbon dioxide gas ($CO_2(aq)$). If a pressure reduction is experienced, $CO_2$ gas will be released (Madland, 2005). To keep the amount of $CO_2(aq)$ stable at equilibrium it is stated from Le Chatelier's principle that the reaction process will go towards the left. As the number of bicarbonate ions in the solution decreases, the reaction in Eq. 2.57 will go towards the right – according to Le Chatelier – which reduces the number of protons ($H^+$). In other words, given that the partial pressure of $CO_2$ is high enough; pressure reduction will contribute to (re-)precipitation of $CaCO_3(s)$ and increased pH in the solution.

In some cases it can be of interest to determine whether a precipitation process will occur or not, with basis in a certain reaction balance. A reaction quotient can be used in this work when real ion concentrations are known. This quotient, usually referred to as the ion product ($Q$), is calculated the same way as the solubility product ($K_{sp}$), but with the known concentrations (Sienko & Plane, 1974). Computations of $Q$ and $K_{sp}$ are compared, and the three possible outcomes are as follows:

| | |
|---|---|
| $Q < K_{sp}$ | Undersaturated solution, precipitation will not occur. |
| $Q = K_{sp}$ | Solution in equilibrium, precipitation process may start. |
| $Q > K_{sp}$ | Supersaturated solution, precipitation will occur. |

An easy and quite common way of comparing the values of $Q$ and $K_{sp}$ is to calculate the $Q/K_{sp}$ ratio. Logarithmic values are often used in the calculations, typically when the values are of very high orders of magnitude, and let us easily deal with positive and negative numbers. In such cases, the ratio will be negative for undersaturated solutions and positive for supersaturated ones, while solutions at equilibrium are indicated by a ratio equal to zero; $\log[Q/K_{sp}] = \log[1] = 0$.

Ekofisk has been mentioned as a carbonate field where compaction of chalk has been experienced after seawater injection was started. The reservoir temperature at Ekofisk is typically close to 130 °C, and calculations show that when seawater gets in contact with chalk at this temperature, several minerals are supersaturated and will precipitate. These minerals are listed in Table 2.1 with their $\log_{10}[Q/K_{sp}]$ values showing to which extent they are supersaturated (Hiorth et al., 2008).

Table 2.1: *The supersaturated (positive ratios) minerals when seawater is flooded through chalk at 130 °C and 8 bar. For comparison, equivalent values are listed for Ekofisk Formation (EF) brine. (From Hiorth et al. (2008)).*

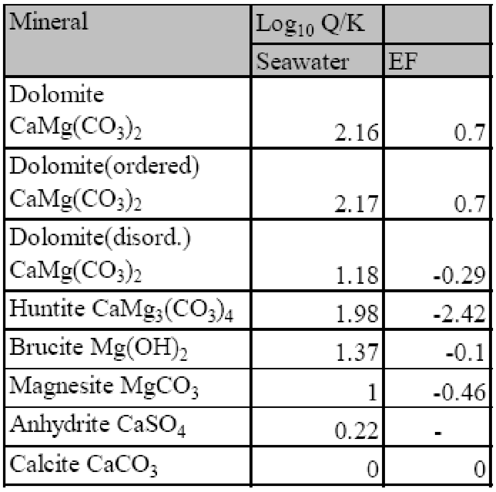

| Mineral | $\log_{10} Q/K$ | |
|---|---|---|
| | Seawater | EF |
| Dolomite $CaMg(CO_3)_2$ | 2.16 | 0.7 |
| Dolomite(ordered) $CaMg(CO_3)_2$ | 2.17 | 0.7 |
| Dolomite(disord.) $CaMg(CO_3)_2$ | 1.18 | -0.29 |
| Huntite $CaMg_3(CO_3)_4$ | 1.98 | -2.42 |
| Brucite $Mg(OH)_2$ | 1.37 | -0.1 |
| Magnesite $MgCO_3$ | 1 | -0.46 |
| Anhydrite $CaSO_4$ | 0.22 | - |
| Calcite $CaCO_3$ | 0 | 0 |

Most of these minerals contain either calcium ($Ca^{2+}$) or carbonate ($CO_3^{2-}$) or both, and when these common ions from a solution in equilibrium with calcite (chalk) precipitate as solids, the balance will be disturbed. In an attempt to re-establish equilibrium calcite (calcium carbonate) will dissolve from the solid formation into the solution. Or, to quote the well formulated concluding remark by Heggheim et al. (2004): “Enhanced dissolution of chalk is obtained if one or both of the common ions, $Ca^{2+}$ and $CO_3^{2-}$, is chemically removed from the solution.” *Where* this dissolution process occurs is an interesting topic. A reasonable assumption is that dissolution mainly takes place at the intergranular contacts, as they will experience the higher stresses within a bulk (Hiorth et al., 2008).

### 2.4.3 Ion substitution

Even though dissolution of chalk is a very reasonable explanation of the experienced water weakening, this cannot be the main mechanism alone. Dissolution processes are typically related to ion concentrations out of balance, so that solid material will dissolve until equilibrium is reached – as described in Paragraph *2.4.1 Dissolution*. But if this was the main mechanism, chalk exposed to distilled water (DW) would in the main be weakened by the lack of common ions (like calcium and carbonate) – and this does not tally with the reality (Korsnes et al., 2006b).

The strength and stability of chalk is affected when flooded with brines containing different ions, for instance $Ca^{2+}$, $Mg^{2+}$ and $SO_4^{2-}$. Extensive research has shown this. By analyzing the brine for chemical components (ions) both before and after flooding through chalk, many interesting observations have been made, and from them the theory of *ion substitution* has grown. Madland et al. (2011) flooded $MgCl_2$ brines through different types of outcrop chalk, and independent of the chalk type it was found that “a significant loss of magnesium and a considerable additional amount of calcium are detected in the effluent”. The same observations were made by Øvstebø (2009) for Stevns Klint chalk and in this present work for Liège chalk. Korsnes et al. (2006b) also observed this by slowly flooding seawater through chalk at high temperature (130 °C), and explained it to be a substitution process – illustrated by Fig. 2.17 – where $Mg^{2+}$ from the brine substitutes $Ca^{2+}$ on the solid chalk surface, and solid magnesium carbonate is formed. This substitution, where dolomite ($Ca,Mg(CO_3)_2$) is created, would lead to a change in the structure on the chalk surface, since the magnesium ions are much smaller than $Ca^{2+}$ ions. Such a transformation may affect the mechanical strength of the chalk.

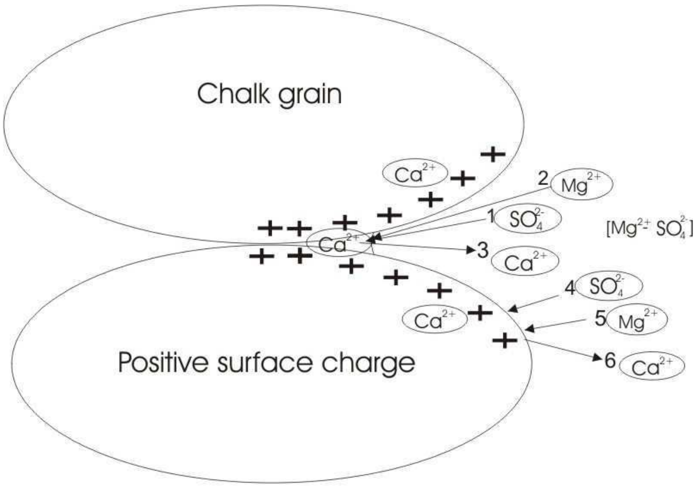

Figure 2.17: *Suggested mechanism for enhanced water weakening of chalk, on the basis of surface active ions and surface charge. (From Korsnes et al. (2006b)).*

In general, chalk's mechanical strength is related to the stability of the *intergranular contacts*. To which degree ion substitution actually will affect the mechanical strength of chalk is believed to be dependent on *where*, locally, the substitution process occurs. For example, it is not expected a very large effect on the strength if $Mg^{2+}$-$Ca^{2+}$ substitutions take place on chalk surfaces in pore bodies. On the other hand, such substitution occurring at intergranular contacts would probably be more actuating (Korsnes et al., 2006b), as these contacts are weakly cemented (Risnes et al., 1999) and far more determining for the strength of chalk.

An interesting observation made when flooding magnesium containing brines through chalk during creep, is that the increase in calcium concentration, $[Ca^{2+}]$, in the effluent water happened at the same time as $[Mg^{2+}]$ decreased, and in a quite similar scale. Results obtained by Øvstebø (2009) showed that the sum of $[Ca^{2+}]$ and $[Mg^{2+}]$ in the effluent water during creep was more or less equal to the amount of magnesium in the injected brine. In other words, there seemed to be a more or less one-to-one relation between lost magnesium and produced calcium, and such a result may support the theory of substitution.

However, more recent studies, among others by Madland et al. (2009) and Madland et al. (2011), claim that magnesium loss and calcium production must arise from other processes than this substitution alone. This statement is based on both calculations and observations, as more magnesium is left inside the chalk than what could be due to substitution only. One of the main basis for claiming this, are the calculated number of adsorption sites, i.e. the amount of calcium within the chalk which is accessible for substitution. The calculations were based on some simple analyses on a chalk core similar to the ones typically used for experimental testing – also in this present work. When the calculated number of adsorption sites has been exchanged, the substitution process is expected to cease, or at least slow down considerably. Since the observed calcium production during creep tests typically exceed the calculated accessible amounts, in addition to the observation that magnesium in the effluent water "never" increases to the same level as the injected amounts, substitution cannot be the main deformation mechanism. According to the mentioned calculations, magnesium from the flooded brine will hence rather be precipitated and form new mineral phases. If this happens, both calcite and silicates may be dissolved in considerable amounts and result in additional weakening of the chalk. Precipitated magnesium-bearing carbonates and magnesium-bearing clay-like minerals were detected by using SEM (Scanning Electron Microscope) methods (Madland et al., 2011).

### 2.4.4 Sulphate effects

**Sulphate's effect on the surface charge of chalk**

The surface charge on chalk grains is typically positive in the presence of seawater, due to a higher concentration of positively charged calcium ions than negatively charged sulphate ions (Strand et al., 2005). As a result of this, cations (positively charged) in the aqueous phase in the pores may be repelled from the chalk due to electrostatic repulsion. Especially, cations will be repelled from intergranular contacts, where positively charged surfaces together obstruct them to approach. This will counteract the mentioned substitution reaction, as $Mg^{2+}$ ions would not get close enough to the chalk surface to switch place with calcium ions. But with a larger amount of negatively charged components like sulphate ($SO_4^{2-}$) in the pore fluid, the surface charge may be decreased and substitution processes thereby promoted (Korsnes et al., 2006b). Fig. 2.17 illustrates such a case.

Strand et al. (2005) studied this kind of adsorption of sulphate ions onto the chalk's surface, and by means of a chromatographic method it was shown that the magnitude of adsorption increased with increasing temperature and $[Ca^{2+}]$. Calculations performed by Megawati et al. (2011) showed that there is also a pH dependency on sulphate adsorption. Hiorth et al. (2010) described the adsorption in terms of sulphate ions making complexes with calcium sites at the chalk's surface. The $[SO_4^{2-}]$ was claimed to be highest closer to surface, and decline with an exponential rate away from it – following a so-called Boltzmann type of distribution.

However, it should be mentioned that test results obtained by Madland et al. (2009) and Øvstebø (2009), among others, show that creep deformation of chalk is experienced when continuously flooding $MgCl_2$ brine at high temperature (130 °C). No sulphate was present in these cases, so sulphate is not an absolute need for chalk deformation to occur.

Substitution reactions may still occur in the *pore bodies*, even though sulphate is not present. Korsnes et al. (2006b) proved this by flooding synthetic seawater *without sulphate*, SSW–($SO_4^{2-}$), through chalk at high temperature and still observed some magnesium loss and calcium production. But, no enhanced weakening was experienced. This corresponds to what has already been mentioned for ion substitution; that it is the intergranular contacts that are of most interest when studying mechanical strength of chalk. Hence, it can be claimed that the presence of negatively charged sulphate ions may "help" the substitution process at these contact points and thereby enhance chalk weakening.

Megawati et al. (2011) also investigated the adsorption effect of sulphate, by exposing different types of outcrop chalk to $Na_2SO_4$ brines at 130 °C. They argued that the reduced mechanical strength of chalk may be explained by the "disjoining pressure" at the intergranular contacts. When sulphate is present in amounts large enough to change surface charges, this may result in interactions between the surfaces in terms of repulsive forces. These forces are suggested to originate the so-called total disjoining pressure, and are especially experienced close to the intergranular contacts. A correlation was found between increased magnitudes of disjoining pressure and reduced mechanical strength of chalk.

**Precipitation of sulphate-bearing minerals**

By reconsidering Table 2.1 in Paragraph *2.4.2 Precipitation*, it is seen that one of the calcium bearing supersaturated minerals when flooding seawater through chalk at 130 °C and a pressure of 8 bar, is anhydrite – which also consists of sulphate ($SO_4^{2-}$). Sulphate has been suggested from several sources to be an essential contributor to enhanced chalk dissolution in general. Precipitation together with calcium ions is one way to increase dissolution of chalk, as calcite will dissolve to establish equilibrium. An interesting observation is that this precipitation process is dependent on temperature, in the sense that the solubility of anhydrite experiences a maximum value at a certain temperature, and a retrograde behaviour with temperature in water (Heggheim et al., 2004). In other words the solubility decreases with increasing temperature (above this limit, naturally), and for temperatures as high as 130 °C very small amounts of free sulphate ions will be found in the solution. They will rather easily precipitate as anhydrite ($CaSO_4(s)$), causing a reduction in dissolved calcium and hence an increased dissolution of chalk formation.

Strand et al. (2005), who studied adsorption of sulphate ions onto the chalk’s surface during flooding experiments, experienced that the concentration of produced sulphate would not increase to the same level as the injected amounts. Such an observation supports the theory that an additional amount of sulphate is retained within the chalk material as part of precipitated solids. Hiorth et al. (2010) performed calculations on the loss of sulphate from the injected brine due to sulphate adsorption only. The calculations deviated somewhat from the experimental data obtained by Strand et al. (2005). But by including the contributed loss of sulphate due to anhydrite precipitation to the calculations, a much better fit to the experimental data was achieved.

### 2.4.5 Intergranular Pressure Solution (IPS)

Another important suggestion to attempt being able to explain the water weakening effect is the theory of *intergranular pressure solution* (IPS). This theory has been extensively studied by several different researchers, but despite this it is still poorly understood. However, the general understanding is that pressure solution is a water-assisted so-called physico-chemical process driven by effective stress-induced chemical potential. The process is divided into three steps occurring in series; starting with *dissolution* of solid materials at grain contacts, continuing with *diffusion* (transport) of solutes along the grain boundaries, and ending with *precipitation* at free pore walls (on surface of grains) in a chemically closed system (Rutter, 1983; Paterson, 1995; Renard et al., 1997; Gundersen et al., 2002).

Under conditions in the upper crust, compaction may be caused by (for instance) fracture. Typical for this kind of compaction is the substantial dependence on stress, and that it is more or less independent of time. In the contrary case, compaction creep caused by dissolution and precipitation processes is expected to be time-dependent. Hence, compaction of sediments and sedimentary and fault rocks occurring over geological periods of time seems to involve such dissolution and precipitation processes to a large extent (Zhang & Spiers, 2005). Other deformation mechanisms, such as intergranular sliding, have been proposed to be the main one responsible for compaction as discussed here. However, it has been found that intergranular sliding alone is not able to produce compaction strains in the orders of magnitude that are experienced. Overall deformation beyond this level requires the grains themselves to deform, which also can be explained by the theory of IPS (Fischmeister et al., 1982).

During the IPS process the slowest step will be the one controlling the overall deformation rate of material, as the three process steps occur in series. Finding this rate-limiting step has been the goal in a number of studies, but this work is complex and difficult. Hellmann et al. (2002) are among them who have experienced these difficulties, while Zhang et al. (2002) suggested that precipitation probably is the slowest step.

Over geological time spans IPS is considered an effective mechanism for deformation of both sedimentary and fault rocks. Indirectly, as a result of cementation of pore space, the effect of IPS also contributes to rocks’ losses of porosity and permeability (Gundersen et al., 2002). According to Zhang & Spiers (2005) this theory is especially valid for carbonate reservoirs, which to a great extent experience compaction and deformation.

The main parameters influencing IPS are understood to be grain size, effective stress, temperature, chemistry of pore fluids and mineralogy (Rutter, 1983). Experimental results from Zhang et al. (2002) suggest that compaction strain rates of porous aggregates will be enhanced by decreasing grain size and increased applied stress. In other words, rock deformation as a whole may be related to deformation of the individual grains themselves (Hellmann et al., 2002). This will be further explained (mathematically) in the following with Fig. 2.18 as a good illustration.

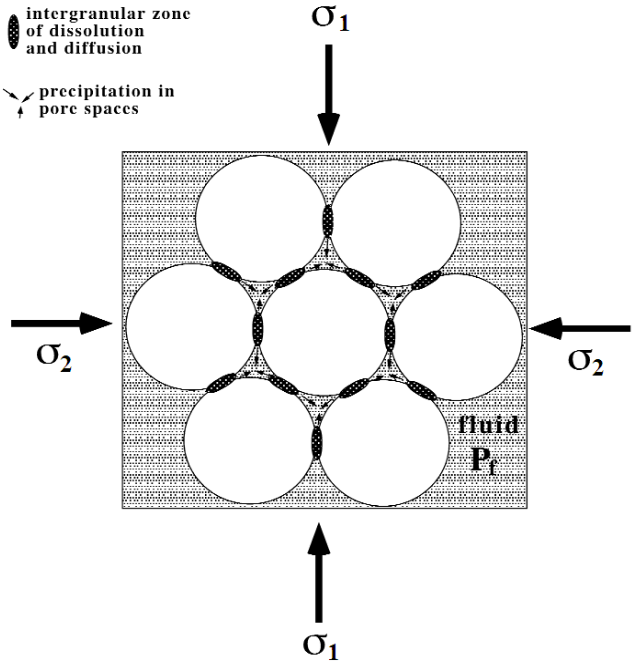

Figure 2.1: *The pressure solution theory; Dissolution and diffusion (dark oval areas) and precipitation will occur when rock grains are subjected to stresses. (From Hellmann et al. (2002)).*

When a rock material as a whole is exposed to stresses, there will also be stresses acting on the individual rock grains both in vertical and horizontal direction – denoted by $\sigma_1$ and $\sigma_2$ in Fig. 2.18, respectively. A pore fluid will be present in the voids between the grains, holding a fluid pressure ($P_f$). Since this fluid pressure is lower than both the mentioned stresses, the balance of Eq. 2.11 defines that the grains will be exposed to a certain effective stress. Fig. 2.18 illustrates the areas in which the three process steps are believed to take place – given that no solids are transported into or out of the system in the long run. Dissolution of solid material and the succeeding diffusion process (spreading) will occur at the boundaries between grains. Dark oval areas mark these areas in the figure. After being dissolved in an area of high stress (high chemical potential), it is believed that precipitation will occur (at interfaces) in pore spaces where the stress is lower (low chemical potential). The cause of this is explained to be the difference in chemical potentials ($\Delta\mu$), mathematically expressed as (Hellmann et al., 2002):

$$\Delta\mu = \mu_\sigma - \mu_{pore} = \left[(\sigma \cdot V_\sigma) - (P_f \cdot V_{P_f})\right] + (F_\sigma - F_{P_f}) \qquad \text{(Eq. 2.59)}$$

where

$\Delta\mu$: Difference in chemical potentials
$\mu_\sigma$: Chemical potential at stressed area
$\mu_{pore}$: Chemical potential in pore space
$\sigma$: Normal stress
$V_\sigma$: Molar volume of σ-stressed solids
$P_f$: Pore fluid pressure
$V_{P_f}$: Molar volume of pore fluid pressure-stressed solids
$F_\sigma$: Helmholtz free energy of σ-stressed solids
$F_{P_f}$: Helmholtz free energy of pore fluid pressure-stressed solids.

The difference in chemical potentials ($\Delta\mu$) is established to be the essential thermodynamic driving force for the overall pressure solution process resulting in deformation. $\Delta\mu$ may also be referred to as the total available free energy, and since this is energy consumed by all three step processes it is possible to find the rate-limiting step via $\Delta\mu$. Because, the division of $\Delta\mu$ among the different processes is believed to be a function of which step is rate-limiting, as the vast majority of the free energy will be consumed by the slowest step (Lehner, 1995). The net result of the step-wise IPS process is compaction of grains at the grain-to-grain boundaries, and as well porosity reduction and (possible) reduction in permeability. If the exerting stresses differ from each other, the deformation rate will be faster in the same direction as the higher stress (Hellmann et al., 2002).

Since dissolution and diffusion processes probably occur at interfaces between grains, the structure of these areas is of importance. Two different models have been suggested for describing contact structure; the *thin film* and the "*island & channel*" model. Fig. 2.19 shows, for both of these models, how dissolved materials at stressed grain contacts are transported via grain boundaries of different structure.

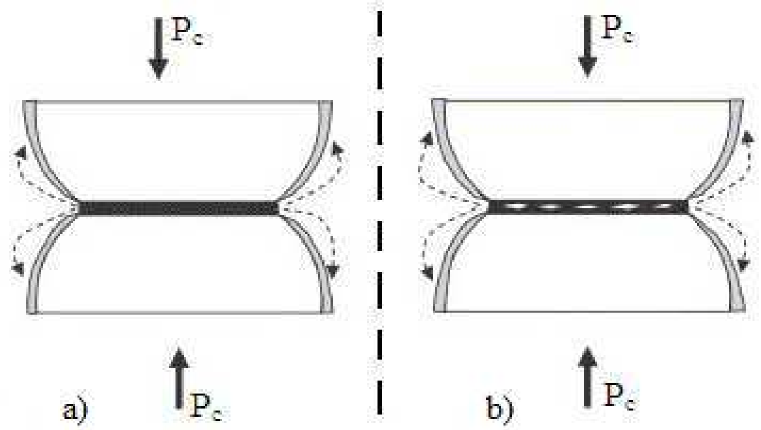

Figure 2.19: *Two models of intergranular pressure solution;* a*) The thin film model, and* b*) the "island & channel" model. (From Zhang & Spiers (2005)).*

The thin film model assumes the presence of a thin water layer (film) which is trapped inside grain contacts. Applied stress will not be able to squeeze out the water (Rutter, 1983). In the "island & channel" model it is assumed that the interfaces possess dynamically roughening contacts of islands and channels penetrated by water (Lehner, 1990). Common for both models is that water present in between grains contacts plays an essential role in the IPS process, both during the dissolving of solid minerals and when dissolved materials are transported (diffused) away from the stressed contact area. These models are only suggested theories, but if they reflect the real case it may be that IPS only occurs at contact areas where water is present in natural conditions. In other words; in contact areas where the surrounding fluid is hydrocarbons or other "dry" fluids, intergranular pressure solution will be inhibited (Zhang & Spiers, 2005).

## 2.5 Mechanical testing

*Please note that the descriptions presented in the Paragraphs* 2.5.1 Standard triaxial compression test *and* 2.5.2 Hydrostatic test *are mainly based on formulations by Korsnes (2007) and Madland (2005), while Paragraphs* 2.5.4 Creep test *and* 2.5.5 Brazilian test *are mainly based on Fjær et al. (2008) – unless otherwise is stated.*

Four different types of mechanical tests were performed during the experimental work of this thesis, and two different types of test cells were used. The *Brazilian tests* were run in a Brazilian test cell (see Paragraph *3.2.3 Brazilian test cell*), while both *standard triaxial compression tests*, the *hydrostatic tests* and the *creep test* were carried out in a triaxial test cell (see Paragraph *3.2.4 Triaxial test cell*).

### 2.5.1 Standard triaxial compression test

Objects – in this case; test samples – that are exposed to external forces will (normally) be deformed. The degree of deformation, measured in strain, is often compared to the stress exerted on the test sample. The stress level depends on the force and the surface area of the sample on which the force acts. A common way of presenting the stress-strain relation is to plot the stress (measured in megapascal) as a function of the percentage value of the resulting strain.

One of the test types that have been carried out during the work with this thesis is the *standard triaxial test*. Such a test is generally made up of two different test phases, namely the hydrostatic and the deviatoric phase. Through the premier phase the test sample is being exposed to the same forces in all directions, increasing simultaneously. The stress elevation continues until reaching a pre-set test level. In the case of testing cylindrical core samples, the axial and radial stresses are the same during such a hydrostatic load.

When the pre-set stress level is achieved, the deviatoric test phase is entered. The different stresses acting on the sample are now not longer equal – they *deviate* from each other. Almost all the chalk cores tested in this experimental work were first loaded hydrostatically before a deviatoric phase was carried out. During this latter part the radial stress was, contrary to the previous phase, kept constant at the already pre-set level. But the axial stress was continued elevating throughout a so-called *compaction test*. In practice, this was obtained by increasing the pressure in axial direction through a piston while holding the surrounding (confining) pressure constant. In general, an "*extension test*" could also have been run, if the axial stress was decreased instead.

When presenting the entire test progress graphically it is common to plot the axial stress ($\sigma_x$) as a function of axial strain ($\varepsilon_x$). A typical plot showing the different classification of phases is presented in Fig. 2.20. It is clearly shown that the curves of both the hydrostatic and the deviatoric test phases are linear, and that a drop in the slope is experienced at the transition from the first to the second phase. The curve forms the basis of calculating two important elasticity parameters, as the slope of the hydrostatic phase gives three times the bulk modulus ($K$), and Young's modulus ($E$) is obtained directly from the slope of the deviatoric phase. This is shown in the Fig. 2.20. The reason why the first slope corresponds to *3K* is that the abscissa axis consists of *axial* strain ($\varepsilon_x$) instead of *volumetric* strain ($\varepsilon_{vol}$), which is three times the magnitude of $\varepsilon_x$ for isotropic materials. If the values on the x-axis rather represented the volumetric strain, *K*-modulus would be corresponding to the slope. Eq. 2.34 and Eq. 2.37 show how the *K*-modulus and the *E*-modulus, respectively, can be calculated from the slope value in an axial stress-axial strain plot.

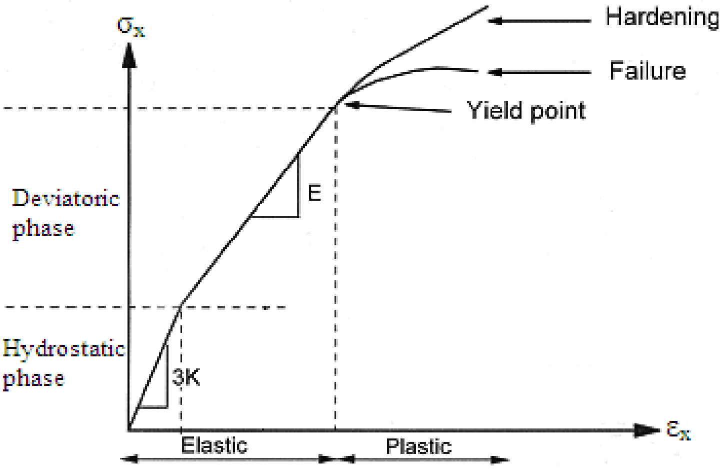

Figure 2.20: *Axial stress ($\sigma_x$) plotted versus axial strain ($\varepsilon_x$) for a standard triaxial test. The yield point and division of the different phases are shown. (From Madland (2005)).*

In addition to the two different test phases, a standard triaxial test can also be split into two parts regarding the elastic properties of the material. Through the whole hydrostatic test phase the material is said to be elastic, as it still has its ability to recover from deformation – to a considerable extent, at least. The first part of the deviatoric test phase also belongs to the so-called elastic phase, until the material “yields” (see Paragraph *2.5.3 Yield*). At this point, the material more or less loses its elastic properties and enters a rather plastic state where it either experience failure or strain hardening. In the axial stress ($\sigma_x$) versus axial strain ($\varepsilon_x$) plot shown in Fig. 2.20, the yield point indicates the transition from the elastic region to the plastic region.

## 2.5.2 Hydrostatic test

Unlike the standard triaxial compression tests, the *hydrostatic tests* are run at only hydrostatic conditions all the way until yield is passed – no deviatoric phase is carried out. But determination of the hydrostatic yield point is done by using the same approach as for the deviatoric one, and the graphical presentation of the test results will be shown in a similar diagram.

But, it should be noticed that the equipment used in this experimental work only makes it possible to perform so-called “quasi-hydrostatic” tests, and not purely hydrostatic tests. The reason is that the used method for measuring (axial) strain, explained in Paragraph *3.2.7 LVDT (Linear Variable Displacement Transducer)*, actually measures the movement of the *piston*. Hence, it is necessary that the piston is resting on top of the tested core sample at any time. In addition, the piston will experience some friction whenever moving. So to make sure that the piston stays in touch with the core a somewhat higher force than ideally must be exerted from the piston, resulting in a slightly higher axial stress than the radial stress from the confining (surrounding) pressure.

Failure is usually not observed under hydrostatic loading. However, at high stress levels pore collapse may give rise to failure. (This is at least the case in chalks, while grain crushing will be the reason in sandstones). But more close-up studies at microscopic level show that such failure is actually caused by local excessive shear forces that are acting through both grains and grain contacts. Based on that, pore collapse may be considered locally distributed shear failure within the material itself (Fjær et al., 2008).

### 2.5.3 Yield

The yield point is considered a measure of a material's mechanical strength, and determines the elastic limit of the tested material. When studying rock materials, the yield point can be understood as the upper limit of stress that the rock can withstand before experiencing pore collapse. The deformation prior to yield will be elastic, which means that the rock will recover and return to its initial shape (more or less) if the stress is removed. Post yield, the material has entered a region of plastic properties where the deformation to a certain degree will be non-reversible.

During the experimental work of this thesis rock material in shape of chalk cores was tested. What happens when yield is reached is that bonds between chalk grains inside the core are broken. In theory the core becomes powder, so that even if the stress is removed the core will not recover 100% and return all to its original shape and size. Determination of the yield point by just reading from a plot with the naked eye is very difficult, as the transition from elastic to plastic region is highly gradually and the yield is more represented by a lasting trend than a single point. There is also more than one way of defining the yield point, but as long as the same method is used consistently the results will be applicable and comparable.

In this thesis each presented yield point represents the point at which the axial stress ($\sigma_x$) versus axial strain ($\varepsilon_x$) curve *starts deviating from the linear trend*. For both the standard triaxial compression tests (deviatoric yield point) and the hydrostatic tests (hydrostatic yield point), the axial stress values at yield will be presented together with the corresponding effective radial stress values; i.e. the difference between the confining pressure and the pore pressure. These conjugate values are called the maximum ($\sigma_1$') and the minimum ($\sigma_3$') principal stresses, respectively, and they form the basis of both the Mohr-coulomb plot (see Paragraph *2.3.6 Mohr-Coulomb criterion*) and the *q-p'* plot (see Paragraph *2.3.7* q-p' *plot*).

### 2.5.4 Creep test

Creep can be defined as a time-dependent deformation that occurs in materials exposed to constant stress at constant temperature. The three other types of tests performed in the work with this thesis involve increasing specific loads on a chalk samples until failure (or yield), but the *creep test* stands out from that. It has been observed that rocks continue experiencing deformation for a long time after there has been a change in the applied stress, and even if the increase in stress is stopped. Creep is said to be related to the visco-elastic behaviour of the solid framework of the rock, and therefore may occur in both dry and wet (fluid saturated) rocks.

This test type is a good way of studying mechanical strength and behaviour post failure (or yield), and has been performed during this work of this reason. Hydrostatic creep tests are generally quite repeatable. (Hence only one such test was carried out in this work, as it was more interesting to perform one longer-lasting test than several short ones. The test was loaded hydrostatically beyond yield before the creep phase was started).

The creep phase can be divided into three stages, as illustrated in Fig. 2.21 where it is indicated how the deformation – measured as strain ($\varepsilon$) – typically will be dependent on the time of the creep phase. In the beginning, the rate of the time-dependent deformation decreases with time. This phase is called *transient* (or primary) creep. After some time, the rate of the dependency stops decreasing and there will be a transition to a *steady state* (or secondary) phase where the deformation rate is constant. Rate of strain (i.e. deformation) per time unit will be linear through this stage.

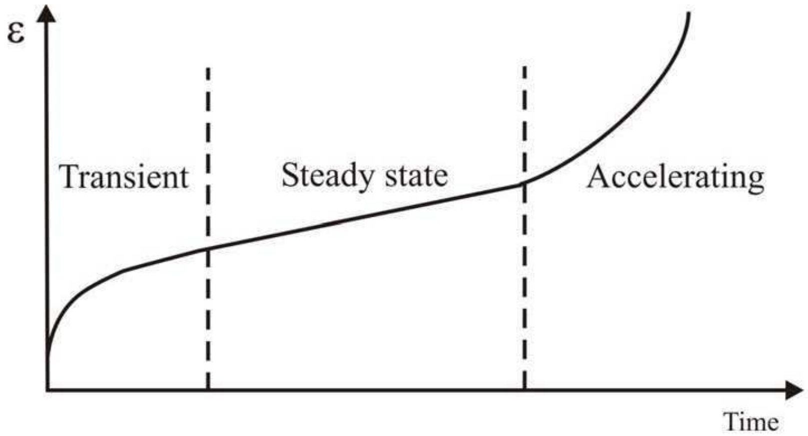

Figure 2.21: *Development of creep strain (ε) plotted versus creep time through the three stages of creep; transient, steady state and accelerating. (From Korsnes (2007)).*

The deformation rate may also increase with time, indicated in the strain-time plot by a bend "upwards" from the linear steady state creep curve. This phenomenon is named acceleration, thereof the name *accelerating* (tertiary) creep. Such creep behaviour is typically observed after some time when certain chemical reactions occur within the core sample. E.g., Madland et al. (2011) performed creep tests on Stevns Klint chalk with both NaCl brine and $MgCl_2$ brine, where the latter is understood to cause extensive chemical reactions. After some time of steady state creep, the cores flooded with $MgCl_2$ brine experienced acceleration in the deformation rate. This was not observed for the NaCl flooded cores.

Another common way of presenting the creep data graphically is by plotting creep strain ($\varepsilon$) versus *logarithmic* creep time. Fig. 2.22 illustrates a typical strain-log[time] plot, and shows how a "strain rate" (or creep rate) is determined from the linear part of the curve.

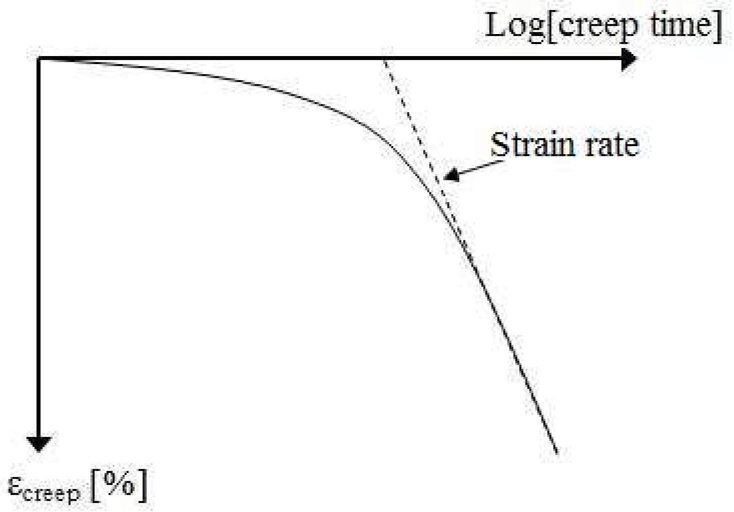

Figure 2.22: *Alternative way of plotting creep deformation data; creep strain (ε) versus* logarithmic *creep time. A "strain rate" is determined from the slope in the steady state phase.*

The strain (creep) rate, usually denoted by *m* [% / Decade], can easily be calculated from the following equation:

$$m = \frac{\varepsilon_2 - \varepsilon_1}{\log[t_2] - \log[t_1]} \qquad \text{(Eq. 2.60)}$$

where $\varepsilon_1$ and $\varepsilon_2$ are the axial strain values (percentages) at creep times $t_1$ and $t_2$ (given in minutes), respectively.

### 2.5.5 Brazilian test

In addition to the compressive strength of rocks the tensile strength is also of interest, but there are several difficulties connected to the performance of a direct uniaxial tension test on rock. As a result of this, a number of "indirect" measurement methods have been developed. The experimental methods are called indirect since they do not generate a homogeneous state of tensile stress in the tested rock. Instead, due to the arrangements and set-up of the experimental work, these methods rather lead to inhomogeneous stresses that are tensile in only some regions of the specimen. Among these indirect measurement tests, the *Brazilian test* is probably the most popular for measuring the tensile strength of a material (Jaeger et al., 2007).

The Brazilian tests is performed by applying a load with two platens diametrically compressed on a cylindrical shaped specimen – in this case; a part of a rock core. The apparatus for a Brazilian test cell is shown in Fig. 2.23 by a simple sketch.

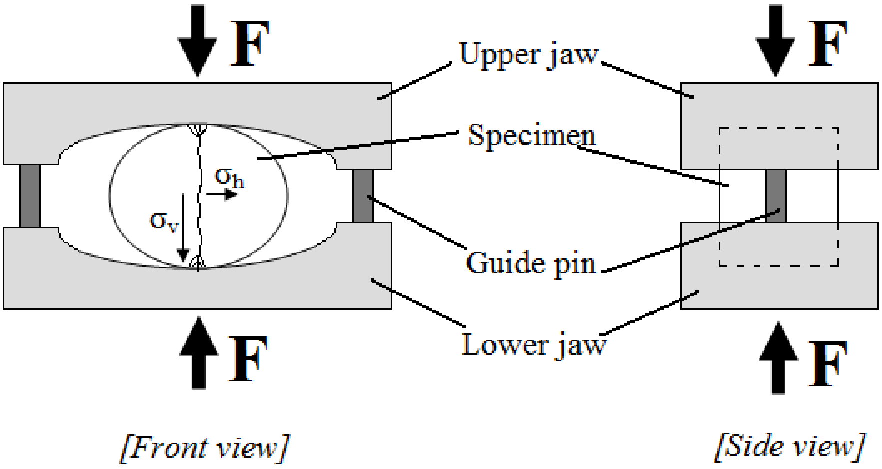

Figure 2.23: *Simple sketch showing the apparatus for a Brazilian test, both the front view and the view from the side. (Inspired by Fjær et al. (2008)).*

The length (*L* [mm]) of the rock cylinder should not be longer than the core's diameter (*D* [mm]), but typically longer than its radius. As the load is increased failure will suddenly occur by an extension fracture in (or close to) the loaded diametrical plane. The applied force is denoted by *F* [N]. Eq. 2.61 and Eq. 2.62 show the relationships between the three mentioned parameters, giving the horizontal ($\sigma_h$ [MPa]) and the vertical ($\sigma_v$ [MPa]) stress close to the centre of the core sample, respectively.

$$\sigma_h = -\frac{2 \cdot F}{\pi \cdot D \cdot L} \tag{Eq. 2.61}$$

$$\sigma_v = \frac{6 \cdot F}{\pi \cdot D \cdot L} \tag{Eq. 2.62}$$

As explained and "chosen" in Paragraph *2.3.1 Stress (σ)* compressive stresses are positive. This means that the vertical stress ($\sigma_v$) in the Brazilian test will be positive, since the compressive load is in this direction, and hence there is a minus in Eq. 2.61 making the horizontal stress negative. Close to the centre of the specimen the compressional stress will always be around three times larger than the tensile stress, and since the compressive *strength* normally will be larger than three times the tensile *strength*, the specimen will always fail in tension. This is also shown in Fig. 2.23. The tensile strength, often called the "Brazilian" strength ($T_{0B}$ [MPa]), is therefore equal to the (absolute value of the) horizontal (tensile) stress at the moment of failure, and given by the following equation:

$$T_{0B} = \frac{2 \cdot F_c}{\pi \cdot D \cdot L} \tag{Eq. 2.63}$$

where $F_c$ [N] is the peak load, i.e. the applied load at which the test sample experience failure.

During the Brazilian test the horizontal and the vertical stress represent the minimum and the maximum principal stresses, respectively. For both the Mohr-Coulomb plot and the *q-p'* plot the principal stresses at failure are of interest, and the tensile (i.e. horizontal) strength obtained from the test can be utilized with the mentioned three-to-one relation between the stresses to determine these values of interest. The minimum ($\sigma_3$ [MPa]) and the maximum ($\sigma_1$ [MPa]) principal stresses can then be given by:

$$\sigma_3 = -T_{0B} \tag{Eq. 2.64}$$

$$\sigma_1 = 3 \cdot T_{0B} \tag{Eq. 2.65}$$

Even though the Brazilian test is both easy to perform and a less time consuming test than many other mechanical tests, the generally accepted view is that at least 10 tests are needed to be able to establish a reasonable average value for the tensile strength.

# 3 Preparations, experimental set-up and procedure

## 3.1 Test material

Throughout the experimental work with this thesis, high porosity outcrop chalk was used. When studying chalk with regards to its properties as a reservoir rock, it would naturally be ideal to perform tests on reservoir chalk which has been in contact with hydrocarbons and reservoir brines at in-situ stresses through geological time. But, compared to outcrop chalk, reservoir chalk is very difficult and expensive both to purchase and to preserve at correct conditions. Regarding the latter, reservoir chalk may be damaged due to coring and preparations of test cores, and general changes in stresses and temperature. Outcrop chalk is available in a much larger quantity, and since it has been found that it has similar properties (porosity and permeability) as reservoir chalk it can be used as a good analogue to “real” materials (Jakobsen, 1996). This accessibility makes it possible to perform “trials and errors” to a larger extent, which often is useful in experimental work for possible progress.

Several places in Europe outcrop chalks are exposed on the surface. One type which has been extensively used in experimental work the last two decades is obtained from the inland quarry of Lixhe (or Hallembaye), right north of Liège, in Belgium. This chalk has been used consistently in the work with this thesis, and will from now on be referred to as “Liège chalk”. Table 3.1 presents some properties of the Liège chalk, which, after several years of studies, are considered to be reasonably well known.

Table 3.1: *Properties of Liège chalk.*

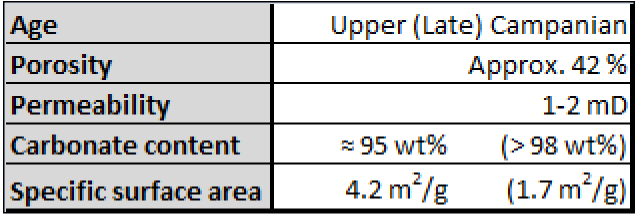

| | | |
|---|---|---|
| **Age** | | Upper (Late) Campanian |
| **Porosity** | | Approx. 42 % |
| **Permeability** | | 1-2 mD |
| **Carbonate content** | ≈ 95 wt% | (> 98 wt%) |
| **Specific surface area** | 4.2 $m^2/g$ | (1.7 $m^2/g$) |

“Traditionally” there has been an acceptance that the carbonate content in Liège chalk is as high as > 98 wt% (Hjuler & Fabricius, 2009). However, new measurements performed by Megawati et al. (2011) suggest that the composition of Liège chalk differs somewhat from this value, as three different measurement methods have been used and all of them resulted in a less content of carbonates; approximately 95 wt%. The remaining 5 wt% is mainly silicates. Hjuler & Fabricius (2009) found that half of the non-carbonate part is silica, and that all this silica is present as the mineral quartz ($SiO_2$). Hence, according to the results by Megawati et al. (2011) the silica content may also be somewhat higher than the traditionally suggested < 2 wt%.

A variance in measured properties are also found for the specific surface area, as Hjuler & Fabricius (2009) presented the value 1.7 $m^2/g$ and Megawati et al. (2011) obtained a value more than twice as high; 4.2 $m^2/g$. These experienced differences can probably be explained by a certain degree of heterogeneity in the Liège chalk. The fact that different chalk blocks from the same area of the quarry even have provided different results, support this idea. But properties of reservoir rocks will also typically be heterogeneous, so the Liège chalk is regarded as an ideal material for methodical studies. When studying chalks, especially porosity and the content of silica within the rock material are of interest. As mentioned earlier, there exists a general understanding that these two parameters highly affect the mechanical properties of the chalk as a whole, in the way that increased porosity and decreased silica content will decrease the chalk strength, generally (DaSilva et al., 1985). From the “classification” mentioned by Risnes (2001) Liège chalk is considered to be a weak rock material.

As seen in Table 3.1 the Liège chalk is a sedimentary rock from the late Campanian time, i.e. found in the upper Campanian strata. Subdivisions of the geological time scale actual for Liège chalk is shown in the overview in Fig. 3.1.

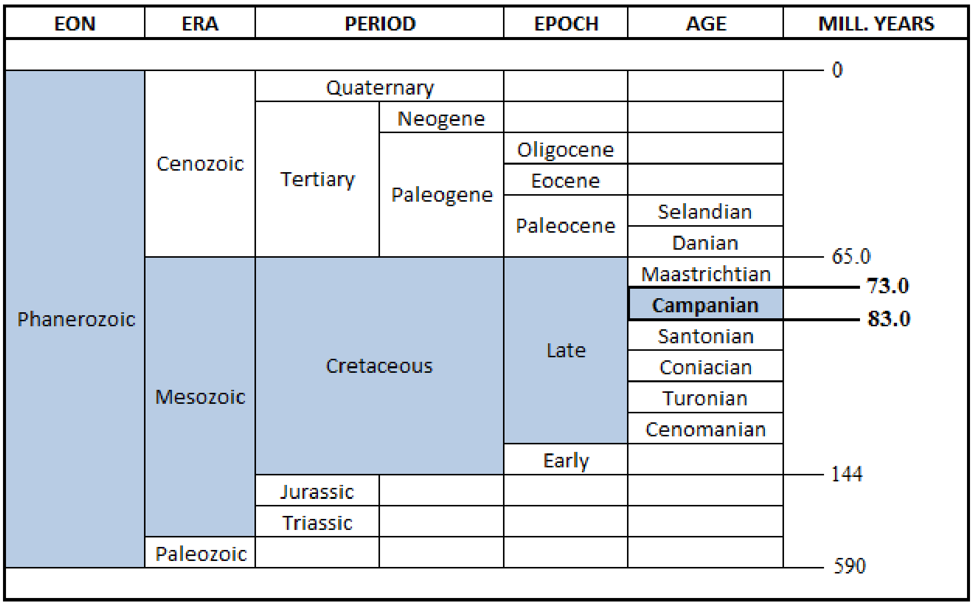

Figure 3.1: *Subdivision of the geological time scale actual for Liège outcrop chalk. (Please note that the time scale is not in accordance with the “sizes” of the different Eras, Periods, Epochs and Ages. In this figure, only the general named division is shown). (Inspired by Bjørlykke (1989)).*

At the laboratories at University of Stavanger, chalk from Liège is only one of several types of outcrop chalks that are extensively studied. The most common other types are outcrop chalk from Aalborg (Denmark), Stevns Klint (Denmark) and Kansas (USA). A very good basis for comparison is obtained by using such a wide selection of test materials.

## 3.2 Equipment

### 3.2.1 Equipment for saturating cores

In the experimental part of this thesis, chalk cores were pre-treated two different ways. About half of them were "aged" in a heating chamber at 130 °C prior to testing at the same elevated temperature, but common for all cores is that they were first of all saturated with the testing brine at ambient conditions. In addition to pre-treatment of all cores, determination of the cores' porosities also involved saturating the cores, but distilled water was used for this.

Both when measuring porosity and when saturating the aging cores, all cores were put in a vacuum container at the same time. The cores tested at ambient conditions were saturated one by one and put inside a smaller box without a lid, just slightly larger than the core itself. By putting this box under the fluid inlet in the sealed vacuum container it was possible to save the amount of water used for saturation, as only the small box needed to be filled instead of the whole container. At the lab there were two vacuum containers of different sizes available, but the same vacuum pump was used for them both. By using the smaller container it was therefore also possible to save time, as the time to reach vacuum conditions would be shorter for that one.

Fig. 3.2 shows the vacuum system set-up. Vacuum is generated inside a solid glass container with a heavy lid on top, and a rubber packing between them assures that the chamber is perfectly sealed. Through the lid there are two connections to the chamber, each of them controlled by a valve. An Edwards RV5 vacuum pump is connected to one of them for air suction effect, while a reservoir containing the saturation fluid is connected to the other, to fill the chamber at vacuum conditions. A pressure gauge indicates the pressure inside the container.

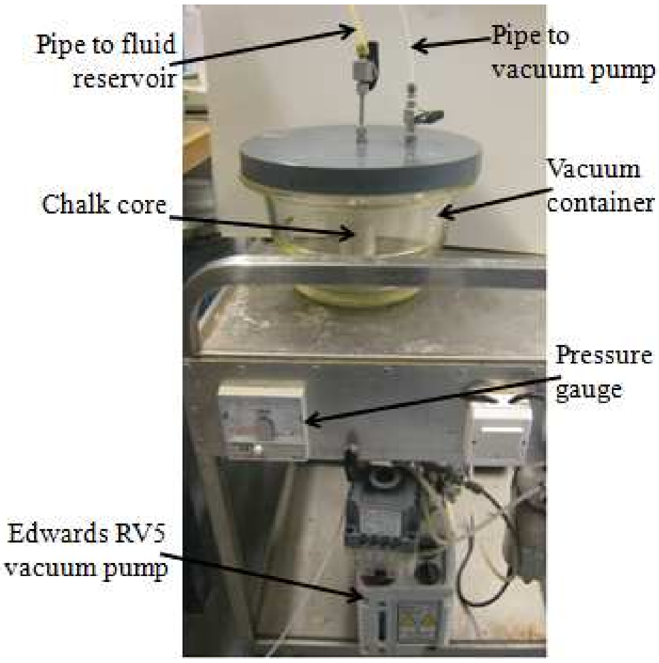

Figure 3.2: *The vacuum system set-up.*

For a description of the use of the vacuum system, please see Paragraph *3.5.1 Preparing the core for testing* (step I).

## 3.2.2 Equipment for aging cores

About half of all the prepared test cores were aged at testing temperature (i.e. 130 °C) after being saturated with test brine. The equipment for aging cores was simply a large, massive aging cell (also just called an “autoclave”). All cores that should be tested at high temperature were aged, and the size of the aging cell made it possible to age them all at once. Since the cores were aged in saturated condition they had to be entirely submerged into brine, and since the aging cell was put in a heating chamber at 130 °C the cell had to be pressurized to prevent the water from boiling. Compressed air of 0.7 MPa ensured this pressure inside the container, which has a design pressure of 1.5 MPa. Fig. 3.3 shows a picture of the aging cell and the connection for air pressure.

Figure 3.3: *The aging cell, with connection for compressed air, used for aging of chalk cores prior to testing.*

## 3.2.3 Brazilian test cell

Brazilian tests are performed for measuring the (indirect) tensile strength of a material, and carried out by using a so-called Brazilian test cell. A short core sample is placed edgewise in between two loading frames, as shown in Fig. 2.22. The frames with the core are then put into the “house”. A steel rod is lowered through the house onto the top of the frame set-up. By the use of a load cell on top of this rod, and a hydraulically operated piston in the external frame around the “house”, the steel rod set-up works as a piston and makes it is possible to expose a diametrical load to the core. A Gilson Pump, Model 307 HPLC, delivers Tellus oil to the piston, and the software application LabVIEW is used to control the pump and log the loading data on a computer.

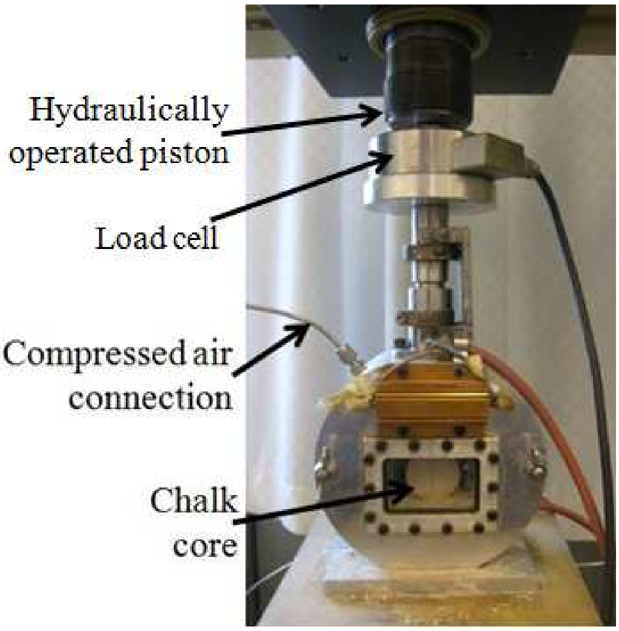

Figure 3.4: *The Brazilian test cell, where a short chalk core is put in between loading frames into the "house", and a hydraulically operated piston loads the core diametrically. A heating element is mounted onto the front cover to be used at high temperature tests, and compressed air ensures pressurizes test conditions.*

This apparatus also makes it possible to perform tests at high temperature, as seen in Fig. 3.4. A heating element is mounted onto a front cover that can seal the test chamber. Since all cores tested in this thesis are brine saturated, and the high temperature tests are carried out at 130 °C, the chamber has to be pressurized to avoid boiling of water. 0.7 MPa compressed air is connected to a vent through the house to prevent this. For tests performed at ambient conditions, it is neither necessary to install the front cover nor the air pressure.

### 3.2.4 Triaxial test cell

Most of the experimental tests were carried out by using a so-called triaxial test cell. As seen in Fig. 3.5 the cell consists of three separated parts – the lower, middle and upper part – all of them made out of steel. To keep the parts assembled as one unit during testing, six or nine solid, threaded steel bolts are tightened through projections in the lower and upper cell part. In this thesis two such test cells were used to be able to perform several deviatoric tests parallel to a long-duration creep test. Except from the number of steel bolts, their appearance and manner of operation are the same.

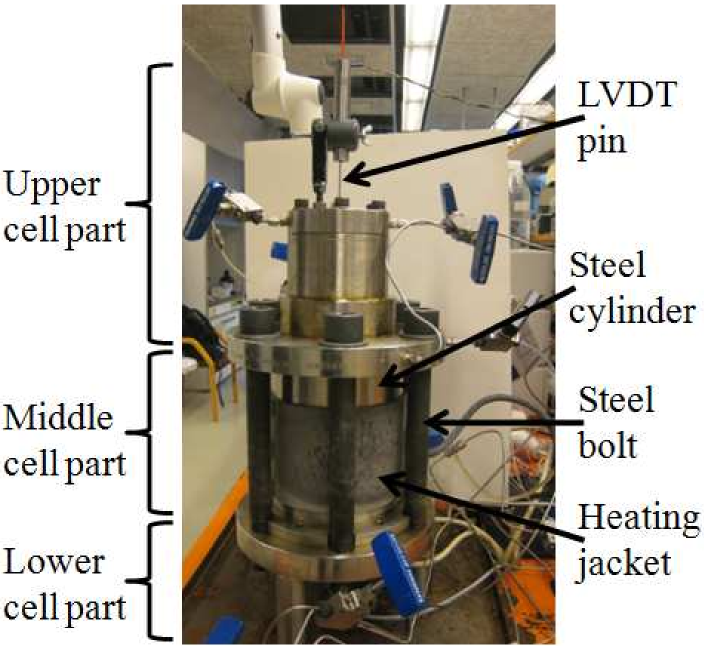

Figure 3.5: *The triaxial test cell.*

The picture above shows only the external view of the cell, which tells nothing about how it is used for testing. Concerning the latter, the principle sketch in Fig. 3.6 shows a “cross section” of the triaxial cell where mainly fluid inlets and outlets as well as the four different parts of the axial piston are pointed out.

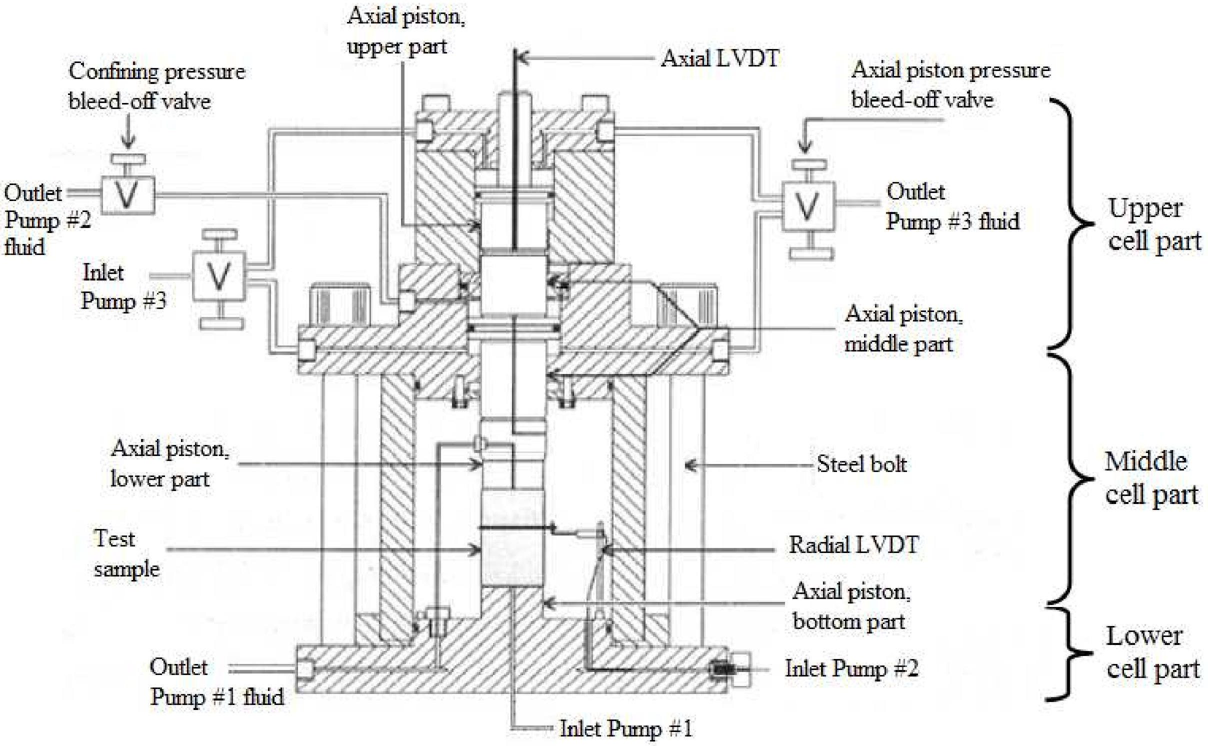

Figure 3.6: *Principle sketch of the triaxial test cell. (Modified from Korsnes (2007)).*

The lower cell part forms the pedestal for where the test action takes place as it consists of a non-moving part onto which the cylindrical test core is placed. This fixed device works as the bottom part of the axial piston where the inlet for circulating fluid is located. “Circulating fluid" will here be used as a general term for the actual test brine which fills the pore system (#1) and is flooded through the test sample. The surface at the inlet is a perforated plain so that the fluid will spread all over the core's bottom surface and hence flow uniformly through it. In addition to the fixed bottom piston part, the axial piston consists of three moving parts above the core; lower, middle and upper. The lower *movable piston* part is mounted on top of the core and leads to the circulating fluid outlet through a pipe connected to the lower *cell* part.

Inlet and lower outlet for the confining fluid (system #2), to fill and drain the chamber around the sample, are also located in the lower cell part. In addition, through this cell part temperature measurement device and equipment for measuring radial deformation of the cylindrical sample are connected.

The middle cell part is a term used for the surrounding area around the test sample where the cylindrical core undergoes radial stress, and is confined by a solid steel cylinder (typically called steel "skirt"). One rubber o-ring in each end of the cylinder makes sure that the confining area is perfectly sealed in between the three cell parts. The confining fluid (system #2) generating radial stress on the test core is hydraulic oil (Marcol oil). By mounting a heating jacket onto the steel cylinder it is possible to elevate the system's temperature.

In the main, the upper cell part consist of the middle and upper movable parts of the axial piston, inlets, outlets and chambers for the piston fluid (system #3) as well as a device for measuring displacement of the piston. Hydraulic Marcol oil is also used as piston fluid and can be led to two chambers (upper and lower), each of them having one inlet and one outlet. By filling and increasing pressure in the upper or lower chamber, it is possible to move the axial piston both downwards and upwards, respectively. In the upper cell part there is also an upper outlet for confining fluid with a bleed-off function. This connection is also used as an inlet for compressed air when emptying the cell for confining fluid through the lower outlet after testing.

Some pressure gauges were used to show the actual confining and piston pressure, as well as the differential pressure through the test core, at any time. Since several different fluid systems, inlets and outlets have been described there are several valves connected to the triaxial cell system. Table 3.2 presents an overview of the most frequently used valves in the different fluid systems, and which inlet, outlet and cell part they are connected to. When the different valves are mentioned in Chapter *3.5 Testing procedure: Hydrostatic, deviatoric and creep test*, they will only be referred to as "upper piston inlet", typically, with no further specification.

Table 3.2: *Overview of the most frequently used valves, showing which fluid system, inlet/outlet and cell part they are connected to.*

| Fluid system | Valve | | Cell part connected to |
|---|---|---|---|
| **#1 Pore (Circulating fluid)** | | Inlet | Lower |
| | | Outlet | Lower |
| | | Bypass test cell | Lower |
| | | Bypass flooding cell | *Independent of cell parts* |
| **#2 Confining (Marcol oil)** | | Inlet | Lower |
| | Lower | outlet | Lower |
| | Upper | outlet | Upper |
| **#3 Piston (Marcol oil)** | Lower | inlet | Upper |
| | Upper | inlet | Upper |
| | Lower | outlet | Upper |
| | Upper | outlet | Upper |

## 3.2.5 Pumps

Three different types of pumps were used in this experimental work. Because of the availability of pumps, and the fact that the pumps have different properties and can be used for different purposes, the pump set-up differed somewhat between the three test cells. An overview of this is shown in Table 3.3:

Table 3.3: *Overview of different types of pumps used for the fluid systems in the three different test cells.*

| Pump No. | Fluid system | Triaxial test cell A Hydrostatic/Deviatoric tests | Triaxial test cell B Creep test | Brazilian test cell |
|---|---|---|---|---|
| **#1** | **Pore (Circulating fluid)** | Gilson | Gilson | N/A |
| **#2** | **Confining (Marcol oil)** | Quizix | Gilson | N/A |
| **#3** | **Piston (Marcol oil)** | Quizix | Teledyne Isco | Gilson |
| **#4** | **Back pressure** | Teledyne Isco *(Marcol oil)* | (gas regulator) | N/A |

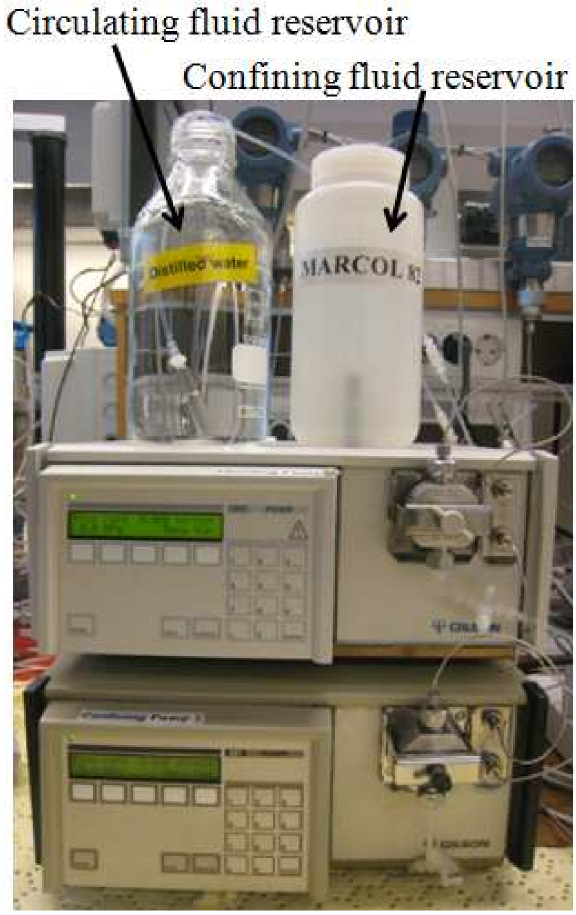

Figure 3.7: *Gilson Pumps, Model 307 HPLC.*

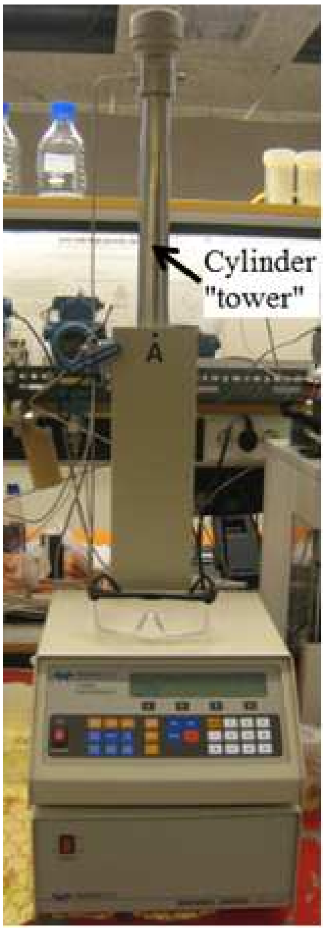

Figure 3.8: *Teledyne Isco Syringe Pump, Model 260D.*

Figure 3.9: *Quizix pumps.*

### Gilson Pump, Model 307 HPLC

One of the most common pumps, used in all test types in this work, is the high pressure *Gilson Pump, Model 307 HPLC*. Gilson pumps like this can deliver constant flow (CF) rates in the range of 0.01-10 ml/min and handle a maximum pressure of 60 MPa. Accuracy of the pressure value is ±0.1 MPa. Gilson pumps are usually controlled via the LabVIEW programme on the computer (please see Paragraph *3.2.9 Computer software*), but may also be controlled manually.

In both triaxial cell set-ups a Gilson pump is connected to the pore fluid system (#1), while in test cell B (creep tests) there is also a Gilson pump delivering Marcol oil to the confining fluid system (#2). Fig. 3.7 shows this set-up with the fluid reservoir placed on top of the two pumps. When used as a pore fluid pump and during loading of confining pressure, the Gilson pump delivers fluids at constant flow. At a certain pre-set limit for maximum confining pressure the pump will stop, and “High pressure limit” will blink in the display at this condition. This way the Gilson pump makes it is possible to keep a steady pressure, as it will start pumping whenever the pressure falls below the set value. However, a “limitation” of the Gilson pump is that it is not able to receive fluids from the system, so if the pressure would increase above the maximum limit, it must be bled off manually with a valve.

### Quizix Pump

The most advanced pump used in this work is the *Quizix Pump*. Two such pumps were used under the hydrostatic and deviatoric tests, for the confining (#2) and the piston (#3) fluid system. They are of different models. The confining pump is a *QX-20000 HC Pump* which can deliver flow rates from 0.00015 to 10 ml/min and handle pressures up to 20 kPSI (137.9 MPa). The piston pump, a *QX-6000 HC Pump*, has a possible flow rate range of 0.001 to 50 ml/min, but cannot handle pressures above 6 kPSI (41.3 MPa). They are shown in Fig. 3.9.

The Quizix pump has several functions; among them are the abilities both to deliver constant fluid flow (CF) and to *withdraw* (receive) fluids from the system. The latter property makes it a perfect pump for keeping constant pressure (CP) values. Another good quality of the Quizix pump is its ability to combine pressure loading with ramp time, i.e. to increase or decrease pressure to a pre-set value over a pre-set time range. This is typically used for hydrostatic loading up to certain confining pressures, and makes it possible to use the same loading rate on all tests. Under all pressure build-ups, a safety pressure was always set somewhat higher than the maximum pressure. Via Quizix PumpWorks, a computer software application, these Quizix pumps were controlled.

### Teledyne Isco Syringe Pump, Model 260D

Like the Quizix pump, the *Teledyne Isco Syringe Pump, Model 260D*, is also able to withdraw fluids from the system. Therefore, two such pumps were used in this work; one to keep the piston pressure (fluid system #3) constant (CP) during the creep test, and one to keep the back pressure constant (CP) during the hydrostatic and deviatoric tests. The manually controlled Teledyne Isco pump can deliver constant flow (CF) rates in the range of 0.001-107 ml/min and the maximum pressure it can handle is 52 MPa. In Fig. 3.8 a Teledyne Isco pump is shown, with its cylinder “tower” which holds the fluid (Marcol oil) reservoir with a capacity of 266 ml.

### 3.2.6 Flooding system

When performing test in a triaxial cell, the “flooding system” refers to the pore fluid part of the test system (#1). This involves the parts connected directly to the test sample, starting from the pore fluid pump (pump #1), via or bypassing a flooding piston cell, through or bypassing the core itself, past the back pressure flooding device and ending at the effluent water outlet. Pump #1 delivers distilled water from a fluid reservoir to the system, but a flooding piston cell can be used to switch the circulating fluid.

A flooding piston cell is a massive, but hollow, steel cylinder. In each end there is a removable lid, and the hollow space is split into two separate chambers by a movable piston. Two double valves give the options of either flooding distilled water bypass the piston cell and directly into the pore fluid system, or to flood the distilled water into the upper piston cell chamber. In the latter case the piston will be pushed downwards, and the fluid in the lower cell chamber (typically test brine) will flow into the system. In all tests performed in triaxial cells in this work, SSW–($SO_4^{2-}$) was the test brine – except the last part of the creep test, where it was switched to SSW. Fig. 3.10 shows a flooding piston cell, while a principle sketch of a cross section of the cell as well as the bypass-cell valve system is shown in Fig. 3.11.

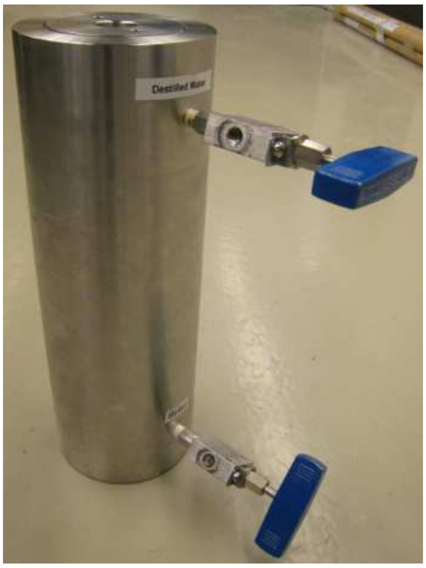

Figure 3.10: *Flooding piston cell.*

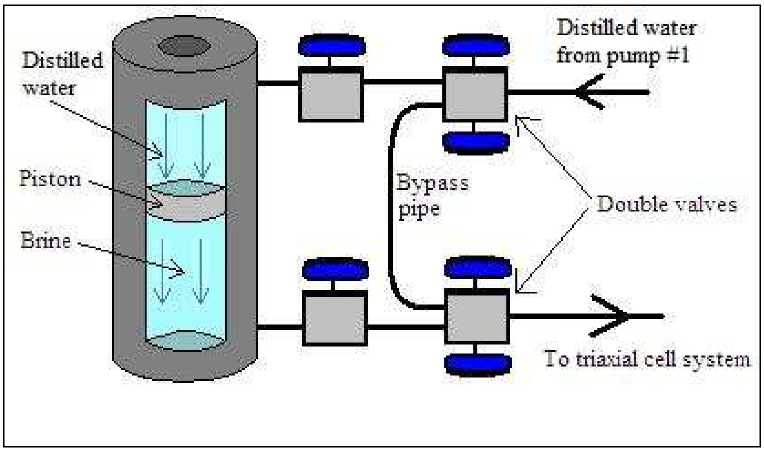

Figure 3.11: *Principle sketch of the flooding piston cell, and how it is connected to the rest of the flooding system.*

About half of the hydrostatic and deviatoric tests, and the creep test, were carried out at elevated test temperature of 130 °C. The circulating fluid would normally start boiling at this temperature, so to avoid this from happening, the pore pressure inside the test sample was increased. A back pressure regulating system was used to build up and control the pore pressure at a pre-set level. Such a system is shown in Fig. 3.12. Circulating fluids move from the outlet in the lower triaxial cell part towards the effluent water outlet, but have to pass the back pressure flooding device. A back pressure hinders the circulating fluid from passing, and the pore pressure therefore increases until the back pressure level is reached. At this point, the pore fluid will continue circulating through the back pressure flooding device at the constant flow (CF) rate from pump #1.

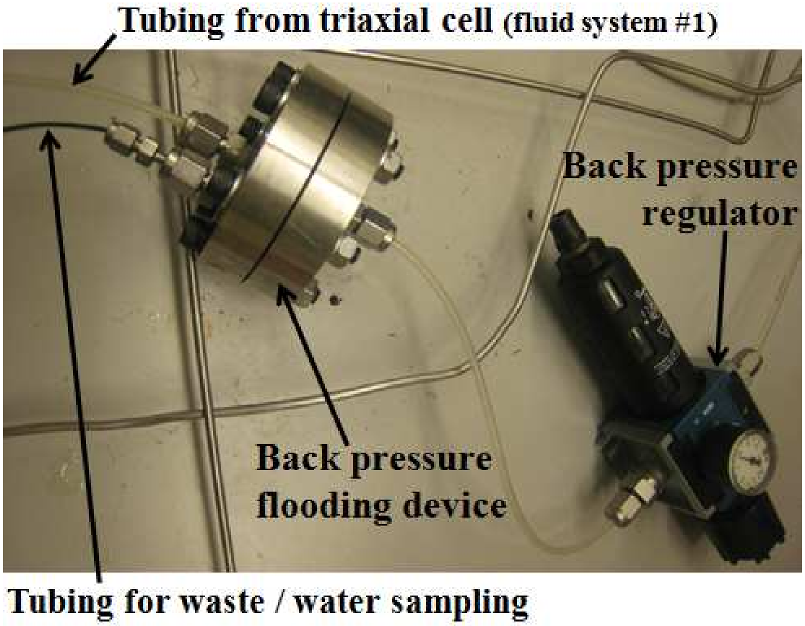

Figure 3.12: *The back pressure regulating system.*

Two different ways have been used to regulate the back pressure. A Teledyne Isco pump was connected to triaxial cell A (hydrostatic and deviatoric tests) to keep the pore pressure constant, while a regulator with the use of pressure support gas ($CO_2$) was used with triaxial cell B. In both cases the pressure was adjusted manually and step-wise. Regarding the creep test it is interesting to see if something happens chemically inside the chalk core. Therefore, the effluent water was sampled (manually) once a day and analyzed for its chemical composition (ion composition).

There were two pressure gauges connected to this flooding system, where one showed the differential pressure (i.e. pressure drop through the core) and the other showed the pore pressure. In all tests, the pore pressure under testing was 0.7 MPa.

### 3.2.7 LVDT (Linear Variable Displacement Transducer)

An external LVDT was used to measure the axial deformation of the test samples (in length). However, it should be noticed that this method actually provides measurements of the *piston*'s displacement, and makes it necessary to use a somewhat extra force on the piston to make sure that the piston rests on top of the core at any time. From the principle sketch in Fig. 3.6 it is shown how the LVDT measuring pin is directly in contact with the middle movable piston part through a hole in the upper piston part. The accuracy of this equipment is ±0.05 mm. (No equipment was used for measuring radial deformation of the samples in this work).

## 3.2.8 Heating system

A so-called heating jacket, controlled by an external regulating system, was mounted onto the steel cylinder of the middle triaxial cell part to elevate the test temperature. In this thesis the test temperature was either ambient (room) temperature or 130 °C. The temperature controlling system allows choosing a pre-set temperature which is kept constant when reached. The device for measuring the actual temperature was a Pt-100 RTD (Resistance Temperature Detector) element connected to the lower cell part. To be exact it is the confining temperature which is measured, as the temperature sensor pin stands out from the cell platform and into the confining area.

## 3.2.9 Computer software

**LabVIEW**

Flooding rates and maximum pressure values for fluid delivery from all Gilson pumps used in this work, were mainly set and controlled via *LabVIEW*; a computer software application. By using LabVIEW it is also possible to log provided test results like flooding rates, pressure and temperature values, deformation of test sample and elapsed test time. One of the great LabVIEW functions is the ability to view all these logged data live while testing as plots in a diagram, as shown in the screen shot in Fig. 3.13. Also data from other pumps not controlled via LabVIEW. In addition, the logging file can be opened as a spreadsheet any time during the tests, so development of test data is continuously available. These properties may help running the tests as similar as possible, and give the opportunity to detect and improve unwanted development before early enough. Spreadsheets containing the logged data are the foundation for making comparable plots from the different tests.

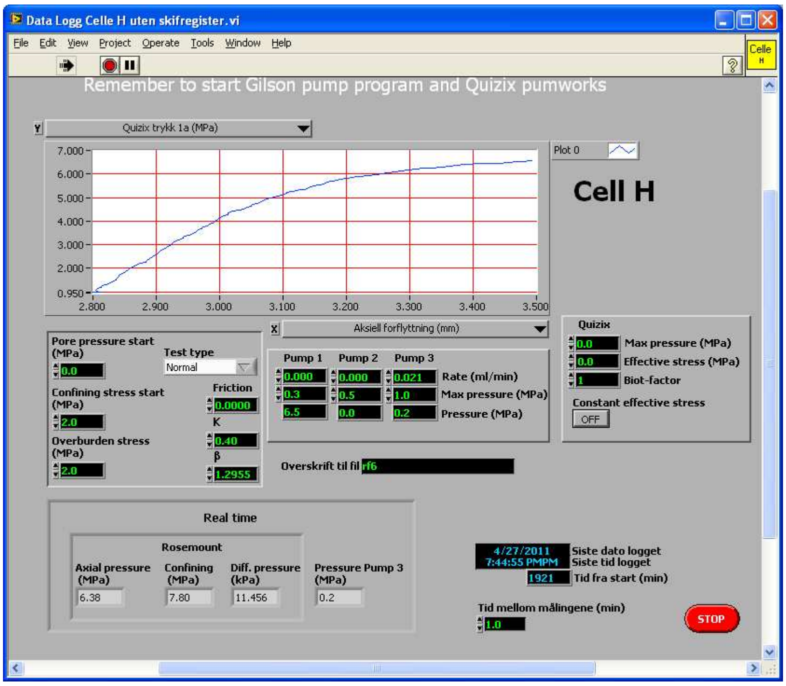

Remember to start Gilson pump program and Quizix pumworks

Quizix trykk 1a (MPa)

Aksiell forflyttning (mm)

Cell H

Pore pressure start (MPa): 0.0
Test type: Normal
Confining stress start (MPa): 2.0
Overburden stress (MPa): 2.0
Friction: 0.0000
K: 0.40
β: 1.2955

| Pump 1 | Pump 2 | Pump 3 | |
|---|---|---|---|
| 0.000 | 0.000 | 0.021 | Rate (ml/min) |
| 0.3 | 0.5 | 1.0 | Max pressure (MPa) |
| 6.5 | 0.0 | 0.2 | Pressure (MPa) |

Quizix
0.0 Max pressure (MPa)
0.0 Effective stress (MPa)
1 Biot-factor
Constant effective stress: OFF

Overskrift til fil rf6

Real time

Rosemount

| Axial pressure (MPa) | Confining (MPa) | Diff. pressure (kPa) | Pressure Pump 3 (MPa) |
|---|---|---|---|
| 6.38 | 7.80 | 11.456 | 0.2 |

4/27/2011 Siste dato logget
7:44:55 PMPM Siste tid logget
1921 Tid fra start (min)

Tid mellom målingene (min): 1.0

Figure 3.13: *Screen shot of the LabVIEW software application, where flooding rates and maximum pressure values can be set and controlled, and live logging data can be shown graphically.*

**Quizix PumpWorks**

Both the Quizix pumps were controlled via the computer software application *Quizix PumpWorks*. Pump state of either constant flow (CF) or constant pressure (CP) can be chosen, and maximum limits can be set. The programme also allows the property of increasing/ decreasing pressure values over a set time period ("ramp time"). Fig. 3.14 shows a screen shot of Quizix PumpWorks.

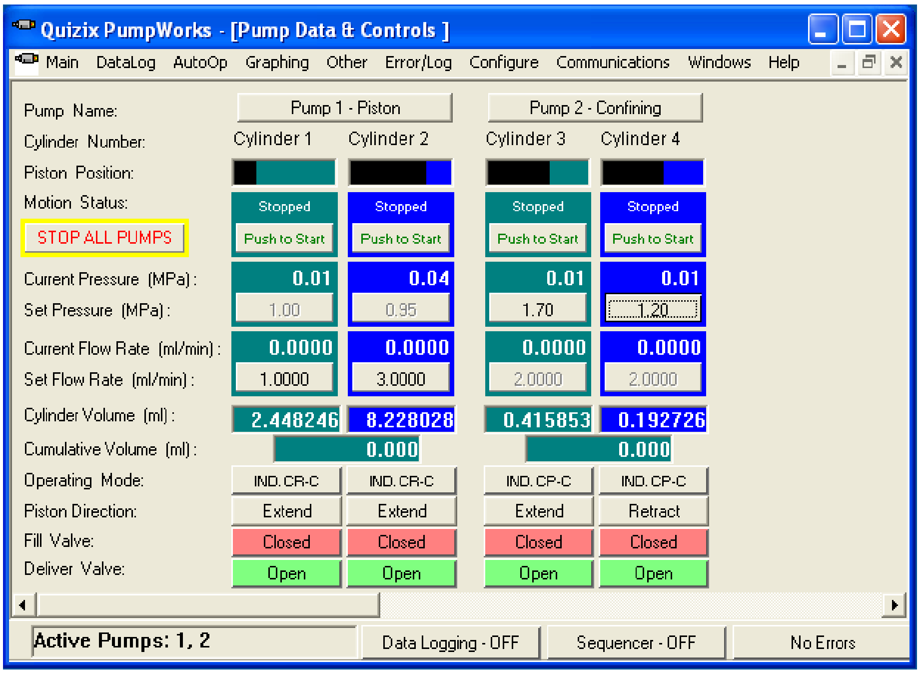

| | | | | |
|---|---|---|---|---|
| Pump Name: | Pump 1 - Piston | | Pump 2 - Confining | |
| Cylinder Number: | Cylinder 1 | Cylinder 2 | Cylinder 3 | Cylinder 4 |
| Piston Position: | | | | |
| Motion Status: | Stopped | Stopped | Stopped | Stopped |
| | Push to Start | Push to Start | Push to Start | Push to Start |
| Current Pressure (MPa) : | 0.01 | 0.04 | 0.01 | 0.01 |
| Set Pressure (MPa) : | 1.00 | 0.95 | 1.70 | 1.20 |
| Current Flow Rate (ml/min) : | 0.0000 | 0.0000 | 0.0000 | 0.0000 |
| Set Flow Rate (ml/min) : | 1.0000 | 3.0000 | 2.0000 | 2.0000 |
| Cylinder Volume (ml) : | 2.448246 | 8.228028 | 0.415853 | 0.192726 |
| Cumulative Volume (ml) : | 0.000 | | 0.000 | |
| Operating Mode: | IND. CR-C | IND. CR-C | IND. CP-C | IND. CP-C |
| Piston Direction: | Extend | Extend | Extend | Retract |
| Fill Valve: | Closed | Closed | Closed | Closed |
| Deliver Valve: | Open | Open | Open | Open |

**Active Pumps: 1, 2**
Data Logging - OFF
Sequencer - OFF
No Errors

Figure 3.14: *Screen shot of the Quizix PumpWorks software application, where constant flooding rates and steady and maximum pressure values can be set and controlled.*

## 3.2.10 Equipment for chemical analysis

One of the very interesting results obtained from creep tests is the chemical analysis of the sampled effluent water. The goal is to examine whether there occurs a change in the ion composition of the water when flooding through the chalk core at test conditions. Dilution of the water samples was the first step, and was performed by a Gilson Syringe Pump, Model 402, in combination with a Gilson Liquid Handler, Model GX-271. They are shown in Fig. 3.16 as number *1* and *2*, respectively. From sample glasses the diluted samples were then filtered into 1.5 ml IC glasses by using the equipment in Fig. 3.15; a syringe with a needle, and an IC Acrodisc 13 mm Syringe Filter from Pall, with 0.2 µm Super (PES) Membrane.

Figure 3.15: *The equipment for filtering diluted samples prior to chemical testing.*
*1: Sample glass of diluted effluent water. 2: Syringe. 3: Needle. 4: Filter. 5: IC glass.*

A Dionex Ion Chromatograph (IC), Model ICS-3000, was utilised for the chemical analysis. This complex device is capable of determining ion concentrations in the prepared IC glass samples. Anions and cations are examined separately by two different parts of the device. The time needed for the machine to analyze one IC glass is usually 6 minutes for the anions and 18 minutes for the cations. The ion chromatograph device consists of elements *3* through *7* pictured in Fig. 3.16; namely an auto sampler where all the IC glass samples are placed, an eluent organizer, a detector/chromatography module, a dual pump and an eluent generator.

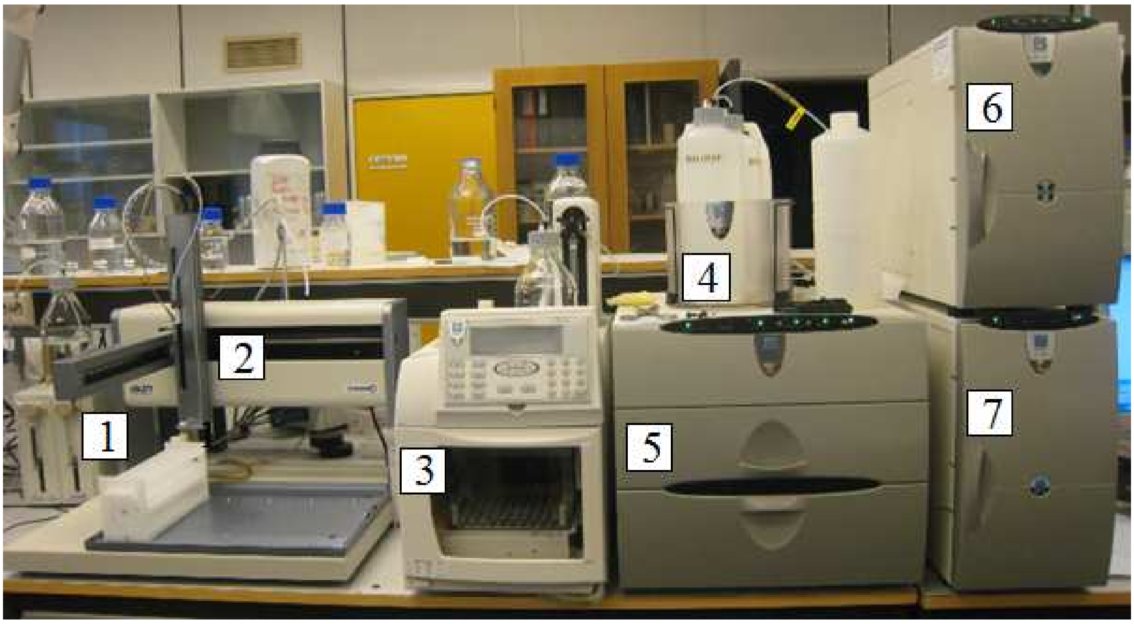

Figure 3.16: *The equipment for diluting effluent water samples (1 and 2) and the complex Dionex Ion Chromatograph, Model ICS-3000 (*3-7*) for chemical analysis.*
1*: Gilson Syringe Pump, Model 402.* 2*: Gilson Liquid Handler, Model GX-271.*
3*: AS (Auto Sampler).* 4*: EO (Eluent Organizer).* 5*: DC (Detector/Chromatography) module.*
6*: DP (Dual Pump).* 7*: EG (Eluent Generator).*

## 3.3 Preparation of test cores

A chalk block from the quarry near Liège was the basis for making all the tested cores. As mentioned, Liège outcrop chalk seems to have some degree of non-homogeneity, so it was important that all cores were made from the same block to make the standard of comparison between the tests as good as possible. In addition, as the cores were drilled out from the block, their top and bottom sides were marked. This was done to make sure that the flooding direction through the core was the same in all cases, i.e. vertically upwards.

Samples that were tested in a triaxial cell were treated to achieve the required test sizes of about 70 mm in length and more precisely 37 mm in diameter (or 38.1 mm for the one core used in the creep test). For a proper basis of comparison all cores should also have smooth and uniform surfaces. 24 shorter cores were prepared for testing in the Brazilian test cell. They had diameters of 37 mm, but values of length typically somewhere in between the radius and the diameter.

### 3.3.1 Drilling

A number of cylindrical cores were drilled out from a chalk block by using a drilling machine with an oversized core bit, as shown in Fig. 3.17. The lengths of these cores were around 200 mm, each of them forming the basis of two test cores. While drilling, the chalk block had to be fastened in a box to be prevented from moving, and water was used as cooling liquid.

Figure 3.17: *The drilling machine.*

To evaporate the water from the cores, they were all put in an oven at 130 °C over night. Due to their coarse surfaces and varying diameter, the cores had to be both shaped and cut to be used in the test cells.

### 3.3.2 Shaping

Shaping of the cores was performed in a turning lathe to achieve the required diameter. The turning lathe is pictured in Fig. 3.18, while Fig. 3.19 shows a close-up view of how the core is mounted in the lathe.

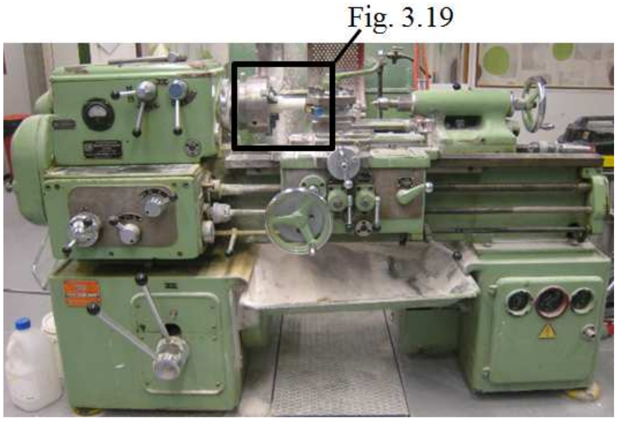

Figure 3.18: *The turning lathe.*

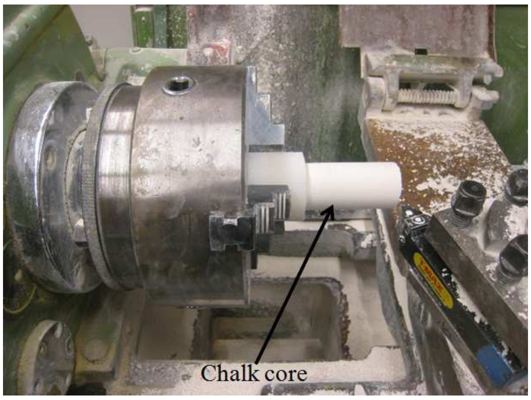

Figure 3.19: *Closer view of how the cylindrical core is mounted in the lathe.*

To obtain a surface as uniform and correct in diameter as possible, the shaping process was carried out in two steps. The roughest outer layer was first removed by shaping the cores to a diameter of about 38.5 mm, before they were “shaved” to their desired diameter of 37 mm (or 38.1 mm for the creep test core).

### 3.3.3 Cutting

After shaping the cores to their desired diameter, they had to be cut to the correct sample length before they could be used in test cells. Fig. 3.20 shows the Struers Discotom-5 Cutting Machine used for this purpose. First, the cores were cut in half. Then, about 15 mm was cut off each end, making the core lengths 70 mm. Perfect cylindrical shapes were obtained as the cut-off wheel (diamond blade) makes plain surfaces and hardly any damage at all on the core ends.

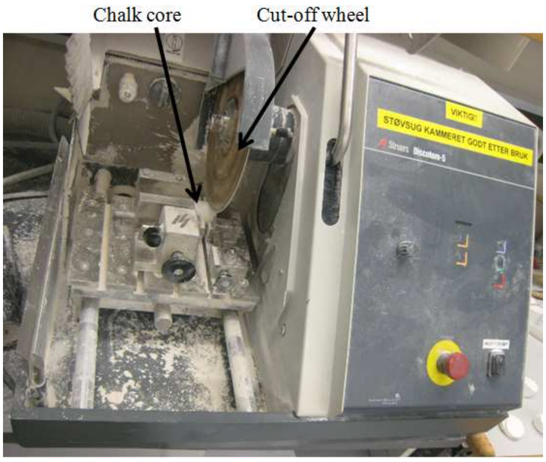

Figure 3.20: *The cutting machine (Struers Discotom-5).*

Some tens of core samples were made like this, distributed on experimental work for two theses, and knowing that there would be some failed tests, some cores could be excluded because of highly deviating porosity or length/diameter, and some cores was expected damaged during aging, etc. In addition, 22 shorter cores were cut for testing in the Brazilian test cell. (Ten of them – to be tested at elevated temperature – were cut from some 70 mm long samples that had already been aged). When (the un-aged) samples had been cut to their test size, they were put back into the oven at 130 °C to evaporate any humidity before porosity could be measured.

### 3.3.4 Determining porosity

For the test samples to be comparable they should all be as similar as possible. Determination of the cores' porosity is one good way to be able to exclude possible cores that are not representative for the assembly, i.e. if their porosities deviate considerably from the average value. After the cores were dried they were weighed one by one on a scale, and their exact lengths and diameters were measured by using a sliding caliper. The cores were then saturated with distilled water in a vacuum container, and again individually weighed on the scale. When having knowledge of each and every core's length, diameter, dry and saturated (wet) weight, the equations Eq. 2.3 through Eq. 2.5 could easily be used to compute the porosity ($\Phi$).

From now on, the samples were stored dry in a heating cabined at 130 °C before being either saturated with or aged in test brine prior to testing.

## 3.4 Mixing test brines

All test cores were saturated with or aged while submerged in the testing brine before testing, and flooded with the same brine during testing. For all tests, the used brine was *synthetic seawater without sulphate* (abbreviated $SSW\text{–}(SO_4^{2-})$), and for the creep test this brine was after some time switched to *synthetic seawater* containing sulphate (abbreviated *SSW*). In addition, this thesis was processed in close co-operation with another thesis (Davidsen, 2011) using the opposite brines, i.e. mainly SSW. Table 3.4 presents the recipes for these two fluids.

Table 3.4: *Recipes for making 1 litre of SSW–($SO_4^{2-}$) (synthetic seawater without sulphate) and 1 litre of SSW (synthetic seawater), in correct order from top to bottom. The salts are mixed into distilled water.*

| Chemical | Amount added to make 1 litre of SSW–($SO_4^{2-}$) | | Amount added to make 1 litre of SSW | |
|---|---|---|---|---|
| | [g/l] | [mol/l] | [g/l] | [mol/l] |
| NaCl | 27.58 | 0.472 | 23.38 | 0.400 |
| KCl | 0.75 | 0.010 | 0.75 | 0.010 |
| $MgCl_2 \cdot 6H_2O$ | 9.05 | 0.045 | 9.05 | 0.045 |
| $CaCl_2 \cdot 2H_2O$ | 1.91 | 0.013 | 1.91 | 0.013 |
| $Na_2SO_4$ | | | 3.41 | 0.024 |
| $NaHCO_3$ | 0.17 | 0.002 | 0.17 | 0.002 |

Salts were added one by one to distilled water, continuously mixed on a magnet stir. After they were all mixed in, distilled water was added until the solution volume was exactly 1 litre, and the brine was then left for mixing for some hours. The mixed brine was filtrated by using a filter paper (from Millipore) with 0.65 μm mesh size, before used for saturation, aging or testing. Fig 3.21 and Fig. 3.22 show equipment and set-up for mixing and filtration of brines, respectively.

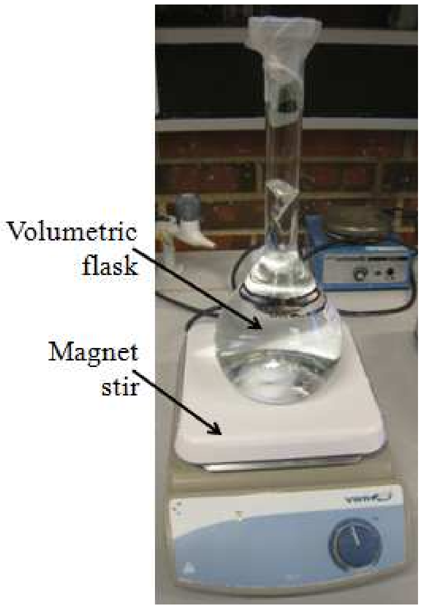

Figure 3.21: *The equipment for mixing brines; magnet stir and volumetric flask.*

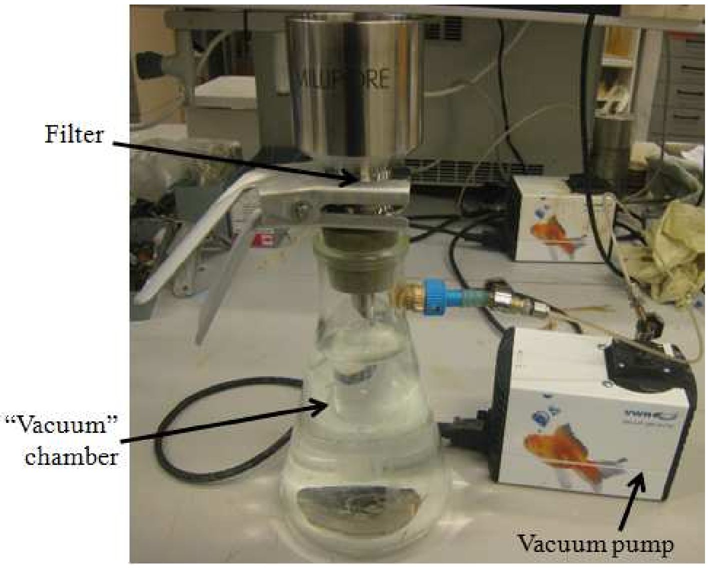

Figure 3.22: *The set-up for brine filtration.*

## 3.5 Testing procedure:
## Hydrostatic, deviatoric and creep test

Both the hydrostatic and deviatoric tests and the creep test were carried out in triaxial test cells. The procedures *during* the tests themselves differed naturally somewhat from each other, but the preparations *before* testing, e.g. mantling and obtaining test conditions, were more or less the same for all these three types of tests. Steps **I** through **VI** below show a rough summary of this general "preparation procedure". Half of the hydrostatic and deviatoric test cores were aged prior to testing. Procedure points topical for testing these cores at elevated temperature (130 °C) have been given the index "Aged".

**I:** Saturated test core with brine at least one day before testing.

**$\mathbf{I_{Aged}}$:** Cores were aged for three weeks while submerged in test brine, and stored in the aging brine in a refrigerator until testing.

**II:** Assembled the triaxial test cell.

**III:** Built up pore and confining pressure to 0.7 MPa and 1.2 MPa, respectively.

**IV:** Flooded 1 pore volume of brine (SSW) through test core.

**$\mathbf{V_{Aged}}$:** Heated the system up to 130 °C, while flooding brine.

**VI:** Lowering the piston onto the test sample.

**Test:** A hydrostatic test, deviatoric test or creep test can be run after the general preparation procedure has been completed.

The full and detailed preparation procedure will be presented chronologically in the following paragraphs, followed by detailed testing procedures for the three test types. Please note that the type of pumps differ between the two triaxial cell set-ups, where hydrostatic and deviatoric tests are carried out in *Triaxial test cell A* and the creep test in *Triaxial test cell B.* (See Table 3.3 for the overview). This causes some slight differences in the procedure as different pumps have different properties and abilities. These differences will be pointed out by separate descriptions.

### 3.5.1 Preparing the core for testing (*step I*)

**Saturating test core with brine at least one day before testing**

All samples tested at ambient conditions, plus the creep test core, were *saturated* with brine (SSW–($SO_4^{2-}$)) at least one day before running test. A chosen core was first placed in a cylindrical box with open top and put inside a vacuum container. The container lid was put on top and placed so that the fluid inlet to the chamber was vertically above the chalk core. The valve at this inlet was closed, but the other valve at the outlet connected to the vacuum pump was open so that air would be sucked out from the chamber when starting the pump. Test brine was poured into the reservoir above the container, and made sure to fill the whole tubing down to the closed chamber inlet – it was important that no air was let inside the chamber when opening the valve to fill the core at vacuum conditions.

Not more than a couple of hours should be needed to achieve “vacuum conditions” (a chamber pressure of 5 Pa, or $5 \cdot 10^{-2}$, was considered acceptable). At this point, the pump valve was closed and the fluid inlet valve opened slightly to fill the box with brine and cover the core. The fluid inlet valve was then closed, and the core left in the vacuum system for one hour to make sure that the brine would fill all pores. During this time the container could be carefully shook a couple of times to “help” the water penetrate the pores. In the end, the pump was disconnected from the lid and the valve opened to let air into the chamber, and the core was kept submerged in the box with a lid at ambient conditions until testing.

**Cores were aged for three weeks while submerged in test brine, and stored in the aging brine in a refrigerator until testing**

Chalk cores that were tested at elevated temperature were all *aged* prior to testing. The reason for doing this was to make sure that the test brine and the chalk were in equilibrium before testing. Since the chalk cores were flooded with brine both before and during testing, this balance would be disturbed and any possible chemical effects yielded by the brine would be enhanced.

After being saturated with brine, all of them together in a large vacuum container, they were put in a large aging cell (also called “autoclave”) and entirely covered with test brine. The aging cell was properly sealed and put in a heating chamber at 130 °C. Compressed air holding a pressure of 0.7 MPa was connected to the chamber inside the cell, to prevent the water from boiling. After three weeks of aging, the cores were put separately in each of their box, fully submerged in aging water from the autoclave cell. Each box was sealed with a lid and extra tightened with tape. As mentioned, it was of interest to keep the brine and chalk in a state of chemical equilibrium before testing a core. To hinder, or at least slow down, any chemical reactions to occur, the test samples were kept cool in a refrigerator until testing.

### 3.5.2 Assembling the triaxial cell (*step II*)

First of all the pipes in the pore fluid system (#1) were filled with the circulating fluid, SSW–($SO_4^{2-}$). After each test, the pipes were filled with distilled water to avoid any possibilities of salt precipitations causing blockage. Hence, prior to every test, the pipes had to be refilled with brine until it seeped out from the bottom part of the axial piston – on which the sample should be placed. A thin layer of brine on this surface would ensure that no air would be flooded through the wet core.

A prepared wet (saturated or aged) test sample was put in a cylindrical shrinking plastic sleeve, about 3 cm longer than the core and open in both ends. On each end face of the core there was put a coffee filter covering the whole surface, to prevent any possible solid particles from the core to enter the pipes. The core was put on the bottom piston part – surrounded by the sleeve, and in the same direction vertically as it had been cored from the block – and he lower movable piston part (see Fig. 3.6) was mounted on top of the core. To reduce the risk of leakage of confining fluid into the core, high silicone vacuum grease (from Dow Corning) and two rubber o-rings were put on the piston parts just above and underneath the core. The sleeve was then shrunk around the core and piston parts by using a heating gun (from Wattson Enterprise). The set-up so far is viewed in Fig. 3.23.

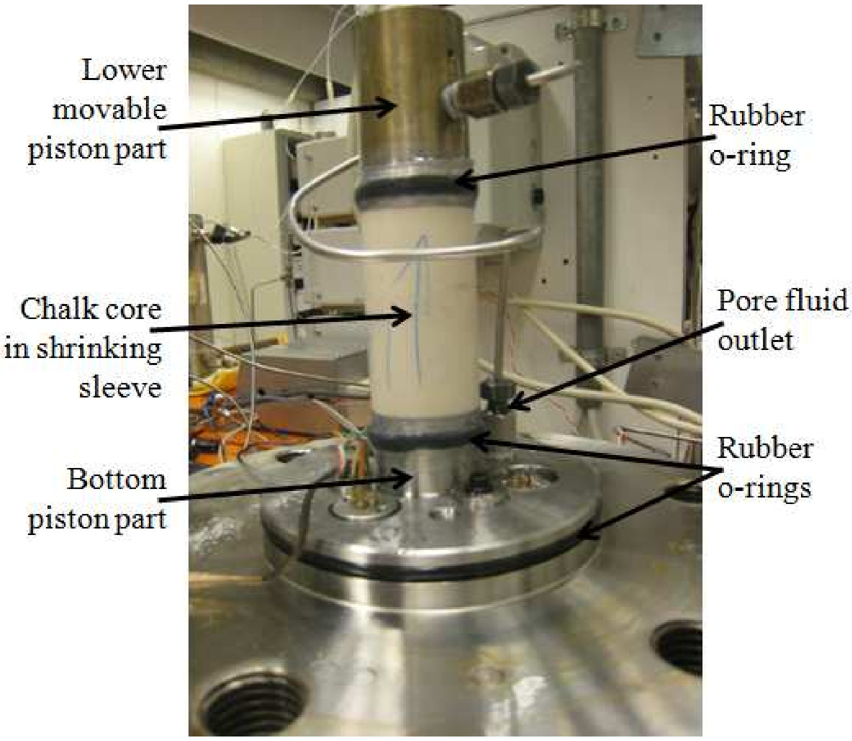

Figure 3.23: *The "internal" set-up of the triaxial test cell, viewed before the middle and upper cell parts were mounted.*

The lowermost rubber o-ring ensured that the connection between the lower (platform) and the middle cell part would be entirely sealed, as the steel cylinder ("skirt") was put in top of the platform. The lower confining outlet valve was closed and the confined area around the test core was filled with Marcol oil to the top of the skirt. Two things were checked before mounting the upper cell part (or steel lid) onto the skirt; that the movable piston was at its upper position, and that the upper confining outlet valve was open so that excess confining fluid could be removed while fitting the steel lid. Another rubber o-ring attached to the steel lid made sure that the whole confining area was sealed. To make sure that the cell parts were properly assembled to withstand high confining pressures, the six/nine massive, threaded steel bolts connected the upper and lower cell parts to each other. In the end, the LVDT pin was mounted on the very top of the cell. As the measurement pin goes through a hole in the upper movable piston part, it is important that it can move freely vertically without touching the hole walls. A compressed coil spring was also attached to press the LVDT pin in vertical direction down onto the middle movable piston part.

### 3.5.3 Building up pore and confining pressure (*step III*)

To avoid boiling of the pore fluid when testing aged cores at 130 °C, a pore pressure was built up to 0.7 MPa. And to avoid leakage of pore fluid from the core out to the confining area, the confining pressure was kept 0.5 MPa above the pore pressure at any time during the gradual pressure build-up. (The shrinking sleeve should hinder leakage the other way around). For the basis of comparison between aged cores (tested at high temperature) and "un-aged" cores (tested at ambient temperature), these mentioned pressure build-ups were also performed for the latter tests (un-aged/ambient).

**Building up confining pressure to 0.5 MPa**
First, LabVIEW was started, the confining inlet valve opened, and pump #2 set to a constant flooding (CF) rate of 2 ml/min and a maximum pressure of 0.5 MPa. The lower confining outlet valve was closed, but the upper one was first held open to release any possible air inside the confining area. When also the upper confining outlet valve was closed the confining pressure started increasing, and did so until the maximum limit was reached and the pump stopped.

*Triaxial cell A*: The confining pump was then set to constant pressure (CP) at 0.5 MPa.
*Triaxial cell B*: The CF rate was then set to a lower value, typically 0.2 ml/min, just to make sure that the pump would start and the pressure quickly stabilized again if the confining pressure should drop.

**Building up pore and confining pressure to 0.7 MPa and 1.2 MPa, respectively**
Starting at pore and confining pressure values of zero and 0.5 MPa, the pressures were gradually built up to the mentioned values. By adjusting the confining pressure it was kept constantly 0.5 MPa above the pore pressure. Pump #1 was set to deliver a CF rate of 2 ml/min, and as soon as brine started seeping out from the waste outlet – i.e. the end of the circulating fluid system, meaning that no air was left in the pipes – the back pressure was increased to 0.7 MPa. During the whole pressure build-up, both the inlet valve to the test core and the bypass test cell-valve (bypassing the whole triaxial cell) were kept open. When the pore pressure reached the values of 0.4 MPa, 0.6 MPa and finally 0.7 MPa, the pump #1 CF rate was step-wise reduced to 1 ml/min, 0.1 ml/min and 0.05 ml/min, respectively. In the end, when the pressure had reached their set-values, the pore fluid would again be able to pass the back pressure flooding device with the CF rate delivered by pump #1.

*NB: For tests at effective radial stress (confining pressure minus pore pressure) of 0.3 MPa, the confining pressure was not elevated higher than 1.0 MPa.*

### 3.5.4 Flooding 1 pore volume of testing brine through core (*step IV*)

All cores were flooded with testing brine, SSW–($SO_4^{2-}$) prior to testing; one pore volume (PV) during 24 hours. The main reason for doing this was to disturb the established equilibrium between the chalk and the pore fluid, and to enhance any possible chemical effects by the brine on the chalk's strength.

For each and every test core a flooding rate equivalent to 1 PV/24 hrs was calculated, and with very few exceptions this rate was 0.021 ml/min. When the pore and confining pressure were stabilized at the levels of 0.7 MPa and 1.2 MPa (or 1.0 MPa), respectively, pump #1 was set to a CF rate of the calculated value (0.021 ml/min). As soon as it was made sure that the pore pressure was stable at this low flooding rate, the bypass test cell-valve was closed, so that all delivered brine was flooded through the core. LabVIEW was set to log every five minutes, and the test cell was left for 24 hours – unless it was an aged core which was to be tested at high temperature (see the next paragraph). The flooding rate of 1 PV/24 hrs was held constant throughout the testing.

### 3.5.5 Heating (*step $V_{Aged}$*)

Some time after the brine flooding had started, the cell was heated to an elevated test temperature. When the heating element was turned on with a set temperature of 130 °C, the temperature started to gradually increase. This would cause the confining fluid (Marcol oil) to expand, so a spring relieve valve – connected to the upper confining outlet – had to be used to release some Marcol oil and keep the confining pressure stable at 1.2 MPa. When the set temperature was reached and stabilized, the upper confining outlet valve was closed and the cell left flooding to the next day (1 pore volume in 24 hours).

*Triaxial cell A*; Hydrostatic and deviatoric tests:
During heating the confining pump (Quizix) was stopped, because otherwise it would have received considerable amounts of fluid from the cell as the fluid expanded.
*Triaxial cell B*; Creep test:
The CF rate of confining fluid was typically increased to 2 ml/min during heating, to ensure that the confining pressure would quickly be stabilized at 1.2 MPa if it of some reason should drop below this value. After heating it was reduced to 0.2 ml/min again, typically.

*NB: Only the aged cores were tested at elevated temperature.*

### 3.5.6 Lowering the piston (*step VI*)

After (almost) 24 hours of flooding, the piston parts in the upper cell part were lowered to get in contact with the core. By opening all valves (two inlets and two outlets) and setting pump #3 to a CF rate of 1 ml/min, the upper and lower piston chambers were filled with Marcol oil. When no more air bubbles would seep out from the chamber, the lower inlet and upper outlet valve were closed. The pressure in the upper chamber would increase and eventually exceed the friction force obstructing the piston to move downwards. While moving downwards, excess fluid from the lower chamber was drained out, and the movement was viewed in LabVIEW by plotting the axial movement versus the piston pressure. Logging rate was changed from every five minutes to every half a minute, and kept at this rate throughout the testing. A safety piston pressure was set a few bar (typically 0.3-0.4 MPa) higher than the friction pressure, which typically was 0.6 MPa. So when the piston reached the core, the piston pressure would increase rapidly to this level and the pump would stop. This way, it was clear that the piston had landed, and it would rest on top of the core.

The testing could now be initiated. Further procedures for the three test types executed in the triaxial cells – starting from the moment the piston reached the test sample – are described in Paragraphs *3.5.7 Hydrostatic test*, *3.5.8 Deviatoric test* and *3.5.9 Creep test*.

### 3.5.7 Hydrostatic test

*Please note that both the two hydrostatic tests were carried out by using the* Triaxial test cell A *set-up, where a Gilson pump delivered test brine to fluid system #1, and Quizix pumps were connected to fluid systems #2 and #3 for delivery of confining and piston fluid, respectively.*

**Loading**

At the moment the piston landed on top of the test core, the piston pump (#3) was switched from CF to a CP set value of about 0.3 MPa above the experienced friction pressure during lowering. The set value of 0.9 MPa was therefore used, almost exclusively. The reason why it was set a bit higher than actually necessary was to be absolutely sure that the piston was in contact with the core at any time during the hydrostatic loading. This type of load is therefore just as well called “quasi-hydrostatic”.

During hydrostatic loading, the live plotted diagram in LabVIEW showed axial movement of the piston (i.e. axial deformation of the core) as a function of the confining pressure. The loading itself was carried out by using the “AutoOp” function on the confining Quizix pump (#2). This is an automatically controlled ramping operation which allows to choose a certain “ending set pressure” value and a set “ramp time”. In other words, it is possible to decide how long time the pump shall be running to reach a certain pressure, and this gives the opportunity of using the constant and same loading rate (MPa/min or min/MPa) during all hydrostatic loadings and tests.

For the hydrostatic tests the confining pressure was built up from 1.2 MPa to an ending set pressure of 12.7 MPa. Ramp time was set to 430 minutes, or 7 hours 10 minutes, which gives a loading rate of about 37.4 minutes per MPa pressure increase. The Quizix PumpWorks programme continuously measured the pressure and controlled the pump to deliver Marcol oil as required for a steady pressure build-up. Table 3.5 contains an overview of the (typical) pump settings and set values during the hydrostatic tests, as well as the LabVIEW settings.

Table 3.5: *Overview of the (typical) pump settings and set values, and LabVIEW settings, during* hydrostatic *testing. (CF: Constant flooding rate. CP: Constant pressure. SP: Safety pressure).*

| Pump No. | Pump type | Fluid system | Settings and set values |
|---|---|---|---|
| **#1** | **Gilson** | **Pore (Circulating fluid)** | CF = 1 PV/24 hrs<br>(0.021 ml/min) |
| **#2** | **Quizix** | **Confining (Marcol oil)** | Start pressure = 1.2 Mpa<br>Ending set pressure = 12.7 MPa<br>SP = 13.0 MPa<br>Ramp time = 430 minutes |
| **#3** | **Quizix** | **Piston (Marcol oil)** | CP = 0.9 Mpa<br>SP = 1.1 MPa |
| **#4** | **Teledyne Isco** | **Back pressure (Marcol oil)** | CP = 0.7 MPa |

| LabVIEW settings | |
|---|---|
| **Diagram view:** | Axial movement [mm] vs. Confining pressure [MPa] |
| **Logging rate:** | Every 0.5 min. |

**Unloading**

During the hydrostatic loading, the test sample would eventually go into failure. The yield point was registered as the maximum principal stress, while the effective radial stress at the yield point was used as $\sigma_3$'. When the ending set pressure was reached, the confining pump automatically switched to a CP mode at 12.7 MPa. The confining pressure was then unloaded back to 1.2 MPa by using the AutoOp function again. Also the piston pressure was unloaded this way. Ending set pressure for the confining and the piston pump was set to be 1.2 MPa and 0.8 MPa, respectively, and a ramp time of 120 minutes was used. Neither safety pressure values nor LabVIEW settings were changed.

*NB: For tests at effective radial stress (confining pressure minus pore pressure) at 0.3 MPa and 0.5 MPa, this part was not needed, as the confining pressure was already at test level.*

### 3.5.8 Deviatoric test

*Please note that all deviatoric tests were carried out by using the* Triaxial test cell A *set-up, where a Gilson pump delivered test brine to fluid system #1, and Quizix pumps were connected to fluid systems #2 and #3 for delivery of confining and piston fluid, respectively.*

Deviatoric tests were executed for many different values of effective radial stress, i.e. confining pressure minus pore pressure. Since the pore pressure was held constant at 0.7 MPa in all tests, this means that the confining pressure had to be increased to a certain level. Unless for tests carried out at an effective radial stress of 0.3 MPa or 0.5 MPa. In those cases, no extra confining load was needed from the values of 1.0 MPa or 1.2 MPa, and the deviatoric testing could be initiated at the moment the piston landed on top of the core.

### Hydrostatic loading

Confining pressure build-up to a level corresponding to the correct radial stress for the test was done hydrostatically – the exact same way as explained in Paragraph *3.5.7 Hydrostatic test* under the headline “*Loading*”. (The only differences were the ending set confining pressure and its related safety pressure, and the ramp time. Under all hydrostatic loadings the safety pressure was set to a value of 0.3 MPa above the ending set pressure).

The “ending set pressure” was set to a value 0.7 MPa (= pore pressure) above the wanted effective radial stress, and the ramp time was calculated by multiplying the standard loading rate (≈ 37.4 min/MPa, see the previous paragraph about the AutoOp function) with the needed *increase* in confining pressure. E.g., for a test to be run at effective radial stress of 4.0 MPa, the ending set pressure for the confining pump was set to be (4.0 MPa + 0.7 MPa) 4.7 MPa. Hence, a confining pressure increase of (4.7 MPa – 1.2 MPa) 3.5 MPa was needed. By multiplying this value with the loading rate, the ramp time was obtained which in this case would be (3.5 MPa · 37.4 min/MPa) 130.9 minutes.

### Deviatoric testing

When the confining pressure eventually reached the set level, pump #2 automatically switched to a CP (constant pressure) mode at the set pressure value and the deviatoric test could be started immediately. This was simply done by changing the piston pump (#3) to a CF (constant flow) mode with a flow rate of 0.01 ml/min. The piston safety pressure was typically set to 8.0 MPa. (The test core would typically yield before reaching this level by a clear margin). Settings for LabVIEW and the pumps during the deviatoric testing are shown in Table 3.6. As the axial stress increased, the test sample would eventually go into failure (yield). $\sigma_1$’ and $\sigma_3$’ were registered as the yield point and the effective radial stress, respectively. The deviatoric test was considered finished some time after passing yield.

Table 3.6: *Overview of the (typical) pump settings and set values, and LabVIEW settings, during* deviatoric *testing. (CF: Constant flooding rate. CP: Constant pressure. SP: Safety pressure).*

| Pump No. | Pump type | Fluid system | Settings and set values |
|---|---|---|---|
| **#1** | **Gilson** | **Pore<br>(Circulating fluid)** | CF = 1 PV/24 hrs<br>(0.021 ml/min) |
| **#2** | **Quizix** | **Confining<br>(Marcol oil)** | CP = (effective radial stress + 0.7 MPa)<br>SP = (CP value + 0.3 MPa) |
| **#3** | **Quizix** | **Piston<br>(Marcol oil)** | CF = 0.01 ml/min<br>SP = 8.0 MPa |
| **#4** | **Teledyne Isco** | **Back pressure<br>(Marcol oil)** | CP = 0.7 MPa |

| LabVIEW settings | |
|---|---|
| **Diagram view:** | Axial movement [mm] vs. Piston pressure [MPa] |
| **Logging rate:** | Every 0.5 min. |

### 3.5.9 Creep test

*Please note that the creep test was carried out by using the* Triaxial test cell B *set-up, where two Gilson pumps delivered test brine to fluid system #1 and Marcol oil to the confining fluid system (#2), while a Teledyne Isco pump controlled the piston fluid system (#3).*
*Please also note that the creep test core was the only sample of the high temperature (130° C) tested cores which was* not *aged prior to testing. Just like the cores tested at ambient temperature, it was only saturated with testing brine, SSW–($SO_4^{2-}$), one day before testing.*

When the piston had landed on top of the test sample, the specific preparations for the creep test could be started. Similar to the deviatoric tests the creep test was also hydrostatically loaded to a certain confining pressure level before the test itself was initiated. Since the confining fluid system (#2) was connected to a Gilson pump, and no AutoOp function was available, the loading was done by using a constant flow (CF) rate of 0.05 ml/min. The creep test was decided to be carried out at a constant confining pressure of 12.0 MPa. Hence, pump #2 was set to a maximum pressure at this level.

For a (quasi-)hydrostatic loading, the piston pressure was increased to a constant (CP) level of 0.85 MPa when reaching the core, and kept at this level throughout the creep test. During the hydrostatic pressure build-up the core sample would eventually go into failure (yield), and the loading rate was decreased after this. When the confining pressure after some hours (*in this case*: nine hours) reached 12.0 MPa, pump #2 stopped delivering fluids to the system – and by this, the creep period was started. The CF rate was increased a bit to 0.2 ml/min, to rapidly be able to stabilize at 12.0 MPa in case of a pressure drop.

For chemical analyses of the brine flooded through the chalk core, one water sample was taken of the effluent water every day of the creep test. In addition, a water sample of the standard brine was taken before it was flooded through the core. By doing this, it was possible to compare the change in ion concentrations in the water after flooding.

When the creep had lasted for exactly five weeks, the circulating fluid was changed from SSW–($SO_4^{2-}$) to SSW (containing sulphate). This was mainly done to investigate if any change in deformation rate was experienced. The creep test was continued like this for four more weeks, still saving one water sample for each day.

### 3.5.10 Finishing the triaxial cell tests

After the test was finished, the piston was first of all raised back to its upper position by switching all the four piston valves; i.e. lower inlet and upper outlet valve should be opened, the other two closed. The piston pump (#3) was set to a CF rate of 1.0 ml/min.

*For tests performed at elevated temperature*:
When the piston had “left” the core, the heating element was turned off. This would cause the temperature, and hence also the confining pressure, to decrease, so to keep the pressure stable the CF rate of the confining pump was set to 2 ml/min. After some few hours the temperature had sunk to such a level that it was possible to dismantle it with bare hands.

When the piston arrived at its upper position, the pressure in the lower chamber was bled off. All three pumps were stopped and the back pressure decreased to zero. The pore pressure would sink, and then the confining pressure was bled off through the upper outlet valve. Afterwards, compressed air (0.7 MPa) was connected to this valve, and confining fluid was removed through the lower outlet. In the end, the inlets were closed and the cell was taken apart and cleaned.

### 3.5.11 Chemical analysis of effluent water

Throughout the creep test, daily water samples had been taken of the effluent water for chemical testing. The samples were diluted 200 times with distilled water and filtered into IC glasses for use in the ion chromatograph device. Due to the amount of water samples, the samples taken when flooding with SSW–($SO_4^{2-}$) were tested separately from the ones when flooding SSW. For each of these two batches there were made four IC glasses of standard SSW–($SO_4^{2-}$) solution, four of standard “H-sal” solution and two of distilled water to be used as concentration references. All IC glasses were placed in a rack and put in the autosampler device, and two test programmes were made – one anion test and one cation test. Some hours after starting the programmes, the results could be analyzed and plotted in diagrams of ion concentration in effluent water versus creep time.

Chemical analysis like this was also performed for water samples of the water that had been in the aging cell with the cores for three weeks. Two such samples were compared to two standard SSW–($SO_4^{2-}$) solutions in the IC device.

## 3.6 Testing procedure: Brazilian test

The Brazilian test is generally a quite quick test to perform, as it is easy to install the sample in the test cell and the loading time before failure usually only takes some few minutes. However, executing a Brazilian test at high temperature takes considerably longer time. The *test* procedure is more or less the same, but the time it takes to reach the correct test temperature before every test slows down the progress, and the loading of the piston takes extra time since the chamber pressure of 0.7 MPa has to be exceeded before the core is actually loaded. In the following, the test procedure at ambient conditions is first described, and then the additional info for testing at elevated temperature is given.

**Ambient testing conditions**
12 shorter test samples had already been shaped and cut, saturated with distilled water for porosity measurements, and put in a heating chamber for drying. A straight vertical line had been drawn on samples cut from the same core, to make sure that they were put into the loading cell with the same orientation. After drying, they were all saturated with SSW–($SO_4^{2-}$) brine before being tested one by one in the Brazilian test cell. Each of them was placed edgewise in between the two loading frames, which again was put inside the cell

"house". The steel rod was lowered to rest on top of the upper frame, the load cell was placed on top of the rod, and the piston in the external loading frame was manually lowered to a position just above the load cell by using a hand pump.

Then, the Gilson pump was started, delivering Tellus oil to the piston at a CF rate of 0.5 ml/min. The pump was controlled via LabVIEW, where also the live load onto the core was plotted versus time. Logging rate was typically set to every 0.01 (or 0.001) minute. The sample was loaded diametrically until it suddenly experience failure. This is usually clearly seen on the sample itself, but is also indicated in the logging data (plot) as a sudden considerable drop in the load. The load at the point of failure, referred to as "peak force" ($F_c$ [N]), can be used in Eq. 2.63 together with the sample's diameter and length to calculate the "Brazilian" tensile strength ($T_{0B}$ [MPa]).

### High temperature (130 °C) conditions

Ten test samples were cut from five different 70 mm long cores that had already been aged and kept cool in a refrigerator. (Each core should be cut into three test samples, but due to "difficulties" during cutting the number of samples was reduced to ten). The porosity listed for these samples in the results is the average value of the ten samples, assumed that each of them holds the same porosity as the 70 mm core it was cut from.

All of the ten samples were put together in a small aging cell, fully covered by the aging brine they had been submerged in. The aging cell was sealed and put in a heating chamber over night. Before testing the next day, the aging cell was cooled down so that the water would not boil when opening it. These samples were tested at high temperature conditions, i.e. at 130 °C. One by one, the tests were executed as explained for the Brazilian tests at ambient conditions in the previous paragraph. But some additional moves were carried out to achieve correct testing conditions. Prior to the very first test, the front cover with the heating element was sealed, and heating started. Compressed air at 0.7 MPa was connected to the testing chamber, but the valve was kept closed. When the chamber temperature had reached and stabilized at 130 °C, the first core was put in the loading frame. All the samples were properly sparged with testing brine so that they would not get dry during testing. In addition, a small "cup" located below the loading frame, was also filled with brine. The front cover was then mounted to seal the testing chamber, and the compressed air valve was opened to pressurize the chamber. During this time of installing a new sample into the cell, the temperature typically sunk with 7-10 °C. For the temperature to re-stabilize at 130 °C, the test cell was left for half an hour, approximately.

At stable temperature conditions, the Gilson pump was started and the test carried out the same way as described for tests at ambient conditions (previous paragraph). The only difference was that the piston force first needed to exceed the upwards directed force from the chamber pressure before the sample actually experienced any load. In the load versus time plot in LabVIEW, this "transition" was identified as a horizontal line, i.e. a constant load value, used as a reference point (correction point) for the actual load of the core.

# 4 Results

First of all, it should be noted that the experimental work in this thesis was carried out in close co-operation with another master thesis, Davidsen (2011). A total number of 57 chalk cores were prepared and tested in several different manners. The tests were executed in combinations of four different test types (Brazilian, hydrostatic, deviatoric with different effective radial stresses, and creep tests), two different temperature conditions (ambient and 130 °C) and two different brines – synthetic seawater *without* sulphate, SSW–($SO_4^{2-}$), and synthetic seawater, SSW (containing sulphate). The matrix in Table 4.1 shows an overview of how these different "variables" were combined for all the 57 tested cores.

Table 4.1: *Overview of how many cores that were tested with the different combinations of test types, types of brines and testing conditions.*

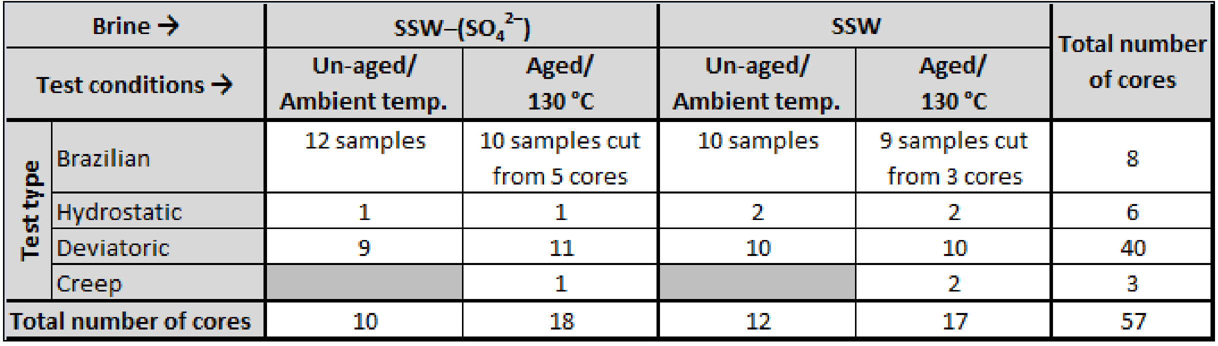

| Brine → | | SSW–($SO_4^{2-}$) | | SSW | | Total number of cores |
|---|---|---|---|---|---|---|
| Test conditions → | | Un-aged/ Ambient temp. | Aged/ 130 °C | Un-aged/ Ambient temp. | Aged/ 130 °C | |
| Test type | Brazilian | 12 samples | 10 samples cut from 5 cores | 10 samples | 9 samples cut from 3 cores | 8 |
| | Hydrostatic | 1 | 1 | 2 | 2 | 6 |
| | Deviatoric | 9 | 11 | 10 | 10 | 40 |
| | Creep | | 1 | | 2 | 3 |
| Total number of cores | | 10 | 18 | 12 | 17 | 57 |

*All samples tested at ambient temperature were only saturated with testing brine before tested – they were "un-aged" – while all samples tested at 130 °C were aged at the same temperature prior to testing.*

The type of brine is the parameter which distinguishes this thesis from the parallel work done by Davidsen (2011). But for the great basis of comparison all results from both studies will be presented and treated in the following – first for SSW–($SO_4^{2-}$) tested samples and then the results from Davidsen (2011) where cores were saturated/aged and tested with SSW.

Each chalk sample has been given a simple name consisting of the letters "LK" and a given number, where the "L" indicates chalk from Liège, "K" represents the person from the lab crew who was responsible for drilling out the chalk cores, and the numbers separate the samples from each other. In the two following tables, Table 4.2 and Table 4.3, some parameters for measuring porosities, and the porosities themselves, are listed for all the 57 core samples. The first table shows the overview of cores saturated and tested with SSW–($SO_4^{2-}$) brine, while the second table contains the equivalent info for tests where SSW brine was used.

The average porosity of all 57 chalk cores was calculated to be <u>39.57%</u> with a standard deviation of ± 0.51%.

Table 4.2: *Overview of porosities and parameters for finding them, for all cores tested with SSW–($SO_4^{2-}$) brine.*

| Test core | Diameter [mm] | Length [mm] | Pore volume [ml] | Bulk volume [ml] | Porosity [%] | Test temperature |
|---|---|---|---|---|---|---|
| LK38 | 36.99 | 68.28 | 29.49 | 73.38 | 40.19 | Ambient temp. |
| LK46 | 36.99 | 66.34 | 28.16 | 71.29 | 39.50 | Ambient temp. |
| LK48 | 36.97 | 70.12 | 29.89 | 75.27 | 39.71 | Ambient temp. |
| LK64 | 37.01 | 70.22 | 30.38 | 75.54 | 40.22 | Ambient temp. |
| LK66 | 37.02 | 68.84 | 29.77 | 74.10 | 40.18 | Ambient temp. |
| LK67 | 36.99 | 70.32 | 30.20 | 75.57 | 39.96 | Ambient temp. |
| LK68 | 36.96 | 68.99 | 29.48 | 74.02 | 39.83 | Ambient temp. |
| LK92 | 36.99 | 70.19 | 29.49 | 75.43 | 39.10 | Ambient temp. |
| LK93 | 37.01 | 70.05 | 30.11 | 75.36 | 39.96 | Ambient temp. |
| LK98 | 37.00 | 70.15 | 30.12 | 75.43 | 39.93 | Ambient temp. |
| LK27 | 37.13 | 68.93 | 29.39 | 74.64 | 39.38 | 130 °C |
| LK41 | 37.00 | 65.81 | 28.55 | 70.76 | 40.35 | 130 °C |
| LK47 | 37.03 | 70.03 | 29.47 | 75.42 | 39.07 | 130 °C |
| LK49 | 37.01 | 68.85 | 29.32 | 74.07 | 39.59 | 130 °C |
| LK50 | 36.96 | 69.53 | 29.49 | 74.60 | 39.53 | 130 °C |
| LK51 | 37.03 | 70.01 | 30.30 | 75.40 | 40.19 | 130 °C |
| LK52 | 37.00 | 70.10 | 30.23 | 75.37 | 40.11 | 130 °C |
| LK57 | 36.99 | 70.18 | 30.17 | 75.42 | 40.00 | 130 °C |
| LK58 | 36.97 | 70.13 | 30.21 | 75.28 | 40.13 | 130 °C |
| LK59 | 37.02 | 70.10 | 30.02 | 75.45 | 39.79 | 130 °C |
| LK62 | 37.00 | 70.36 | 30.43 | 75.65 | 40.22 | 130 °C |
| LK63 | 36.96 | 70.24 | 29.41 | 75.36 | 39.03 | 130 °C |
| LK65 | 37.03 | 70.22 | 29.70 | 75.62 | 39.27 | 130 °C |
| LK69 | 36.97 | 70.17 | 29.45 | 75.33 | 39.10 | 130 °C |
| LK70 | 36.94 | 70.16 | 29.89 | 75.19 | 39.75 | 130 °C |
| LK72 | 36.92 | 70.16 | 30.22 | 75.11 | 40.23 | 130 °C |
| LK74 | 36.96 | 70.13 | 29.78 | 75.24 | 39.58 | 130 °C |
| LK79 | 38.08 | 70.03 | 32.07 | 79.76 | 40.21 | 130 °C |

Of the 28 cores saturated and tested with SSW–($SO_4^{2-}$) brine, ten were tested at ambient conditions; nine of these were tested in deviatoric tests and one (LK66) was tested hydrostatically.

Five (LK27, LK41, LK49, LK63 and LK72) of the 18 cores that were aged and tested at elevated temperature, were cut into smaller samples for testing in the Brazilian cell. One (LK79) was tested in a creep test, one (LK52) was tested hydrostatically and 11 deviatoric tests were performed at 130 °C.

Table 4.3: *Overview of porosities and parameters for finding them, for all cores tested with (sulphate containing) SSW brine.*

| Test core | Diameter [mm] | Length [mm] | Pore volume [ml] | Bulk volume [ml] | Porosity [%] | Test temperature |
|---|---|---|---|---|---|---|
| LK4 | 36.96 | 72.70 | 30.97 | 78.00 | 39.71 | Ambient temp. |
| LK71 | 36.97 | 70.08 | 30.03 | 75.23 | 39.92 | Ambient temp. |
| LK75 | 37.00 | 70.17 | 28.61 | 75.45 | 37.92 | Ambient temp. |
| LK80 | 36.95 | 70.32 | 28.85 | 75.40 | 38.26 | Ambient temp. |
| LK82 | 36.95 | 70.19 | 29.24 | 75.27 | 38.85 | Ambient temp. |
| LK84 | 36.97 | 70.16 | 29.76 | 75.31 | 39.51 | Ambient temp. |
| LK85 | 36.99 | 69.93 | 29.59 | 75.15 | 39.38 | Ambient temp. |
| LK87 | 36.97 | 69.90 | 29.18 | 75.04 | 38.89 | Ambient temp. |
| LK89 | 37.03 | 70.09 | 30.05 | 75.48 | 39.81 | Ambient temp. |
| LK96 | 37.01 | 70.05 | 29.88 | 75.36 | 39.65 | Ambient temp. |
| LK97 | 36.98 | 70.22 | 30.13 | 75.42 | 39.95 | Ambient temp. |
| LK99 | 36.99 | 70.18 | 30.08 | 75.42 | 39.88 | Ambient temp. |
| LK7 | 37.04 | 70.00 | 29.95 | 75.43 | 39.71 | 130 °C |
| LK11 | 37.05 | 70.07 | 29.42 | 75.54 | 38.94 | 130 °C |
| LK15 | 36.99 | 69.86 | 29.33 | 75.07 | 39.07 | 130 °C |
| LK17 | 37.02 | 70.11 | 29.59 | 75.46 | 39.21 | 130 °C |
| LK18 | 36.96 | 70.07 | 29.97 | 75.18 | 39.87 | 130 °C |
| LK19 | 37.05 | 70.25 | 30.12 | 75.74 | 39.77 | 130 °C |
| LK20 | 36.97 | 70.15 | 29.27 | 75.30 | 38.87 | 130 °C |
| LK21 | 37.03 | 70.11 | 29.73 | 75.51 | 39.37 | 130 °C |
| LK25 | 36.99 | 69.98 | 29.79 | 75.20 | 39.61 | 130 °C |
| LK26 | 37.09 | 70.17 | 29.95 | 75.81 | 39.50 | 130 °C |
| LK28 | 36.93 | 69.41 | 29.20 | 74.35 | 39.27 | 130 °C |
| LK29 | 37.00 | 69.98 | 30.18 | 75.24 | 40.11 | 130 °C |
| LK32 | 36.98 | 69.78 | 29.95 | 74.95 | 39.96 | 130 °C |
| LK34 | 37.10 | 70.30 | 29.34 | 76.00 | 38.61 | 130 °C |
| LK35 | 36.99 | 69.95 | 29.54 | 75.17 | 39.30 | 130 °C |
| LK94 | 37.00 | 70.18 | 29.52 | 75.46 | 39.12 | 130 °C |
| LK95 | 36.98 | 69.91 | 29.73 | 75.09 | 39.59 | 130 °C |

For the 29 cores tested by Davidsen (2011) with sulphate containing SSW brine, 12 cores were tested at ambient temperature. Two (LK4 and LK97) of them hydrostatically, and the other ten were deviatoric tests.

The 17 cores tested at high temperature were divided into four groups of test types. Three (LK25, LK32 and LK35) of them were further cut to become Brazilian test samples, two (LK95 and LK95) creep tests were performed, two (LK20 and LK34) were tested hydrostatically while the remaining ten were used in different deviatoric tests.

## 4.1 Synthetic seawater without sulphate, SSW–($SO_4^{2-}$)

Some of the main and underlying objectives of this work were to obtain as-good-as-possible estimates of the chalk's failure envelope (in a *q-p'* plot) at different testing conditions and with different brines, and to find the cohesion ($S_0$) and friction angle ($\varphi$) of the chalk. Several Brazilian tests, hydrostatic tests and deviatoric tests were executed to be able to determine these parameters. The minimum ($\sigma_3$') and maximum ($\sigma_1$') principal stresses at failure from each test were used as basis for a Mohr circle and a plotting point in the *q-p'* plot. When a number of tests had been performed, the cohesion, friction angle and failure envelope could be determined. In the following subsections, results from mechanical tests where SSW–($SO_4^{2-}$) was used as brine are presented in tables, Mohr plots and *q-p'* plots. When considering the *q-p'* plot, the results from the Brazilian tests and the hydrostatic tests contributed to plotting points closer to the *q*-axis and the *p'*-axis, respectively.

First, the tests of un-aged cores at ambient conditions will be regarded, followed by results from aged cores tested at high temperature (130 °C). The creep test results will be presented in the end.

### 4.1.1 Un-aged cores tested at ambient temperature

**Results in tables**

The results from Brazilian, the hydrostatic and the nine deviatoric tests (listed as "Dev.") executed with SSW–($SO_4^{2-}$) brine at ambient temperature are listed in Table 4.4, while Table 4.5 contains more detailed result information from the Brazilian tests.

Table 4.4: *Overview of results from mechanical tests where un-aged samples were tested at ambient conditions with SSW–($SO_4^{2-}$) brine.*

| Test type | Test core | Porosity [%] | $\sigma_3$' [MPa] | $\sigma_1$' [MPa] | *q* [MPa] | *p'* [MPa] | *E*-modulus [GPa] | *K*-modulus [GPa] |
|---|---|---|---|---|---|---|---|---|
| Brazilian | *(see Table 4.5)* | 39.49 | -0.46 | 1.38 | 1.84 | 0.15 | | |
| 0.3 MPa Dev. | LK68 | 39.83 | 0.3 | 5.2 | 4.9 | 1.93 | 1.376 | |
| *0.5 MPa Dev.* | *LK48* | *39.71* | *0.5* | *4.2* | *3.7* | *1.73* | *1.480* | |
| avg(0.5 MPa Dev.) | LK48/LK46 | | 0.5 | 4.5* | 4.0 | 1.83 | 1.357* | |
| *0.5 MPa Dev.* | *LK46* | *39.50* | *0.5* | *4.8* | *4.3* | *1.93* | *1.234* | |
| 1.0 MPa Dev. | LK38 | 40.19 | 1.0 | 6.2 | 5.2 | 2.73 | 1.262 | |
| 1.2 MPa Dev. | LK93 | 39.96 | 1.2 | 6.2 | 5.0 | 2.87 | 1.299 | |
| 2.3 MPa Dev. | LK67 | 39.96 | 2.3 | 8.4 | 6.1 | 4.33 | 1.577 | |
| 4.0 MPa Dev. | LK64 | 40.22 | 4.0 | 9.3 | 5.3 | 5.77 | 1.508 | |
| 7.0 MPa Dev. | LK92 | 39.10 | 7.0 | 11.4 | 4.4 | 8.47 | 1.907 | |
| 8.0 MPa Dev. | LK98 | 39.93 | 8.0 | 12.5 | 4.5 | 9.50 | 1.805 | |
| Hydrostatic | LK66 | 40.18 | 10.2 | 10.7 | 0.5 | 10.37 | | 0.689 |

(**The listed value is an average value from two similar deviatoric tests, both executed with an effective radial stress of 0.5 MPa*).

As a general trend, it is obvious that the yield points ($\sigma_1$') increase with increasing degree of radial support ($\sigma_3$') for the deviatoric tests. Two deviatoric tests (LK48 and LK46) are run with an effective radial stress of 0.5 MPa. For comparison, the values of yield point and *E*-modulus representing this radial stress will be given as the average values between the two tests. When regarding the Mohr circle plots and the *q*-*p'* plot, the $\sigma_3$' and $\sigma_1$' values from the table above are the basis material. They are directly used when drawing a Mohr circle, and the *q* and *p'* values can be calculated from these two parameters only. For every deviatoric test the *E*-modulus is given, and *K*-modulus for the hydrostatic test is also listed. The porosity listed for the Brazilian tests in Table 4.4 is the average porosity value of the twelve shorter samples tested in the Brazilian cell. $\sigma_3$' and $\sigma_1$' based on these tests are directly determined from the average Brazilian tensile strength ($T_{0B}$) of all the Brazilian tests, and easily calculated by using Eq. 2.64 and Eq. 2.65, respectively.

Table 4.5: *Overview of results from the Brazilian testing of un-aged samples at ambient temperature with SSW–($SO_4^{2-}$) brine.*

| Core sample | Diameter [mm] | Length [mm] | Pore volume [ml] | Bulk volume [ml] | Porosity [%] | Peak force [kN] | $T_{0B}$ [MPa] |
|---|---|---|---|---|---|---|---|
| LK (5.1) | 36.98 | 24.30 | 10.25 | 26.10 | 39.27 | 0.61 | 0.44 |
| LK (5.2) | 36.96 | 24.89 | 10.70 | 26.70 | 40.07 | 0.80 | 0.55 |
| LK (5.3) | 36.95 | 21.62 | 9.40 | 23.18 | 40.55 | 0.68 | 0.54 |
| LK (6.1) | 36.98 | 22.83 | 9.75 | 24.52 | 39.76 | 0.73 | 0.55 |
| LK (6.2) | 36.97 | 24.04 | 10.30 | 25.81 | 39.91 | 0.76 | 0.54 |
| LK (7.1) | 36.99 | 22.06 | 9.54 | 23.71 | 40.24 | 0.41 | 0.32 |
| LK (7.2) | 36.98 | 19.91 | 8.48 | 21.38 | 39.66 | 0.50 | 0.43 |
| LK (7.3) | 36.98 | 21.18 | 8.92 | 22.75 | 39.21 | 0.56 | 0.46 |
| LK (8.1) | 36.96 | 21.90 | 9.10 | 23.50 | 38.73 | 0.46 | 0.36 |
| LK (8.2) | 36.97 | 20.39 | 8.30 | 21.89 | 37.92 | 0.46 | 0.39 |
| LK (8.3) | 37.00 | 20.43 | 8.63 | 21.97 | 39.29 | 0.46 | 0.38 |
| LK (9.1) | 36.96 | 22.84 | 9.62 | 24.50 | 39.26 | 0.76 | 0.57 |
| **Average** | | | | | **39.49** | | **0.46** |
| **Standard deviation** | | | | | | | **0.08** |

Table 4.5 shows an overview of test results for the twelve Brazilian test samples, as well as data used for calculating their porosities. The average Brazilian tensile strength was found to be $\overline{T}_{0B} = 0.46\,\mathrm{MPa}$ with a standard deviation of ± 0.08 MPa. The samples' porosities and the parameters used to calculate them are also listed in Table 4.5.

**Example of graphical attainment of yield point and elasticity moduli data**

As explained in Paragraph *2.5.3 Yield* the maximum principal stress ($\sigma_1$') for hydrostatic and deviatoric tests is defined as the axial stress value at which the test material goes into failure (starts yielding), or graphically in an axial stress versus axial strain plot; the stress value at which the curve starts deviating from the linear trend. Such an example is stated in Fig. 4.1 where the stress-strain plot is shown for the deviatoric test of LK93, tested at ambient conditions with SSW–($SO_4^{2-}$) brine. For this core, the effective radial stress (confining pressure minus pore pressure) was held constant at 1.2 MPa ($\sigma_3' = 1.2$ MPa), and yield was observed when the axial stress had been increased to 6.2 MPa ($\sigma_1' = 6.2$ MPa). These values are listed in Table 4.4.

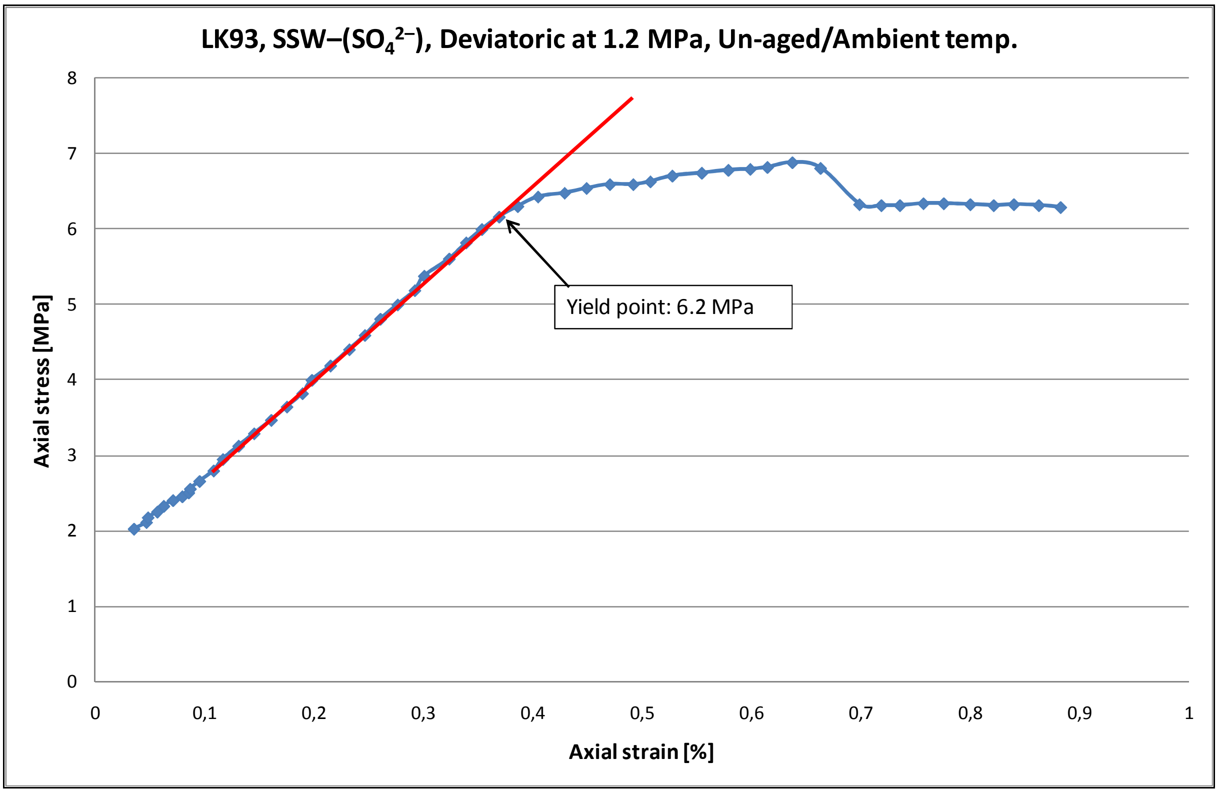

Figure 4.1: *Typical axial stress versus axial strain plot for a deviatoric test.* Here*: LK93, saturated and tested with SSW–(*$SO_4^{2-}$*) brine as circulating fluid at ambient conditions, and at an effective radial stress of 1.2 MPa. The yield point was determined to be 6.2 MPa for this test.*

Table 4.4 also contains elasticity moduli for the tests, which are also found from the axial stress versus axial strain plot – but from the logging data prior to yield. That is, when the material still behaves elastically. For hydrostatic tests a *K*-modulus is found as described in Paragraph *2.3.3 Bulk modulus (*K*-modulus)* while *E*-modulus (see Paragraph *2.3.4 Young's modulus (*E*-modulus)* is determined from deviatoric tests.

For the same deviatoric test (LK93) as presented in Fig. 4.1, Fig. 4.2 shows how a linear regression line is drawn in the stress-strain plot to fit a section of the plotted curve prior to yield. The slope of this linear line (in this case: 12.99 MPa) is the basis for simple calculation of the elastic modulus. For hydrostatic tests the slope value can be divided by 30 to obtain the bulk modulus (*K*) in GPa (see Eq. 2.34), while the *E*-modulus [GPa] for deviatoric test is calculated by dividing the slope by 10 (see Eq. 2.37). In the deviatoric test of LK93, the *E*-modulus is therefore equal to 1.299 GPa, which is also listed in Table 4.4.

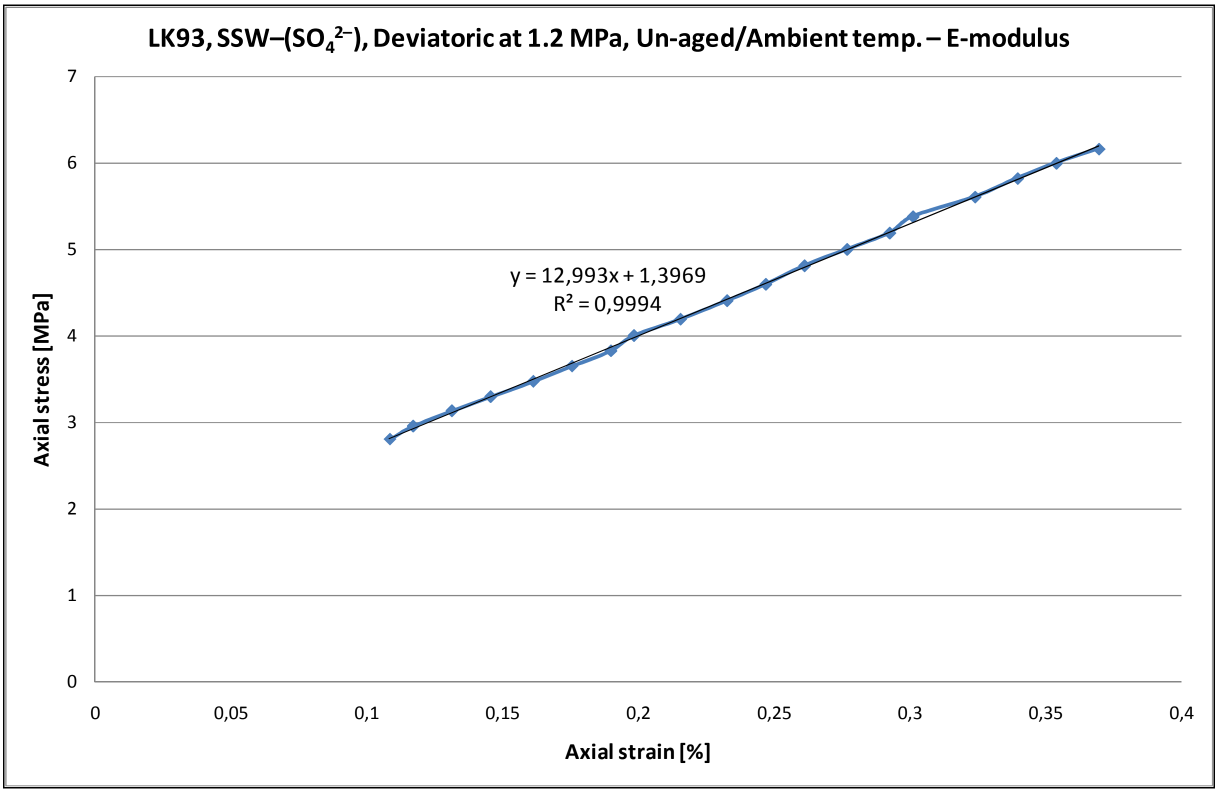

Figure 4.2: *Typical axial stress versus axial strain plot for the elastic part of a deviatoric test before yield has been reached.* Here*: LK93, saturated and tested with SSW–($SO_4^{2-}$) brine as circulating fluid at ambient conditions, and at an effective radial stress of 1.2 MPa. The E-modulus was determined to be 1.299 GPa for this test.*

Based on the assumption that chalk behaves like an isotropic material, deformation can also be expressed in terms of *volumetric* strain. From the deduction of Eq. 2.29 it becomes clear that the volumetric strain for such a material is three times the magnitude of the axial strain. From an axial stress versus volumetric strain plot for a hydrostatic test prior to yield, the *K*-modulus [GPa] can be determined by dividing the slope of the linear curve by 10. Fig. 4.3 shows how a linear regression line is drawn in the stress-strain plot to fit a section of the plotted curve prior to yield – equivalent to the case in Fig. 4.2 for Young's modulus. In this case, the slope of the linear line is 6.89 MPa, and the value of *K* is thus equal to 0.689 GPa.

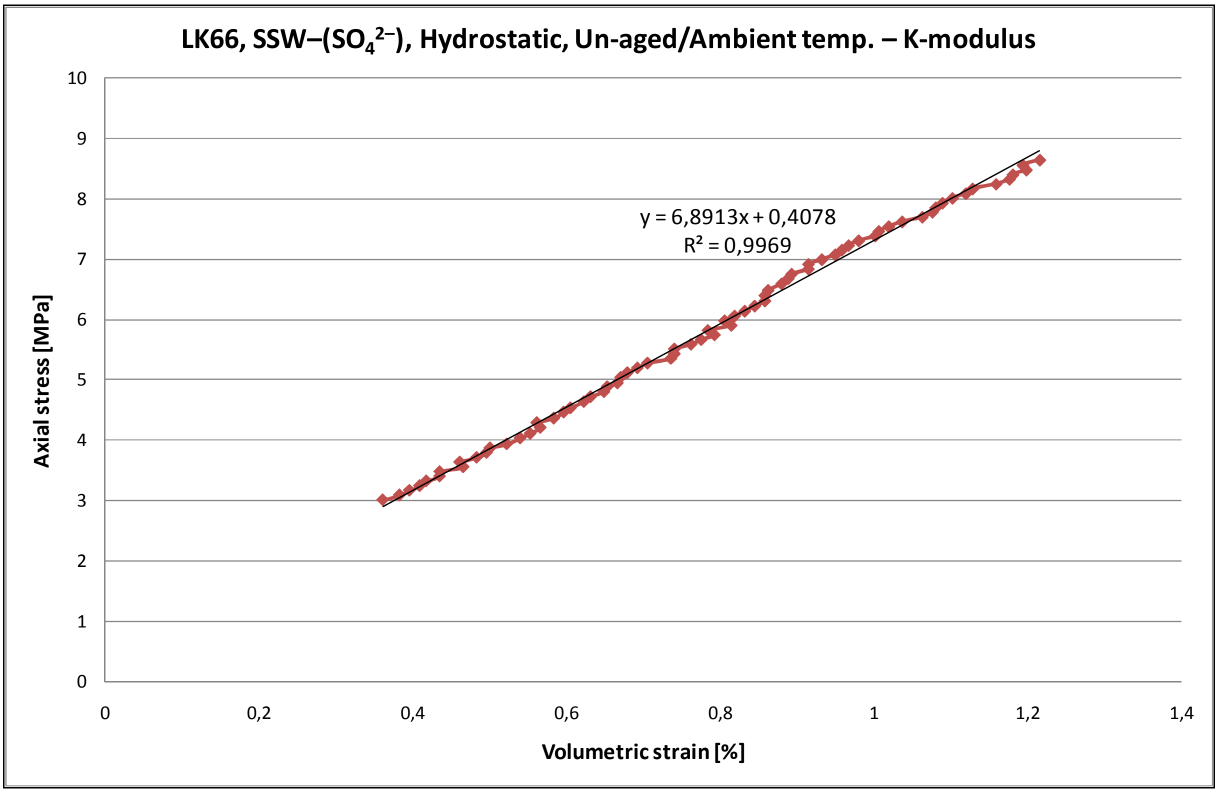

Figure 4.3: *Typical axial stress versus volumetric strain plot for the elastic part of a hydrostatic test before yield has been reached.* Here*: LK66, saturated and tested with SSW–($SO_4^{2-}$) brine as circulating fluid at ambient conditions. The* K*-modulus was determined to be 0.689 GPa for this test.*

### Mohr plot and *q-p'* plot

As mentioned, the minimum and maximum principal stressed obtained from a test can be used directly in a $\tau$–$\sigma$ diagram to draw a Mohr circle. The two values define the lower and upper intersection point with the $\sigma$-axis, respectively, and the difference in between them is therefore equal to the diameter of the circle. Results from Brazilian and deviatoric tests may be plotted as Mohr circles together in a $\tau$–$\sigma$ diagram. The actual results from the tests carried out on un-aged samples tested at ambient temperature with the use of SSW–($SO_4^{2-}$), are presented as Mohr circles in Fig. 4.4. (Results from hydrostatic tests are often not plotted as Mohr circles because of small difference between $\sigma_1$' and $\sigma_3$').

The Mohr circle for a Brazilian test will intersect the $\tau$-axis, as the minimum principal stress will be negative. This intersection point with the $\tau$-axis can be regarded as a good estimate for the cohesion ($S_0$) of the chalk material. (At least for chalks there is a good correspondence between this intersection point and $S_0$). A linear line can be drawn so that it touches the leftmost Mohr circles, i.e. the circles representing tests with lower effective radial stresses. This line is called "failure line", and the Mohr circle for the Brazilian test will be good as a reference for "guiding" the failure line towards the $\tau$–axis, and thus determining the cohesion. When the units on both diagram axes are of equal magnitudes of order, the angle between the failure line and the horizontal $\sigma$-axis defines the friction angle ($\varphi$), and by using Eq. 2.40 and Eq. 2.43 it is easy to compute the friction coefficient ($\mu$) and failure angle ($\beta$), respectively.

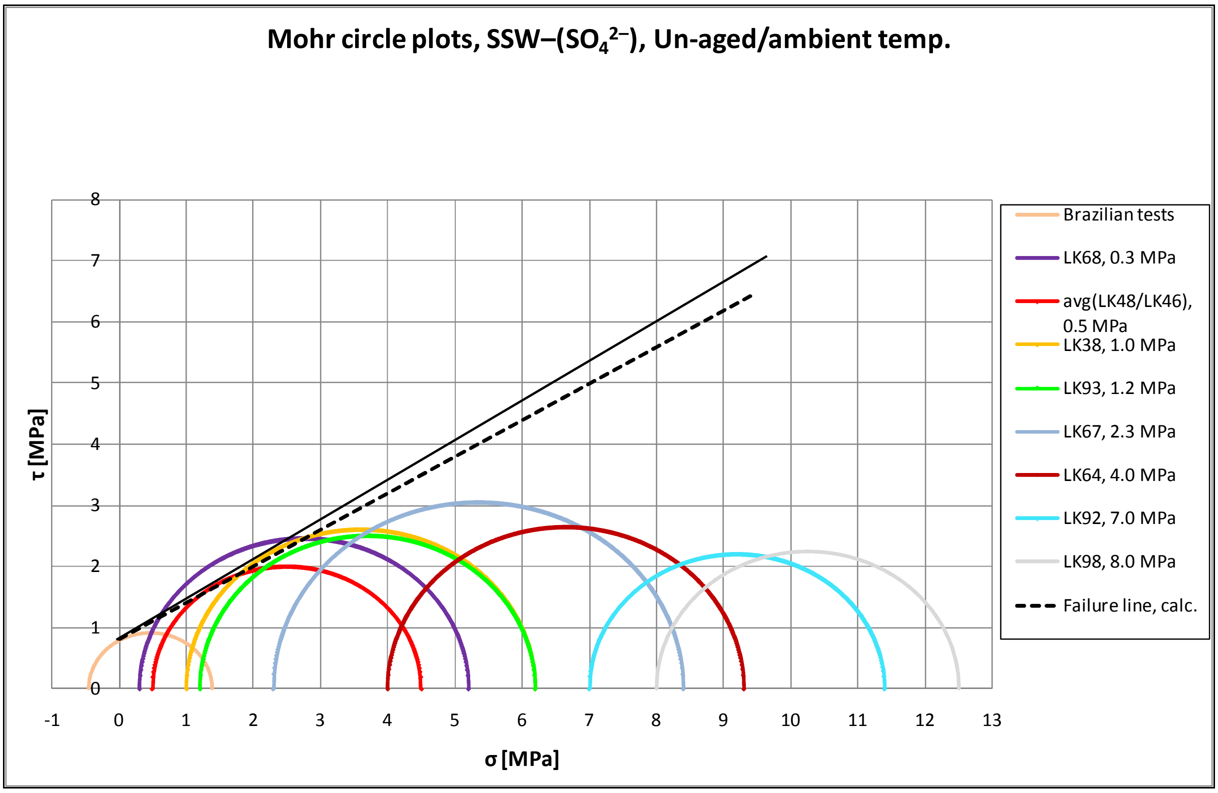

Figure 4.4: *Mohr circles for Brazilian and deviatoric tests carried out on un-aged cores at ambient temperature with the use of SSW–($SO_4^{2-}$) as test brine. Based on some of the leftmost circles a failure line can be drawn (solid line). Alternatively, the failure line can be calculated (dotted line) from the* q-p’ *plot in Fig. 4.5. Cohesion* ($S_0$) *and friction angle* (φ) *can be determined directly from the failure line(s).*

From the actual results presented in Fig. 4.4, an attempt of drawing a failure line can be made. This is often very difficult as it is not easy to tell which and how many circles that should be equalled by the linear line. In this case the mechanical strength results of LK68 (*0.3 MPa Dev.*) are considered to be deviant from the “norm”, in the sense that it seems abnormally strong. This is also indicated by the yield point listed in Table 4.4, which is higher than both the deviatoric tests at 0.5 MPa effective radial stress. LK68 is therefore ignored when drawing the failure line. From the resulting drawn line it is possible to determine the cohesion and the friction angle, and based on the latter, the failure angle and friction coefficient are calculated. All these parameters are listed to the left in Table 4.6.

In addition to the drawn failure line based on the Mohr circles, there is another “more reliable” way of determining the failure line. Namely by calculating it, based on the *q-p’* plot presentation. The procedure will be explained in the following.

A failure envelope is obtained from the *q-p’* plot when a proper number of tests have been performed. Consisting of a linear shear failure line for lower *p’* values and a changeover to an end cap for higher *p’* values, the failure envelope as a whole delimits the elastic area for the material. At the end cap part of the curve, pore collapse is suggested to be the dominating failure mechanism. Fig. 4.5 shows the *q-p’* plot for all mechanical tests performed on un-aged cores at ambient temperature, saturated with synthetic seawater without sulphate.

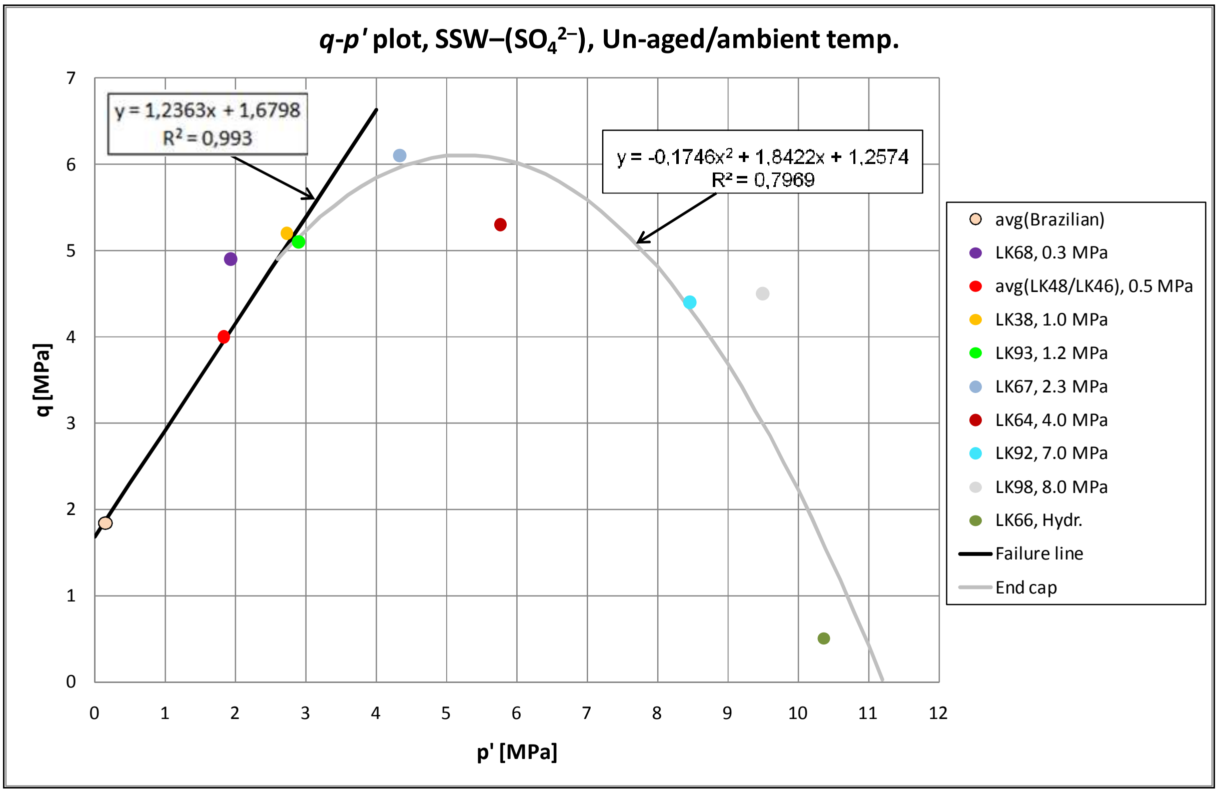

Figure 4.5: q-p’ *plot for Brazilian, deviatoric and hydrostatic tests carried out on un-aged cores at ambient temperature with the use of SSW–($SO_4^{2-}$) as test brine. The failure line is found from a linear regression, while the end cap line is estimated by the use of second order polynomial regression.*

Plotting points for some of the tests carried out at lower effective radial stresses form a linear trend, and the Brazilian test result is a very good “guiding point” for this trend line. By using a linear regression for these points, a “calculated” shear failure line is obtained. Similar to the case when drawing the failure line in the Mohr diagram, LK68 is also here neglected, and only the average value of the two 0.5 MPa deviatoric tests is used. (The following test samples were included for the linear regression; Brazilian tests, avg(LK48/LK46), LK38, LK93). This yields a very good fit with the plotting result points, as the $R^2$ value for the shear calculated shear failure line is ≈0.99.

As explained in Paragraph *2.3.7* q-p’ *plot*, the slope of this line and its intersection point with the *q*-axis can be used in Eq. 2.52 and Eq. 2.53 to calculate the friction angle ($\varphi$) and the cohesion ($S_0$), respectively. These parameters, as well as their corresponding failure angle and friction coefficient, are listed to the right in Table 4.6, while the corresponding failure line is drawn as a dotted line in Fig. 4.4.

Table 4.6: *Overview of cohesion (*$S_0$*), friction angle (φ), failure angle (β) and friction coefficient (μ) values determined for un-aged cores tested at ambient temperature by the use of SSW–(*$SO_4^{2-}$*) as testing brine. The values are obtained from the drawn failure line based on Mohr circles (to the left) and the calculated failure line based on the* q-p’ *plot.*

| **Mechanical parameter** | **Drawn failure line, based on Mohr circles** | **Calculated failure line, based on *q*-*p'* plot** |
|---|---|---|
| $S_0$ [MPa] | 0.85 | 0.81 |
| $\varphi$ [°] | 33 | 31 |
| β [°] | 62 | 60 |
| $\mu$ | 0.65 | 0.60 |

From Table 4.6 it is seen that there is a fairly good match between the results from the two different failure lines. The good match between them tells that the method of calculating the parameters and (regression) failure line from the *q-p’* plot is highly acceptable. For comparison in the discussion part of this thesis, only the *q-p’* plot based failure lines will be regarded.

In the presentations within this thesis, second order polynomial regression is used for estimating the end cap parts of the failure envelopes. Plotting points stretching from the transition from the linear trend of the shear failure line to the hydrostatic test result, are included for this regression. (These test samples are; avg(LK48/LK46), LK38, LK93, LK67, LK64, LK92, LK98, LK66). In this case, for un-aged cores tested at ambient temperature with SSW–($SO_4^{2-}$) as test brine, the results are scattered in such a manner that the second order polynomial regression does not give a too good match with the experimental data. However, relative to the other end cap lines estimated within this thesis, the $R^2$ value of ≈0.80 is more or less the average. In the same manner as the Brazilian result is a good guiding point for orientation of the shear failure line, the result from the hydrostatic test gives a good indication of where the end cap line will “end” (relative to the *p’*-axis).

## 4.1.2 Aged cores tested at 130 ℃

**Results in tables**

Results from Brazilian tests, the hydrostatic test and the eleven deviatoric tests with varying degree of radial support – all carried out with SSW–($SO_4^{2-}$) brine at high temperature (130 °C) – are listed in Table 4.7.

Table 4.7: *Overview of results from mechanical tests where aged samples were tested at 130 °C with SSW–($SO_4^{2-}$) brine.*

| Test type | Test core | Porosity [%] | $\sigma_3'$ [MPa] | $\sigma_1'$ [MPa] | $q$ [MPa] | $p'$ [MPa] | $E$-modulus [GPa] | $K$-modulus [GPa] |
|---|---|---|---|---|---|---|---|---|
| Brazilian | *(see Table 4.8)* | 39.69 | -0.51 | 1.53 | 2.08 | 0.17 | | |
| 0.3 MPa Dev. | LK50 | 39.53 | 0.3 | 4.4 | 4.1 | 1.67 | 1.155 | |
| 0.5 MPa Dev. | LK62 | 40.22 | 0.5 | 4.9 | 4.4 | 1.97 | 1.277 | |
| 0.8 MPa Dev. | LK69 | 39.10 | 0.8 | 5.4 | 4.6 | 2.33 | 1.378 | |
| 1.0 MPa Dev. | LK57 | 40.00 | 1.0 | 6.2 | 5.2 | 2.73 | 1.346 | |
| 1.2 MPa Dev. | LK70 | 39.75 | 1.2 | 6.7 | 5.5 | 3.03 | 1.094 | |
| 1.5 MPa Dev. | LK65 | 39.27 | 1.5 | 7.4 | 5.9 | 3.47 | 1.169 | |
| 1.8 MPa Dev. | LK74 | 39.58 | 1.8 | 8.3 | 6.5 | 3.97 | 1.172 | |
| 2.3 MPa Dev. | LK58 | 40.13 | 2.3 | 7.1 | 4.8 | 3.90 | 1.186 | |
| 3.0 MPa Dev. | LK59 | 39.79 | 3.0 | 8.1 | 5.1 | 4.70 | 1.355 | |
| 4.0 MPa Dev. | LK47 | 39.07 | 4.0 | 9.0 | 5.0 | 5.67 | 1.134 | |
| 7.0 MPa Dev. | LK51 | 40.19 | 7.0 | 11.8 | 4.8 | 8.60 | 1.360 | |
| Hydrostatic | LK52 | 40.11 | 10.3 | 10.8 | 0.5 | 10.47 | | 0.587 |

Yield point and elasticity modulus for each test is found by using the same methods as described in the example for tests at ambient temperature. Also here, there is a clear increasing trend in yield point values with increasing degree of radial support for the deviatoric tests. However, there are a couple of values which does not match this trend, in the radial stress range of 1.5-3.0 MPa. It is not easy to tell which values are most representative from only one test at each radial stress value. More detailed result information showing how the average $T_{0B}$ is found from the ten individual Brazilian tests is given in Table 4.8. This value, from which the $\sigma_3$' and $\sigma_1$' are easily calculated, was determined to be $\overline{T_{0B}} = 0.51\,\mathrm{MPa}$ with a standard deviation of ± 0.08 MPa.

Table 4.8 also contains the porosity value of each sample. It should be noted that the ten Brazilian test samples were cut from five 70 mm cores which had already been aged. It was impossible to determine porosity for each of the cut samples, as they were to be submerged in aging brine until testing. Thus, their dry weights could not be measured. Of this reason, the porosity listed for a sample in Table 4.8 is equal to the measured porosity of the 70 mm core which the sample was cut from. As long as no other option is possible, this should be an acceptable assumption. In addition it should be noticed that during high temperature Brazilian tests, the test chamber holds a pressure of 0.7 MPa. The piston load must first exceed this pressure to get in contact with the loading frames, and a correction factor is therefore subtracted from the peak force (load) to obtain the actual force that the sample was exposed to at failure. These correction factors are also listed in Table 4.8.

Table 4.8: *Overview of results from the Brazilian testing of aged samples at 130 °C with SSW–($SO_4^{2-}$) brine.*

| Core sample | Diameter [mm] | Length [mm] | Porosity [%] | Peak force* [kN] | Correction factor [kN] | $T_{0B}$ [MPa] |
|---|---|---|---|---|---|---|
| LK27 B | 36.95 | 24.36 | 39.38 | 0.65 | 0.237 | 0.46 |
| LK41 B | 36.96 | 21.82 | 40.35 | 0.70 | 0.270 | 0.55 |
| LK41 M | 36.96 | 20.66 | 40.35 | 0.61 | 0.233 | 0.51 |
| LK41 T | 36.96 | 20.95 | 40.35 | 0.58 | 0.254 | 0.47 |
| LK49 M | 36.94 | 20.12 | 39.59 | 0.67 | 0.242 | 0.57 |
| LK49 T | 36.94 | 22.54 | 39.59 | 0.80 | 0.223 | 0.60 |
| LK63 B | 36.95 | 22.68 | 39.03 | 0.87 | 0.208 | 0.66 |
| LK63 M | 36.95 | 22.51 | 39.03 | 0.52 | 0.248 | 0.39 |
| LK63 T | 36.95 | 22.76 | 39.03 | 0.64 | 0,255 | 0.48 |
| LK72 B | 36.95 | 23.47 | 40.23 | 0.62 | 0.238 | 0.45 |
| **Average** | | | **39.69** | | | **0.51** |
| **Standard deviation** | | | | | | **0.08** |

(**The listed peak force includes the correction factor*).

### Mohr plot and *q-p'* plot

Based on the minimum and maximum principal stresses obtained and listed in Table 4.7, Mohr circles can be drawn for all the different tests. The diagram in Fig. 4.6 contains Mohr circle plots for the Brazilian and all deviatoric tests carried out at high temperature with the use of SSW–($SO_4^{2-}$) as brine.

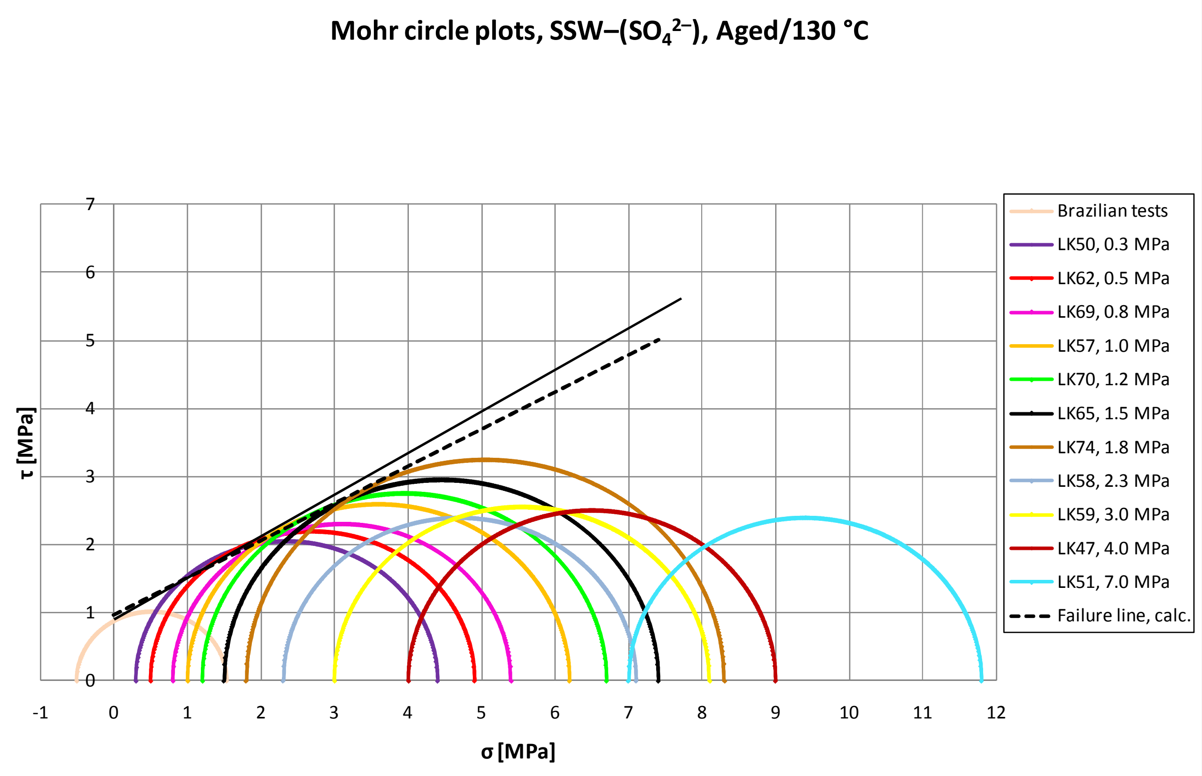

Figure 4.6: *Mohr circles for Brazilian and deviatoric tests carried out on aged cores at 130 °C with the use of SSW–($SO_4^{2-}$) as test brine. Based on some of the leftmost circles a failure line can be drawn (solid line). Alternatively, the failure line can be calculated (dotted line) from the* q-p' *plot in Fig. 4.7. Cohesion* ($S_0$) *and friction angle* (φ) *can be determined directly from the failure line(s).*

A failure line can be drawn in the Mohr diagram, tangent to some of the Mohr circles of low effective radial stresses (low *p’* values) and guided towards the *τ*-axis by the Mohr circle from the Brazilian tests. This line is shown as a solid linear line in Fig. 4.6. For another estimate of the failure line, the shear failure line from the *q-p’* plot is calculated by using a linear regression. The corresponding failure line in the Mohr plot is plotted in Fig. 4.6 as a dotted line. (The following test samples were included for the linear regression; Brazilian tests, LK50, LK62, LK69, LK57, LK70, LK65, LK74).

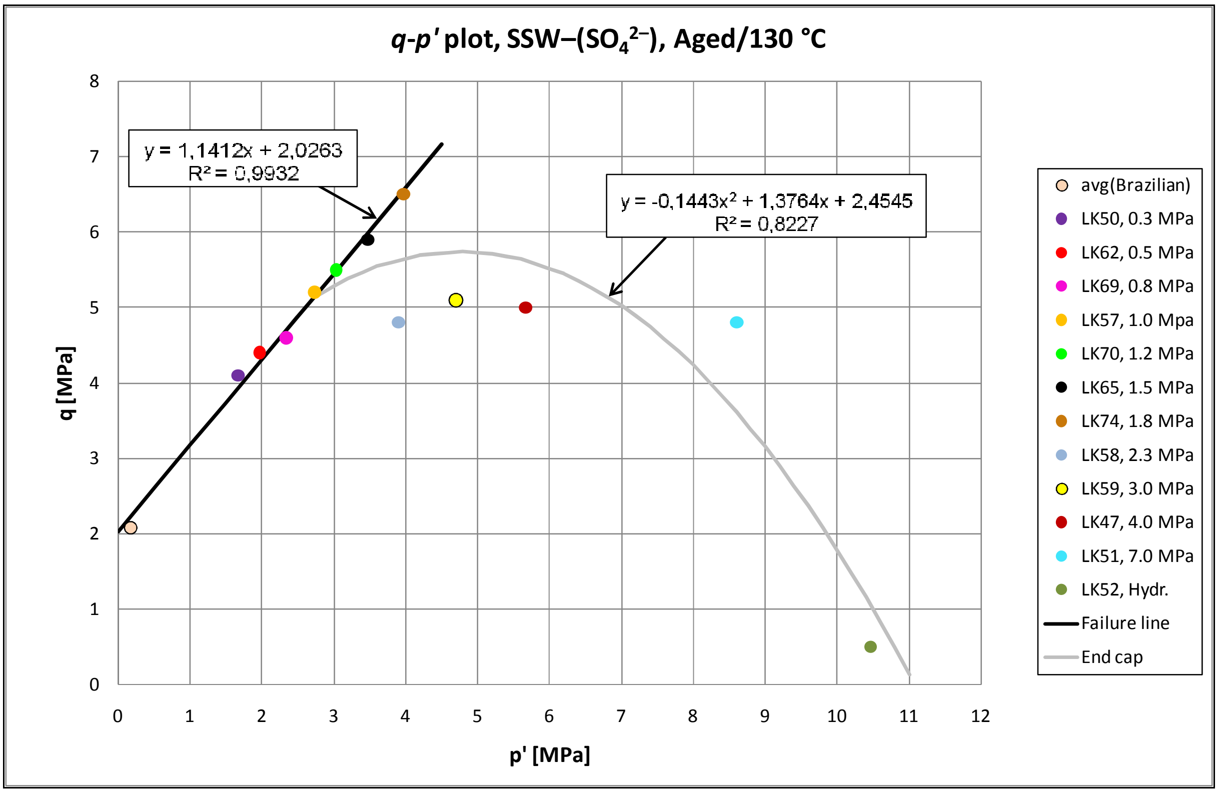

Figure 4.7: q-p’ *plot for Brazilian, deviatoric and hydrostatic tests carried out on aged cores at 130 °C with the use of SSW–(SO$_4^{2-}$) as test brine. The failure line is found from a linear regression, while the end cap line is estimated by the use of second order polynomial regression.*

Fig. 4.7 shows the *q-p’* plot for the results from all tests listed in Table 4.7, as well as the failure line and end cap line calculated by regression methods. There is a very good linear trend for the results from tests at radial stress up to 1.8 MPa, with an R$^2$ value of ≈0.99. But for these results it is really difficult to determine how the transition from failure line to the end cap line will be, as the plotting points in the (apparent) transition area are highly scattered. For instance, there is a significant drop in *q* value from the 1.8 MPa deviatoric test to the 2.3 MPa deviatoric test, even though the *p’* values are very much alike. A second order polynomial regression was used to achieve the end cap line shown in Fig. 4.7. The R$^2$ value for this line is ≈0.82. (The following the test samples were included for this regression; LK70, LK65, LK74, LK58, LK59, LK47, LK51, LK52).

From both the failure line drawn in the Mohr plot (Fig. 4.6) and the failure line calculated from the *q-p’* plot (Fig. 4.7), the cohesion and friction angle can be directly interpreted. These values, as well as their respective calculated failure angles and friction coefficients, are listed in Table 4.9. Again, there is a relatively good match between the two methods, which indicates that the way of calculating the failure line from the *q-p'* plot is acceptable. For comparison in the discussion part of this thesis, only the *q-p'* plot based failure line will be regarded.

Table 4.9: *Overview of cohesion (*$S_0$*), friction angle (*φ*), failure angle (*β*) and friction coefficient (*μ*) values determined for aged cores tested at 130 °C by the use of SSW–(*$SO_4^{2-}$*) as testing brine. The values are obtained from the drawn failure line based on Mohr circles (to the left) and the calculated failure line based on the* q-p' *plot.*

| **Mechanical parameter** | **Drawn failure line, based on Mohr circles** | **Calculated failure line, based on *q*-*p'* plot** |
|---|---|---|
| $S_0$ [MPa] | 0.93 | 0.97 |
| $\varphi$ [°] | 32 | 29 |
| β [°] | 61 | 59 |
| $\mu$ | 0.62 | 0.55 |

### 4.1.3 Creep test

One chalk core, LK79, was prepared and saturated with SSW–($SO_4^{2-}$) brine for creep testing at a constant confining pressure of 12.0 MPa at high temperature (130 °C). Ideally, for the basis of comparison, more than one test of each type should be executed. But since creep tests have been experienced to be fairly repeatable, only one sample saturated with SSW–($SO_4^{2-}$) was tested in this present work to rather obtain results from a longer-lasting creep phase.

Unlike all other core samples tested at 130 °C in this present work, none of the creep test cores were aged prior to testing. After being saturated with testing brine, LK79 was flooded with the same brine for 24 hours at a flooding rate of 1 PV/day which was held constant throughout the whole creep test. To obtain creep the set creep testing conditions, a hydrostatic loading up to the creep stress level was performed before the test was left to creep at this stress level. During this loading, the hydrostatic yield point and *K*-modulus for the sample were measured. These parameters are listed in Table 4.10 together with the axial strain experienced during loading.

Table 4.10: *Overview of mechanical parameters for the creep test core, obtained from the hydrostatic loading up to the creep stress level (12.0 MPa confining pressure). The test core was not aged, but tested at 130 °C while flooded with SSW–($SO_4^{2-}$) at the rate of 1 PV/day.*

| **Test core** | **Porosity [%]** | **Yield point [MPa]** | ***K*-modulus [GPa]** | **Axial strain during hydrostatic loading [%]** |
|---|---|---|---|---|
| LK79 | 40.21 | 8.2 | 0.924 | 0.55 |

A hydrostatic yield point was determined from the point at which the axial stress-axial strain curve started deviating from the linear trend, while the *K*-modulus value was calculated from the slope of the linear trend. Examples showing how these parameters are determined graphically are given in Fig. 4.1 through Fig. 4.3. The test was left to creep immediately after the set creep stress level was obtained by hydrostatic loading. Brine was continuously circulated through the core during testing.

The first five weeks the chalk core was flooded with SSW–($SO_4^{2-}$) brine (i.e. the same brine as it was saturated with before testing), but the circulating fluid was changed to sulphate containing SSW after 50,110 minutes of creep. This way, sulphate was introduced to the chalk and any possible difference observed in deformation rate or the chemical composition of the brine could hence be related to the presence of sulphate.

Creep test data for LK79 will in the following be presented graphically in two ways. The axial creep strain can be plotted as a function of creep time, as shown in Fig. 4.8. Such a plot focuses on the development of deformation through time, and yields a very good figuration for investigating the effect of introducing new brines with new ion compositions to the chalk. It is seen that a significant increase in deformation rate was experienced from about one day after SSW flooding was started. A more profound discussion regarding the creep test results will be presented in Chapter *5.3 Creep behaviour*.

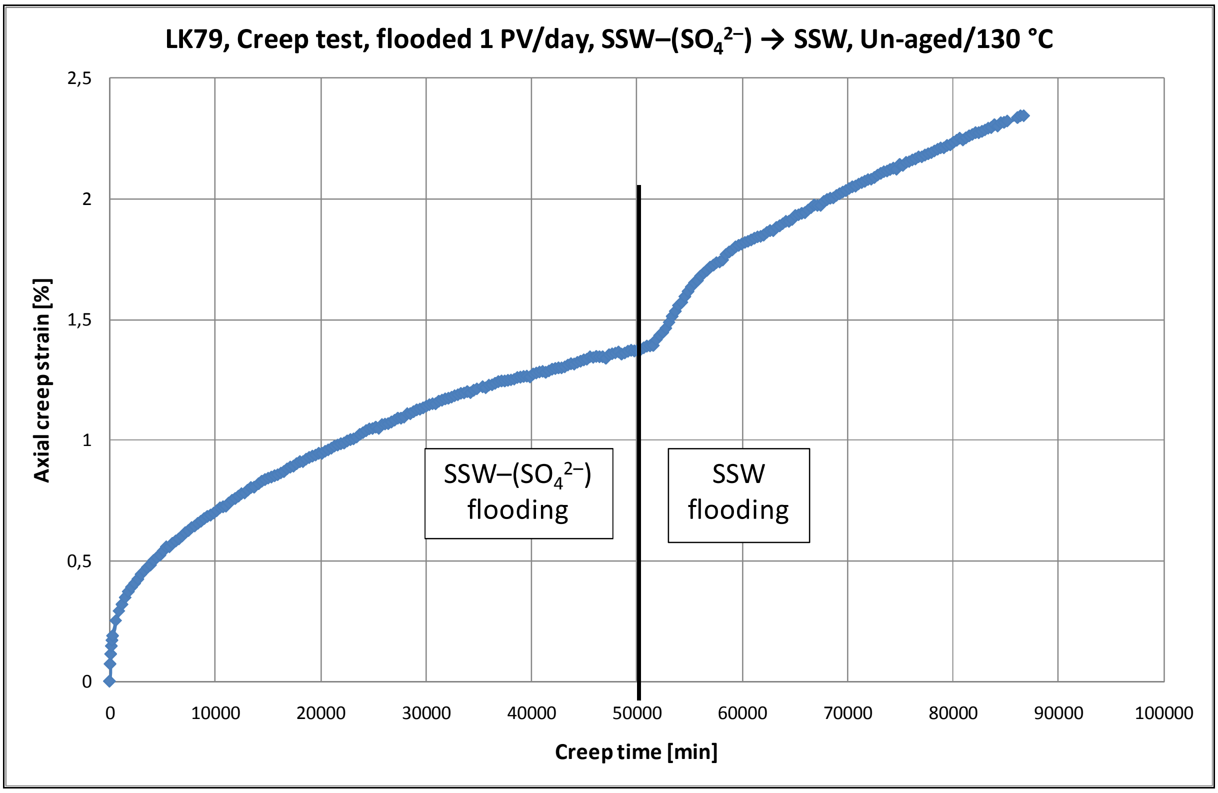

Figure 4.8: *Creep curve (axial creep strain versus creep time) for LK79; Un-aged sample, creep test executed at confining pressure level of 12.0 MPa at 130 °C. The test was flooded with SSW–($SO_4^{2-}$) brine at the rate of 1 PV/day the first 50,110 minutes, before the circulating fluid was changed to SSW at the same flooding rate.*

Another way of presenting the creep data is by plotting axial creep strain versus *logarithmic* creep time, as have been done for LK79 in Fig. 4.9. The creep curve in such a plot will eventually achieve a more or less linear shape, and the strain rate can be calculated from the slope of the linear curve section by using Eq. 2.60. Since LK79 was flooded with two different circulating fluids in two phases a strain rate value has been calculated for each flooding phase, with basis on the last logging points (before switching brine).

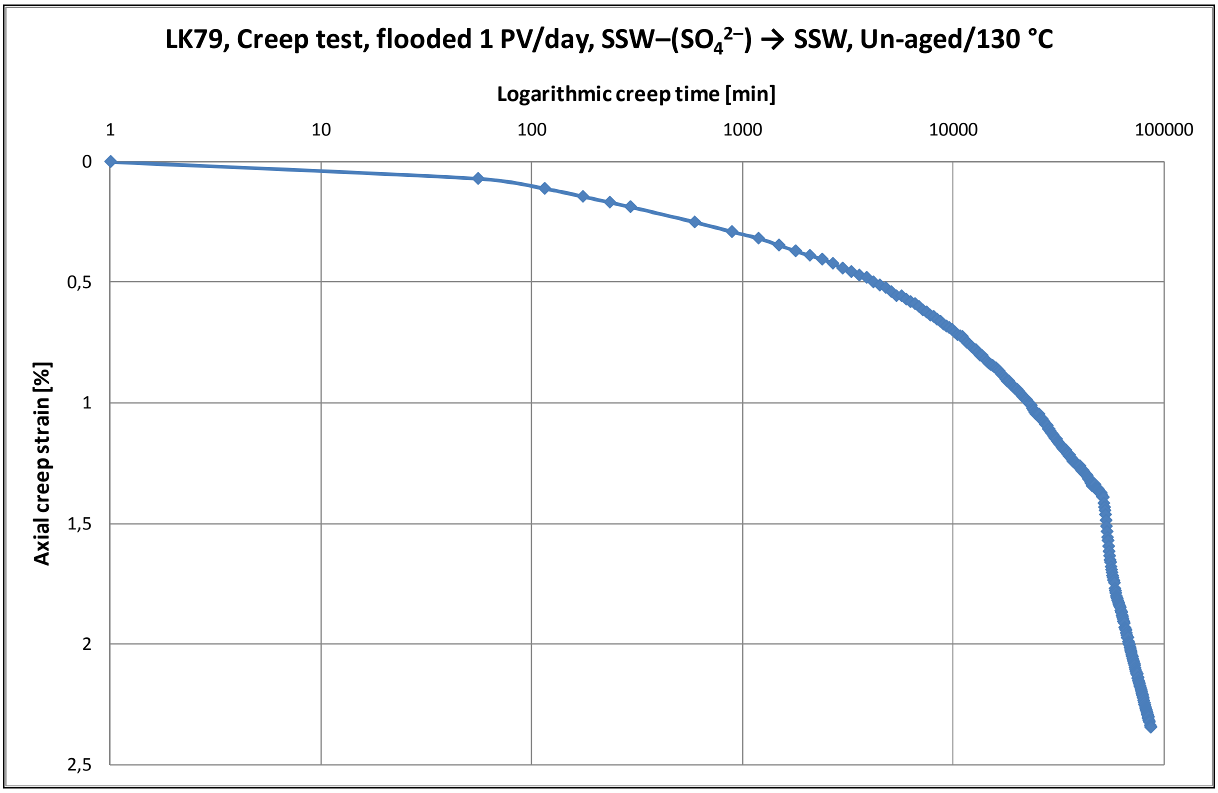

Figure 4.9: *Creep curve (axial creep strain versus* logarithmic *creep time) for LK79; Un-aged sample, creep test executed at confining pressure level of 12.0 MPa at 130 °C. The test was saturated with SSW–($SO_4^{2-}$) brine and flooded with this fluid at the rate of 1 PV/day the first 50,110 minutes, before the circulating fluid was changed to SSW at the same flooding rate.*

As also seen from Fig. 4.8, an additional deformation rate is observed when introducing sulphate to the chalk – naturally. In the latter plot where the x-axis contains logarithmic time, a steeper curve corresponds to a higher strain rate. Calculated strain rates are listed in Table 4.11, together with the creep time at the last logging point ($t_2$, $\varepsilon_2$) used in the calculations. The strain rate measured when flooding SSW is in this case a factor of almost 2.8 higher than what was observed for synthetic seawater without sulphate.

Table 4.11: *Overview of calculated strain rate values for the two flooding phases of the LK79 creep test. Creep times at the last logging points* ($t_2$, $\varepsilon_2$) *used in the calculations are also listed.*

| **Test core** | **Circulating fluid** | **Creep time at end point [min]** | **Strain rate [ % / Decade ]** |
|---|---|---|---|
| LK79 | SSW–($SO_4^{2-}$) | 45,016 | 1.15 |
| | SSW | 84,306 | 3.21 |

Results from chemical analyses of the effluent water sampled during creep, will be presented in Paragraph *4.3.2 Chemical results from creep tests*.

## 4.2 Synthetic seawater, SSW

*Please note that results from all tests performed by the use of SSW as testing brine have been provided from Davidsen (2011), a parallel master thesis. The only difference between the work performed in these two theses have been the presence of sulphate ($SO_4^{2-}$) in saturating and testing brine. Thus, the effect of sulphate can be studied.*

In the following, all results from experimental work where SSW has been used as testing brine are presented in tables, Mohr plots and *q-p'* plots. First, the tests of un-aged cores at ambient conditions will be considered. Then, results from aged cores tested at high temperature (130 °C) will follow, and in the end the creep tests will be presented.

### 4.2.1 Un-aged cores tested at ambient temperature

**Results in tables**

Similar to the experimental work performed and described in this thesis, the same types of tests were executed by Davidsen (2011) with synthetic seawater (SSW) as testing brine. Both Brazilian tests, deviatoric tests at different effective radial stresses and hydrostatic tests were carried out with SSW. Results from all tests performed on un-aged cores, saturated and tested with SSW at ambient temperature, are given in Table 4.12. The listed yield point value ($\sigma_1$') and elasticity modulus for each test is determined by the use of the method explained for the example in Paragraph *4.1.1 Un-aged cores tested at ambient temperature*.

Table 4.12: *Overview of results from mechanical tests, where un-aged samples were tested at ambient conditions with SSW brine.*

| Test type | Test core | Porosity [%] | $\sigma_3$' [MPa] | $\sigma_1$' [MPa] | *q* [MPa] | *p'* [MPa] | *E*-modulus [GPa] | *K*-modulus [GPa] |
|---|---|---|---|---|---|---|---|---|
| Brazilian | *(see Table 4.13)* | 39.82 | -0.61 | 1.83 | 2.43 | 0.20 | | |
| 0.3 MPa Dev. | LK80 | 38.26 | 0.3 | 5.6 | 5.3 | 2.07 | 1.465 | |
| 0.5 MPa Dev. | LK71 | 39.92 | 0.5 | 5.8 | 5.3 | 2.27 | 1.320 | |
| 0.8 MPa Dev. | LK87 | 38.89 | 0.8 | 6.8 | 6.0 | 2.80 | 1.302 | |
| 1.0 MPa Dev. | LK82 | 38.85 | 1.0 | 7.0 | 6.0 | 3.00 | 1.597 | |
| 1.5 MPa Dev. | LK89 | 39.81 | 1.5 | 7.4 | 5.9 | 3.47 | 1.394 | |
| 2.0 MPa Dev. | LK75 | 37.92 | 2.0 | 8.4 | 6.4 | 4.13 | 1.450 | |
| 3.0 MPa Dev. | LK85 | 39.38 | 3.0 | 9.5 | 6.5 | 5.17 | 1.622 | |
| 4.0 MPa Dev. | LK84 | 39.51 | 4.0 | 9.5 | 5.5 | 5.83 | 1.534 | |
| 7.0 MPa Dev. | LK96 | 39.65 | 7.0 | 12.0 | 5.0 | 8.67 | 1.349 | |
| 8.0 MPa Dev. | LK99 | 39.88 | 8.0 | 12.3 | 4.3 | 9.43 | 1.540 | |
| Hydrostatic | LK4 | 39.71 | 9.6 | 10.1 | 0.5 | 9.77 | | 0.907 |
| Hydrostatic | LK97 | 39.95 | 10.2 | 10.3 | 0.1 | 10.23 | | 0.703 |

Ten deviatoric tests and two hydrostatic tests were executed under these conditions. Just like the test results for chalk samples exposed to SSW–($SO_4^{2-}$), there is a clear increasing trend in yield point values ($\sigma_1$') with increasing effective radial stresses ($\sigma_3$') for the deviatoric tests. The values listed in the top row in Table 4.12 are based on average values from all the ten samples tested in the Brazilian cell. Minimum ($\sigma_3$') and maximum ($\sigma_1$') principal stress for the Brazilian tests are easily calculated from the average Brazilian tensile strength, which was calculated to be $\underline{\overline{T_{0B}} = 0.61\,\text{MPa}}$ with a standard deviation of ± 0.04 MPa. Table 4.13 shows the basic data and results from the individual Brazilian tests used to obtain the average values of $T_{0B}$ and porosity.

Table 4.13: *Overview of results from the Brazilian testing of un-aged samples at ambient temperature with SSW brine.*

| Core sample | Diameter [mm] | Length [mm] | Pore volume [ml] | Bulk volume [ml] | Porosity [%] | Peak force [kN] | $T_{0B}$ [MPa] |
|---|---|---|---|---|---|---|---|
| LK (1.1) | 37.00 | 21.60 | 9.21 | 23.22 | 39.66 | 0.82 | 0.65 |
| LK (1.2) | 37.00 | 20.43 | 8.71 | 21.97 | 39.65 | 0.64 | 0.54 |
| LK (1.3) | 37.00 | 22.00 | 9.55 | 23.65 | 40.37 | 0.83 | 0.65 |
| LK (2.1) | 36.96 | 21.06 | 8.92 | 22.59 | 39.48 | 0.68 | 0.56 |
| LK (2.2) | 36.96 | 22.49 | 9.66 | 24.13 | 40.03 | 0.82 | 0.63 |
| LK (2.3) | 36.96 | 20.78 | 8.93 | 22.29 | 40.05 | 0.71 | 0.58 |
| LK (3.1) | 36.93 | 19.80 | 8.40 | 21.21 | 39.61 | 0.67 | 0.58 |
| LK (3.2) | 36.93 | 20.76 | 8.86 | 22.24 | 39.84 | 0.72 | 0.59 |
| LK (4.1) | 36.95 | 23.30 | 9.92 | 24.98 | 39.70 | 0.91 | 0.67 |
| LK (4.2) | 36.95 | 20.34 | 8.68 | 21.81 | 39.80 | 0.74 | 0.63 |
| **Average** | | | | | **39.82** | | **0.61** |
| **Standard deviation** | | | | | | | **0.04** |

### Mohr plot and *q-p'* plot

Mohr circles for the Brazilian tests and all the deviatoric tests executed with SSW at ambient conditions are plotted in Fig. 4.10. The basic data for drawing these circles are the yield point values and effective radial stress values listed in Table 4.12. In the same manner as described for tests run with SSW–($SO_4^{2-}$) brine it is possible to draw a failure line “by hand” in the Mohr plot which is tangent to (some of) the circles representing tests of low radial stress (or low *p'* values). The Mohr circle representing the Brazilian tests provides a good guidance for the intersection point with the $\tau$-axis.

In Fig. 4.10, the drawn failure line is shown by the black, solid linear line. From the Mohr circle for the 0.3 MPa deviatoric test (LK80), it seems that the same observation is made as for the 0.3 MPa deviatoric test when SSW–($SO_4^{2-}$) brine was used for testing at ambient temperature (LK68); The test sample seems to be a bit stronger (i.e. has a somewhat higher yield point) than the trend from the other tests at low radial stresses. In this case, for LK80, the deviation from the trend is not as significant as for LK68, so it will still be taken into account when comparing results in the “Discussion” part of this thesis. Nevertheless, when drawing the failure line the Mohr circle for LK80 (see Fig. 4.10) is ignored.

The dotted failure line shown in the Mohr plot in Fig. 4.10 is obtained from an alternative method, namely by calculation based on plotted points in the *q-p'* plot in Fig. 4.11. The *q-p'* plot is based on the same data as the Mohr plot, just fabricated in a new manner. So by estimating the shear failure line in the *q-p'* plot, a corresponding failure line (dotted) is obtained for the Mohr plot.

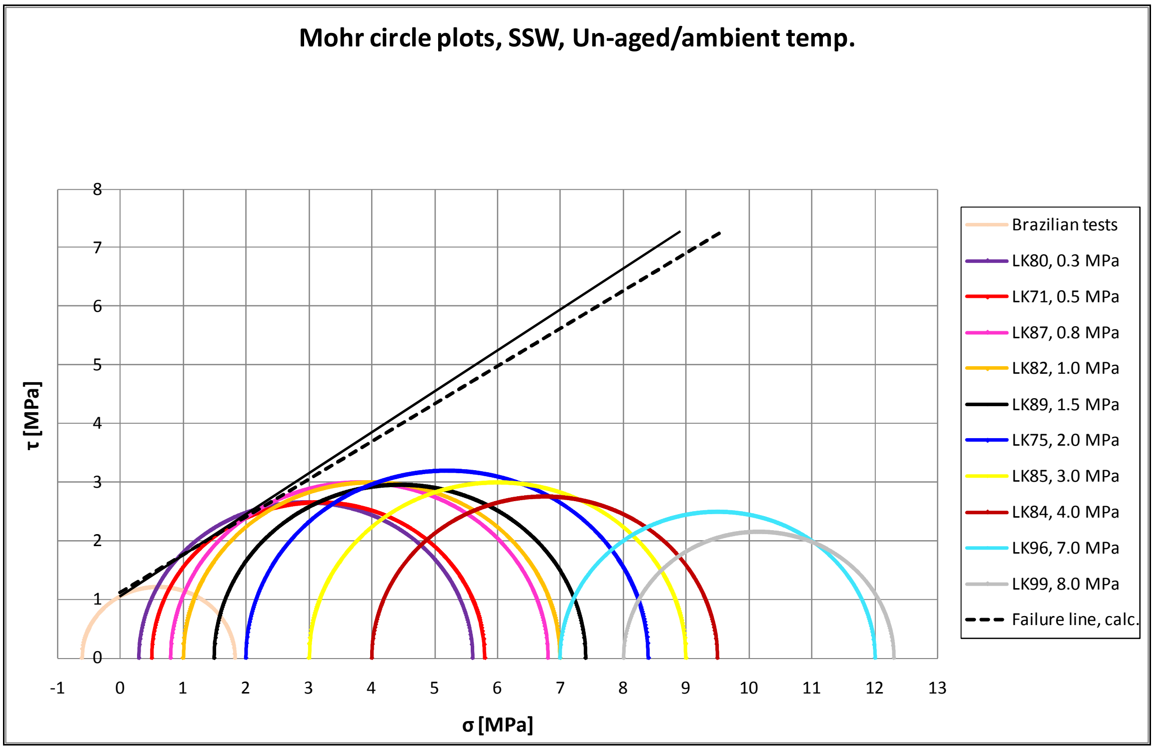

Figure 4.10: *Mohr circles for Brazilian and deviatoric tests carried out on un-aged cores at ambient temperature with the use of SSW as test brine. Based on some of the leftmost circles a failure line can be drawn (solid line). Alternatively, the failure line can be calculated (dotted line) from the* q-p' *plot in Fig. 4.11. Cohesion* ($S_0$) *and friction angle* ($\varphi$) *can be determined directly from the failure line(s).*

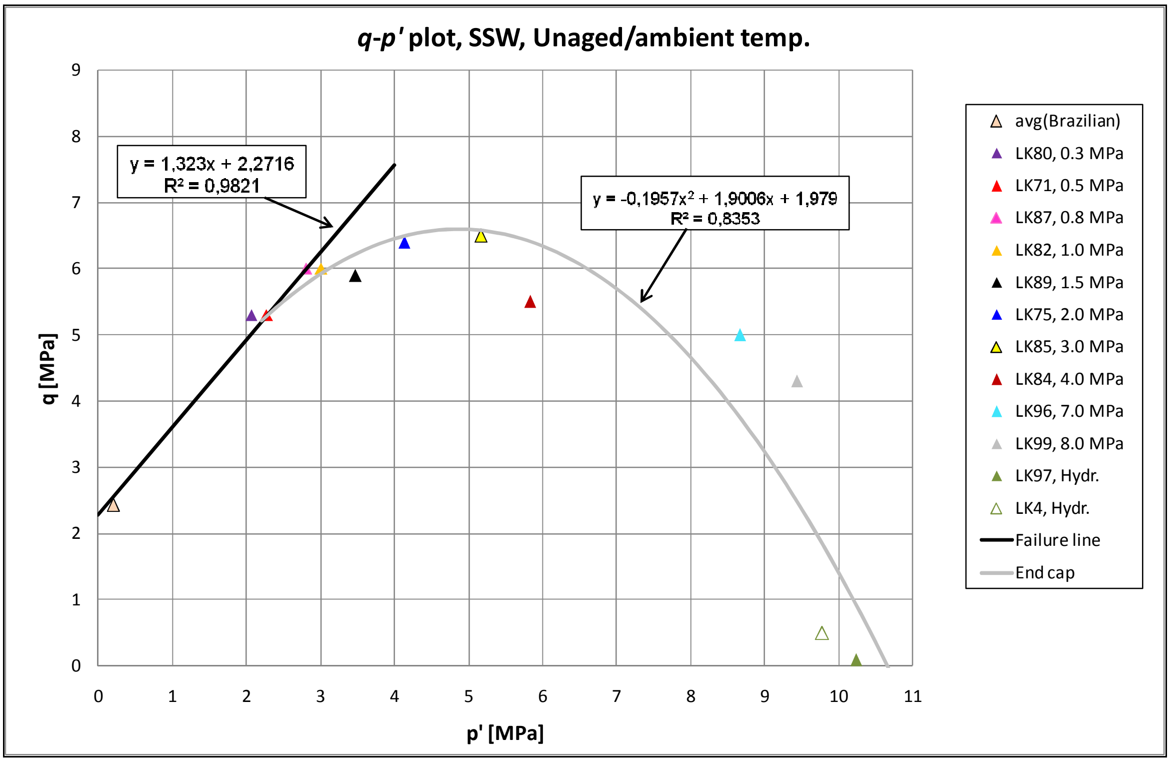

Figure 4.11: q-p' *plot for Brazilian, deviatoric and hydrostatic tests carried out on un-aged cores at ambient temperature with the use of SSW as test brine. The failure line is found from a linear regression, while the end cap line is estimated by the use of second order polynomial regression.*

The basis for the calculated failure line are the *q-p'* plotting points for tests at lower effective radial stresses. As these plotting points form a somewhat linear trend, a linear regression can be used to calculate the so-called shear failure line. (The test samples included for the linear regression are as follows: Brazilian tests, LK80, LK71, LK87, LK82). From this regression line it is further possible to calculate the cohesion and friction angle, and to draw the calculated failure line in the Mohr diagram. This line is comparable with the manually drawn line. Both these lines can be represented by their corresponding cohesion and friction angle, which further can be used to calculate the failure angle and friction coefficient. Table 4.14 contains the overview of these four parameters for each of the two drawn failure lines. As seen, the values are quite alike, and especially the cohesion. When comparing these parameters with others obtained in this thesis, only the values based on the *q-p'* plot regression will be considered.

Table 4.14: *Overview of cohesion (*$S_0$*), friction angle (*$\varphi$*), failure angle (*$\beta$*) and friction coefficient (*$\mu$*) values determined for un-aged cores tested at ambient temperature by the use of SSW as testing brine. The values are obtained from the drawn failure line based on Mohr circles (to the left) and the calculated failure line based on the* q-p' *plot.*

| **Mechanical parameter** | **Drawn failure line, based on Mohr circles** | **Calculated failure line, based on *q*-*p'* plot** |
|---|---|---|
| $S_0$ [MPa] | 1.10 | 1.11 |
| $\varphi$ [°] | 36 | 33 |
| β [°] | 63 | 61 |
| $\mu$ | 0.73 | 0.64 |

In addition to the shear failure line, the failure envelope drawn in the *q-p'* plot also consists of the end cap line. A second order polynomial regression is here used to estimate this curve. (Plotting points for all the deviatoric tests and both the two hydrostatic tests were included in this second order polynomial regression). In this case, the linear regression showed that the included plotting points form a good fit with the suggested failure line, with an $R^2$ value equal to ≈0.98. To achieve a very good fit for the end cap line, a large number of test should be executed. From the (relatively) few tests carried out in this thesis, and by the use of the mentioned regression, the $R^2$ value is ≈0.84. Ideally this match indicator should be higher, but still; this is the highest $R^2$ value achieved for any estimated end cap line within this thesis.

### 4.2.2 Aged cores tested at 130 ℃

**Results in tables**

Davidsen (2011) also performed high temperature Brazilian, deviatoric (10) and hydrostatic (2) tests on aged cores. Table 4.15 shows the overview of the resulting data from these tests, all of them performed with SSW as aging and testing brine.

Table 4.15: *Overview of results from mechanical tests, where aged samples were tested at 130 °C with SSW brine.*

| Test type | Test core | Porosity [%] | $\sigma_3'$ [MPa] | $\sigma_1'$ [MPa] | $q$ [MPa] | $p'$ [MPa] | *E*-modulus [GPa] | *K*-modulus [GPa] |
|---|---|---|---|---|---|---|---|---|
| Brazilian | *(see Table 4.16)* | 39.62 | -0.27 | 0.81 | 1.1 | 0.09 | | |
| 0.3 MPa Dev. | LK28 | 39.27 | 0.3 | 3.4 | 3.1 | 1.33 | 0.794 | |
| 0.5 MPa Dev. | LK17 | 39.21 | 0.5 | 4.2 | 3.7 | 1.73 | 0.947 | |
| 0.8 MPa Dev. | LK11 | 38.94 | 0.8 | 5.2 | 4.4 | 2.27 | 0.810 | |
| 1.0 MPa Dev. | LK29 | 40.11 | 1.0 | 5.4 | 4.4 | 2.47 | 0.998 | |
| 1.2 MPa Dev. | LK26 | 39.50 | 1.2 | 5.6 | 4.4 | 2.67 | 0.932 | |
| 1.5 MPa Dev. | LK7 | 39.71 | 1.5 | 6.1 | 4.6 | 3.03 | 0.930 | |
| 2.3 MPa Dev. | LK15 | 39.07 | 2.3 | 6.5 | 4.2 | 3.70 | 1.116 | |
| 4.0 MPa Dev. | LK18 | 39.87 | 4.0 | 8.1 | 4.1 | 5.37 | 1.097 | |
| 6.0 MPa Dev. | LK21 | 39.37 | 6.0 | 9.2 | 3.2 | 7.10 | 1.150 | |
| 6.5 Mpa Dev. | LK19 | 39.77 | 6.5 | 8.8 | 2.3 | 7.27 | 1.022 | |
| Hydrostatic | LK34 | 38.61 | 6.9 | 7.4 | 0.5 | 7.05 | | 0.556 |
| Hydrostatic | LK20 | 38.87 | 7.1 | 7.6 | 0.5 | 7.29 | | 0.478 |

For each test the yield point and elasticity modulus is listed. The example in Paragraph *4.1.1 Un-aged cores tested at ambient temperature* describes how these values are determined graphically. The standard trend of increasing yield points ($\sigma_1$’) with increasing degree of effective radial stress ($\sigma_3$’) is also observed here.

Table 4.16: *Overview of results from the Brazilian testing of aged samples at 130 °C with SSW brine.*

| Core sample | Diameter [mm] | Length [mm] | Porosity [%] | Peak force* [kN] | Correction factor [kN] | $T_{0B}$ [MPa] |
|---|---|---|---|---|---|---|
| LK25 (1) | 37.02 | 22.42 | 39.61 | 0.43 | 0.277 | 0.12 |
| LK25 (2) | 37.02 | 22.23 | 39.61 | 0.45 | 0.241 | 0.16 |
| LK25 (3) | 37.02 | 23.01 | 39.61 | 0.62 | 0.261 | 0.27 |
| LK32 (1) | 36.89 | 23.53 | 39.96 | 0.84 | 0.250 | 0.44 |
| LK32 (2) | 36.89 | 18.74 | 39.96 | 0.53 | 0.289 | 0.22 |
| LK32 (3) | 36.89 | 25.36 | 39.96 | 0.80 | 0.260 | 0.36 |
| LK35 (1) | 36.97 | 22.77 | 39.30 | 0.75 | 0.241 | 0.38 |
| LK35 (2) | 36.97 | 23.71 | 39.30 | 0.50 | 0.265 | 0.17 |
| LK35 (3) | 36.97 | 21.23 | 39.30 | 0.60 | 0.268 | 0.27 |
| **Average** | | | **39.62** | | | **0.27** |
| **Standard deviation** | | | | | | **0.10** |

(**The listed peak force values include the correction factor*).

Table 4.16 shows detailed data for the nine Brazilian test samples, including their porosities and calculated $T_{0B}$. These nine shorter samples were cut from three 70 mm cores which had already been aged. This made it impossible to measure porosity for each of the samples. It has therefore been assumed that the porosity of a sample is equal to the porosity of the 70 mm core it was cut from.

The Brazilian tensile strength ($T_{0B}$) is dependent on the peak force (load) at failure. When running Brazilian tests at high temperature, the sealed testing chamber holds a pressure of 0.7 MPa which has to be exceeded for the piston to get in contact with the loading frames. By taking the correction factor – also listed in Table 4.16 – into account, the actual load exerted to the sample is obtained. Hence, the correct value of $T_{0B}$ can be calculated, and for this assembly of samples the average value is $\underline{\overline{T_{0B}} = 0.27\,\text{MPa}}$ with a standard deviation of ± 0.10 MPa. This value is the basis for calculating the minimum and maximum principal stress for the Brazilian tests, listed in the top row in Table 4.15.

### Mohr plot and *q-p'* plot

One way of presenting results from mechanical tests graphically is to draw Mohr circles based on the minimum ($\sigma_3$') and maximum ($\sigma_1$') principal stress values. The values listed in Table 4.15 – obtained from Brazilian and deviatoric tests on aged cores tested at 130 °C with SSW brine – are used as a basis for the Mohr circle plots in Fig. 4.12. A failure line is drawn as a tangent to some of the circles representing deviatoric tests at low radial stresses. This is reflected by the solid linear line in Fig. 4.12. The leftmost Mohr circle, representing the Brazilian tests, is very valuable for determining the orientation of the failure line.

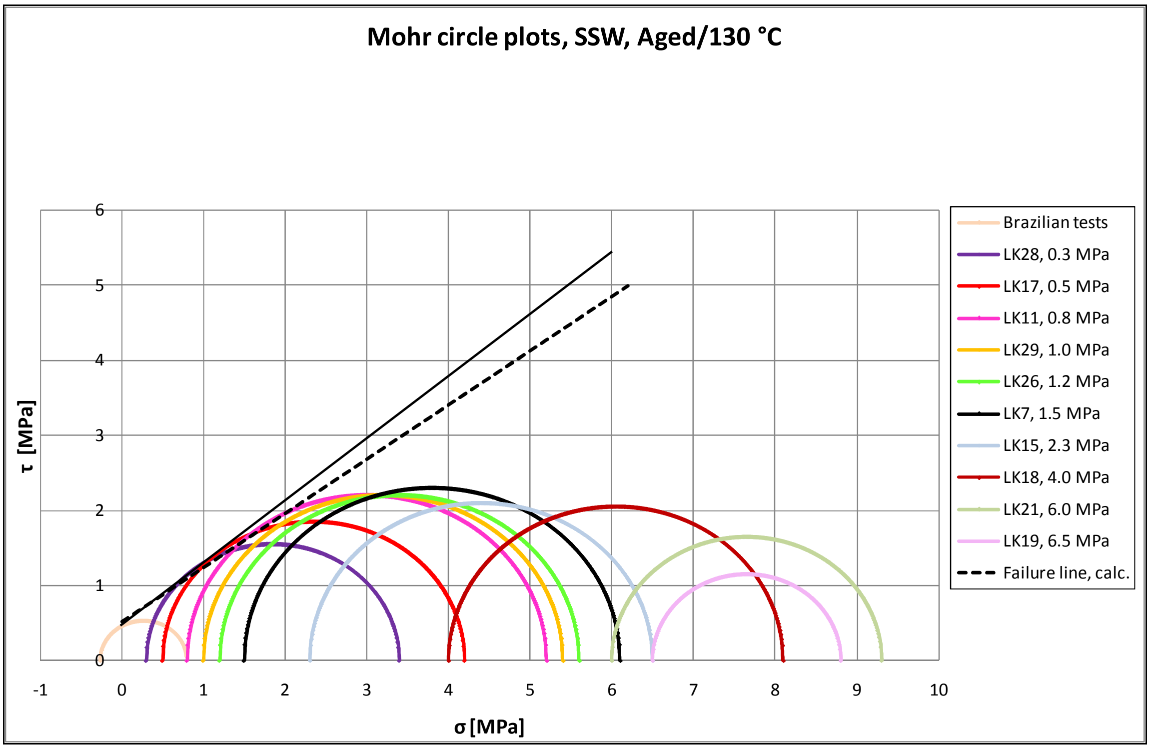

Figure 4.12: *Mohr circles for Brazilian and deviatoric tests carried out on aged cores at 130 °C with the use of SSW as test brine. Based on some of the leftmost circles a failure line can be drawn (solid line). Alternatively, the failure line can be calculated (dotted line) from the* q-p' *plot in Fig. 4.13. Cohesion* ($S_0$) *and friction angle* (φ) *can be determined directly from the failure line(s).*

A *q-p'* plot can also be created from the same basis values as the Mohr circle plots. Based on the shear failure line in the *q-p'* plot, a corresponding (calculated) failure line can be drawn in the Mohr diagram. This is shown as a dotted line in the Mohr diagram (Fig. 4.12).

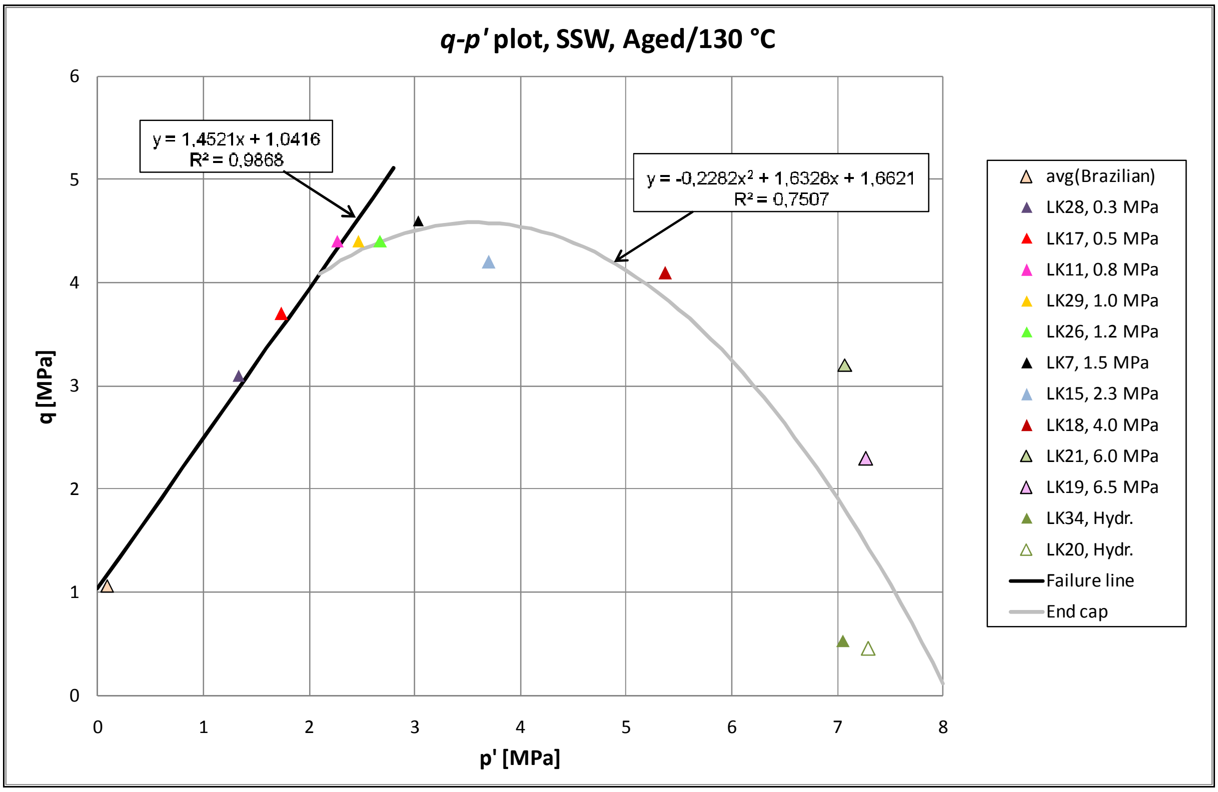

Figure 4.13: q-p' *plot for Brazilian, deviatoric and hydrostatic tests carried out on aged cores at 130 °C with the use of SSW as test brine. The failure line is found from a linear regression, while the end cap line is estimated by the use of second order polynomial regression.*

In Fig. 4.13 results from mechanical testing are presented in terms of the parameters *q* and *p'*. The failure envelope can be estimated based on these results. A linear regression is used for calculating the shear failure line, while a second order polynomial regression is used for the end cap line. (When considering the tests listed to the right in Fig. 4.13, the linear regression is based on the five first tests from the top, while the tests LK29 through LK34 form the basis for the end cap regression line).

Table 4.17: *Overview of cohesion (*$S_0$*), friction angle (φ), failure angle (β) and friction coefficient (μ) values determined for aged cores tested at 130 °C by the use of SSW as testing brine. The values are obtained from the drawn failure line based on Mohr circles (to the left) and the calculated failure line based on the* q-p’ *plot.*

| **Mechanical parameter** | **Drawn failure line, based on Mohr circles** | **Calculated failure line, based on *q*-*p'* plot** |
|---|---|---|
| $S_0$ [MPa] | 0.47 | 0.52 |
| $\varphi$ [°] | 40 | 36 |
| β [°] | 65 | 63 |
| $\mu$ | 0.84 | 0.72 |

The parameters listed in Table 4.17 reflect the solid (drawn) failure line and the dotted (*q-p’* based) failure line in Fig. 4.12. Cohesion values ($S_0$) and friction angles ($\varphi$) are determined directly from the linear lines, while the failure angles ($\beta$) and the friction coefficients ($\mu$) are both calculated based on $\varphi$. Again, the drawn line is experienced to fit the calculated line pretty well. For comparison with other similar results from other tests, only the line calculated from the *q-p’* plot will be taken into account.

### 4.2.3 Creep tests

For creep testing while flooding SSW, two chalk cores were prepared and saturated; LK94 and LK95. But, even though the tests were carried out at high temperature (130 °C) these samples were not aged prior to testing, like all the other cores tested at high temperature were. Each of these cores was first saturated with SSW before flooded with the same brine for 24 hours at a flooding rate of 1 PV/day. This flooding rate was held constant throughout the testing procedure. A hydrostatic loading up to 12.0 MPa confining pressure was performed and the test was then left to creep at this stress level. Table 4.18 shows the yield points and *K*-moduli, as well as the experienced axial strain, for the two cores during the hydrostatic loading.

*NB*: Due to a mistake with a closed valve on the flooding piston cell, LK95 was unintentionally flooded with distilled water (DW) instead of SSW during the whole hydrostatic loading and the first 9,602 minutes of the creep test. At this moment, the mistake was detected and circulating fluid was switched to SSW. Both the yield point and the *K*-modulus (during the hydrostatic loading) and the creep strain experienced through the first part of the creep were affected by the DW flooding.

Table 4.18: *Overview of mechanical parameters for the two creep test cores, obtained from the hydrostatic loading up to the creep stress level (12.0 MPa confining pressure). The test cores were not aged, but loaded/tested at 130 °C while flooded with SSW/DW at the rate of 1 PV/day.*

| Test core | Flooding fluid | Porosity [%] | Yield point [MPa] | *K*-modulus [GPa] | Axial strain during hydrostatic loading [%] |
|---|---|---|---|---|---|
| LK94 | SSW | 39.12 | 8.4 | 0.655 | 0.85 |
| LK95 | DW* | 39.59 | 9.6 | 0.814 | 0.52 |

(**Due to a mistake, this core was flooded with distilled water during the hydrostatic loading*).

The hydrostatic yield points were determined from the point at which the axial stress-axial strain curve started deviating from the linear trend, while the *K*-modulus values were calculated from the slope of the linear trend. Examples of these kinds of determinations are shown graphically in Fig. 4.1 through Fig. 4.3. A comparison of the measured values for the two different tests tells that the strength of chalk is higher when DW is present, as a higher stress was needed for the core to experience failure. The *K*-modulus is also noticeable higher, while the total deformation (axial strain) during the hydrostatic loading was a factor of 1.63 higher for the SSW flooded core. Even though the DW flooding was done by a mistake, these comparable results give an indication on how ions in seawater like brines can affect the strength and deformation of chalk.

When the creep stress level was reached through hydrostatic loading, the tests were left to creep while flooding brine. LK94 was exclusively flooded with synthetic seawater during the whole creep test. The execution of the LK95 creep test turned out to be somewhat different from the initial plan. The original idea was namely to flood SSW through the chalk sample during creep until steady state creep was reached, and then “remove” the sulphate in the brine by switching circulating fluid to SSW–($SO_4^{2-}$). Ergo, the opposite of what was done in the creep test of LK79. (See Paragraph *4.1.3 Creep test*). This action would contribute to the studies of the effect of sulphate present in the brine, as for instance a decrease in deformation rate would indicate that presence of sulphate leads to additional deformation.

In addition to studying the effect of sulphate, creep tests give the opportunity of introducing brines of several different compositions to the chalk in specific orders. When regarding the possible dissolution of calcium carbonate ($CaCO_3$), it has been presented in Paragraphs *2.4.1 Dissolution* and *2.4.2 Precipitation* that a lack of certain common ions may trigger such dissolution, as there does not exist an equilibrium state. On the other hand, if the pore fluid contains a calcium concentration much *higher* than the amount needed to be in chemical equilibrium with the chalk, no dissolution should be triggered by this. In such a case, and if dissolution was the main deformation mechanism, deformation would probably be decreased significantly, or even ceased. Since a case like this would have been very interesting to study, the initial plan was to introduce a modified SSW–($SO_4^{2-}$) brine to the chalk – containing ten times the normal amount of calcium – after some time of "standard" SSW–($SO_4^{2-}$) flooding. The reason for using synthetic seawater *without* sulphate for this experiment was to neglect the opportunity of anhydrite ($CaSO_4$) precipitation, as sulphate in the aqueous phase tends to react strongly with calcium. But, as a result of the mistake of flooding DW instead of SSW from the beginning, it was decided to shorten the period of SSW flooding and rather only introduce standard SSW–($SO_4^{2-}$) solution.

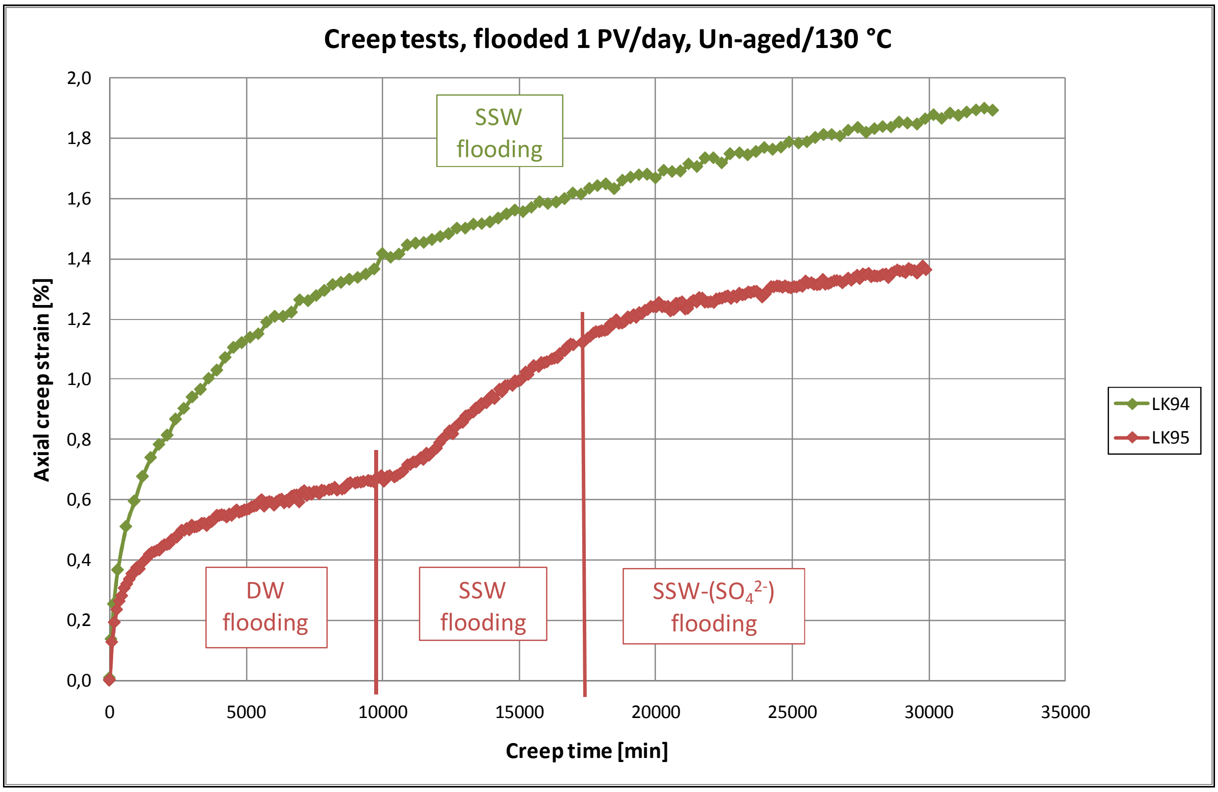

Figure 4.14: *Creep curves (axial creep strain versus creep time plots) for LK94 and LK95; Un-aged chalk cores tested at 130 °C while continuously being flooded with different circulating fluids at a rate of 1 PV/day.*

Fig. 4.14 shows the creep curves for these two creep tests, plotted in an axial creep strain versus creep time diagram. The curves show that LK94 was flooded with SSW throughout the whole creep period of 32,040 minutes. The test was finished at this time due to a high differential pressure through the core sample, indicating that the core (at the outlet) was blocked probably as a result of anhydrite ($CaSO_4$) precipitation. An increase in the differential pressure was detected already after less than 18,000 minutes of creep. About 24 hours after, at creep time of 19,447 minutes, the flooding rate from pump #1 (pore system) was halved to

0.5 PV/day in an attempt to be able to carry out the LK94 test as long as possible. The test could therefore be run for additional 13,600 minutes before it was decided to finish it and start a new test. It is worth noticing that even though the flooding rate was halved, no clear change is observed in the creep behaviour of the core.

LK95 was flooded with DW the first 9,602 minutes of creep before SSW flooding was initiated, and at a creep time of 16,811 minutes circulation fluid was switched to sulphate less SSW–($SO_4^{2-}$). At the moment of writing this paragraph, logging data not longer than until 29,910 minutes of creep time were available. The first flooding phase shows that the chalk sample experienced deformation less than half of what was experienced for the SSW flooded LK94 through the same period of time. The introduction of SSW to LK95 increased the deformation rate significantly, while the deformation rate (curve slope) seems to decrease somewhat when sulphate is removed after 16,811 minutes. Both these changes in deformation rate were observed from about one day after injection start of the new brine. Further comparison of creep strain values between the different creep tests is treated in Chapter *5.3 Creep behaviour*.

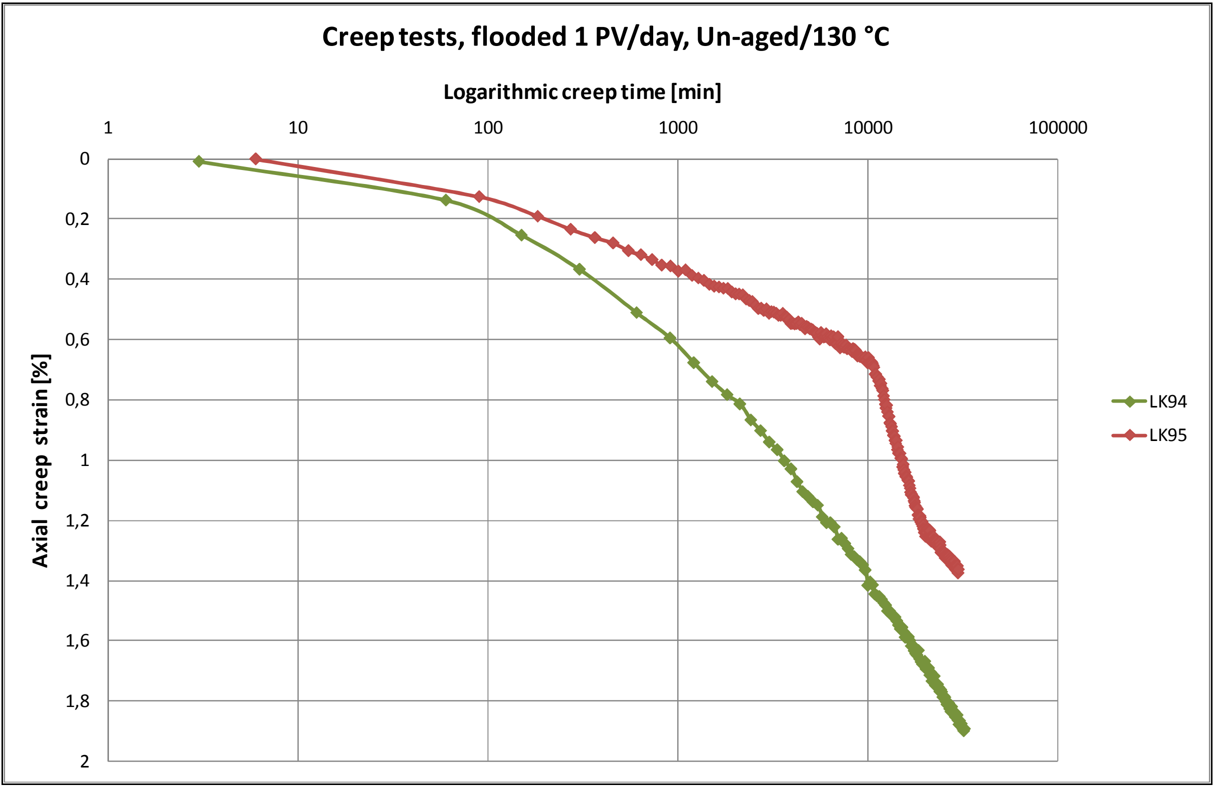

Figure 4.15: *Creep curves (axial creep strain versus* logarithmic *creep time plots) for LK94 and LK95; SSW saturated un-aged chalk cores tested at 130 °C while continuously being flooded with different circulating fluids at a rate of 1 PV/day.*

In Fig. 4.15 the creep data for LK94 and LK95 have been plotted as axial creep strain versus *logarithmic* creep time, where Eq. 2.60 can be used to calculate strain rates from the linear sections of the curves which eventually will be observed. Strain rate values have been calculated for each of the three flooding phases of the LK95 test, based on the last logging points before circulating fluid was switched. Strain rates calculated for both LK94 and LK95 are listed in Table 4.19, together with the creep time at the last logging point ($t_2$, $\varepsilon_2$) used in the calculations.

Table 4.19: *Overview of calculated strain rate values for each of the flooding phases of the LK94 and LK95 creep tests. Creep times at the last logging points* ($t_2$, $\varepsilon_2$) *used in the calculations are also listed.*

| **Test core** | **Circulating fluid** | **Creep time at end point [min]** | **Strain rate [ % / Decade ]** |
|---|---|---|---|
| LK94 | SSW | 31,086 | 0.98 |
| LK95 | DW | 9,006 | 0.36 |
| | SSW | 16,416 | 1.46 |
| | SSW–($SO_4^{2-}$) | 29,910 | 0.81 |

It is interesting to see how the strain rates vary for the different circulating fluids, as distilled water (DW) yields the lowest rate while the absolute highest rate is observed when flooding SSW. When switching from SSW to sulphate less SSW–($SO_4^{2-}$) the strain rate is almost halved. However, by comparing the SSW flooding phases for LK94 and LK95 a noticeable difference is observed. This has probably something to do with the shortened SSW flooding time for LK95 which only lasted for about 7,200 minutes, compared to the 32,000 minutes long-lasting SSW flooding of LK94. The difference would not be this large if LK95 had been flooded with SSW for a longer period of time, as the strain rate probably would have been decreased by that.

Results from chemical analyses of the effluent water sampled during creep, will be presented in Paragraph *4.3.2 Chemical results from creep tests*.

## 4.3 Chemical results

Within this present work, chalk has been exposed to seawater like brines in different situations. Especially at high temperatures it is understood that chemical reactions occur when chalk gets in contact with water containing certain ion components. In an attempt to explain and describe these chemical reactions, samples of the brine which has been in contact with chalk in different situations can be analyzed chemically and compared to the standard brine solutions.

Chemical analyses were performed for two situations where chalk material was exposed to synthetic seawater without sulphate. Both under aging and during creep tests chemical reactions are expected to occur. By studying samples of the brine after aging/testing and comparing their ion compositions with the standard SSW–($SO_4^{2-}$) solution, relative changes in the different ion concentrations can be observed. Equivalent analyses are carried out by Davidsen (2011) for SSW brine, and hence it is also possible to study if the presence of sulphate affects the chemical reactions.

Chemical results from the aging process and the creep tests are presented in the two following subsections.

### 4.3.1 Chemical results from the aging process

All chalk cores that were tested at high temperature (130 °C) – except from the creep test core – were aged prior to testing. This process was carried out by saturating the cores with testing brine and keeping them submerged in the brine in a sealed aging cell at 130 °C for three weeks. In Table 4.20 the ions present in SSW–($SO_4^{2-}$) brine are listed with their respective amounts both before and after aging.

Table 4.20: *Overview of ion concentrations observed in standard solutions of SSW–($SO_4^{2-}$) and SSW brine (“before aging”), and in the respective brines after being used for aging chalk cores at 130 °C for three weeks.*

| **Ion component** | **Concentration in SSW–($SO_4^{2-}$) brine** | | **Concentration in SSW brine** | |
|---|---|---|---|---|
| | **before aging [mol/l]** | **after aging [mol/l]** | **before aging [mol/l]** | **after aging [mol/l]** |
| $K^+$ | 0.010 | 0.010 | 0.010 | 0.010 |
| $Na^+$ | 0.474 | 0.491 | 0.450 | 0.455 |
| $Ca^{2+}$ | 0.013 | 0.042 | 0.013 | 0.035 |
| $Mg^{2+}$ | 0.045 | 0.020 | 0.045 | 0.020 |
| $Cl^-$ | 0.597 | 0.629 | 0.525 | 0.545 |
| $SO_4^{2-}$ | | | 0.024 | 0.015 |

As seen for both brines, a change in concentration is experienced for all ion components except one; Potassium is the only component seeming to be absolutely unaffected by the contact with chalk. When SSW–($SO_4^{2-}$) is used as aging brine, magnesium ($Mg^{2+}$) is the only component which experiences a decrease in concentration. The trends are similar when sulphate containing SSW is used during aging, and the decrease in [$Mg^{2+}$] is in fact observed to be the same for the two brines. The concentration of sulphate ($SO_4^{2-}$) in the SSW brine is also observed to decrease. As a first-hand observation when regarding the relative changes, it is interesting to notice that the calcium ($Ca^{2+}$) concentration increases for both brines, but to a higher level when sulphate is not present.

These chemical results will be further discussed in Paragraph *5.4.1 Chemical changes under aging*.

## 4.3.2 Chemical results from creep tests

In collaboration with Davidsen (2011) chemical results from three different creep tests were obtained. During all of the creep tests the effluent water, which had been flooded through the core at a rate of 1 PV/day, was sampled daily. These samples were analysed in an ion chromatograph to study the development of the different ion components through the creep. By introducing new brines with different compositions to the chalk, different creep behaviour was observed. By studying the chemical results from the same time of creep, possible trends and changes may be linked to the change in deformation rate, e.g. Hence, the chemical analyses are very interesting objects for investigation. The three creep test cores were LK94, LK79 and LK95, and the chemical results from each of them will be presented in the following.

In Paragraph *5.4.2 Chemical changes during creep* attempted explanations of some of these observations will be given.

**LK94 Flooded with SSW only**

LK94 turned out to be the "simplest" creep test as it was only flooded with SSW through the whole time of creep, 32,040 minutes. Fig. 4.16 shows the results from the chemical analysis of the water samples as development of different ion concentrations versus the creep time. (Please note that the curves of sodium ($Na^+$) and chloride ($Cl^-$) are related to the secondary concentration axis, i.e. to the right, due to their high concentrations compared to the other ions present). For each ion component, a dotted horizontal line is also plotted in the diagram to show the concentration initially in the injected brine. A deviation from this standard line indicates that the ion component is involved in a reaction of chemical kind.

First of all, at about 9,800 minutes of creep there is a peak in all concentration curves (except chloride). But since this peak is common for all components, and since the next logging points seem to follow the trend seen before the peak, this deviation point is probably caused by a "diluting error" or something similar.

When regarding concentration development throughout the test, both potassium ($K^+$), sodium ($Na^+$) and chloride ($Cl^-$) are produced in the same amounts as injected, more or less, and none of them therefore seem to react with the chalk. But for the other ions present, interesting developments are seen. Especially the first 10,000 minutes of creep, large amounts of injected magnesium are retained within the chalk core, at the same time as a lot of calcium is being produced at much higher concentration than the content in standard SSW.

It is also interesting to see that none of them reaches the original concentration during the creep time, but rather stabilize at certain concentrations deviating from the injected amounts. From about 16-17,000 minutes of creep, [$Mg^{2+}$] and [$Ca^{2+}$] are fairly stable. Magnesium production in the very first sample was only 47% of the injected concentration, while it stabilizes at about 80% of the standard value. Equivalent values can also be calculated for calcium, for which production in the first sampling was a factor 2.73 higher than in the standard brine, and the concentration at stabilization was about 16% higher (factor 1.16). In addition to magnesium, also sulphate ($SO_4^{2-}$) is lost inside to core. The sulphate production is more or less constant through the whole period of creep at an average concentration of 72% of the initial value. Hence, during a creep of more than 32,000 minutes significant amounts of sulphate are also removed from the aqueous solution.

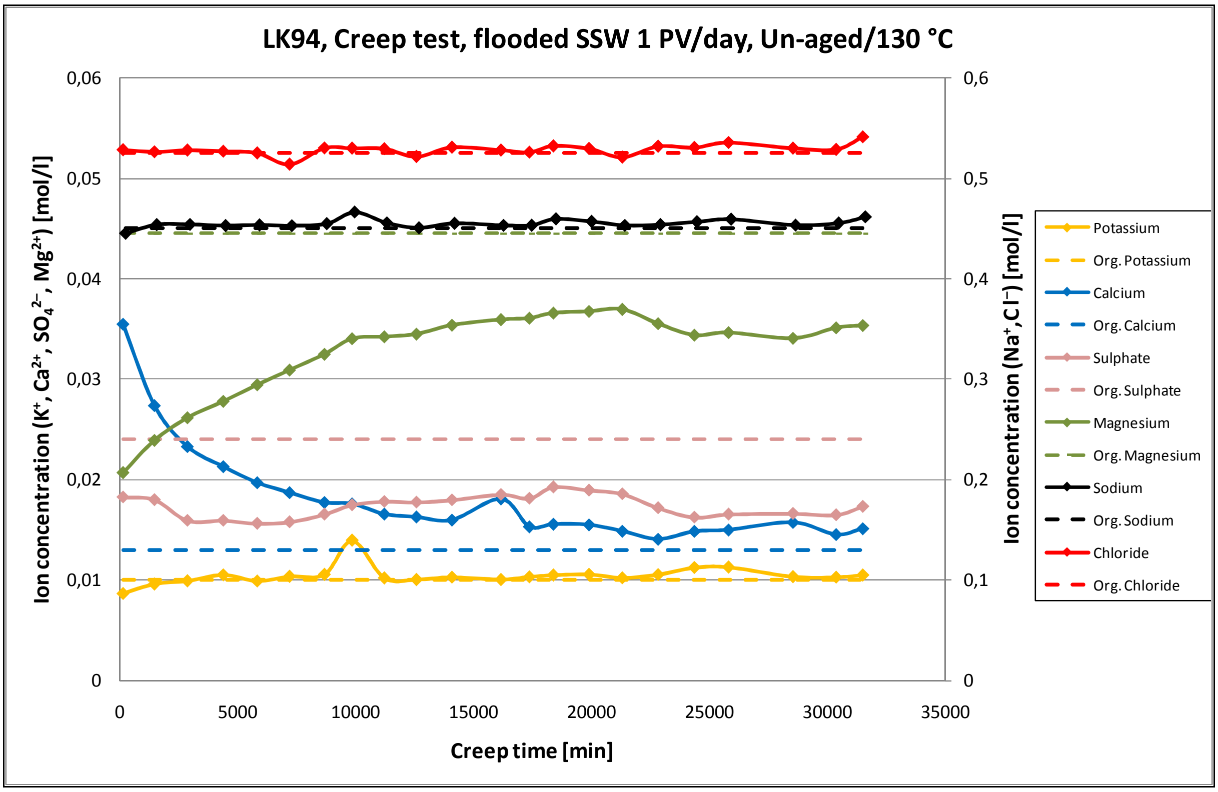

Figure 4.16: *Results from the chemical analysis of the effluent water (sampled daily) during the creep test of LK94; Un-aged chalk core tested at 130 °C. SSW brine was flooded throughout the whole test at a rate of 1 PV/day. [$Na^+$] and [$Cl^-$] are related to the secondary axis (to the right) due to their high concentration values compared to the other ion components.*

An increase in the differential pressure was detected, probably due to precipitation of anhydrite ($CaSO_4$). To reduce the possible precipitation rate so that the flooding outlet from the core would not be totally blocked, and so that the creep test could last longer, the flooding rate was halved at a creep time of 19,447 minutes. It is interesting to see that the concentrations of magnesium and sulphate in the effluent seem to decrease somewhat from this point in time. At the same time, there also seems to be a slight decrease in calcium production – but this trend is not as clear as for the other two ions, and the calcium production even seems to start increasing again a couple of days after.

### LK79 Flooded with SSW–($SO_4^{2-}$) → SSW

In contrast to LK94, LK79 was saturated with SSW–($SO_4^{2-}$) brine prior to the creep test, and flooded with this brine the first 50,110 minutes of creep time. At this time, circulating fluid was switched to SSW and hence sulphate was introduced to the chalk. In total, the test was run for nine weeks, and SSW was flooded throughout this period of time. Every day one sample from the effluent water was stored for chemical analysis of the ion composition, and the results from this analysis is shown in Fig. 4.17. Both the logging point at 41,600 and 75,000 minutes of creep deviate significant from the general curve trends. But as long as the next plotting points follow the initial trend these deviation points do probably not reflect actual concentration changes, but are rather caused by diluting errors or so. The vertical line through the diagram represents the time for starting SSW injection, and dotted horizontal lines reflect the ion concentrations in standard solutions of the brines. Sodium ($Na^+$) and chloride ($Cl^-$) are related to the secondary concentration axis.

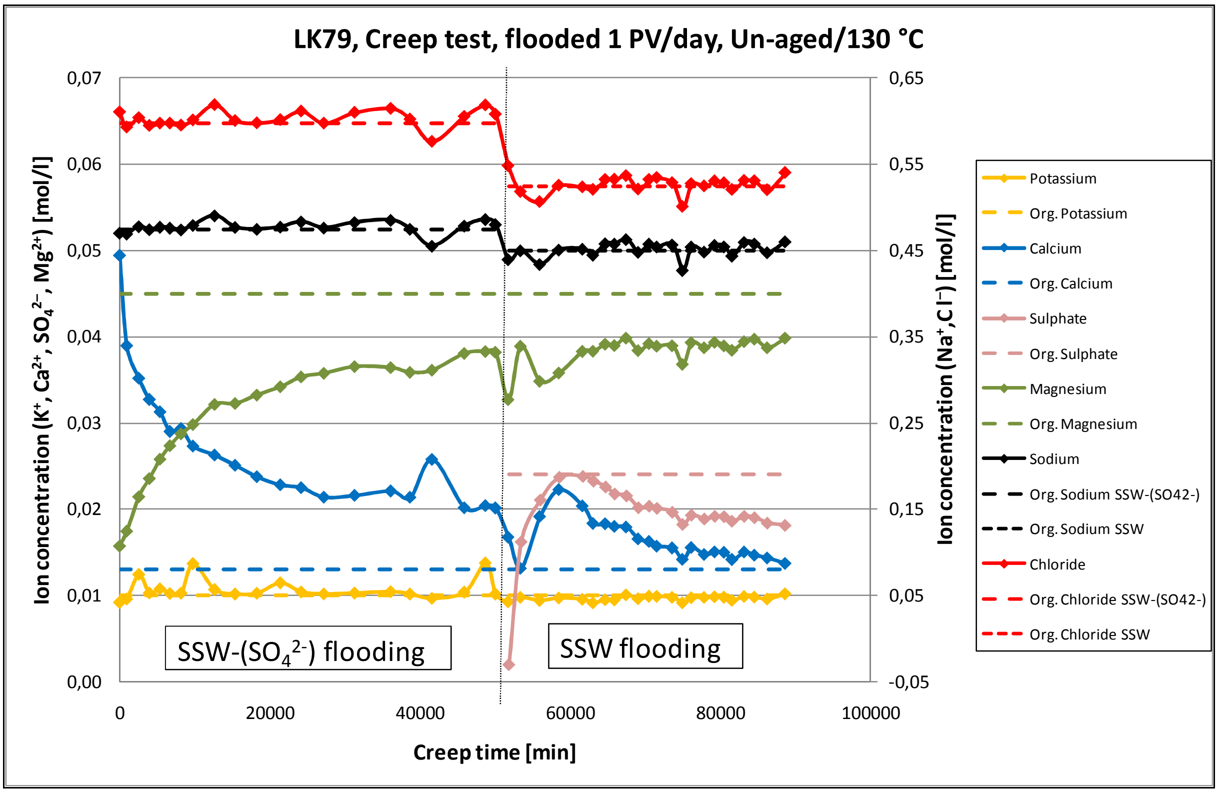

Figure 4.17: *Results from the chemical analysis of the effluent water (sampled daily) during the creep test of LK79; Un-aged chalk core tested at 130 °C. SSW–($SO_4^{2-}$) brine was flooded at a rate of 1 PV/day the first 50,110 minutes, before SSW was started flooding at the same rate. [$Na^+$] and [$Cl^-$] are related to the secondary axis (to the right) due to their high concentration values compared to the other ion components.*

Independent on the flooding fluid neither potassium, sodium nor chloride seem to react with the chalk, as no noticeable changes in concentrations are seen. For magnesium and calcium, on the other hand, large changes are detected in terms of comprehensive magnesium ($Mg^{2+}$) loss and additional calcium ($Ca^{2+}$) production - especially the first 25,000 minutes of creep. Compared to their injected amounts, the very first water sample contained calcium at a factor of 3.80 higher than the standard while only about 35% of the injected magnesium was produced. Short time before the SSW injection was started, from about 45,000 minutes of creep, both [$Mg^{2+}$] and [$Ca^{2+}$] seem to stabilize at certain levels. But none of them match the injected amounts, as magnesium stabilizes at about 86% of the standard concentration, and calcium production “never” drops to the standard level.

At the moment of sulphate was added to the pore fluid several changes occurred. Due to different sodium and chloride concentrations in the two brines both of these components experienced a drop in production. However, they immediately stabilized at the standard concentration level. When regarding development of magnesium concentration immediately after introducing sulphate, some strange results are seen. A noticeable drop is first observed, but followed by a “jump” back to a value matching the stable trend before SSW flooding was initiated. The next sampling point shows another drop, and then a series of sample analyses indicate an increase in concentration up to a new stable level.

The measured calcium behaviour is also somewhat special connected to the introduction of sulphate. Immediately after the switch of brines, a drop in [$Ca^{2+}$] is detected. Sulphate content in the effluent increased relatively quickly to its injected amount. After the mentioned drop, [$Ca^{2+}$] followed the sulphate concentration trend throughout the rest of the creep – the concentration of calcium in the effluent was consistently 4 mmol/l less than [$SO_4^{2-}$]. From the creep time value of 63,100 minutes the sulphate production (and the calcium production) started decreasing, and did so throughout the testing. When the test was ended, the concentration of calcium in the effluent water did no longer exceed the injected calcium amounts. Similar to the case for LK94, the creep test eventually had to be terminated due to blockings in the circulating fluid system (probably caused by anhydrite precipitation). An increasing differential (and pore) pressure indicated this.

### LK95 Flooded with DW → SSW → SSW–($SO_4^{2-}$)

The last creep test carried out (LK95) was commenced with an unintended flooding with distilled water (DW). This mistake was simply caused by a closed valve, and when it was detected after 9,602 minutes of creep SSW flooding was started. Five days later, sulphate was “removed” from the circulating fluid by changing to SSW–($SO_4^{2-}$) brine (at creep time of 16,811 minutes). Hence, this test consisted of three flooding phases. Daily water sampling for chemical testing was terminated after 22,950 minutes, and the results are shown in Fig. 4.18. (The meaning of vertical and horizontal lines and the secondary concentration axis are the same as described for the two other creep tests in the previous).

The fact that the core was saturated with SSW prior to testing explains the amounts of ion components in the first flooding phase (DW). As the distilled water displaced the SSW already present, some higher concentrations were registered in the effluent for the very first water sample. After SSW flooding was started all ion concentrations in the effluent increased, but only [$Ca^{2+}$], [$Na^{+}$] and [$Cl^{-}$] increased immediately. The two latter components increased to the levels of their injected amounts, while the calcium concentration was first observed as a peak at a factor 3.84 higher than the standard concentration. This kind of peak for the calcium concentration when changing flooding fluid from DW to seawater like brine is a common observation for those types of tests. At this point in time, barely any magnesium or sulphate was produced, but in the next water sample large increases in [$Mg^{2+}$] and [$SO_4^{2-}$] were observed, as well as a significant drop in [$Ca^{2+}$]. Magnesium and sulphate production immediately stabilized at levels at around 65% and 90% of their original concentrations in the brine, respectively.

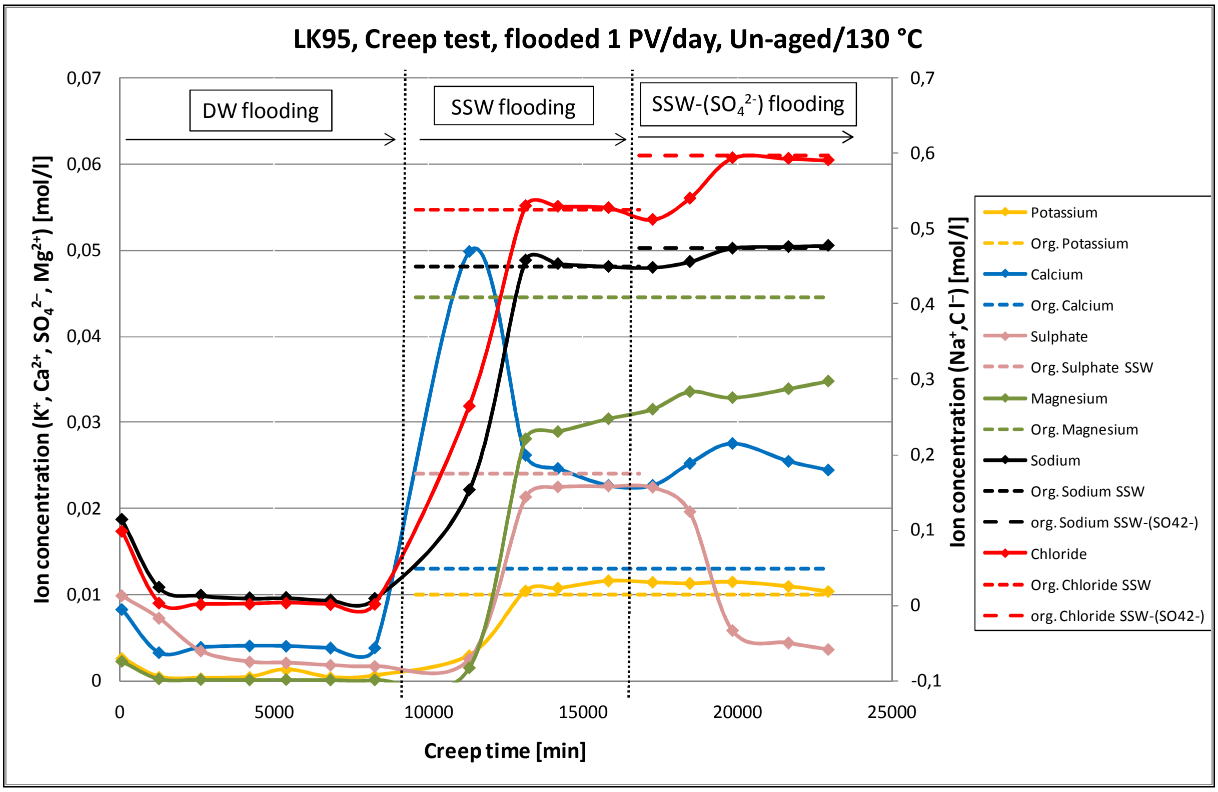

Figure 4.18: *Results from the chemical analysis of the effluent water (sampled daily) during the creep test of LK95; Un-aged chalk core tested at 130 °C. Distilled water (DW) was flooded at a rate of 1 PV/day the first 9,602 minutes. Then, SSW was started flooding at the same rate until 16,811 minutes of creep, before SSW–(SO$_4^{2-}$) was flooded until the end of testing. [Na$^+$] and [Cl$^-$] are related to the secondary axis (to the right) due to their high concentration values compared to the other ion components.*

When flooding of the last brine was started, magnesium production seems to increase further. An increase in calcium is also noticed in the effluent water, while the sulphate concentration decreases significantly (as no more sulphate is injected). When the sulphate reaches and stabilizes at a minimum level, calcium concentration appears as a peak, and starts decreasing again. Potassium, sodium and chloride are all more or less produced in the same amounts as injected for the last two flooding phases.

# 5 Discussion

In the main, all tests in this present work in collaboration with Davidsen (2011) were carried out as combinations of either:

- *un-aged cores tested at ambient temperature* or
  *aged cores tested at high temperature (130 °C),*

and by using either:

- *synthetic seawater (SSW)* or
  *synthetic seawater without sulphate (SSW–($SO_4^{2-}$))*

as saturation and testing brine.

From this, four different combinations of "testing conditions" are obtained. By comparing tests in certain manners it is possible to study both the *effect of temperature and aging* on the mechanical strength of chalk, as well as the *effect of sulphate* present in the testing brine. In the following, these effects are studied by comparing yield point, Young's modulus ($E$) and bulk modulus ($K$) for several different tests, as well as parameters like cohesion ($S_0$) and friction angle ($\varphi$) and failure envelopes obtained from different $q$-$p'$ plots.

(Please notice that when comparing results from deviatoric tests, only tests of equal effective radial stresses are listed (in pairs). This is done to consider only the entirely comparable tests. It should also be noticed that all values listed in tables are obtained from one individual test only, unless otherwise is stated. Ideally, to be sure that such a value is representative it should be calculated as an average from a number of tests. Due to time limitations, obtaining results from different tests *at several different radial stresses* has been prioritized rather than performing several identical tests. At least, this was needed to at all being able to estimate cohesion, friction angle and failure envelopes).

Further, there will be one section concerning creep behaviour, and one last section considering chemical aspects related to the aging process and water sampling during the creep tests.

## 5.1 Effect of temperature

The effect of temperature and aging on the mechanical strength of chalk is first studied for tests performed by using SSW–($SO_4^{2-}$) as testing brine, and then for tests where the testing brine used was SSW.

### 5.1.1 SSW–($SO_4^{2-}$)

*All tests considered in this subsection were performed by the use of SSW–($SO_4^{2-}$) as testing brine.*

**Yield point**

For the good overview, Table 5.1 contains observed yield points listed in pairs for tests of similar type (or the same effective radial stress) performed at ambient and high temperature. The pairwise differences and difference ratios are also calculated and listed. For all the tests, SSW–($SO_4^{2-}$) was used as testing brine. The yield point values are found from Table 4.4 and Table 4.7 in the result presentations.

Table 5.1: *Comparison of yield points ($\sigma_1$') obtained from different test types at ambient temperature and 130 °C – by using SSW–($SO_4^{2-}$) as testing brine. The difference (130 °C value minus ambient value) and ratio between yield point values for the two testing temperatures is given for each test type.*

| Test type | $\sigma_1$' [MPa] | | Difference [MPa] | Difference ratio |
|---|---|---|---|---|
| | Un-aged/Ambient | Aged/130 °C | | |
| Brazilian | 1.38 | 1.53 | 0.15 | 1.11 |
| 0.5 MPa Dev. | 4.5* | 4.9 | 0.4 | 1.09 |
| 1.0 MPa Dev. | 6.2 | 6.2 | 0.0 | 1.00 |
| 1.2 MPa Dev. | 6.2 | 6.7 | 0.5 | 1.08 |
| 2.3 MPa Dev. | 8.4 | 7.1 | –1.3 | 0.85 |
| 4.0 MPa Dev. | 9.3 | 9.0 | –0.3 | 0.97 |
| 7.0 MPa Dev. | 11.4 | 11.8 | 0.4 | 1.04 |
| Hydrostatic | 10.7 | 10.8 | 0.1 | 1.01 |
| Average | | | | 1.02 |

(**The listed value is an average value from two similar deviatoric tests, both executed at ambient temperature with an effective radial stress of 0.5 MPa*).

No clear temperature dependency is observed when comparing the yield points for samples tested with SSW–($SO_4^{2-}$) brine. For almost all test types the yield point values are very much alike. And even though the highest yield points in most cases are found in high temperature tests, there are two test types where the opposite is observed, as well as one test type where the same yield point was experienced for both ambient and high test temperature. The difference ratio also provides a good basis for comparison, as it considers the *relative* differences instead of the magnitudes only. As the difference ratio varies around 1, and the average ratio is more or less equal to 1, the yield points for high and ambient temperature tests are generally so alike that no clear trend is observed.

**Elasticity moduli**

Other parameters which could be of interest to regard, are the elasticity moduli obtained from deviatoric and hydrostatic tests. Table 5.2 and Table 5.3 contain *E*-modulus and *K*-modulus values, respectively, measured for the comparable deviatoric and hydrostatic tests at ambient and high temperature. (I.e. elasticity moduli values for the same tests as considered in Table 5.1).

Table 5.2: *Comparison of* E-*modulus values for deviatoric tests at different effective radial stresses performed at ambient temperature and 130 °C – by using SSW–*($SO_4^{2-}$)* as testing brine. The difference (ambient value minus 130 °C value) and ratio between* E-*modulus values for the two testing temperatures is given for each test type.*

| Test type | *E*-modulus [GPa] | | Difference [GPa] | Difference ratio |
|---|---|---|---|---|
| | Un-aged/Ambient | Aged/130 °C | | |
| 0.5 MPa Dev. | 1.357* | 1.277 | 0.080 | 1.063 |
| 1.0 MPa Dev. | 1.262 | 1.346 | –0.084 | 0.938 |
| 1.2 MPa Dev. | 1.299 | 1.094 | 0.205 | 1.187 |
| 2.3 MPa Dev. | 1.577 | 1.186 | 0.391 | 1.330 |
| 4.0 MPa Dev. | 1.508 | 1.134 | 0.374 | 1.330 |
| 7.0 MPa Dev. | 1.907 | 1.360 | 0.547 | 1.402 |
| Average | | | | 1.208 |

(**The listed value is an average value from two similar deviatoric tests, both executed at ambient temperature with an effective radial stress of 0.5 MPa*).

*E*-modulus can be defined as a measure of a material's resistance against uniaxial compression, or as a measure of the stiffness of the material. (See Paragraph *2.3.4 Young's modulus (*E-*modulus)*). As a general trend, it seems that the *E*-modulus is measured to be higher when tests are carried out at low temperature, i.e. that these cores are more rigid. Only in the case of 1.0 MPa effective radial stress the high temperature test experienced the highest *E*-modulus. Another trend which is observed is that *E*-modulus values increase with increasing degree of radial support (i.e. with increasing confining pressure). No such trend seem to be valid for the high temperature tests, and hence also the difference and difference ratios between low and high temperature tests increase with increasing radial stress. The core sample experiencing the definitely highest Young's modulus of 1.907 GPa, is an un-aged core tested at ambient temperature with a high degree of radial support during testing (7.0 MPa effectively).

In other words, at low effective radial stresses it is difficult to determine whether the testing temperature affects the material's stiffness. But as the radial support increases it seems more evident that high temperature and/or aging may reduce the material's resistance against uniaxial compression. The average difference ratio of 1.208 is not entirely valid as there is one increasing and one "constant" trend in the compared data, but it still tells that *E*-modulus values for ambient temperature tested cores are the higher, in the overall perspective.

Table 5.3: *Comparison of* K-*modulus values for hydrostatic tests at ambient temperature and 130 °C – with SSW–*($SO_4^{2-}$)* as testing brine. The difference (high – low) and ratio between* K-*modulus values for the two testing temperatures is given.*

| Test type | *K*-modulus [GPa] | | Difference [GPa] | Difference ratio |
|---|---|---|---|---|
| | Un-aged/Ambient | Aged/130 °C | | |
| Hydrostatic | 0.689 | 0.587 | 0.102 | 1.174 |

The same observation is made for bulk modulus values at same testing conditions and also with SSW–($SO_4^{2-}$) as testing brine. *K*-modulus for the hydrostatic test run at ambient temperature was a factor 1.174 higher than for the high temperature test. However, this difference is not tremendous. And as only one test has been performed for each temperature condition with this testing brine it is difficult to tell whether this is a representative observation, knowing that such values may vary largely in between identically run tests.

### *q-p'* plots – Failure envelopes and mechanical parameters

In the *q-p'* diagram in Fig. 5.1, results from all tests performed by the use of SSW–($SO_4^{2-}$) as testing brine have been plotted. With basis in a linear and a second order polynomial regression, a failure envelope has been estimated for each testing temperature. (The failure envelopes are presented separately in Fig. 4.5 and Fig. 4.7. In the respective subsections, more detailed information is given on how these failure envelope lines are obtained). Each failure envelope is composed by two parts, where the linear leftmost line is called the shear failure line and the curved line to the right is called the end cap line.

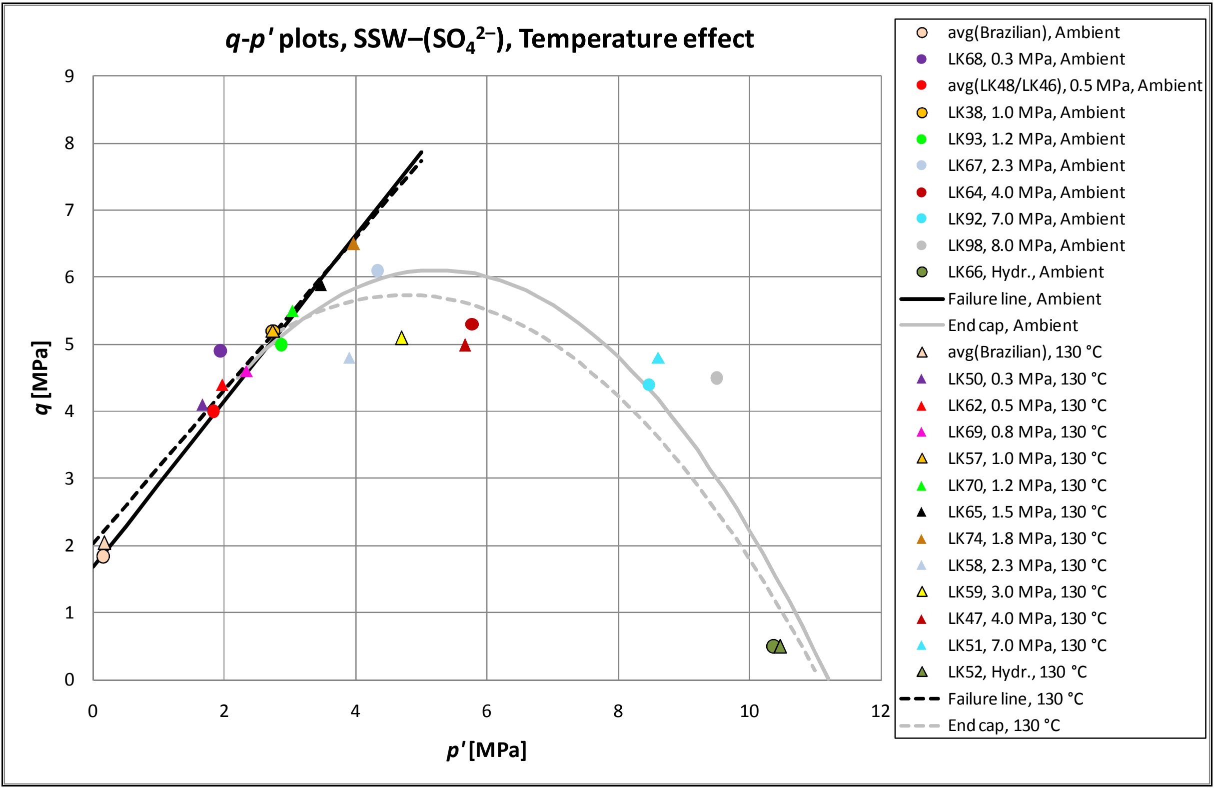

Figure 5.1: *Comparison of* q-p' *plots with respect to temperature effect, for tests performed with SSW–($SO_4^{2-}$) as test brine. The solid failure envelope line represents tests at ambient temperature, while the dotted line represents the high temperature tests.*

As seen from the diagram, the estimated failure lines for low and high temperature testing are very much alike. It is interesting to see that the transitions from the linear to the curved line for these two failure envelopes appear to occur for the same *q-p'* combination, more or less. However, it must be mentioned that such transitions are very difficult to determine, in addition to the fact that these estimations are based on the assumption of a second order polynomial fit for the end cap line. These uncertainties should be taken into account, but as a general and rough interpretation these measurements are of course interesting.

The shear failure line for ambient temperature tests has a slightly steeper slope, and since the transition points are almost equal it intersects the *q*-axis at a lower value. From Eq. 2.52 and Eq. 2.53, in addition to the related explanations in Paragraph *2.3.7* q-p' *plot*, it is thereby known that the determined friction angle ($\varphi$) is higher and the cohesion ($S_0$) lower for the ambient temperature tests when comparing to the tests at high temperature. Since the failure angle ($\beta$) and the friction coefficient ($\mu$) are both directly determined from $\varphi$, these will naturally also be (slightly) higher for the tests at ambient conditions. Brazilian tests are really valuable for determination of the shear failure line and affect both the slope and the intersection point with the *q*-axis to a large extent. The maximum principal stress ($\sigma_1$') was found to be a bit higher for the tests at 130 °C. (See Table 5.1). This reflects a somewhat higher strength, and logically corresponds to a higher cohesion value – which can be considered as the *inherent shear strength* of the material.

As seen from Table 5.1 the yield points observed for the similar test types (equal radial support) were in most cases very alike. This is also seen from the *q-p'* plot, as the dots (ambient temperature) and the triangles (130 °C) are mainly mixed. The end cap line for the high temperature tests is estimated to follow a trend below the ambient temperature end cap line. Usually, such an observation is equivalent with a weaker material – but as already discussed for the yield points listed in Table 5.1 it is really difficult to notice any typical trend for these mechanical data. In addition, results from hydrostatic tests are valuable for determination of the end cap line's orientation towards the *p'*-axis. The results from the two hydrostatic tests seem independent of the testing temperature as they almost overlap in the *q-p'* plot, and as long as the transition point for the two failure envelopes also seemed very alike, the end cap lines should not be supposed to deviate too much from each other. Ideally, more tests should be performed at the different effective radial stresses, to make sure that the results were actually representative. The present results are highly "exposed" to naturally variations in between the cores.

Table 5.4: *Comparison of cohesion* ($S_0$)*, friction angle* ($\varphi$)*, failure angle* ($\beta$) *and friction coefficient* ($\mu$) *values for tests at ambient temperature and 130 °C – with SSW–*($SO_4^{2-}$) *as testing brine. The values are obtained from the failure lines calculated from the* q-p' *plots.*

| Mechanical parameter | Un-aged/Ambient | Aged/130 °C | Difference ratio (high / low) |
|---|---|---|---|
| $S_0$ [MPa] | 0.81 | 0.97 | 1.20 |
| $\varphi$ [°] | 31 | 29 | 1.07 |
| β [°] | 60 | 59 | 1.02 |
| $\mu$ | 0.60 | 0.55 | 1.09 |

Table 5.4 shows the values of cohesion, friction angle, failure angle and friction coefficient calculated based on the two shear failure lines plotted in Fig. 5.1, and the pairwise difference ratios. When comparing the pairwise values it is evident that the rough comparison method mentioned earlier (based on Eq. 2.52 and Eq. 2.53) is applicable. When regarding the values it is interesting to see that the cohesion based on the high temperature tests is "as much as" a factor 1.20 higher than for the low temperature tests. Considering this ratio alone, it may seem a bit high compared to all observations showing no significant difference in between results from the different testing temperatures. However, when comparing with equivalent difference ratios presented in the three following subsections, this is definitely the lowest. The friction

angles are very alike, as suggested from the slopes of the shear failure lines, so these parameters do not seem to be very temperature dependent when tested with SSW–($SO_4^{2-}$).

### Summary

From the data compared and discussed in this subsection, no specific temperature effect has been observed on the mechanical strength for chalks saturated and tested/flooded with SSW–($SO_4^{2-}$). The only "trend" observed was an increasing trend in *E*-modulus values with increasing radial support for low temperature tests. But for high temperature tests no such trend was observed.

### 5.1.2 SSW

*All tests considered in this subsection were performed by the use of SSW as testing brine.*

**Yield point**

Yield point values for comparable tests performed at ambient and high temperature are listed in Table 5.5. These values were originally listed as results in Table 4.12 and Table 4.15, but this new combined table makes the comparison process a lot easier. In addition, the pairwise differences and difference factors are given for each test type.

Table 5.5: *Comparison of yield points ($\sigma_1$') obtained from different test types at ambient temperature and 130 °C – by using SSW as testing brine. The difference (ambient value minus 130 °C value) and ratio between yield point values for the two testing temperatures is given for each test type.*

| Test type | $\sigma_1'$ [MPa] | | Difference [MPa] | Difference ratio |
|---|---|---|---|---|
| | Un-aged/Ambient | Aged/130 °C | | |
| Brazilian | 1.83 | 0.81 | 1.02 | 2.26 |
| 0.3 MPa Dev. | 5.6 | 3.4 | 2.2 | 1.65 |
| 0.5 MPa Dev. | 5.8 | 4.2 | 1.6 | 1.38 |
| 0.8 MPa Dev. | 6.8 | 5.2 | 1.6 | 1.31 |
| 1.0 MPa Dev. | 7.0 | 5.4 | 1.6 | 1.30 |
| 1.5 MPa Dev. | 7.4 | 6.1 | 1.3 | 1.21 |
| 4.0 MPa Dev. | 9.5 | 8.1 | 1.4 | 1.17 |
| Hydrostatic | 10.2* | 7.5* | 2.7 | 1.36 |
| Average | | | | 1.45 |

(**Each of the listed values is an average value obtained from two hydrostatic tests executed at the same temperature*).

In contrast to the data from tests run by using SSW–($SO_4^{2-}$) as test brine, there seems to be a consistent trend in the observed yield points when sulphate is present in the brine. For every test type, i.e. all degrees of radial support, the ambient condition test experienced a higher yield point. In other words, the cores tested at high temperature were the weaker. Except from the Brazilian tests and the deviatoric tests at the lowest effective radial stress, the difference factors are fairly similar to each other. Excluded the two mentioned tests, yield points from ambient temperature tests are on average a factor 1.29 higher than for the tests at 130 °C. (Included the two tests the average value increases to 1.45, as seen in Table 5.5. But by including them the standard deviation increases significantly from 0.07 to 0.33). Apparently, there is a certain degree of temperature dependence on the mechanical strength of chalk when sulphate containing SSW is used for saturation, aging and flooding.

**Elasticity moduli**

When considering the rigidity of the test cores, there also seems to be a temperature dependency. For all the regarded deviatoric tests, the *E*-modulus values were substantially higher for the low temperature tests, as shown in Table 5.6. Another interesting observation, unlike the standard observation for yield points, is that there is no clear trend that the Young's modulus values change with the degree of radial support (confining pressure) for tests at the same temperature. For increasing values of $\sigma_3$' (effective radial support) only every other *E*-modulus value increase.

Table 5.6: *Comparison of* E*-modulus values for deviatoric tests at different effective radial stresses performed at ambient temperature and 130 °C – by using SSW as testing brine. The difference (ambient value minus 130 °C value) and ratio between* E*-modulus values for the two testing temperatures is given for each test type.*

| Test type | *E*-modulus [GPa] | | Difference [GPa] | Difference ratio |
|---|---|---|---|---|
| | Un-aged/Ambient | Aged/130 °C | | |
| 0.3 MPa Dev. | 1.465 | 0.794 | 0.671 | 1.845 |
| 0.5 MPa Dev. | 1.320 | 0.947 | 0.373 | 1.394 |
| 0.8 MPa Dev. | 1.302 | 0.810 | 0.492 | 1.607 |
| 1.0 MPa Dev. | 1.597 | 0.998 | 0.599 | 1.600 |
| 1.5 MPa Dev. | 1.394 | 0.930 | 0.464 | 1.499 |
| 4.0 MPa Dev. | 1.534 | 1.097 | 0.437 | 1.398 |
| Average | | | | 1.557 |

If anything should be considered to be a trend, it would be that the *E*-modulus for the lowest and the highest radial supports for high temperature tests, are by far the lowest and highest measured values, respectively. But, it should be noticed that from the lowest to the second highest value of effective radial support considered, there is only a difference of 1.2 MPa. While from the second highest $\sigma_3$' to the very highest there is a jump of 2.5 MPa. Hence, observing a higher value for the 4.0 MPa deviatoric test than for the others should not be very unlikely, but may indicate a slight increase in *E*-modulus with radial support, nevertheless.

The 0.3 MPa deviatoric test at high temperature is one of the two tests which was suggested could be neglected when calculating the average difference ratio in yield points, as it contributed to an extra high standard deviation. (See previous subsection regarding yield points). It seems that that test core was abnormally weak, with conspicuously low yield point and *E*-modulus value compared to "trends" from the other tests. If the 0.3 MPa deviatoric tests are ignored, the *E*-moduli achieved from ambient temperature tests are on average a factor 1.500 higher (or 50% higher) than for high temperature tests with a standard deviation of 0.093. By including the 0.3 MPa deviatoric tests the equivalent values of 1.557 and 0.154 are obtained, respectively. As an overall observation, the Young's modulus at least seems to be temperature dependent when sulphate is present in SSW brine, in the manner that the chalk is less resistant against uniaxial compression at higher temperatures.

Table 5.7: *Comparison of* K*-modulus values for hydrostatic tests at ambient temperature and 130 °C – with SSW as testing brine. The difference (high – low) and ratio between* K*-modulus values for the two testing temperatures is given.*

| Test type | *K*-modulus [GPa] | | Difference [GPa] | Difference ratio |
|---|---|---|---|---|
| | Un-aged/Ambient | Aged/130 °C | | |
| Hydrostatic | 0.805* | 0.517* | 0.288 | 1.557 |

(**Each of the listed values is an average value obtained from two hydrostatic tests executed at the same temperature*).

Both of the two hydrostatic tests were carried out at each of the temperature conditions when SSW was used for testing. By applying the average values of both yield and bulk modulus (*K*) more representative data can be compared, probably. These average *K*-modulus values are shown in Table 5.7 together with their reciprocal difference and ratio. There is a significant difference between results from the two temperature conditions, as the average bulk modulus value for the ambient temperature tests is a factor as much as 1.557 higher than what was observed for the tests at 130 °C. (Worth noticing, even though it is most probably irrelevant, is that this factor is identical to the average factor calculated for the *E*-modulus values for deviatoric tests at the same testing conditions, when including all comparable tests). This can be interpreted in the manner that aged cores tested at high temperature have a weaker ability to resist hydrostatic compression.

### *q-p'* plots – Failure envelopes and mechanical parameters

Experimental results from all tests carried out by the use of SSW as test brine, are plotted in the *q-p'* plot shown in Fig. 5.2, and a failure envelope for each of the two temperature conditions is estimated and drawn. (The failure envelopes are presented separately in Fig. 4.11 and Fig. 4.13. More detailed information on how these failure envelope lines are obtained, is given in the respective subsections).

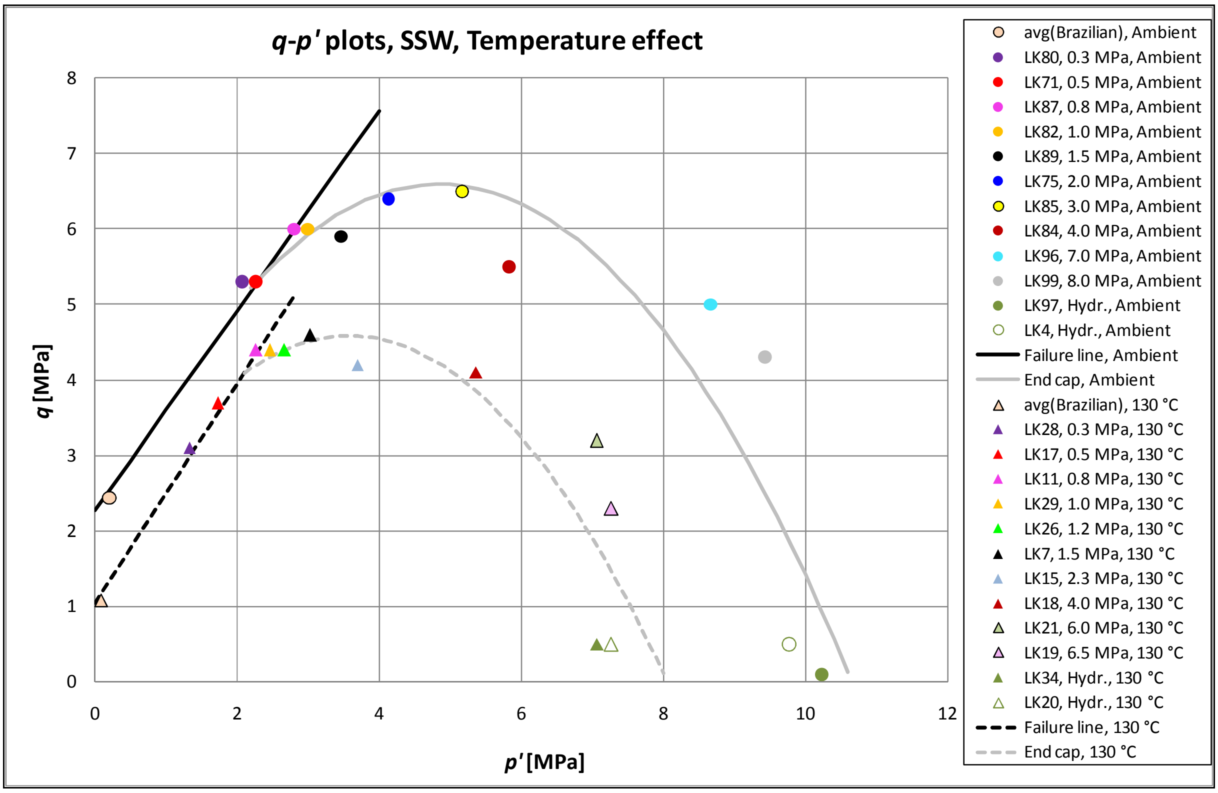

Figure 5.2: *Comparison of* q-p' *plots with respect to temperature effect, for tests performed with SSW as test brine. The solid failure envelope line represents tests at ambient temperature, while the dotted line represents the high temperature tests.*

For the same temperature conditions as considered in Fig. 5.1 for cores tested with SSW–($SO_4^{2-}$), where the failure envelopes hardly could be separated from each other, Fig. 5.2 shows that when sulphate is present it is quite evident that temperature and aging affect the mechanical strength of the chalk. The failure envelope representing the high temperature tests on aged cores (dotted lines) clearly lies below the estimated lines for ambient temperature tests (solid lines). Since the failure envelope defines the elastic area in the *q-p'* diagram, the chalk appears to be weaker when it is aged and exposed to high temperature during testing (when SSW is present). In other words, the material will go into failure at an earlier stage of stress loading – an observation which corresponds to the observations in yield points, listed in Table 5.5. As the shear failure line and the end cap line constituting the failure envelope for high temperature tests both are related to lower *q* and *p'* values, these test cores are understood to be weaker both when considering shear failure and failure by pore collapse. (The failure mechanism related to the end cap line is mainly pore collapse).

When roughly considering the linear shear failure lines it is clear that the cohesion ($S_0$) obtained from the high temperature tests is by far the lowest, since the dotted line intersects the vertical axis at a much lower value of *q*. But for increasing values of *p'* the failure lines slightly approach each other, telling that the slope is steeper for the line representing high temperature tests, and hence the friction angle ($\varphi$) must also be a bit higher for these tests. Even though the shear failure lines are clearly separable, the major difference is however registered for the end cap lines. This may indicate that the major reduction in mechanical strength is observed for conditions where pore collapse is believed to be the main failure mechanism.

Table 5.8: *Comparison of cohesion (*$S_0$*), friction angle (*$\varphi$*), failure angle (*$\beta$*) and friction coefficient (*$\mu$*) values for tests at ambient temperature and 130 °C – with SSW as testing brine. The values are obtained from the failure lines calculated from the* q-p' *plots.*

| Mechanical parameter | Un-aged/Ambient | Aged/130 °C | Difference ratio (high / low) |
|---|---|---|---|
| $S_0$ [MPa] | 1.11 | 0.52 | 2.13 |
| $\varphi$ [°] | 33 | 36 | 1.09 |
| $\beta$ [°] | 61 | 63 | 1.03 |
| $\mu$ | 0.64 | 0.72 | 1.13 |

From each of the estimated linear shear failure lines, the mechanical parameters listed in Table 5.8 can be calculated. As already suggested from the shallow "analysis", the cohesion and friction angle obtained from the high temperature tests are significantly lower and slightly higher, respectively, than the values obtained from tests at ambient conditions. In fact, the cohesion related to low temperature tests is calculated to be more than the double of the value related to high temperature tests. As this parameter mirrors the inherent shear strength, this observation supports that the aged chalk cores tested at high temperature are the weaker. (At least for stress conditions where shear failure is believed to be the main failure mechanism). The differences in failure angle and friction coefficient are directly dependent on the friction angle values, which are observed to be 9% higher for tests performed at high temperature. Similar to the observation shown in Table 5.4 for the calculated parameters when the test brine used was SSW–($SO_4^{2-}$), the temperature condition providing the higher cohesion also gives the lower friction angle.

**Summary**

It seems quite evident that when chalk cores are exposed to SSW (containing sulphate) during aging and testing at high temperature (130 °C), their general strength is weakened – both in terms of mechanical strength, like seen from yield points, failure envelopes and the cohesion, as well as the ability to resist both uniaxial and hydrostatic compression, seen from the elasticity moduli.

## 5.2 Effect of sulphate ($SO_4^{2-}$)

When studying the temperature effects in Chapter *5.1 Effect of temperature*, it was observed that there was no clear temperature dependency when using SSW–($SO_4^{2-}$) as testing brine, while tests carried out with SSW as test brine showed a clear difference in results for the low and high temperature tests. The only difference when comparing these two observations is the presence of sulphate in the test brine. Hence, a certain degree of sulphate effect has been revealed already.

In the following, the effect of sulphate presence on the mechanical strength of chalk is first considered for un-aged cores tested at ambient temperature, and then for high temperature tests where aged chalk cores were treated. The exact same table set-ups will be presented here as done for the temperature effect studies, except that here, results from using different test brines are compared for the same temperature conditions.

### 5.2.1 Ambient temperature

*All tests considered in this subsection were performed on un-aged chalk cores at ambient temperature.*

**Yield point**

In Table 5.9 the yield point values obtained from comparable tests carried out by the use of the two different testing brines, are listed. Initially, these values were listed as results in Table 4.4 and Table 4.12, but they are here combined in a new manner to make the comparison process much easier. Table 5.9 also contains the pairwise differences and difference factors calculated for each test type.

Even though the differences in yield points are not major when comparing the two different brines, it is interesting to see that the tests involving SSW experienced a higher yield point for all test types except two. The exceptions are the tests with the higher radial support, but there does not seem to be a very clear trend that the difference in yield points decrease with increasing radial support. Hence, the differences may just be caused by naturally variations. However, the difference ratios are decreasing with increasing radial support, but also from these values it is difficult to tell whether this is a standard or just incidental case. When comparing tests with the two different test brines, the average difference factor with respect to the SSW–($SO_4^{2-}$) tests is slightly more than 1, indicating that the higher yield points are in general related to SSW tests. But the fact that neither difference values nor difference factors are very high, and that there is not a consistency related to which test brine generates the highest yield point, these variations may be regarded as results of natural variations. At least, it is difficult to tell if the presence of sulphate has affected the yield points at ambient temperature.

Table 5.9: *Comparison of yield points ($\sigma_1$') obtained from different test types by the use of SSW–($SO_4^{2-}$) and SSW as testing brine – at ambient temperature. The difference (SSW value minus SSW–($SO_4^{2-}$) value) and ratio between yield point values for the two testing brines is given for each test type.*

| Test type | $\sigma_1$' [MPa] | | Difference [MPa] | Difference ratio |
|---|---|---|---|---|
| | SSW–($SO_4^{2-}$) | SSW | | |
| Brazilian | 1.38 | 1.83 | 0.45 | 1.33 |
| 0.5 MPa Dev. | 4.5* | 5.8 | 1.3 | 1.29 |
| 1.0 MPa Dev. | 6.2 | 7.0 | 0.8 | 1.13 |
| 4.0 MPa Dev. | 9.3 | 9.5 | 0.2 | 1.02 |
| 7.0 MPa Dev. | 11.4 | 12.0 | 0.6 | 1.05 |
| 8.0 MPa Dev. | 12.5 | 12.3 | –0.2 | 0.98 |
| Hydrostatic | 10.7 | 10.2** | –0.5 | 0.95 |
| Average | | | | 1.11 |

(**The listed value is an average value from two similar deviatoric tests, both executed at an effective radial stress of 0.5 MPa and with SSW–($SO_4^{2-}$) as testing brine*).

(***The listed value is an average value obtained from two hydrostatic tests executed by the use of SSW as testing brine*).

A general understanding and theory is that presence of sulphate in pore fluids within chalk may contribute to additional weakening and deformation of the chalk. However, this is not observed here for ambient temperature testing, and if any trend can be noticed at all it would rather tell the opposite.

**Elasticity moduli**

The same "lack of trends" is observed for the Young's modulus values measured for the deviatoric tests compared. As seen from Table 5.10, the *E*-modulus was higher for testing with SSW in two out of five comparable tests, and hence there is no consistency seen when considering this. But it could be mentioned that the average difference ratio tells that the slightly overall higher *E*-modulus values are observed for testing with SSW–($SO_4^{2-}$).

Table 5.10: *Comparison of* E-*modulus values for deviatoric tests at different effective radial stresses, performed by using SSW–($SO_4^{2-}$) and SSW as testing brine – at ambient temperature. The difference (SSW–($SO_4^{2-}$) value minus SSW value) and ratio between* E-*modulus values for the two testing brines is given for each test type.*

| Test type | *E*-modulus [GPa] | | Difference [GPa] | Difference ratio |
|---|---|---|---|---|
| | SSW–($SO_4^{2-}$) | SSW | | |
| 0.5 MPa Dev. | 1.357* | 1.320 | 0.037 | 1.028 |
| 1.0 MPa Dev. | 1.262 | 1.597 | –0.335 | 0.790 |
| 4.0 MPa Dev. | 1.508 | 1.534 | –0.026 | 0.983 |
| 7.0 MPa Dev. | 1.907 | 1.349 | 0.558 | 1.414 |
| 8.0 MPa Dev. | 1.805 | 1.540 | 0.265 | 1.172 |
| Average | | | | 1.077 |

(**The listed value is an average value from two similar deviatoric tests, both executed at an effective radial stress of 0.5 MPa and with SSW–($SO_4^{2-}$) as testing brine*).

The main reason for this is probably the high values obtained from the 7.0 MPa and 8.0 MPa deviatoric tests, which stand out from the rest. However, even though the difference ratios for some comparable tests show that there is some degree of relative difference, the fact that no brine consistently gives the higher values makes it difficult to make any statements based on these data. In other words, no specific sulphate effect is observed for the Young's modulus.

Table 5.11: *Comparison of* K-*modulus values for hydrostatic tests where SSW–($SO_4^{2-}$) and SSW were used as testing brine – at ambient temperature. The difference (high – low) and ratio between* K-*modulus values for the two testing brines is given.*

| Test type | *K*-modulus [GPa] | | Difference [GPa] | Difference ratio |
|---|---|---|---|---|
| | SSW–($SO_4^{2-}$) | SSW | | |
| Hydrostatic | 0.689 | 0.805* | 0.116 | 1.168 |

(**The listed value is an average value obtained from two hydrostatic tests executed by the use of SSW as testing brine*).

Since only one hydrostatic test was performed with the use of SSW–($SO_4^{2-}$) as testing brine the validity of the measured bulk modulus could be questioned. Based on the obtained data listed in Table 5.11, the average value measured from the two SSW tests is almost 17% higher than for the SSW–($SO_4^{2-}$) test. However, it should be noticed that the average value for the SSW tests is actually based on the two *K*-modulus values of 0.703 GPa and 0.907 GPa, and the smallest of these are very similar to the value observed from the SSW–($SO_4^{2-}$) test. Hence, the "actual" *K*-modulus for SSW–($SO_4^{2-}$) tests could in theory be a lot different from the listed value. It is impossible to predict if another test would have increased or decreased the *K*-modulus value, so the uncertainty of this and the large difference between the two obtained values from the SSW tests (0.204 GPa) makes it very difficult to claim whether the sulphate has an effect on the bulk modulus or not.

### *q-p'* plots – Failure envelopes and mechanical parameters

Results from all tests performed at ambient temperature are plotted in the *q-p'* plot shown in Fig. 5.3. Two failure envelopes are drawn in the *q-p'* diagram, each of them related to different testing brines. (These failure envelopes are presented separately in Fig. 4.5 and Fig. 4.11. Their respective subsections contain more detailed information on how these failure envelopes are obtained).

First of all, a somewhat strange observation is made from the *q-p'* plot as the end cap lines cross each other for higher *p'* values. But this explained by the observation in yield points, which turned out to be lower for the SSW flooded tests only for the tests at the highest $\sigma_3$' values (8.0 MPa deviatoric tests and hydrostatic tests). As described earlier, it is very difficult to estimate the end cap lines. But the estimated shear failure lines usually give a better fit with the data, which indicates that they are probably more reliable. Based on the shear failure lines drawn in Fig. 5.3, it is seen that the line representing SSW–($SO_4^{2-}$) test lies below the line related to the SSW tests. From this, it may be suggested that chalk is somewhat weaker when exposed to SSW–($SO_4^{2-}$) at ambient conditions – at least for low radial support. The end cap line also indicates this, until it crosses the end cap line representing SSW tests at a *p'* value of about 7.6 MPa.

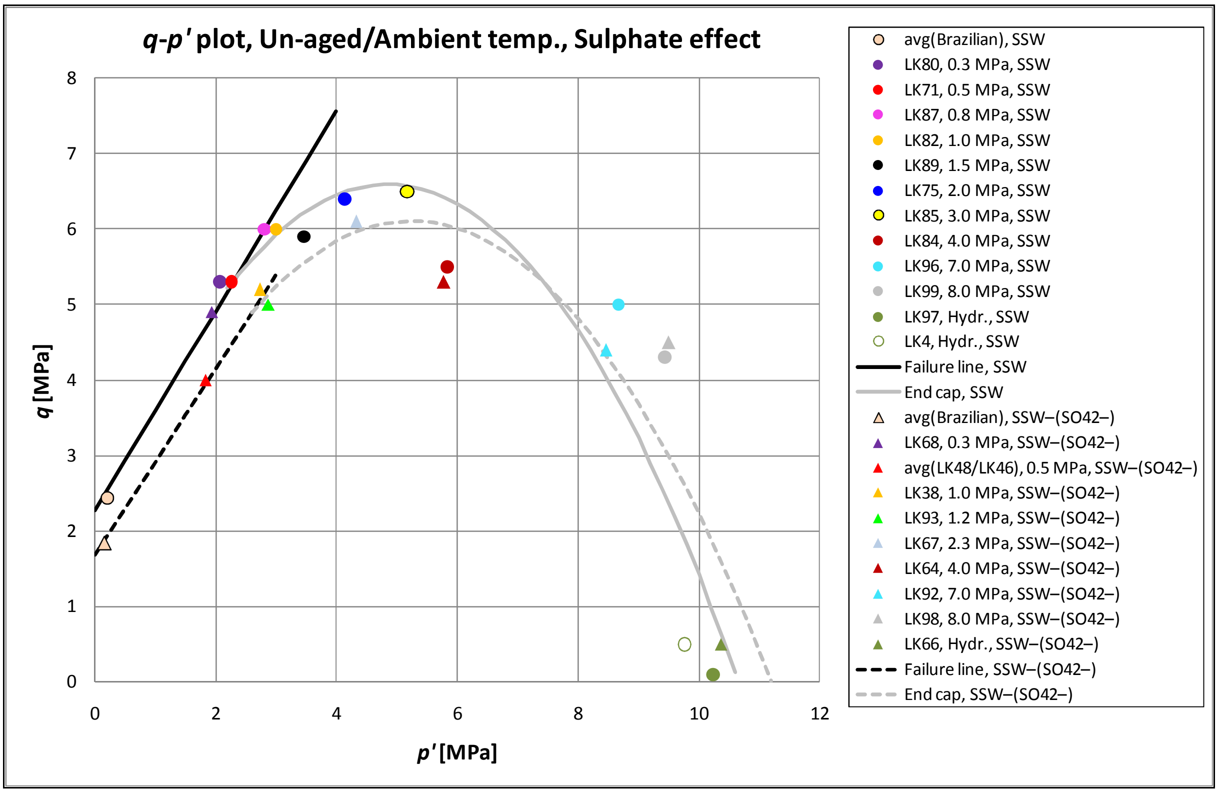

Figure 5.3: *Comparison of* q-p' *plots with respect to sulphate effect, for tests performed at ambient temperature. The solid failure envelope line represents tests where SSW was used as testing brine, while the dotted line is connected to tests performed by the use of SSW–($SO_4^{2-}$).*

A quick look at the linear shear failure lines tells that cores tested with SSW brine experience a higher cohesion (due to higher intersection with the *q*-axis) and a slightly higher friction angle (due to a steeper line). These rough observations correspond to the calculated values listed in Table 5.12.

Table 5.12: *Comparison of cohesion* ($S_0$)*, friction angle* (φ)*, failure angle* (β) *and friction coefficient* (μ) *values for tests executed with SSW–($SO_4^{2-}$) and SSW as testing brine – at ambient temperature. The values are obtained from the failure lines calculated from the* q-p' *plots.*

| **Mechanical parameter** | **SSW–($SO_4^{2-}$)** | **SSW** | **Difference ratio (high / low)** |
|---|---|---|---|
| $S_0$ [MPa] | 0.81 | 1.11 | 1.37 |
| $\varphi$ [°] | 31 | 33 | 1.06 |
| β [°] | 60 | 61 | 1.02 |
| $\mu$ | 0.60 | 0.64 | 1.07 |

The calculated friction angles for tests performed by using the two different brines are very much alike. This is also seen from the *q-p'* plot, where the slope is almost equal for the two shear failure lines. Calculated cohesion values, on the other hand, differ more significantly from each other, and the cohesion obtained from SSW tests happens to be as much as a factor 1.37 higher than observed for SSW–($SO_4^{2-}$) tests. By this, the inherent shear strength should be higher for cores tested with SSW, and this is compatible with the observations made by simply regarding the yield point comparisons in Table 5.9.

**Summary**

From some individual observations, both based on the yield points, the failure lines and their related mechanical parameters, it could be suggested that the chalk appears to be weaker when tested with SSW–($SO_4^{2-}$) than when SSW was used as testing brine at ambient temperature. In other words; the chalk seems to be stronger when sulphate is present in the brine. But due to small differences, as well as the inconsistencies in the data as described in the previous, it is difficult to tell if these observations are results of the sulphate presence or only natural variations within the chalk. At least, when considering the whole spectrum of tests, and the whole failure lines.

However, if only the shear failure lines are considered, including only the tests at lower radial support where shear failure seems to be the main failure mechanism, it may be suggested that the SSW filled cores are the stronger. It is interesting to see that this is the opposite from the observations at high temperature (see Paragraph *5.2.2 High temperature (130 °C)*).

### 5.2.2 High temperature (130 ℃)

*All tests considered in this subsection were performed on aged chalk cores at high temperature (130 °C).*

**Yield point**

For the comparable tests performed by the use of the two different testing brines (SSW–($SO_4^{2-}$) and SSW), the comparable yield point values are listed in pairs in Table 5.13. These values were listed as results in Table 4.7 and Table 4.15, but by recombining them like done in Table 5.13 it is easier to compare the values. In addition, this new table also contains the pairwise differences and difference factors calculated for each test type.

Table 5.13: *Comparison of yield points ($\sigma_1$') obtained from different test types by the use of SSW–($SO_4^{2-}$) and SSW as testing brine – at 130 °C. The difference (SSW–($SO_4^{2-}$) value minus SSW value) and ratio between yield point values for the two testing brines is given for each test type.*

| Test type | $\sigma_1$' [MPa] | | Difference [MPa] | Difference ratio |
|---|---|---|---|---|
| | SSW–($SO_4^{2-}$) | SSW | | |
| Brazilian | 1.53 | 0.81 | 0.72 | 1.89 |
| 0.3 MPa Dev. | 4.4 | 3.4 | 1.0 | 1.29 |
| 0.5 MPa Dev. | 4.9 | 4.2 | 0.7 | 1.17 |
| 0.8 MPa Dev. | 5.4 | 5.2 | 0.2 | 1.04 |
| 1.0 MPa Dev. | 6.2 | 5.4 | 0.8 | 1.15 |
| 1.2 MPa Dev. | 6.7 | 5.6 | 1.1 | 1.20 |
| 1.5 MPa Dev. | 7.4 | 6.1 | 1.3 | 1.21 |
| 2.3 MPa Dev. | 7.1 | 6.5 | 0.6 | 1.09 |
| 4.0 MPa Dev. | 9.0 | 8.1 | 0.9 | 1.11 |
| Hydrostatic | 10.8 | 7.5* | 3.3 | 1.44 |
| Average | | | | 1.26 |

(**The listed value is an average value obtained from two hydrostatic tests executed by the use of SSW as testing brine*).

The first striking observation is that yield points for all test types were found to be higher when cores were tested with SSW–($SO_4^{2-}$) brine. Based on this alone, it seems that chalk is weaker when sulphate is present at high temperature conditions. When considering the differences and difference factors in between the yield points obtained from the same type of test, or the same degree of radial support, the results from two test types stand out from the others. For all the deviatoric tests there is a trend of a fairly constant difference ratio of 1.16 with a standard deviation of 0.07. But as seen from Table 5.13 the overall average ratio from the compared tests is higher, 1.26, and with a much larger standard deviation of 0.24. This is a result of the much higher difference ratios observed from the Brazilian and the hydrostatic tests. The difference in maximum principal stress values ($\sigma_1$') in between the Brazilian tests is not extraordinary high compared to the other test types, but the relative ratio stands out as the absolutely highest and thereby contributes to an increased average value and a considerably increased standard deviation. For the hydrostatic tests, the difference is measured to be as high as 3.3 MPa, which is very high compared to the other test types. But since the stresses handled in the hydrostatic tests are quite high, the difference does not generate a very high relative ratio – but still enough to increase both the average difference ratio and the standard deviation.

Even though the difference ratios are not very high, the fact that the magnitude of all of them is above 1 indicates a consistent trend; Namely, that the chalk goes into failure at lower stress exposure (i.e. is weaker) when sulphate is present in the pore fluid.

**Elasticity moduli**

Similar to what was observed for the yield points, there seems to be a consistent trend that also the *E*-modulus is lower for chalk when filled with SSW brine than in the cases where sulphate is not present. Or, the resistance against uniaxial compression seems reduced when sulphate is contained in the testing brine. Measured *E*-modulus values obtained from the comparable deviatoric tests, only differed by the testing brine, are listed in Table 5.14. On average, for cores tested with synthetic seawater without sulphate the *E*-modulus value is obtained to be a factor 1.298 higher than for SSW filled chalk cores.

Table 5.14: *Comparison of* E*-modulus values for deviatoric tests at different effective radial stresses, performed by using SSW–($SO_4^{2-}$) and SSW as testing brine – at 130 °C. The difference (SSW–($SO_4^{2-}$) value minus SSW value) and ratio between* E*-modulus values for the two testing brines is given for each test type.*

| Test type | *E*-modulus [GPa] | | Difference [GPa] | Difference ratio |
|---|---|---|---|---|
| | SSW–($SO_4^{2-}$) | SSW | | |
| 0.3 MPa Dev. | 1.155 | 0.794 | 0.361 | 1.455 |
| 0.5 MPa Dev. | 1.277 | 0.947 | 0.330 | 1.348 |
| 0.8 MPa Dev. | 1.378 | 0.810 | 0.568 | 1.701 |
| 1.0 MPa Dev. | 1.346 | 0.998 | 0.348 | 1.349 |
| 1.2 MPa Dev. | 1.094 | 0.932 | 0.162 | 1.174 |
| 1.5 MPa Dev. | 1.169 | 0.930 | 0.239 | 1.257 |
| 2.3 MPa Dev. | 1.186 | 1.116 | 0.070 | 1.063 |
| 4.0 MPa Dev. | 1.134 | 1.097 | 0.037 | 1.034 |
| Average | | | | 1.298 |

It seems that the E-modulus value for the SSW tests increase somewhat in magnitude with increasing confining pressure (or effective radial stress). As the equivalent values for SSW–($SO_4^{2-}$) tests seem to be independent on the confining pressure, the *E*-modulus values thereby approach each other for higher radial stresses. This is indicated by decreased difference values and ratios with increasing degree of radial support. Since the only difference in between the two brines is the presence of sulphate, then sulphate may affect (reduce) the stiffness of the chalk. However, if the presence of sulphate is the explanation of the observed differences, this makes it difficult to explain the apparently approaching *E*-modulus for higher radial stresses.

For the *K*-modulus obtained from hydrostatic tests and compared in Table 5.15, it is difficult to tell if there is an effect of the sulphate present in the SSW brine. The bulk modulus measured for the test run by using SSW–($SO_4^{2-}$) is a factor 1.135 higher than the average value obtained from the SSW tests. But, in one of the two hydrostatic tests executed by the use of SSW as test brine, the *K*-modulus was found to be 0.556 GPa. Hence, just like the case when studying any possible sulphate effect for ambient temperature tests, more hydrostatic tests should be carried out both with the use of SSW and SSW–($SO_4^{2-}$) to achieve a good basis for comparison. From these very few and uncertain measurements it is very difficult, if not impossible, to tell whether there is a sulphate effect on the bulk modulus or not.

Table 5.15: *Comparison of* K-*modulus values for hydrostatic tests where SSW–($SO_4^{2-}$) and SSW were used as testing brine – at 130 °C. The difference (high – low) and ratio between* K-*modulus values for the two testing brines is given.*

| Test type | *K*-modulus [GPa] | | Difference [GPa] | Difference ratio |
|---|---|---|---|---|
| | SSW–($SO_4^{2-}$) | SSW | | |
| Hydrostatic | 0.587 | 0.517* | 0.070 | 1.135 |

(**The listed value is an average value obtained from two hydrostatic tests executed by the use of SSW as testing brine*).

### *q-p'* plots – Failure envelopes and mechanical parameters

Results from all tests performed on aged cores at high temperature (130 °C) are plotted in the *q-p'* plot shown in Fig. 5.4. The *q-p'* diagram also contains two drawn failure envelopes, and each of them is related to the different test brines. (The failure envelopes are presented separately in Fig. 4.7 and Fig. 4.13, and more detailed information on how these failure envelopes are obtained is given in the subsections related to them).

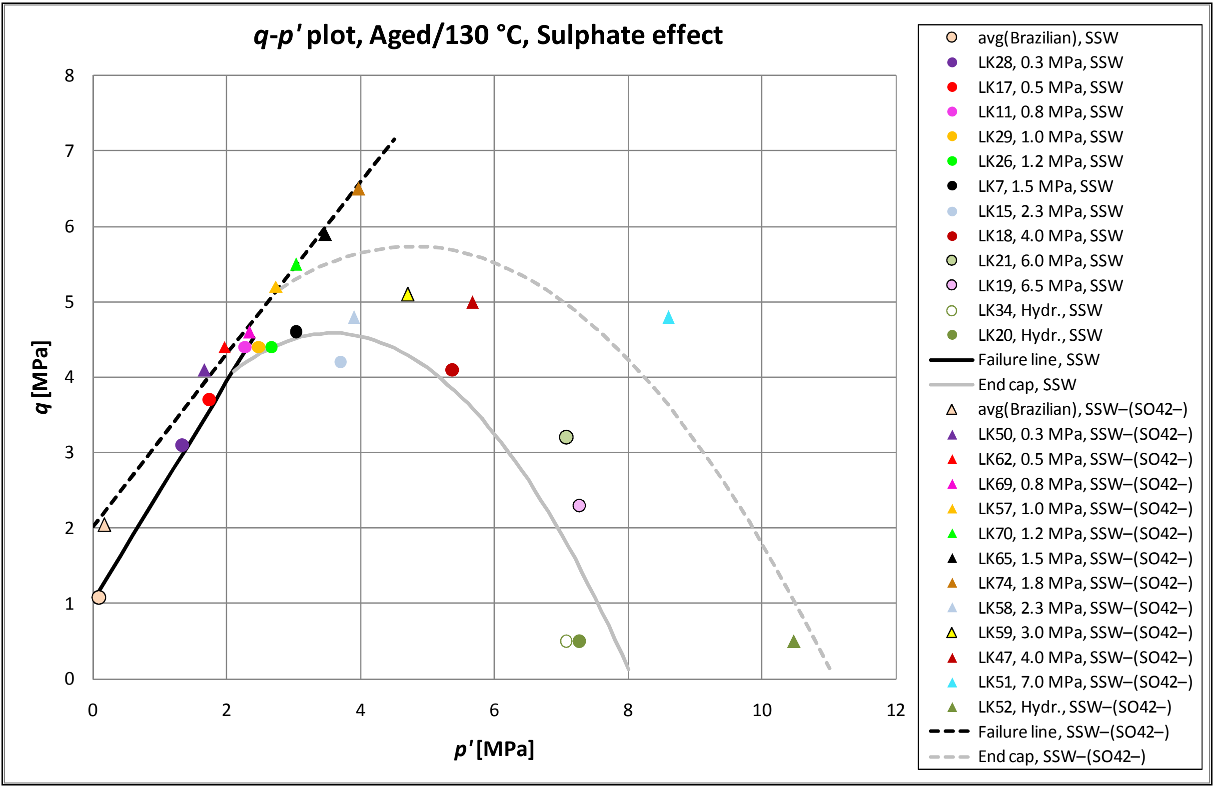

Figure 5.4: *Comparison of* q-p' *plots with respect to sulphate effect, for tests performed at 130 °C. The solid failure envelope line represents tests where SSW was used as testing brine, while the dotted line is connected to tests performed by the use of SSW–($SO_4^{2-}$).*

Fig. 5.4 clearly shows that the failure envelope estimated for the tests executed by the use of SSW as testing brine, is situated underneath the envelope drawn for SSW–($SO_4^{2-}$) tests. In other words, SSW filled chalk cores tested at high temperature are clearly weaker when sulphate is present. Especially for the end cap part the difference is significant. This diagram depicts graphically the observations made for the yield point comparisons in Table 5.13. The shear failure lines are not as different as the end cap line, but the line estimated for SSW tests is still placed clearly below the line representing SSW–($SO_4^{2-}$) tests. From the slopes of the shear failure lines, and their intersection points with the *q*-axis, it is clear that the cohesion is determined to be considerably lower for chalk cores filled with SSW. A higher friction angle is determined for these cores, due to the steeper linear shear failure line. Numerical values for these mechanical parameters are calculated and listed in Table 5.16.

Table 5.16: *Comparison of cohesion (*$S_0$*), friction angle (*$\varphi$*), failure angle (*$\beta$*) and friction coefficient (*$\mu$*) values for tests executed with SSW–(*$SO_4^{2-}$*) and SSW as testing brine – at 130 °C. The values are obtained from the failure lines calculated from the* q-p’ *plots.*

| Mechanical parameter | SSW–($SO_4^{2-}$) | SSW | Difference ratio (high / low) |
|---|---|---|---|
| $S_0$ [MPa] | 0.97 | 0.52 | 1.87 |
| $\varphi$ [°] | 29 | 36 | 1.24 |
| β [°] | 59 | 63 | 1.07 |
| $\mu$ | 0.55 | 0.72 | 1.31 |

It is interesting to see that the inherent shear strength (cohesion) is almost halved when sulphate is present in the testing brine. Hence, it is evident that the sulphate has a weakening effect on chalk at high temperature, especially for lower radial supports (confining pressures). The difference in friction angle calculated in this case – i.e. in between SSW tests and SSW–($SO_4^{2-}$) tests at high temperature – is also the absolute largest observed within this thesis. This difference propagates to the failure angle and especially to the friction coefficient, which is seen to be 31% higher for the SSW tests.

**Summary**

The essence from these comparisons is that there appears to be a clear sulphate effect on chalk exposed to high temperature. The presence of sulphate seems to reduce the mechanical strength of chalk noticeably. It is also interesting to notice that this is the opposite from what was observed when comparing tests with different brines at *ambient* temperature – at least for lower radial stresses for which shear failure is the main failure mechanism.

## 5.3 Creep behaviour

**Graphical and tabulated compilations of creep data**

In this section, compilations of different kinds for the three creep tests will be presented. For the record; These tests were carried out on un-aged chalk cores exposed to a constant confining pressure of 12.0 MPa and high temperature (130 °C). Firstly, Fig. 5.5 shows the creep curves for all the tests together in an axial creep strain versus creep time plot.

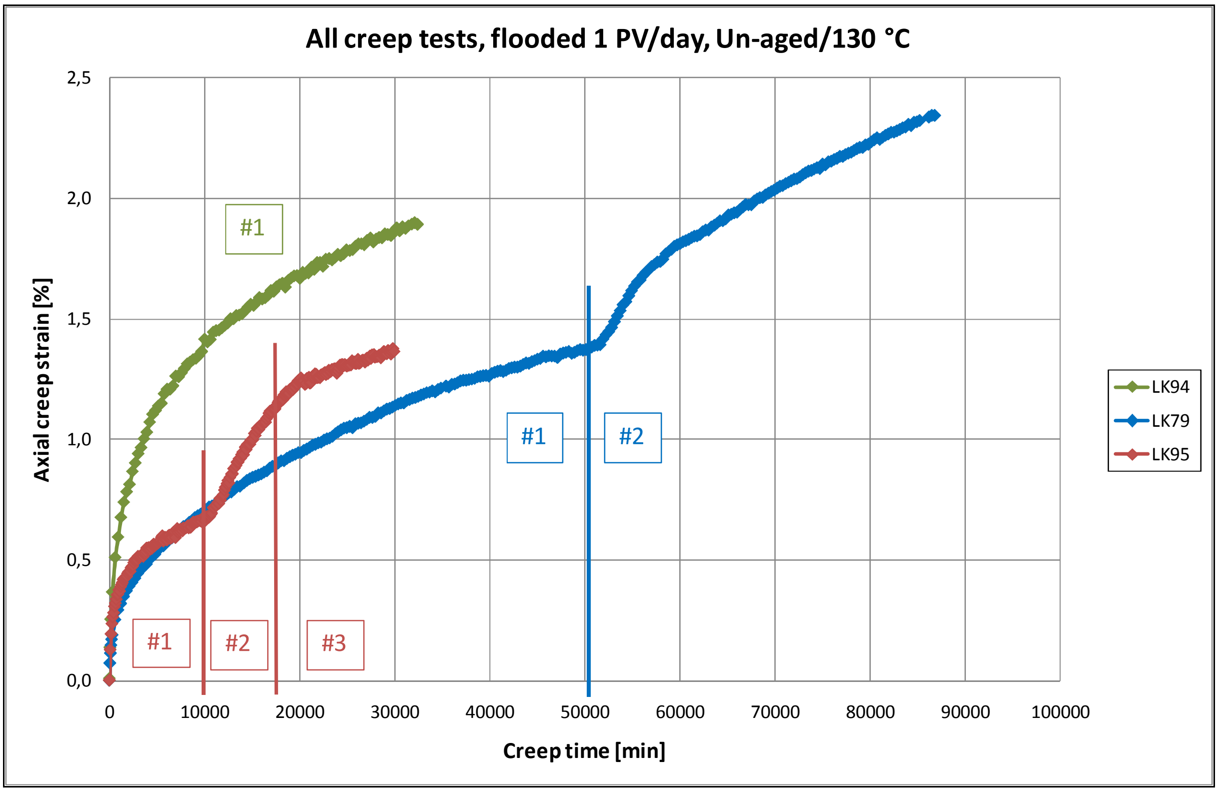

Figure 5.5: *Compilation of all creep curves (axial creep strain versus creep time plots); Un-aged chalk cores, saturated with SSW (LK94 and LK95) or SSW–($SO_4^{2-}$) (LK79), tested at 130 °C while continuously being flooded with different circulating fluids at a rate of 1 PV/day. The different flooding phases for each test are separated by vertical lines and identified by numbers 1 through 3.*

The three cores tested were LK79, LK94 and LK95. The two latter were both saturated with SSW brine before testing, while LK79 was saturated with synthetic seawater without sulphate, SSW–($SO_4^{2-}$). During the creep tests the cores were continuously flooded with different fluids at a rate of 1 pore volume per day. When considering a test, a “flooding phase” defines the period where the circulating fluid is unchanged. LK94 was only flooded with one brine, SSW, throughout the whole testing period, and therefore only one flooding phase is defined for this core. LK79 was first flooded with SSW–($SO_4^{2-}$) brine and after some time this fluid was switched to SSW. LK95 was, by a mistake, first flooded with distilled water (DW), then SSW and at last SSW–($SO_4^{2-}$) brine. The two latter tests hence consisted of two and three different flooding phases, respectively. The flooding phases are all of unequal time lengths, and the changes in flooding fluids are therefore shown in Fig. 5.5 by vertical lines of the same colour as the creep curve they are related to. For the overview, Table 5.17

contains info about circulating fluid, length of time and axial strain for each flooding phase for the three creep tests.

Table 5.17: *Overview of the different flooding phases (1-3) for the three creep tests. For each test, the circulating fluid is listed together with the time spent and axial strain achieved in the different flooding phase. The rightmost columns show the cumulated time and strain values through the phases for each test.*

| Test core | | Flooding phase #1 | | Flooding phase #2 | | Flooding phase #3 | | Total | |
|---|---|---|---|---|---|---|---|---|---|
| | | Creep time [min] ↓ | Axial creep strain [%] ↓ | Creep time [min] ↓ | Axial creep strain [%] ↓ | Creep time [min] ↓ | Axial creep strain [%] ↓ | Creep time [min] ↓ | Axial creep strain [%] ↓ |
| LK95 | Circulating fluid → | DW | | SSW | | SSW–($SO_4^{2-}$) | | | |
| | Time / Strain → | 9,602 | 0.660 | 7,209 | 0.449 | 13,099 | 0.254 | 29,910 | 1.363 |
| LK79 | Circulating fluid → | SSW–($SO_4^{2-}$) | | SSW | | | | | |
| | Time / Strain → | 50,110 | 1.371 | 36,668 | 0.971 | | | 86,778 | 2.342 |
| LK94 | Circulating fluid → | SSW | | | | | | | |
| | Time / Strain → | 32,040 | 1.900 | | | | | 32,040 | 1.900 |

As an overview of the test processes and the different parts of each test, Table 5.17 can be very advantageous. But for comparison of deformation, it is not very easy to use, since none of the flooding phases are of equal time. In addition, total time length of the three tests varied significantly. Hence, to be able to compare accumulated axial strain when different fluids are flooded through the cores, Table 5.18 is presented with this information. Every time a change in flooding fluid was made for one of the creep tests, the creep time at that moment was registered. These creep time "moments" are listed in the leftmost column in Table 5.18. The accumulated strain for each test is given at these points of time together with the fluid type flooded since the previous point of time. This way it is possible to study and compare the fluid types' effect on deformation of chalk.

Table 5.18: *Overview of all creep times at which flooding fluids were changed for the three creep tests. The creep time values are listed to the left, and for each point of time the accumulated axial creep strain so far is listed for each of the creep tests, as well as the fluid flooded since the previous point of time.*

| Creep time [min] | LK79 | | LK94 | | LK95 | |
|---|---|---|---|---|---|---|
| | Accumulated ax. creep strain [%] | Circulating fluid | Accumulated ax. creep strain [%] | Circulating fluid | Accumulated ax. creep strain [%] | Circulating fluid |
| 9,602 | 0.687 | SSW–($SO_4^{2-}$) | 1.367 | SSW | 0.660 | DW |
| 16,811 | 0.878 | SSW–($SO_4^{2-}$) | 1.596 | SSW | 1.109 | SSW |
| 29,910 | 1.137 | SSW–($SO_4^{2-}$) | 1.851 | SSW | 1.363 | SSW–($SO_4^{2-}$) |
| 32,040 | 1.171 | SSW–($SO_4^{2-}$) | 1.900 | SSW | | |
| 50,110 | 1.371 | SSW–($SO_4^{2-}$) | | | | |
| 86,778 | 2.342 | SSW | | | | |

## Observations and interpretations

The most conspicuous observation from the combined creep plots in Fig. 5.5 is the similarity between the plots representing LK79 and LK95 in the very first creep phase (called the transient phase). These curves are almost inseparable until 9,602 minutes of creep, when the circulating fluid was changed for LK95. The most interesting, however, is that fluids with totally different compositions were used during this time for the two tests. Since LK95 was flooded with DW while the circulating fluid for LK79 was synthetic seawater brine without sulphate, it is interesting to notice that these fluids generated more or less the same deformation rate in this period of time, (0.660% and 0.687%, respectively). When flooding DW, no chemical reactions can occur with the chalk, naturally. Since the creep strain observed when flooding SSW–($SO_4^{2-}$) brine is so much alike, this should indicate that no extensive chemical interactions take place during flooding with this brine either. Only a slight difference in strain of 0.027% is observed for the first 9,602 minutes of creep between these two brines. However, it should be noticed that from the slopes of the curves, it seems that LK95 would have flattened out if continued flooding with distilled water, while LK79 is seen to continue with a relatively stable deformation. Hence, on a longer time basis a larger difference in creep deformation would probably have been seen between DW flooding and SSW–($SO_4^{2-}$) flooding.

But when considering the results from the chemical tests, it is also difficult to explain the similarity the first 9,602 minutes of creep. (See Fig. 4.17 and Fig. 4.18). Because the chemical results show that no calcium is produced in the effluent for the DW flooded test, while considerable calcium amounts are produced for LK79 (as well as magnesium is retained within the chalk). Hence, when flooding with SSW–($SO_4^{2-}$), dissolution of calcite from the chalk occurs to a large extent, and especially in the very beginning of the test. It is difficult to present a reasonable explanation on why LK79 and LK95 experience about the same deformation in this period of time, when extensive chalk dissolution only occurs for one of them. One possible explanation, however, may be that the achieved strain values during the hydrostatic loading prior to these two tests are very much alike. The strain achieved during the hydrostatic loading of LK79 was measured to be 0.55% (see Table 4.10) while the equivalent value for LK95 was 0.52% (see Table 4.18). These values may indicate that the tests had very similar strain “speed” when entering the creep phase, and their behaviour during the first time of creep would therefore be alike. As already mentioned, from about 10,000 minutes of creep they seem to split apart, as the deformation rate of the DW flooded core (LK95) seems to decrease.

When considering LK94, which was flooded with SSW through the same period of time, a much larger deformation is observed. (See Fig. 5.5 and Table 5.18). After 9,602 minutes of creep, the core flooded with SSW had experienced an axial strain value of approximately twice the magnitudes of the two other tests. This indicates that the presence of sulphate has a significant effect on the strength of chalk at high temperature conditions, as the only difference between the SSW and the SSW–($SO_4^{2-}$) brine is the sulphate components. When further comparing only LK79 and LK94, it is seen that the deformation rate for both of them decreased with time after passing 10,000 minutes, but still it seems that the slope of the curve for LK94 (SSW) was somewhat higher throughout the test. For each of the points of time in Table 5.18, the accumulated strain increased a bit more (or equally) for LK94 (SSW) than for LK79 (SSW–($SO_4^{2-}$)). These two brines can be compared for the first 32,040 minute of creep, which was the time at which LK94 had to be terminated. Since the strain-time curves for both LK79 and LK94 experienced lower slopes after a creep time of about 10,000 minutes, the difference ratio in between them would be reduced from the observed ratio of 1.99 at creep time of 9,602 minutes. At termination of LK94, the SSW flooded core (LK94) had experienced strain of a factor 1.62 higher than for the core flooded with seawater without sulphate (LK79). This should be considered a significant difference, which can (only) be explained by the sulphate present in SSW.

Reconsidering the two tests with the similar deformation experiences for the first 9,602 minutes (LK79 and LK95), a tremendous increase in deformation rate was observed when circulating fluid was changed from DW to SSW for LK95. Compared to LK79 which was still flooded with synthetic seawater *without* sulphate at this time of creep, the deformation for LK95 was much larger after introducing SSW containing sulphate. At last, after 50,110 minutes of creep, also the circulating fluid for LK79 was changed to SSW. After about 10,000 minutes of SSW flooding, the deformation rate seemed to stabilize at a constant slope. This deformation rate was higher (had a steeper slope) than what was observed when flooding with SSW–($SO_4^{2-}$) brine. And since this was observed even though the core had already been deforming for more than 50,000 minutes, it seems evident that the presence of sulphate contributes to an additional deformation. The opposite change was made for LK95; SSW was flooded from 9,602 minutes until 16,811 minutes of creep, and then the sulphate was “removed” by switching brine to SSW–($SO_4^{2-}$). As the sulphate was not present in the pore fluid anymore, it was clearly seen that the deformation rate decreased and the strain-time curve tended to flatten out.

The reason why the test of LK94 (SSW) had to be finished earlier than planned, was that the differential pressure through the test core started increasing already before 18,000 minutes of creep was reached. After this was noticed, the flooding rate was halved in an attempt to reduce the pace of the pressure increase and hence be able to continue the testing for a longer time. However after 32,000 minutes, the fluid outlet “from” the chalk core was almost entirely blocked, causing the pore pressure to increase dramatically. For comparison, such an increase in the differential pressure was not observed for LK79 during the 50,110 minutes of flooding with synthetic seawater *without* sulphate. But after less than 40,000 minutes of SSW flooding, this test also had to be terminated for the same reason. Most likely, the increase in differential pressure when SSW was flooded can be considered as a result of precipitation of anhydrite ($CaSO_4$). Due to precipitation of solids like this, fluids may be obstructed from moving through pipes and tubings as they get filled and blocked.

*To sum up so far*; The overall observation from comparing the creep tests is that sulphate presence increases the deformation rate and weakens the chalk significantly.

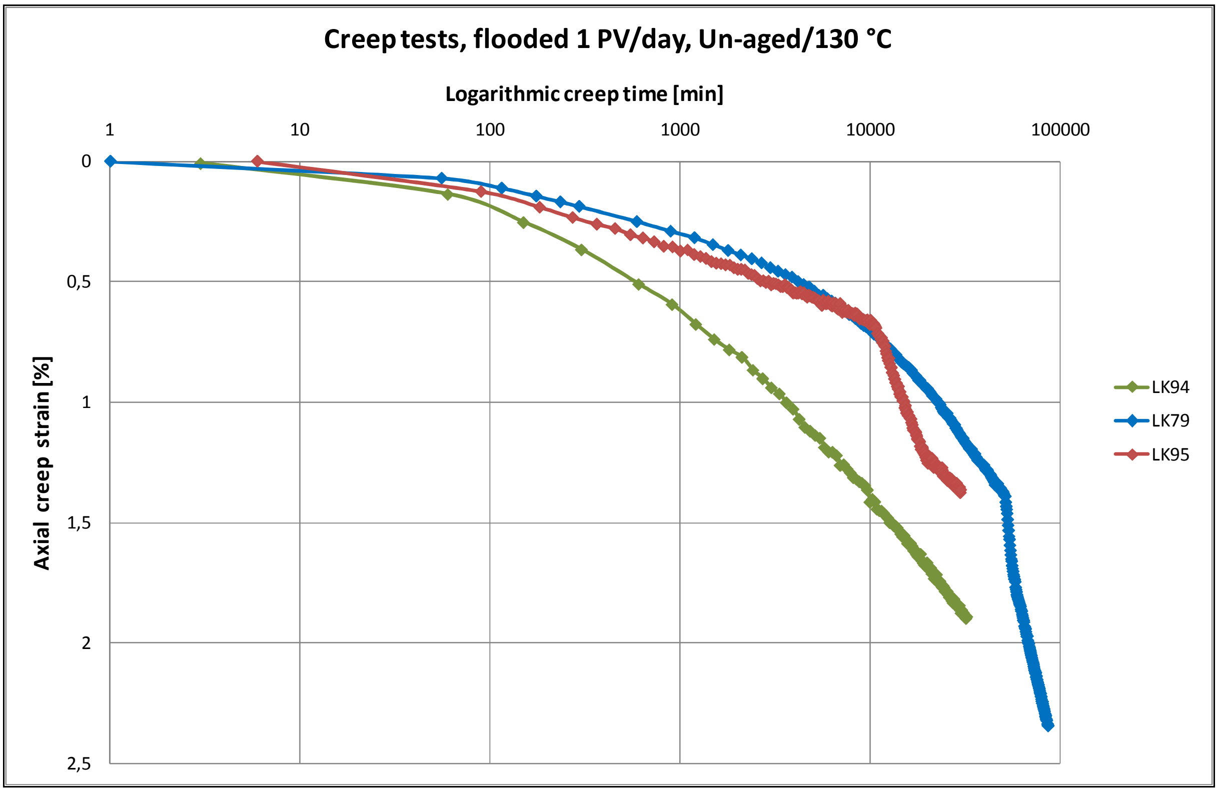

Figure 5.6: *Compilation of all creep curves (axial creep strain versus* logarithmic *creep time plots); Un-aged chalk cores, saturated with SSW (LK94 and LK95) or SSW–($SO_4^{2-}$) (LK79), tested at 130 °C while continuously being flooded with different circulating fluids at a rate of 1 PV/day.*

Fig. 5.6 shows another graphical presentation of the creep data, where the axial creep strain is plotted as a function of *logarithmic* creep time. For the last part of each flooding phase, a strain rate value can be calculated from the plots in Fig. 5.6. These calculated values are listed for all three creep tests in Table 5.19 for comparison.

Table 5.19: *Overview of the strain rates estimated for the different flooding phases of the three creep tests.*

| Test core | Flooding phase | Circulating fluid | Strain rate [ % / Decade ] |
|---|---|---|---|
| LK94 | #1 | SSW | 0.98 |
| LK79 | #1 | SSW–($SO_4^{2-}$) | 1.15 |
| | #2 | SSW | 3.21 |
| LK95 | #1 | DW | 0.36 |
| | #2 | SSW | 1.46 |
| | #3 | SSW–($SO_4^{2-}$) | 0.81 |

Each test consists of a flooding phase with SSW brine, and the strain rate for each of those can be compared. However, the second flooding phase for LK95 only lasted for 7,209 minutes while the SSW flooding phases for the other two tests lasted for more than 30,000 minutes. The strain rate value calculated for LK95 may therefore not be comparable to the others. But the values found for LK79 and LK94 should be comparable, even though SSW was used in the second and "first" flooding phase, respectively. As also could be seen from the slopes in Fig. 5.6, the strain rate found for LK94 is lower than for LK79. (A steeper curve corresponds to a higher strain rate). In fact, the strain rate found for LK79 is a factor as much as 3.28 higher than the calculated strain rate value for LK94. In an attempt to explain this high difference, the differences in between the SSW flooding phase for each of the cores should be regarded. The main difference is that LK79 was flooded with SSW–($SO_4^{2-}$) for more than 50,000 minutes before SSW was introduced to the chalk core, so this may be the reason for the clearly observed difference in strain rate.

For the flooding phases where SSW–($SO_4^{2-}$) was flooded there is also a difference. But the difference factor (1.42) is not at all as high as mentioned for the SSW flooding phases, and several different factors may effect the calculated values – especially the value for LK95. The fact that LK95 had already been flooded with two different fluids before SSW injection was initiated, may be a factor which affects the calculated strain rate. In addition, LK79 was flooded with SSW–($SO_4^{2-}$) during flooding phase #1 for 50,110 minutes, while the SSW–($SO_4^{2-}$) flooding phase for LK95 only lasted for 13,099 minutes. (See Table 5.17). Thus, the differences between the SSW–($SO_4^{2-}$) flooding phases for these two tests are difficult to explain. To be able to study any effects in a proper manner, only one "variable" (or difference) should be considered at a time.

Strain rate values which should be highly comparable are the one from the SSW flooding phase of LK94 and the value from the SSW–($SO_4^{2-}$) flooding phase of LK79. Both of these flooding phases were #1 for their respective tests, and lasted for several tens of thousands of minutes. By comparing these, any possible sulphate effect on the strain rate may be observed. For LK94 (SSW) the strain rate was found to be 0.98 %/Decade, while the equivalent value for the SSW–($SO_4^{2-}$) flooding phase of LK79 was calculated to be 1.15 %/Decade. By comparing the slopes of the end sections of the first flooding phases in Fig. 5.6, it is seen that LK79 has a somewhat higher strain rate (steeper curve). The strain rate obtained from the SSW–($SO_4^{2-}$) flooding (LK79) is a factor 1.17 higher than for the SSW flooding.

**Summary**

From investigating the creep behaviour, it has seems that SSW, i.e. the presence of sulphate, tends to increase deformation rate and decrease the mechanical strength of chalk at high temperature. When sulphate is *introduced* to a flooding system (*SSW–($SO_4^{2-}$) flooding → SSW flooding*) the chalk will be weakened and deform more, while the opposite is observed when sulphate is *removed* from the aqueous solution.

An observation made for the first 10,000 minutes of creep phase can be a subject for discussion; DW and synthetic seawater without sulphate produced very similar axial strain curves with respect to the creep time. Chemical results show that only in the case for SSW–($SO_4^{2-}$) flooding, there were large changes in ion concentrations in the effluent water. Especially, a lot of extra calcium was produced, and these ions have to come from the chalk. One possible explanation may be that the strain values achieved during the hydrostatic loading prior to creep were almost identical for the two tests, and hence they would have the same strain "speed" when entering the creep phase.

## 5.4 Chemical aspects

It is a common understanding that chemical reactions occur when chalk is exposed to certain brines containing specific ion components, and especially at high temperatures. By comparing this present work with test results obtained by Davidsen (2011), it is possible to study to what extent the presence of sulphate in seawater like brines will affect the strength of chalk. In connection with this, it is interesting to investigate what kind of chemical reactions that may occur within brine saturated chalks.

One way of investigating this is by studying any possible changes in ion concentrations in different situations where chalk is in contact with brines. This is the case for all of the test types run in the work with this thesis, but water samples of the effluent water were only stored for the creep test. All chalk cores that were tested at high temperature were aged prior to testing, and also during this aging process some chemical reactions are expected to occur. To be able to investigate the effect of aging, water samples from the aging brine (in which the chalk cores were submerged in under aging) were analyzed chemically and compared with the standard brine solution.

The two following subsections will deal with the chemical results from the aging process and the creep tests.

### 5.4.1 Chemical changes under aging

As shown in Paragraph *4.3.1 Chemical results from the aging process* some changes in the ion composition are observed under aging. The aging causes changes in ion concentrations for the components present in SSW–($SO_4^{2-}$) and SSW, and these changes as well as the difference ratio for each component are listed in Table 5.20.

Table 5.20: *Overview of* concentration changes *and* difference ratios *in ion concentrations observed under aging of chalk cores submerged in SSW–(*$SO_4^{2-}$*) and SSW brine. "After – before" reflect that the values are listed with respect to the concentrations before aging. Aging was performed at 130 °C for three weeks.*

| Ion component | SSW–($SO_4^{2-}$) brine | | SSW brine | |
|---|---|---|---|---|
| | Change [mol/l] (after – before) | Ratio (after / before) | Change [mol/l] (after – before) | Ratio (after / before) |
| $K^+$ | 0 | 1.000 | 0 | 1.000 |
| $Na^+$ | 0.017 | 1.036 | 0.005 | 1.011 |
| $Ca^{2+}$ | 0.029 | 3.231 | 0.022 | 2.692 |
| $Mg^{2+}$ | –0.025 | 0.444 | –0.025 | 0.444 |
| $Cl^-$ | 0.032 | 1.054 | 0.020 | 1.038 |
| $SO_4^{2-}$ | | | –0.009 | 0.625 |

A positive "change" value reflects that concentration was observed to be higher in the brine *after* aging, and should typically indicate that minerals found initially within the core have been dissolved into the aqueous solution. A negative “change” value, corresponding to a ratio value less than 1, indicates that the amount of dissolved ions for a component has decreased.

Common for both brines is that the amount of potassium ($K^+$) remains unchanged during the aging process, and that the observed magnesium ($Mg^{2+}$) concentrations are the exact same – both before and after aging. For the SSW–($SO_4^{2-}$) brine magnesium is the only component which experience a reduction in concentration, while the sulphate amounts present in SSW brine are also reduced. In other words, both these components seem to react with the chalk in some manner and are therefore removed from the aqueous phase. Sodium ($Na^+$), chloride ($Cl^-$) and calcium ($Ca^{2+}$) all increase in concentration under aging for both brines. Knowing that the extra calcium typically comes from dissolved calcite, the change in $[Ca^{2+}]$ is interesting when investigating the water weakening effect of chalk.

It is worth noticing that the loss in magnesium in this case seems independent of the presence of sulphate, as $[Mg^{2+}]$ decreases with the exact same amount for both brines. As described in Paragraph *2.4.3 Ion substitution*, magnesium has typically been proposed to participate in an ion substitution process with calcium ions at the chalk surface with the result of weakening of the chalk (Korsnes et al., 2006b). A one-to-one relationship has often been observed, based on common observations (from experimental flooding tests) showing a good match between the magnesium amounts lost from the aqueous solution and the amounts of additional calcium produced.

When studying the magnitudes of the changes in more details, it is observed that an additional amount of 0.029 mol/l calcium is observed in the brine after aging when sulphate is not present. This increased calcium concentration is most likely a result of calcite (chalk) dissolution, and this observation states that dissolution of calcium occurs to a significant extent also when there is no sulphate present in the pore fluid. Even if substitution should be an important mechanism, magnesium loss to the chalk does not explain all of this dissolved calcium as “only” 0.025 mol/l $Mg^{2+}$ is removed from the water phase. Other explanations have been presented for observed changes in magnesium and calcium concentrations, and among others, Madland et al. (2011) suggested such observations to rather be related to dissolution-precipitation processes where magnesium bearing minerals are precipitated inside the chalk, typically. This theory does not have the same limitations as the substitution theory, where it is found that only a certain amount of calcium is accessible for being substituted, and seems thus more reasonable when regarding the amounts of both magnesium and calcium which are dealt with.

It is interesting to compare the mentioned values with the results from aging chalk submerged in SSW, as the main difference between these two brines is the presence of sulphate. First of all it is observed that 0.009 mol/l $SO_4^{2-}$ is lost from the brine, while 0.007 mol/l less calcium is dissolved, compared to the case of SSW–($SO_4^{2-}$) brine. These values coincide relatively well, and the changes in the SSW brine can probably be explained by precipitation of anhydrite ($CaSO_4(s)$), in the main. At higher temperatures, like 130 °C, anhydrite has a retrograde behaviour with water and therefore has a very low solubility at these temperature conditions (Heggheim et al., 2004). But an additional amount of 0.002 mol/l sulphate is lost compared to what can be explained by this precipitation process, and adsorption may be a reasonable explanation for this extra loss. Megawati et al. (2011) are among them who have performed experimental work related to sulphate adsorption in high porosity chalk at high temperature (130 °C). Outcrop chalk from Liège – which has been used in the experimental work with this thesis – was one of the chalk types used for demonstrating this kind of sulphate behaviour.

The difference ratios provide an indication of the *relative* change in the ion concentrations, as only the difference values do not tell “the whole truth”. The amounts of both $Na^+$ and $Cl^–$ are experienced to increase in values of (almost) the same order of magnitude as the $[Ca^{2+}]$ increase and $[Mg^{2+}]$ loss. Especially, the chloride increase is even higher than the calcium increase in SSW–($SO_4^{2–}$), and more than double of the lost amounts of sulphate in SSW. However, the initial concentrations of sodium and chloride are several times higher than the initial $[Ca^{2+}]$, $[Mg^{2+}]$ and $[SO_4^{2–}]$ as seen from Table 4.20. A large increase in the amount of mol/l is therefore not necessarily equivalent with a large relative increase compared to the initial state. The difference ratios listed in Table 5.20 for both sodium and chloride show that the concentrations measured after aging are just a very small factor larger than what was measured initially. This is the same case for both brines. When considering calcium, for instance, the concentration has increased with a factor of more than 3.2 in SSW–($SO_4^{2–}$) and almost a factor of 2.7 when sulphate is present in the brine. In addition, the difference ratios indicate that more than half of the magnesium initially present has been removed from the solution, while the sulphate concentration after aging was found to be less than 2/3 of the start concentration.

### 5.4.2 Chemical changes during creep

*In the following, the creep tests carried out within this work will be discussed with respect to the chemical analyses of the daily samples of the effluent water. All observations are based on Fig. 4.16, Fig. 4.17 and Fig. 4.18. They contain the diagrams for ion concentrations (in the effluent water) plotted as a function of creep time for the three creep tests LK94, LK79 and LK95, respectively.*

*First, some general observations obtained from all three tests will be presented, while some more detailed observations for each of the three tests will be taken into consideration afterwards.*

**No changes in sodium [$Na^+$] or chloride [$Cl^-$] concentration**

For all tests, the produced amounts of sodium and chloride in the effluent water during creep were more or less the exact same amounts as injected into the core. This observation is similar to what was observed under aging of chalk cores. Hence, it is quite evident that these ion components do not tend to react with chalk.

**Correlation between magnesium ($Mg^{2+}$), calcium ($Ca^{2+}$) and sulphate ($SO_4^{2-}$) presence**

Observations through the years have shown that there is usually a very strong correlation between lost magnesium and produced calcium when flooding seawater like brines during creep at high temperature. Among others, Øvstebø (2009) experienced that the sum of produced $Mg^{2+}$ and $Ca^{2+}$ was more or less equal to the amount of injected magnesium, when $MgCl_2$ brine was flooded through outcrop chalk from Stevns Klint. In this present work, the same type of test has been carried out but with different brines and Liège outcrop chalk. However, the same correlation has also been observed for the creep tests performed within these studies. The following explanations are given with basis in the circulating fluids used in this present work (as well as the example from the observations by Øvstebø (2009) where $MgCl_2$ brine was used, to see that calcium is not needed in the flooding brine for these observations to be made).

When considering flooding phases where SSW–($SO_4^{2-}$) was used as circulating brine, the sum of produced amounts of magnesium and calcium was almost perfectly equal to the sum of injected $Mg^{2+}$ and $Ca^{2+}$. This is shown in the first creep phase in Fig. 5.8 for LK79. The same observation was made for SSW flooding, but the presence of sulphate "complicates" the situation a bit. When comparing only the produced [$Mg^{2+}$] and [$Ca^{2+}$] with the injected concentrations of these, it is found that the initial values are somewhat higher than what is detected in the effluent water. But by adding the *"lost" amount* of sulphate to the produced magnesium and calcium, the match with the injected $Mg^{2+}$ and $Ca^{2+}$ becomes very good. This is shown in Fig. 5.7 and Fig. 5.8 (last part) for LK94 and LK79, respectively. For convenience, the following relations are put up based on the mentioned observations during creep, when flooding with (*a*) $MgCl_2$, (*b*) SSW–($SO_4^{2-}$) and (*c*) SSW brine.

$$(a)\ [\mathrm{Mg}^{2+}]_{\mathrm{injected}} \approx [\mathrm{Mg}^{2+}]_{\mathrm{produced}} + [\mathrm{Ca}^{2+}]_{\mathrm{produced}} \quad \text{(Eq. 5.1)}$$

$$(b)\ [\mathrm{Mg}^{2+}]_{\mathrm{injected}} + [\mathrm{Ca}^{2+}]_{\mathrm{injected}} \approx [\mathrm{Mg}^{2+}]_{\mathrm{produced}} + [\mathrm{Ca}^{2+}]_{\mathrm{produced}} \quad \text{(Eq. 5.2)}$$

$$(c)\ [\mathrm{Mg}^{2+}]_{\mathrm{injected}} + [\mathrm{Ca}^{2+}]_{\mathrm{injected}} \approx [\mathrm{Mg}^{2+}]_{\mathrm{produced}} + [\mathrm{Ca}^{2+}]_{\mathrm{produced}} + [\mathrm{SO_4}^{2-}]_{\text{"lost"}} \quad \text{(Eq. 5.3)}$$

The latter relation may be explained by the theory that the lost sulphate “sequestrates”, or “binds”, some of the calcium in the aqueous solution. So the $[\mathrm{SO_4}^{2-}]_{\text{"lost"}}$ term in the bottom equation is assumed to be equal to a calcium amount which has been dissolved from chalk but not produced in the effluent.

**Theory of substitution between magnesium ($\mathrm{Mg}^{2+}$) and calcium ($\mathrm{Ca}^{2+}$)**

As mentioned in the previous paragraph, a strong correlation between lost magnesium and produced calcium is commonly observed during high temperature creep tests. To explain and describe the processes which occur inside the chalk when observations like this are made, a number of theories have been suggested through the years. When focusing on the lost magnesium and the additionally produced calcium it is clear that the magnesium is removed from the aqueous solution, somehow, while the calcium has to originate from the chalk. One of the proposed theories attempting to explain a relation between these two individual observations, has been the theory of substitution in terms of magnesium substituting calcium at the chalk’s surface.

More recent studies by Madland et al. (2009) and Madland et al. (2011), among others, claim that the produced $\mathrm{Ca}^{2+}$ and lost $\mathrm{Mg}^{2+}$ have to be caused by other processes than only substitution. One of the backgrounds for this statement is calculations made for the number of adsorption sites, i.e. the calcium amount within the chalk which is accessible for substitution. These calculations are based on basic analyses on a chalk core, similar to the ones used for experimental testing in this present work. When the calculated number of adsorption sites has been exchanged, the substitution process is expected to slow down or even cease. Since the observed calcium production during creep tests commonly exceeds the calculated accessible amounts, it can be claimed that substitution cannot be the main deformation mechanism. Madland et al. (2011) calculated the maximum number of adsorption sites for an example core to be 0.0019 mol. Assumed that magnesium is the only component to substitute calcium, maximum 0.0019 mol magnesium can be removed from the aqueous solution for the purpose of substitution, when magnesium containing brine is flooded through a chalk core during creep.

To compare the value calculated by Madland et al. (2011), the actual removed magnesium amount from one of the tests carried out within this work can be found from some simple assumptions and calculations. This has been done for LK79 as an example. The first flooding phase, where SSW–($\mathrm{SO_4}^{2-}$) was flooded, is used for this calculation, as this brine does not contain other ions than magnesium which typically would react chemically with chalk during the given test conditions. During the flooding period lasting 50,110 minutes, the flow rate used was 0.022 ml/min. The volume of SSW–($\mathrm{SO_4}^{2-}$) brine flooded through this flooding phase will then be:

$$\underline{V_{flooding}} = \frac{Q\,[ml/\min]\cdot t_{flooding}\,[\min]}{1{,}000\,[ml]} = \frac{0.022\,[ml/\min]\cdot 50{,}110\,[\min]}{1{,}000\,[ml]} = \underline{1.102\,l} \quad \text{(Eq. 5.4)}$$

where

$V_{flooding}$: Volume flooded through the core [ml]
$Q$: Flooding rate [ml/min]
$t_{flooding}$: Flooding time [min]

Further in this calculation, to be able to estimate the amount of removed magnesium from the solution, it is of interest to find the *concentration* of the removed amount. As an assumption, this can be done by subtracting the average produced amount in the effluent water sampled during the flooding phase, from the injected amount of magnesium. The average produced magnesium is easily found to be 0.0311 mol/l, and by subtracting this value from the standard concentration of 0.045 mol/l, the concentration of removed magnesium is calculated:

$$\underline{[\mathrm{Mg}^{2+}]_{\mathrm{removed}}} = 0.045 \left[\frac{mol}{l}\right] - 0.0311 \left[\frac{mol}{l}\right] = \underline{0.0139} \left[\frac{mol}{l}\right] \qquad \text{(Eq. 5.5)}$$

The last step to find the amount of magnesium lost to the core during the 50,110 minutes of creep, is to multiply the concentration by the total volume flooded in this period:

$$\underline{n_{Mg^{2+}}} = \left[Mg^{2+}\right]_{removed} \cdot V_{flooding} = 0.0139 \cdot 1.102 = \underline{0.015\, mol} \qquad \text{(Eq. 5.6)}$$

By comparing this amount of lost magnesium to the amount of calcium accessible for substitution, the magnesium amount lost is a factor of 7.89 higher than the amount which could be involved with substitution. The equivalent value can be obtained for the SSW–($SO_4^{2-}$) flooding phase of the LK94 creep test, which was flooded for 32,040 minutes at a constant flow rate of 0.021 ml/min. The same procedure is used, where the average produced magnesium was found to be 0.033 mol/l, $[\mathrm{Mg}^{2+}]_{\mathrm{removed}}$ was equal to 0.012 mol/l, and the lost amount found to be 0.0081 mol. This is a lot lower than in the case of LK79, but is still a factor 4.24 higher than what could be involved with substitution. So even if substitution should be an important process, a lot of magnesium is removed from the solution as results of other processes. Madland et al. (2011) suggested the lost magnesium to be a result of precipitation of magnesium bearing minerals. Since the two tests of LK79 and LK94 show that a lot more magnesium is lost from the brine than what could be due to substitution alone, the precipitation theory mentioned by Madland et al. (2011) is supported.

**LK94 Flooded with SSW only**

With basis in Fig. 4.16, a new Fig. 5.7 is here composed by only the ion components which experienced changes in the produced amounts, when the creep test of LK94 was flooded with SSW throughout the whole creep time of 32,040 minutes. I.e. without sodium, chloride and potassium, as none of them showed any reactions with the chalk. But in addition, to show the relationship between magnesium, calcium and sulphate, as it was described 3 pages ago, a horizontal, black dotted line represents the sum of standard [$Mg^{2+}$] and [$Ca^{2+}$]. In addition, an orange curve is drawn, consisting of the sum of the measured production of calcium and magnesium, as well as loss of sulphate. This curve coincides to a very high degree with the injected amounts represented by the black, dotted line. From the shape of the sulphate concentration line, and the fact that the average produced amount of these tests is only 72% of the standard value, the most likely reaction to occur is precipitation, and the precipitated mineral is probably anhydrite ($CaSO_4$).

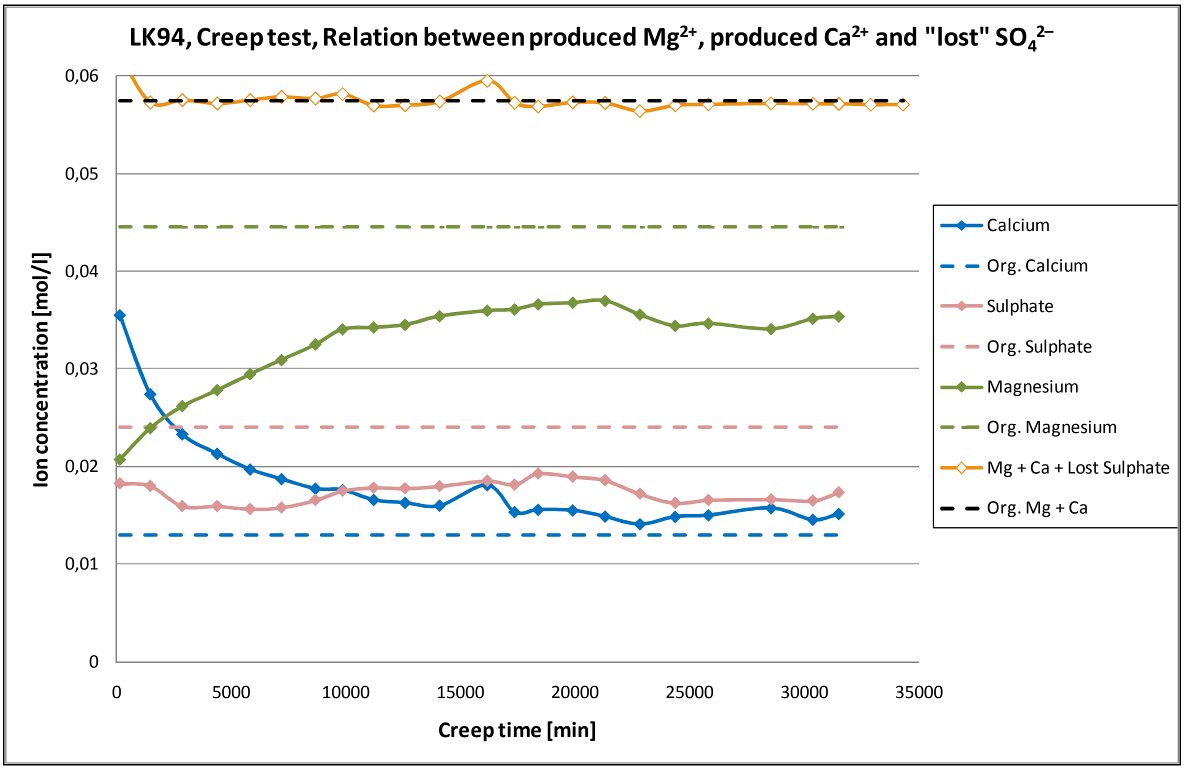

Figure 5.7: *Some results from the chemical analysis of the effluent water (sampled daily) during the creep test of LK94; Un-aged chalk core tested at 130 °C. SSW brine was flooded throughout the whole test at a rate of 1 PV/day. A black, dotted horizontal line is added to the original diagram in Fig. 4.16, representing the sum of standard concentrations of* $Mg^{2+}$ *and* $Ca^{2+}$*. The orange curve reflects the sum of produced* [$Mg^{2+}$], [$Ca^{2+}$] *and lost* [$SO_4^{2-}$].

**Effect of decreasing flooding rate,**

After the flooding rate was halved after ca. 20,000 minutes of creep, for the LK94 creep test, a slight – but still noticeable – decrease in both magnesium, sulphate and calcium production was observed. Since only the volume and time was changed, and not any initial concentrations, it can be difficult to find an explanation for this detection. One possible explanation can be that the ion components stay in the pore space inside the chalk core for a *longer time* due to the lower flooding rate. As a result of this, larger amounts of ions may be able to react with the chalk before reaching the outlet from the core, and are thereby removed from the brine.

**LK79 Flooded with SSW–($SO_4^{2-}$) → SSW**

Unlike the creep test of LK94, LK79 was flooded with two different brines as SSW–($SO_4^{2-}$) was changed to SSW after 50,110 minutes of creep. Also for this test, sodium, chloride and potassium did not experience any specific changes in concentration and are therefore not included in the diagram in Fig. 5.8.

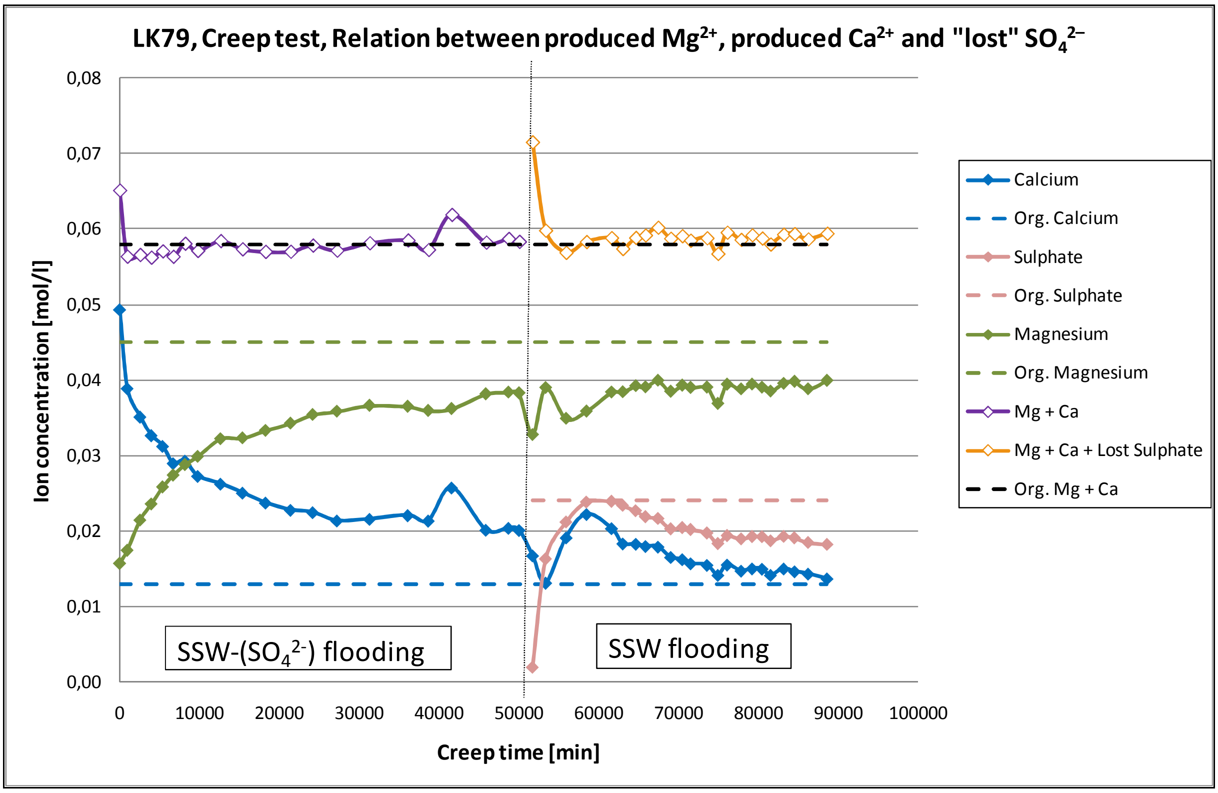

Figure 5.8: *Some results from the chemical analysis of the effluent water (sampled daily) during the creep test of LK79; Un-aged chalk core tested at 130 °C. SSW–($SO_4^{2-}$) brine was flooded at a rate of 1 PV/day the first 50,110 minutes, before SSW was started flooding at the same rate. A black, dotted horizontal line is added to the original diagram in Fig. 4.17, representing the sum of standard concentrations of $Mg^{2+}$ and $Ca^{2+}$. The purple curve reflects the sum of produced [$Mg^{2+}$] and [$Ca^{2+}$], while the orange curve includes also the amount of lost [$SO_4^{2-}$] which (probably) is "bound" to calcium some way.*

As a result of the introduction of sulphate to the pore fluid, by changing flooding brine from SSW–($SO_4^{2-}$) to SSW, there are some peaks and drops in the different measured concentrations. In the first flooding phase, the sum of produced and injected amounts of [$Mg^{2+}$] and [$Ca^{2+}$] are very much alike. The calcium concentration lies on a level above the injected amounts, and should be large enough to cause precipitation of, for instance, anhydrite ($CaSO_4$). But no sulphate is present before SSW is started flooding after 50,110 minutes of creep. At that point of time there is a clear drop in calcium concentration while the sulphate concentration increases gradually. This is an indication that calcium is removed from the aqueous phase, and may be explained by anhydrite precipitation. However, there is also observed a drop in magnesium concentration at the same time. It is difficult to tell for sure what these observations are caused by, and it could even have just something to do with the displacement of the previous brine as a new one is injected.

It takes the sulphate about 8,000 minutes to reach its injected amount, before it started to decrease continuously. Hence, some of the sulphate started being removed from the water solution. The exact same trend is seen for calcium, which should be an applicable indication of anhydrite precipitation to occur. Also in this flooding phase there is a good correlation between the produced magnesium and calcium and the lost sulphate, as shown for the good match between the orange curve and the black, dotted horizontal line.

It should be worth mentioning that even though precipitation of anhydrite has been proposed here, the complexity of seawater like brines makes it very difficult to tell what really happens chemically inside the chalk, as several different processes may occur parallel or in different orders. The removal of sulphate may also be due to adsorption, but this is typically believed to be seen in the very beginning phase of sulphate flooding, as sulphate is totally retained inside the chalk. (Please see descriptions for LK95). In this case for LK79 this does not happen. The sulphate concentration in the effluent immediately starts increasing, but as mentioned it used some 5-6 pore volumes to reach the initial amount. Hence, some sulphate is removed from the aqueous phase in the beginning, at the same time as the calcium drop was observed, and precipitation is thus naturally a suggested process. The reason why there is no typical sign of adsorption, may be that there had already been some adsorption on the chalk's surface of other kinds during the flooding with SSW–($SO_4^{2-}$) prior to the SSW flooding, and that sulphate adsorption somehow was restricted/obstructed.

**<u>LK95 Flooded with DW → SSW → SSW–($SO_4^{2-}$)</u>**

*When here trying to describe the creep test observations of LK95, it will just be referred to the original diagram in Fig. 4.18, instead of repeating the exact same figure here. The reason is that for this creep test, all ion components are mentioned in the discussion, and none of them could therefore be excluded from an eventual new diagram presented here.*

First of all it should be mentioned that the tremendously high calcium peak observed when changing flooding fluid from DW to SSW is a common observation when switching from DW to seawater like brine. (This may be caused by a cation exchange process). But this observation is in fact the directly opposite as observed when another seawater like brine was flooded prior to the SSW. This is seen by comparing with the creep test of LK79, where actually a drop in calcium concentration was observed when changing flooding fluid from SSW–($SO_4^{2-}$) to SSW brine.

Another very interesting observation made when starting SSW flooding after flooding some pore volumes of distilled water (DW) is related to the sulphate reaction. Because, this observation also differs a lot from what was observed from the creep test of LK79 when SSW flooding was started after flooding with SSW–($SO_4^{2-}$). For LK79 there had possibly already occurred some adsorption on the chalk surface when sulphate was introduced. But in this case, for LK95, no such adsorption could have happened prior to the sulphate introduction. Right after flooding fluid was switched from DW to SSW, only $Ca^{2+}$, $Na^{+}$ and $Cl^{-}$ increased "immediately". Both magnesium, sulphate and potassium were clearly retained inside the chalk for a couple of pore volumes flooded, before their concentrations in the effluent rapidly increase. These are all indications which can support adsorption occurring immediately after flooding is started, and continues all the way until no more adsorption can happen.

When regarding the sulphate retention, this may be described by adsorption on positive charged surfaces as a result of electrostatic differences, while the retention of positively charged ions, like magnesium and potassium in this case, may be due to other processes.

Sulphate adsorption on chalk's surface will reduce the surface potential, which may even become negative. If the latter should happen, positive charged ions will be attracted to the surface by electrostatic forces in an attempt to neutralize electrical charges. If clays are present inside the chalk, cation exchange of positively charged ions in the solution may be one way to explain retention of cations inside the chalk. For the cations retained in this creep test of LK95, it could be mentioned that clays in general tend to have a higher affinity towards magnesium than potassium. But, seen from the concentration-time diagram in Fig. 4.18, potassium is retained for a longer time than magnesium. An explanation of this may be that since magnesium has the higher concentration of the two, $Mg^{2+}$ will be expected to obtain an earlier breakthrough than $K^{+}$. However, it should also be noticed that there are suggested several different ways for magnesium to be removed from the water solution. Precipitation as magnesium holding minerals is probably the most common comprehension, but also cation exchange and attraction to negatively charged chalk surface are possible explanations.

### Removing sulphate from the circulating fluid, i.e. changing from SSW to SSW–($SO_4^{2-}$)

When the breakthrough of SSW–($SO_4^{2-}$) brine is detected in the effluent, the sulphate concentration naturally drops and stabilizes at a minimum level. From the start of the drop, calcium production starts increasing, and reaches a peak at the point from which sulphate stabilizes. When comparing with the axial strain-creep time plot at this time, at about 20,000 minutes of creep in Fig. 4.14, a decrease in deformation rate is detected. The strain-time curve tends to "flatten out". Hence, there is a correlation between decreased calcium production and decreased deformation. This corresponds to the observation of a large increase in calcium production at the same time as the deformation rate increased significantly, when SSW replaced DW in the pores (after a creep time of 9,602 minutes).

### Summary – Chemical changes during creep

Precipitation of both sulphate and magnesium bearing minerals seem to occur when continuously flooding seawater like brines through chalk cores during creep testing at high temperature (130 °C). Precipitation like this typically causes disturbances in the equilibrium between solid chalk material and the pore-filling fluid, and solid material will dissolve to re-establish equilibrium. Since the solid material which has to dissolve typically is calcite form the chalk, this overall process may be regarded as a weakening effect on chalk.

# 6 Conclusion

The main objective of the work with this thesis was to investigate any possible effect of sulphate on the mechanical strength of chalk. This work was carried out by performing four different types of tests – hydrostatic, deviatoric, creep and Brazilian tests – where the three first test types were all executed in triaxial test cells, and the latter type was run in a Brazilian test cell. The sulphate effect was studied by using two different brines during testing; synthetic seawater (SSW) and synthetic seawater without sulphate (SSW–($SO_4^{2-}$)). Two different temperature conditions were also used – ambient temperature and high temperature (130 °C) – and hence any possible temperature effects on chalk's mechanical strength could also be considered. One of the underlying goals was to estimate failure envelopes, drawn in *q-p'* diagrams, for the different parameters. Experimental work was performed on high porosity outcrop chalk from Liège, found to hold an average porosity of 39.57%.

The conclusions are separated into two parts, based on whether they are obtained from *triaxial tests* or *creep tests*.

Based on the results obtained from this present work, combined with the results provided by Davidsen (2011), the main conclusions can be summarized as follows:

**Triaxial tests**

- Chalk cores tested at 130 °C were weaker when sulphate was present in the pore fluid. This was especially observed at stress conditions for which pore collapse is the dominating failure mechanism. Yield point values and *E*-modulus values for synthetic seawater *without* sulphate was observed to be a factor of approx. 1.3 higher than what was observed for synthetic seawater containing sulphate.

- Chalk cores tested at ambient temperature did not experience any clear reduction in mechanical strength when sulphate was present in the pore fluid. In fact, a somewhat higher resistance against shear failure was actually observed when the pore fluid contained sulphate.

- Chalk cores tested by the use of synthetic seawater (SSW) as testing brine were clearly weaker when tested at high temperature (130 °C). Especially at stress conditions for which pore collapse is the dominating failure mechanism. Yield point values and elasticity moduli values for ambient temperature tests were observed to be a factor of approx. 1.5 higher than the observations for high temperature tests.

- Chalk cores tested by the use of synthetic seawater without sulphate (SSW–($SO_4^{2-}$)) did not seem to be affected by the testing temperature. Overall, both yield points, Young's moduli, bulk moduli and failure envelopes were very much alike.

**Creep tests**

- The axial strain experienced during creep at high temperature (130 °C) is to a large extent affected by the presence of sulphate in the pore fluid. Axial creep strain experienced during flooding with SSW was found to be a factor 1.62 higher than for SSW–($SO_4^{2-}$) brine (after 32,000 minutes of creep). When sulphate is introduced to the pore space during creep, the deformation rate is significantly increased. On the contrary, when sulphate is removed from the system the deformation rate is observed to decline.

- Chemical analyses of the effluent water sampled during high temperature (130 °C) creep showed that precipitation of magnesium bearing minerals may occur, both when SSW and SSW–($SO_4^{2-}$) brine is continuously flooded.

- Such chemical analyses for high temperature creep tests also showed that precipitation of anhydrite ($CaSO_4$) is likely to occur, when continuously flooding SSW and sulphate apparently is retained inside the chalk.

- The immediate reaction observed for sulphate after being introduced to a pore system, depends on the composition of the previous/prior flooding fluid. When introducing sulphate after flooding with distilled water (DW) adsorption of the sulphate seemed to occur, while this was not clearly seen then SSW–($SO_4^{2-}$) brine had been flooding prior to the sulphate introduction.

# 7 Further work

This present study of sulphate's possible effects on the mechanical strength of chalk could be supplemented with the following points to achieve a better basis for comparison. The overall understanding and interpretations of such possible effects would be better if more data were accessible than the amounts provided from this work.

- Generally, it would have been advantageous for the basis of comparison to perform more tests the exact same ways as already done – especially for deviatoric and hydrostatic tests. Because only one pair of "identical" deviatoric tests were performed (i.e. the same testing brine and temperature), and only one hydrostatic test was carried out for each temperature condition for SSW–($SO_4^{2-}$) brine. To obtain an estimation of the failure envelope, typically, this was a reasonable way of working, but as basis for comparison more data is needed.

- More creep tests can be carried out where sulphate is introduced/removed at certain stages and in certain order. More consistent test progresses, by for instance keeping the times of each flooding phase alike, would make it easier to compare.

- When sampling effluent water for chemical analyses, more frequent sampling can be done to obtain a better understanding of the chemical processes. Especially when changing flooding fluid during creep tests.

- In this present work, un-aged cores were tested at ambient temperature, while aged cores were tested at high temperature. Any possible effect of the aging process could have been studied by also performing high temperature tests on un-aged cores, and opposite.

- As planned to do in the work with this thesis, a SSW–($SO_4^{2-}$) solution containing an abnormally high calcium concentration (typically ten times higher than for SSW) can be introduced to a creep test as a flooding fluid. The reason for not using SSW brine for this, is that the presence of sulphate would most likely cause anhydrite precipitation. Such a large amount of calcium in the pore fluid should make dissolution of additional calcite unnecessary.

# 8 References

Ahlbrandt, T.S., Charpentier, R.R., Klett, T.R., Schmoker, J.W., Schenk, C.J. and Ulmishek, G.F., 2005. *Global Resource Estimates from Total Petroleum Systems,* (pp. 108-109). The American Association of Petroleum Geologists, Memoir 86. ISBN 0-89181-367-5.

Ahr, W.M., 2008. *Geology of Carbonate Reservoirs.* John Wiley & Sons, Hoboken, USA. ISBN 978-0-470-16491-4.

Austad, T., Strand, S., Madland, M.V., Puntervold, T. and Korsnes, R.I., 2008. *Seawater in Chalk: An EOR and Compaction Fluid*. SPE Paper 118431, SPE Reservoir Evaluation & Engineering – Vol. 11, No. 4, pp. 648-654.

Bissell, H.J. and Chilingar, G.V., 1967. *Classification of sedimentary carbonate rocks.* Chilingar, G.V., Bissell, H.J. and Fairbridge, R.W. (Eds.), Carbonate rocks: Origin, Occurrence and Classification. Developments in Sedimentology, 9A, pp. 87-168, Elsevier, Amsterdam, The Netherlands.

Bjørlykke, K., 1989. *Sedimentology and Petroleum Geology*, (pp. 147 & 216). Springer Verlag, Berlin, Germany. ISBN 3-540-17691-8.

D'Heur, M., 1986. *The Norwegian chalk fields*. Spencer, A.M., Holter, E., Campbell, C.J., Hanslien, S.H., Nelson, P.H.H., Nysæther, E. and Ormaasen, E.G. (Eds.), Habitat of Hydrocarbons on the Norwegian Continental Shelf, pp. 77-89, Graham & Trotman Limited, United Kingdom. ISBN 0-86010-833-3.

DaSilva, F., Sarda, J.P. and Schroeder, C., 1985. *Mechanical behavior of chalks. Second North Sea Chalk Symposium, Book II*, Stavanger, Norway.

Davidsen, A., 2011, *A mechanical study of the effect of sulphate*. Master thesis, Department of Petroleum Engineering, Faculty of Science and Technology, University of Stavanger, Norway.

Finsnes, A., 2004. *The effects of CO2 on the mechanical behaviour of high porosity chalk*, (pp. 11). Master thesis, Department of Petroleum Engineering, Faculty of Science and Technology, University of Stavanger, Norway.

Fischmeister, H.F., Artz, E. and Olssen, L.R., 1982. *Particle deformation and sliding during compression of spherical powders: a study by quantitative metallurgy.* Powder Metall – Vol. 21 (1982), pp. 179-187.

Fjær, E., Holt, R.M., Horsrud, P., Raaen, A.M. and Risnes, R., 2008. *Petroleum related rock mechanics – Second Edition.* Elsevier, Amsterdam, The Netherlands. ISBN 978-0-444-50260-5.

Glennie, K.W., 1998. *Petroleum Geology of the North Sea – Fourth Edition.* (pp. 327), Blackwell Scientific Publications, Great Britain. ISBN 0-632-03845-4.

Gundersen, E., Dysthe, D.K., Renard, F., Bjørlykke, K. and Jamtveit, B., 2002. *Pressure solution in sandstone, rate limiting processes and the effect of clays.* Deformation Mechanisms, Rheology and Tectonics: Current Status and Future Perspectives, pp. 41-60, Geological Society of London. ISBN 1-86239-109-2.

Halbouty, M.T., Meyerhoff, A.A., King, R.E., Dott, R.H., Sr., Klemme, H.D. and Shabad, T., 1970. *World's Giant Oil and Gas Fields, Geologic Factors Affecting Their Formation, and Basin Classification – Part I, Giant Oil and Gas Fields.* Halbouty, M.T. (Ed.), Geology of Giant Petroleum Fields, pp. 502-528, The American Association of Petroleum Geologists, Memoir 14.

Heggheim, T., Madland, M.V., Risnes, R. and Austad, T., 2004. *A chemical induced enhanced weakening of chalk by seawater*. Journal of Petroleum Science and Engineering – Vol. 46, 2005, pp. 171-184.

Hellmann, R., Renders, P.J.N, Gratier, J.P. and Guiguet, R., 2002. *Experimental pressure solution compaction of chalk in aqueous solutions – Part 1. Deformation behavior and chemistry.* Hellmann, R. and Wood, S.A. (Eds.), Water-Rock Interactions, Ore Deposits, and Environmental Geochemistry: A Tribute to David A. Crerar, pp. 129-152, Special Publication No. 7, 2002, The Geochemical Society.

Hiorth, A., Cathles, L.M., Kolnes, J., Vikane, O., Lohne, A., Korsnes, R.I. and Madland, M.V., 2008. *A chemical model for the seawater-*$CO_2$*-carbonate system – aqueous and surface chemistry*. International Symposium of the Society of Core Analysts, Abu Dhabi, UAE.

Hiorth, A., Cathles, L.M. and Madland, M.V., 2010. *The Impact of Pore Water Chemistry on Carbonate Surface Charge and Oil Wettability*. Transport in porous media – Vol. 85, No. 1, 2010, pp. 1-21.

Hjuler, M.L. and Fabricius, I.L., 2009. *Engineering properties of chalk related to diagenetic variations of Upper Cretaceous onshore and offshore chalk in the North Sea area.* Journal of Petroleum Science and Engineering 68 (2009), pp. 151-170.

Jakobsen, F., 1996. *Chalk Outcrops – Analogues for Offshore Chalk Reservoirs?* Fifth North Sea Chalk Symposium, Reims, France.

Jaeger, J.C., Cook, N.G.W. and Zimmerman, R.W., 2007. *Fundamentals of Rock Mechanics – Fourth Edition.* Blackwell Publishing, Oxford, United Kingdom. ISBN 978-0-632-05759-7.

Johnson, J.P., Rhett, D.W., 1986. *Compaction Behavior of Ekofisk Chalk as a Function of Stress*. SPE Paper 15872, presented at the 1986 SPE European Petroleum Conference, 20-22 October, London, United Kingdom.

Korsnes, R.I., Strand, S., Hoff, Ø., Pedersen, T., Madland, M.V. and Austad, T., 2006a. *Does the chemical interaction between seawater and chalk affect the mechanical properties of chalk?* Cottheim, A.V., Charlier, R., Thimus, J.F. and Tshibangu, J.P. (Eds.), Eurock 2006, Multiphysics Coupling and Long Term Behaviour in Rock Mechanics, pp. 427-434, Taylor & Francis, London, England. ISBN 0-415-41001-0.

Korsnes, R.I., Madland, M.V. and Austad, T., 2006b. *Impact of brine composition on the mechanical strength of chalk at high temperature.* Cottheim, A.V., Charlier, R., Thimus, J.F. and Tshibangu, J.P. (Eds.), Eurock 2006, Multiphysics Coupling and Long Term Behaviour in Rock Mechanics, pp. 133-140, Taylor & Francis, London, England. ISBN 0-415-41001-0.

Korsnes, R.I., 2007. *Chemical induced water weakening of chalk by fluid-rock interactions. A mechanistic study.* Ph.D. thesis, Department of Petroleum Engineering, Faculty of Science and Technology, University of Stavanger, Norway.

Korsnes, R.I., Madland, M.V., Austad, T., Haver, S. and Røsland, G., 2008. *The effects of temperature on the water weakening of chalk by seawater.* Journal of Petroleum Science and Engineering 60, Issues 3-4, pp. 183-193.

Lehner, F.K., 1990. *Thermodynamics of rock deformation by pressure solution.* Barber, D.J. and Meredith, P.G. (Eds.), Deformation processes in minerals, ceramics and rocks, pp. 296-333, Unwin Hyman, London, United Kingdom. ISBN 0-04-445088-5.

Lehner, F.K., 1995. *A model for intergranular pressure solution in open systems.* Tectonophysics – Vol. 245 (1995), pp. 153-170, Elsevier.

Link, P.K., 2001. *Basic Petroleum Geology – Third Edition.* OGCI Publications, Tulsa, USA. ISBN 0-930972-22-8.

Lucia, F.J., 1999. *Carbonate Reservoir Characterization,* (pp. 82-83). Springer-Verlag, Berlin, Germany. ISBN 3-540-63782-6.

Madland, M.V., 2005. *Water weakening of chalk. A mechanistic study.* Ph.D. thesis, Department of Petroleum Engineering, Faculty of Science and Technology, University of Stavanger, Norway. ISBN 82-7644-257-9.

Madland, M.V., Hiorth, A., Korsnes, R.I., Evje, S. And Cathles, L., 2009. *Rock Fluid Interactions in Chalk exposed to Injection of Seawater, $MgCl_2$, and NaCl Brines with equal Ionic Strength*, Paper A22. 15th European Symposium on Improved Oil Recovery – Paris, France, 27 – 29 April 2009.

Madland, M.V., Hiorth, A., Omdal, E., Megawati, M., Hildebrand-Habel, T., Korsnes, R.I., Evje, S. And Cathles, L.M., 2011. *Chemical Alterations Induced by Rock-Fluid Interactions When Injecting Brines in High Porosity Chalks*. Bear, J. (Ed.), Transport in porous media – Vol. 87, No. 3, 2011, pp. 679-702.

Megawati, M., Hiorth, A. and Madland, M.V., 2011. *The impact of surface charge on the mechanical strength of high porosity chalk.* Preprint submitted to Geochimica et Cosmoshimica Acta.

Miller, .P., 1952. *A portion of the system calcium carbonate-carbon dioxide-water, with geological implications*. American Journal of Science – Vol. 250, pp. 161-203.

Needham, C.E.J. and Jacobs, L., 1995. *From the Chalk to the Palaeozoic, the new frontier in Central Graben exploration.* Hanslien, S. (Ed.), Petroleum Exploration and Exploitation in Norway, NPF Special Publication 4, pp. 53-65, Elsevier, Amsterdam, The Netherlands. ISBN 0-444-81596-1.

North, F.K., 1985. *Petroleum Geology.* Allen & Unwin, Boston, USA. ISBN 0-04-553003-3.

Paterson, M.S., 1995. *A theory for granular flow accommodated by material transfer via an intergranular fluid.* Tectonophysics – Vol. 245 (1995), pp. 135-151, Elsevier.

Reeder, R.J. (Ed.), 1983. *Carbonates: Mineralogy and Chemistry.* Reviews in Mineralogy – Vol. 11, Mineralogical Society of America.

Renard, F., Ortoleva, P. and Gratier, J.P., 1997. *Pressure solution in sandstones: influence of clays and dependence on temperature and stress.* Tectonophysics – Vol. 280 (1997), pp. 257-266, Elsevier.

Risnes, R., Garpestad, O.J., Gilje, M., Oland, L.T., Ovesen, M. and Vargervik, E.,1998. *Strain Hardening and Extensional Failure in High Porosity Chalk.* Eurock ’98, Trondheim, Norway.

Risnes, R. and Flaageng, O., 1999. *Mechanical Properties of Chalk with Emphasis on Chalk Fluid Interactions and Micromechanical Aspects*. Oil & Gas Science and Technology – Rev. IFP – Vol. 54, No. 6, 751-758. Editions Technip.

Risnes, R., 2001. *Deformation and Yield in High Porosity Outcrop Chalk.* Phys. Chem. Earth (A) – Vol. 26, No. 1-2, pp. 53-57.

Risnes, R., Haghighi, H., Korsnes, R.I. and Natvik, O., 2003. *Chalk-fluid interactions with glycol and brines*. Tectonophysics – Vol. 370 (2003), pp. 213-226, Elsevier.

Risnes, R., Madland, M.V., Hole, M. and Kwabiah, N.K., 2005. *Water weakening of chalk – Mechanical effects of water glycol mixtures*. Journal of Petroleum Science and Engineering – Vol. 48, 2005, pp. 21-36.

Roehl, P.O. and Choquette, P.W., 1985. *Carbonate Petroleum Reservoirs.* Springer-Verlag, New York, USA. ISBN 0-387-96012-0.

Rutter, E.H., 1983. *Pressure solution in nature, theory and experiment.* Journal of the Geological Society of London – Vol. 140 (1983), pp. 725-740.

Røgen, B. and Fabricius, I.L., 2002. *Influence of clay and silica on permeability and capillary entry pressure of chalk reservoirs in the North Sea.* Petroleum Geoscience – Vol. 8, pp. 287-293.

Schlumberger Market Analysis 2007. *http://www.slb.com/services/industry_challenges/carbonates.aspx* (May 23rd, 2011)

Scholle, P.A., 1975. *Application of chalk diagenetic studies to petroleum exploration problems (abst.).* American Association of Petroleum Geologists Bulletin v. 59, pp. 2197-2198.

Scholle, P.A., 1977. *Chalk diagenesis and its relation to petroleum exploration: oil from chalks, a modern miracle.* American Association of Petroleum Geologists Bulletin v. 61, pp. 982-1009.

Selley, R.C., 1998. *Elements of Petroleum Geology*, (pp. 239-240). Academic Press, Harcourt Brace & Company, San Diego, USA. ISBN 0-12-636370-6.

Sienko, M.J. and Plane, R.A., 1974. *Chemical principles and properties – Second Edition,* (pp. 346-350), McGraw-Hill, Kogakusha, Tokyo, Japan.

Strand, S., Høgnesen, E.J. and Austad, T., 2005. *Wettability alteration of carbonates – Effects of potential determining ions ($Ca^{2+}$ and $SO_4^{2-}$) and temperature.* Colloids and Surfaces A: Physicochemical and Engineering Aspects – Vol. 275, 2006, pp. 1-10.

Strand, S., Standnes, D.C. and Austad, T., 2006. *New wettability test for chalk based on chromatographic separation of $SCN^-$ and $SO_4^{2-}$.* Journal of Petroleum Science and Engineering 52, Issues 1-4, pp. 187-197.

Sulak, R.M., Nossa, G.R. and Thompson, D.A., 1990. *Ekofisk Field Enhanced Recovery*. Buller, A.T., Berg, E., Hjelmeland, O., Kleppe, J., Torsæter, O. and Aasen, J.O. (Eds.), North Sea Oil and Gas Reservoirs – II, pp. 281-295, The Norwegian Institute of Technology, Graham & Trotman Limited, United Kingdom. ISBN 1-85333-283-6.

Sylte, J.E., Thomas, L.K., Rhett, D.W., Bruning, D.D. and Nagel, N.B., 1999. *Water induced Compaction in the Ekofisk Field.* SPE Annual Technical Conference and Exhibition, 3-6 October 1999, Houston, Texas, USA.

Zenger, D.H., Dunham, J.B. and Ethington, R.L., 1980. *Concepts and models of dolomitization.* Society of Economic Paleontologists and Mineralogists, Special Publication No. 28, Tulsa, USA.

Zhang, X., Salemans, J., Peach, C.J. and Spiers, C.J., 2002. *Compaction experiments on wet calcite powder at room temperature: evidence for operation of intergranular pressure solution.* De Meer, S., Drury, M.R., De Bresser, J.H.P. and Pennock, G.M. (Eds.), Deformation Mechanisms, Rheology and Tectonics: Current Status and Future Perspectives – Vol. 200, pp. 29-39, Geological Society of London, Special Publication; 2002.

Zhang, X. and Spiers, C.J., 2005. *Compaction of granular calcite by pressure solution at room temperature and effects of pore fluid chemistry.* International Journal of Rock Mechanics and Mining Sciences – Vol. 42, pp. 950-960.

Øvstebø, K.A., 2009. *The effect of water chemistry and temperature on chalks mechanical strength by the use of equilibrium water and 0.109 M $MgCl_2$ at 130 °C.* Bachelor thesis, Department of Petroleum Engineering, Faculty of Science and Technology, University of Stavanger, Norway.

# Appendix A – Plots from tests using SSW–($SO_4^{2-}$)

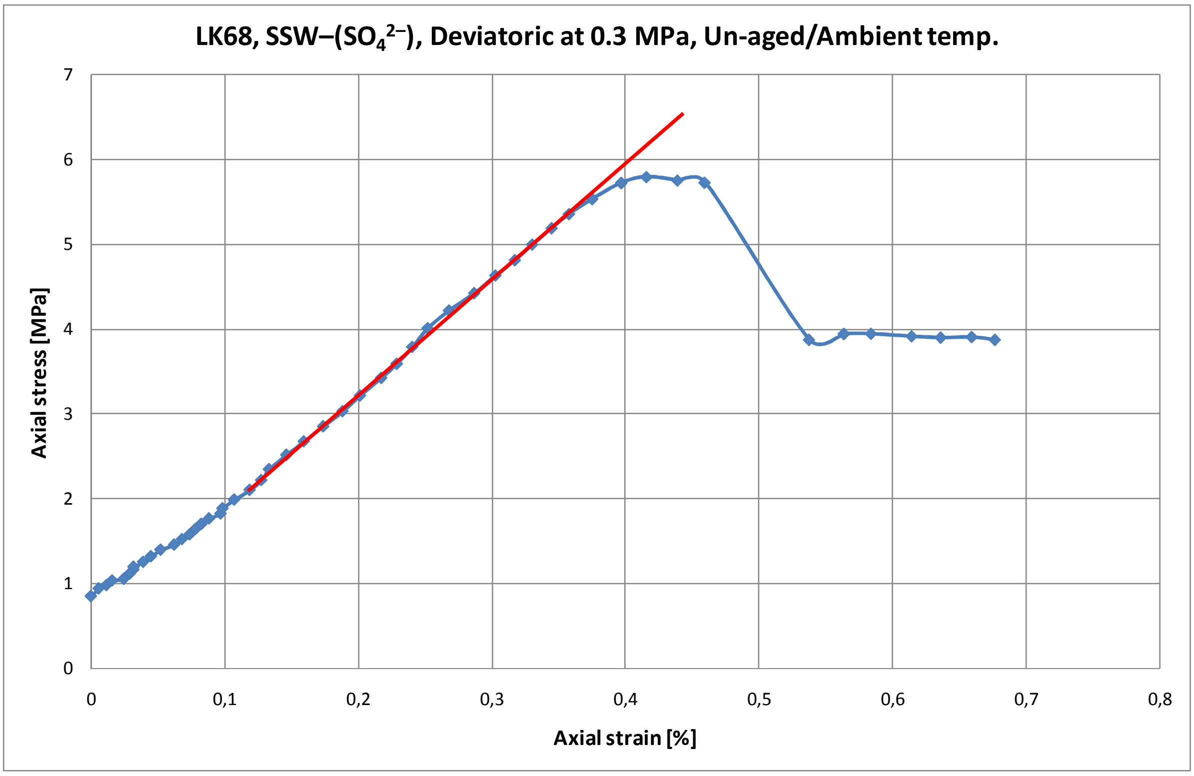

Figure A-1: *Axial stress versus axial strain plot for a 0.3 MPa deviatoric test performed on LK68 with SSW-($SO_4^{2-}$) flooding at ambient temperature*

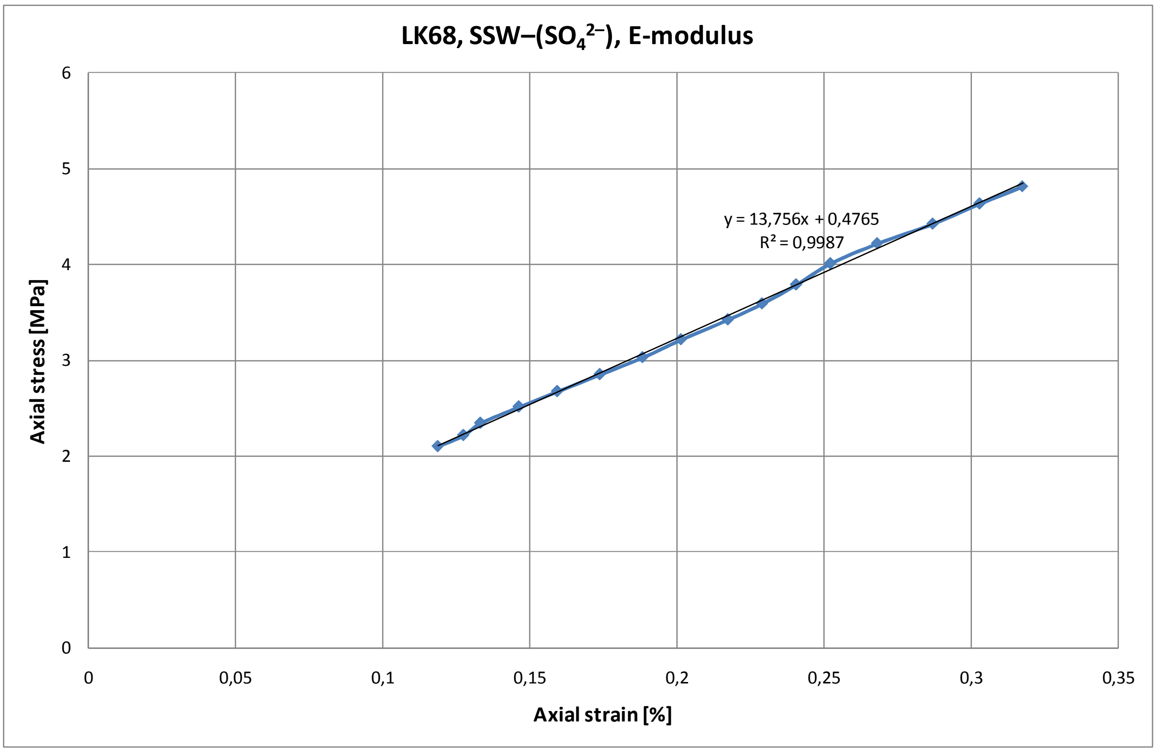

Figure A-2: *Section of the Axial stress versus axial strain plot for the 0.3 MPa deviatoric test performed on LK68 with SSW-($SO_4^{2-}$) flooding at ambient temperature used to estimate the Young's modulus*

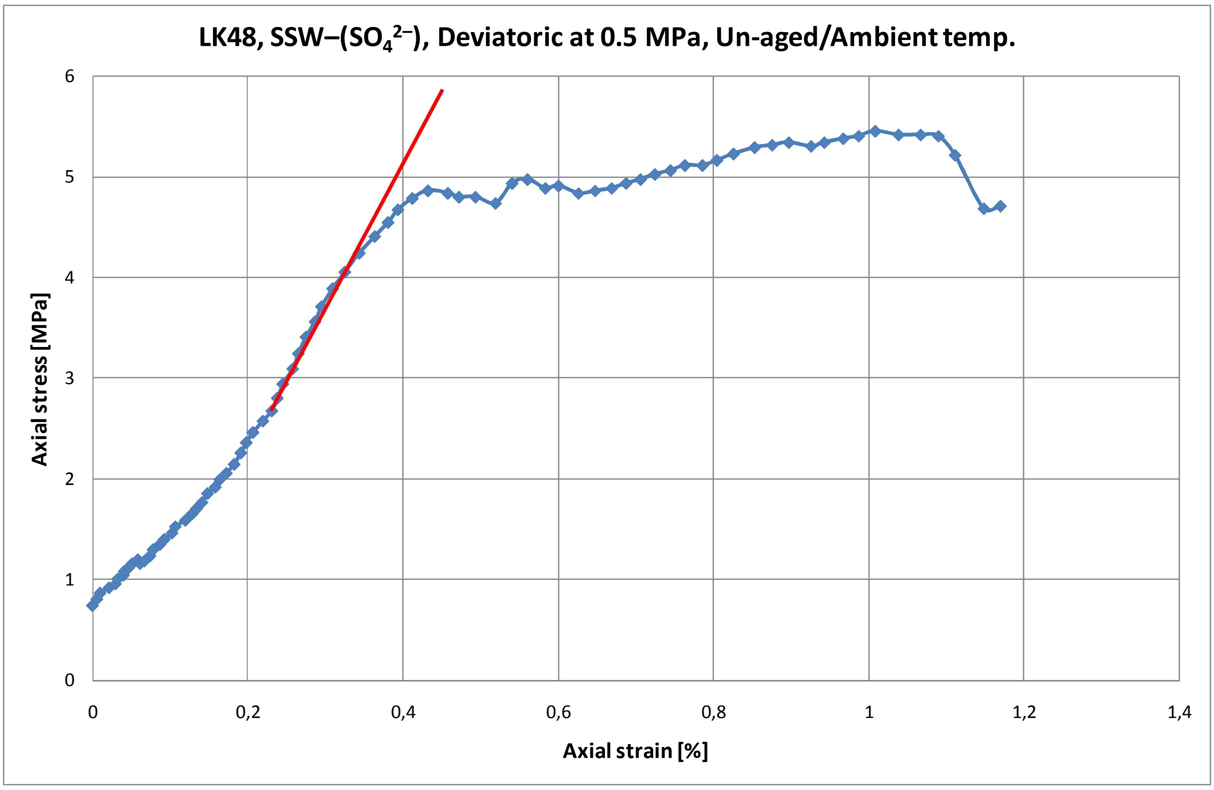

Figure A-3: *Axial stress versus axial strain plot for a 0.5 MPa deviatoric test performed on LK48 with SSW-($SO_4^{2-}$) flooding at ambient temperature*

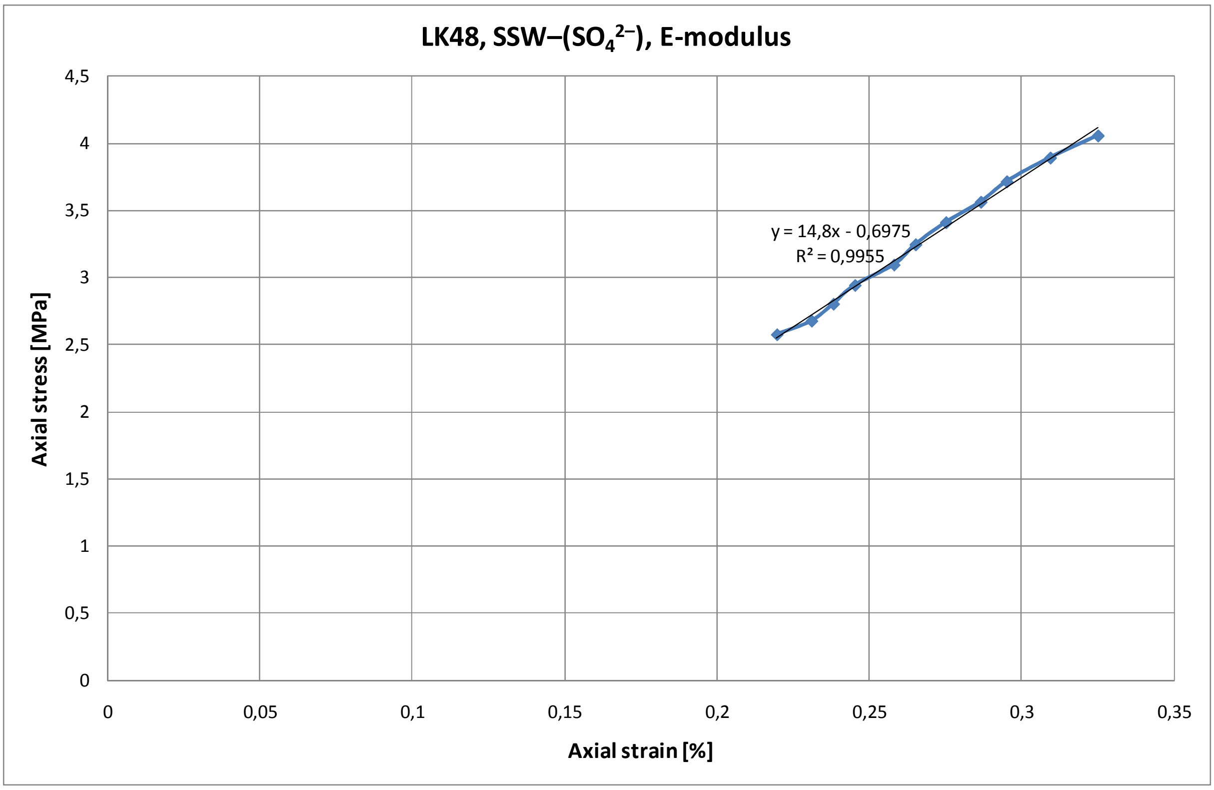

Figure A-4: *Section of the Axial stress versus axial strain plot for the 0.5 MPa deviatoric test performed on LK48 with SSW-($SO_4^{2-}$) flooding at ambient temperature used to estimate the Young's modulus*

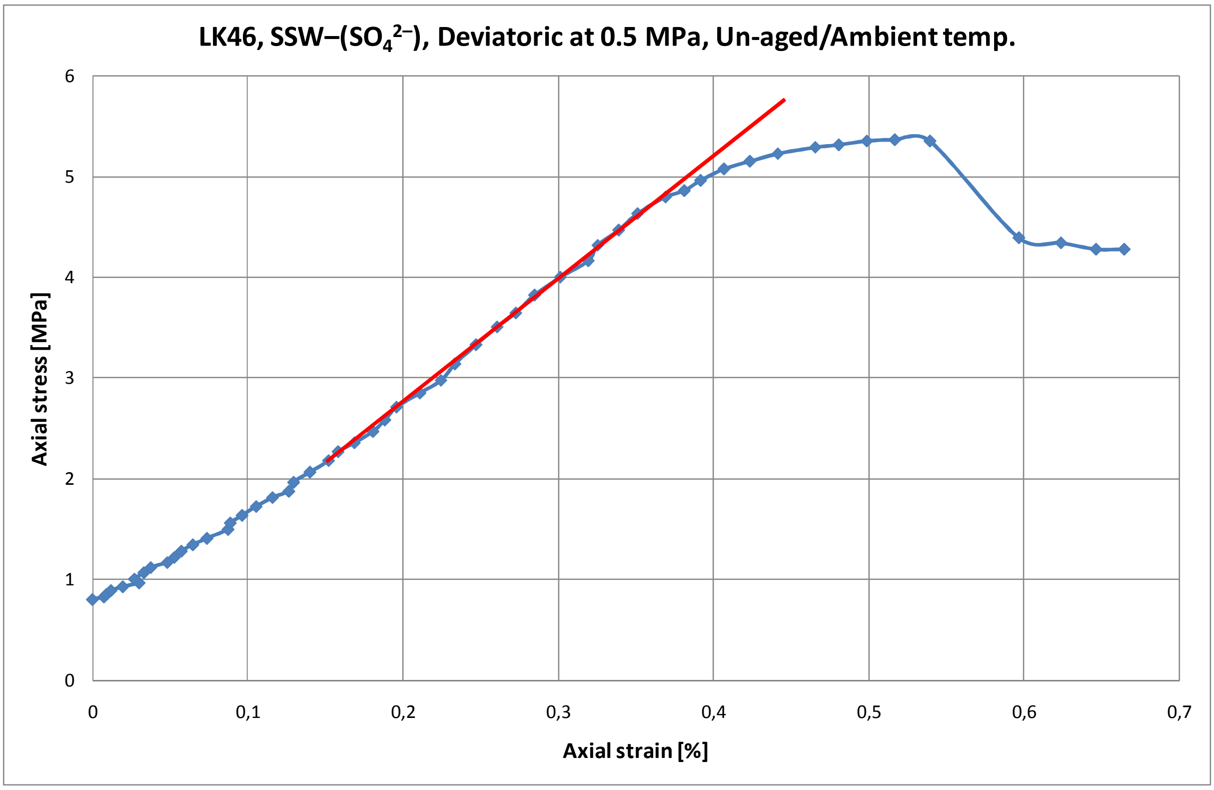

Figure A-5: *Axial stress versus axial strain plot for a 0.5 MPa deviatoric test performed on LK46 with SSW-($SO_4^{2-}$) flooding at ambient temperature*

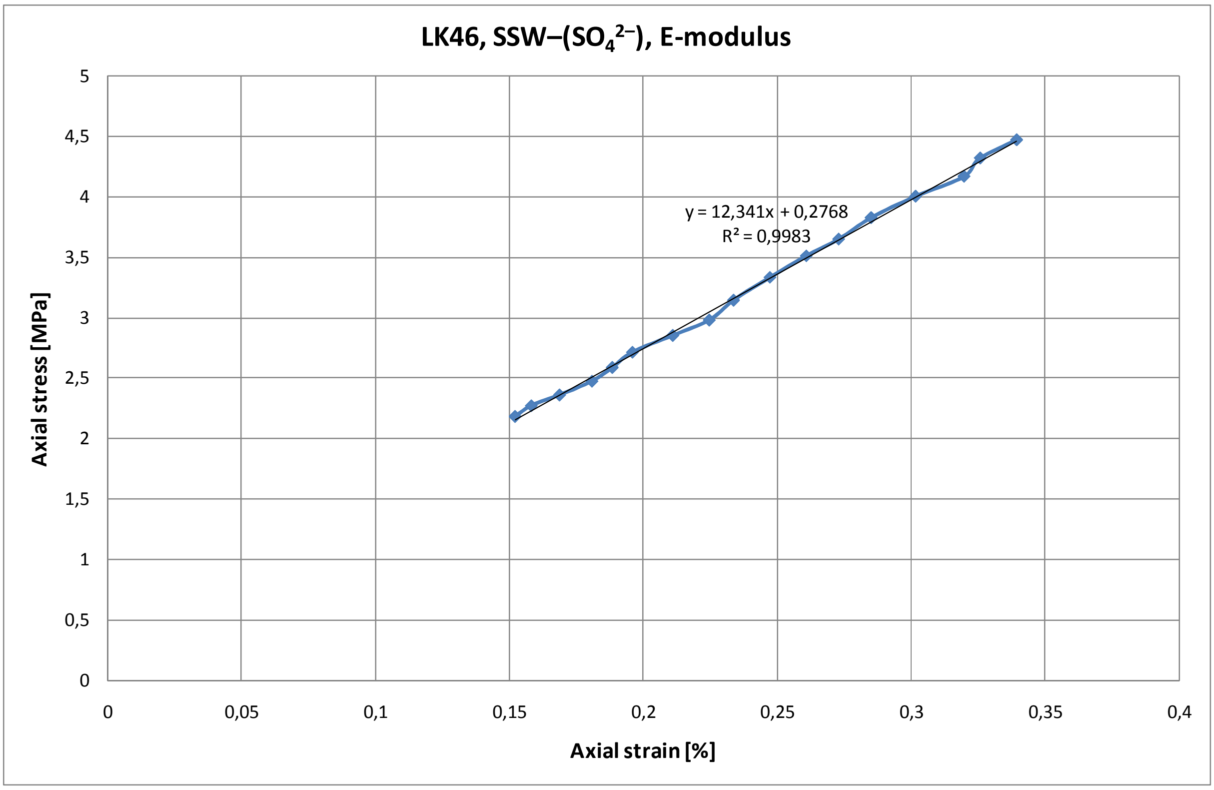

Figure A-6: *Section of the Axial stress versus axial strain plot for the 0.5 MPa deviatoric test performed on LK46 with SSW-($SO_4^{2-}$) flooding at ambient temperature used to estimate the Young's modulus*

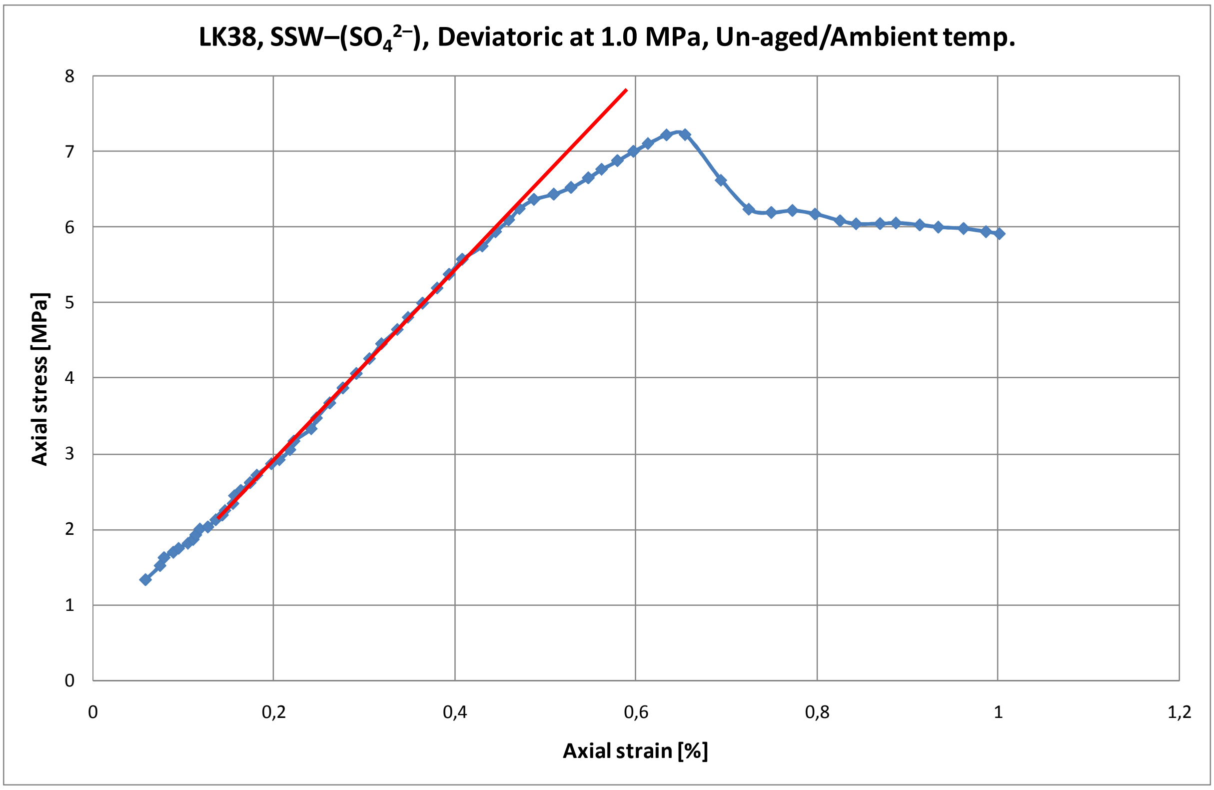

Figure A-7: *Axial stress versus axial strain plot for a 1.0 MPa deviatoric test performed on LK38 with SSW-($SO_4^{2-}$) flooding at ambient temperature*

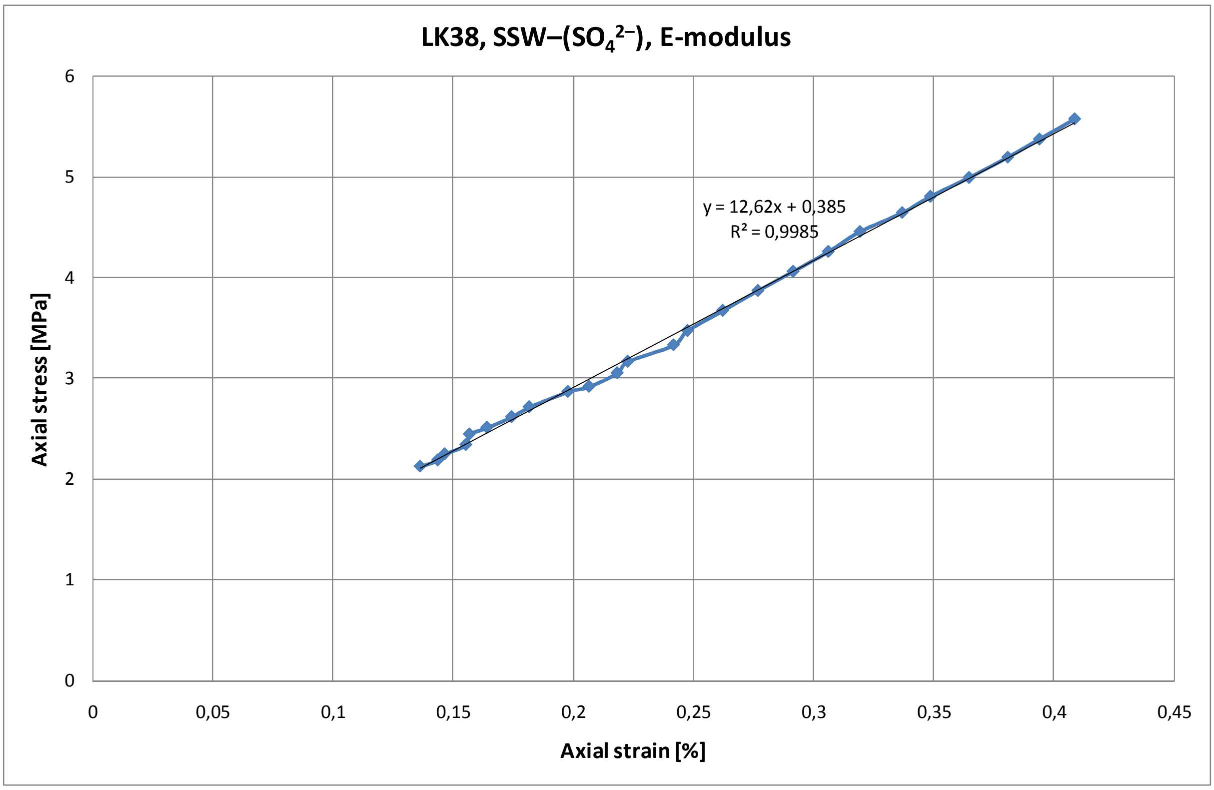

Figure A-8: *Section of the Axial stress versus axial strain plot for the 1.0 MPa deviatoric test performed on LK38 with SSW-($SO_4^{2-}$) flooding at ambient temperature used to estimate the Young's modulus*

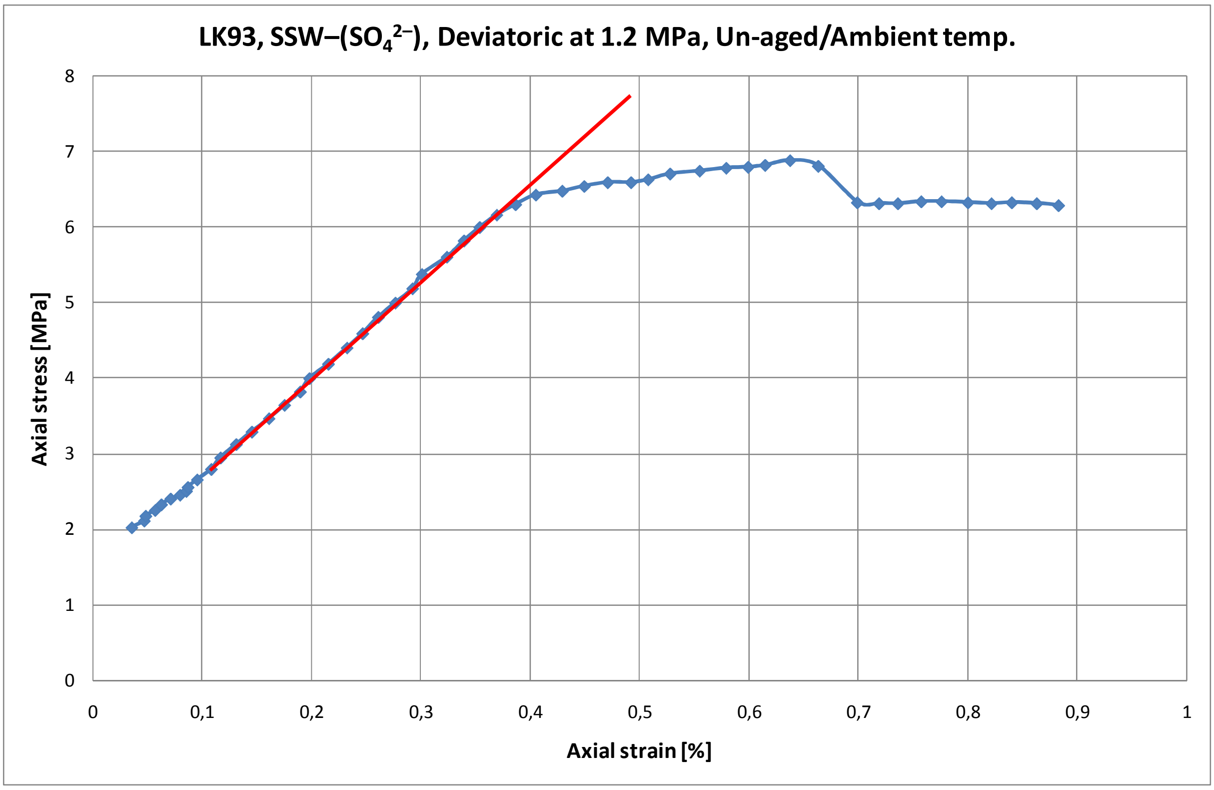

Figure A-9: *Axial stress versus axial strain plot for a 1.2 MPa deviatoric test performed on LK93 with SSW-($SO_4^{2-}$) flooding at ambient temperature*

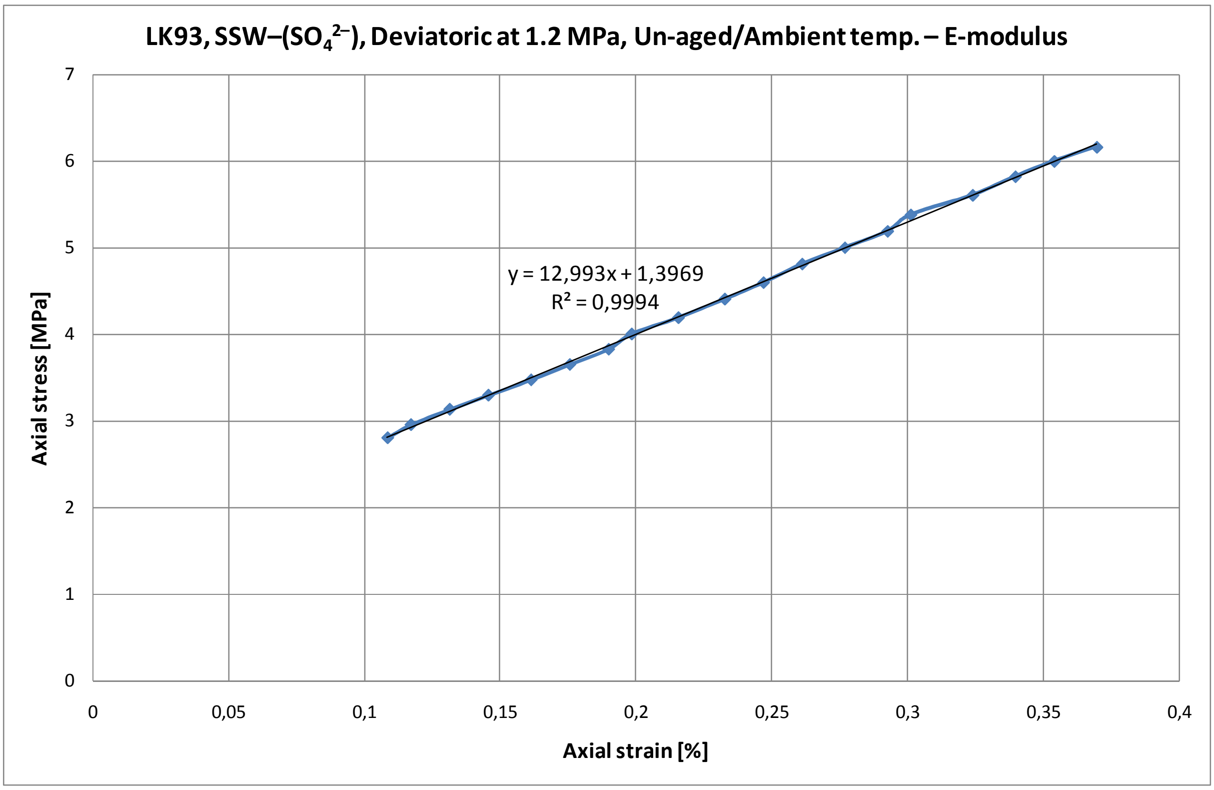

Figure A-10: *Section of the Axial stress versus axial strain plot for the 1.2 MPa deviatoric test performed on LK93 with SSW-($SO_4^{2-}$) flooding at ambient temperature used to estimate the Young's modulus*

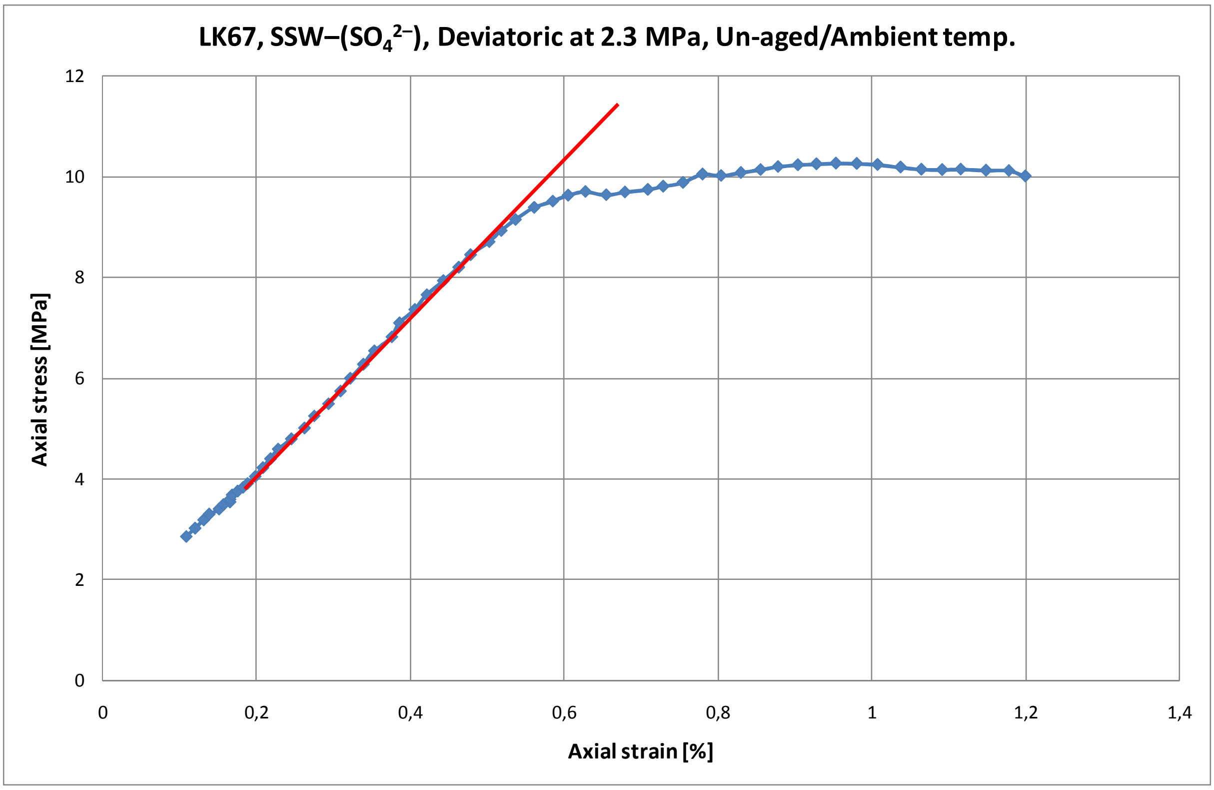

Figure A-11: *Axial stress versus axial strain plot for a 2.3 MPa deviatoric test performed on LK67 with SSW-($SO_4^{2-}$) flooding at ambient temperature*

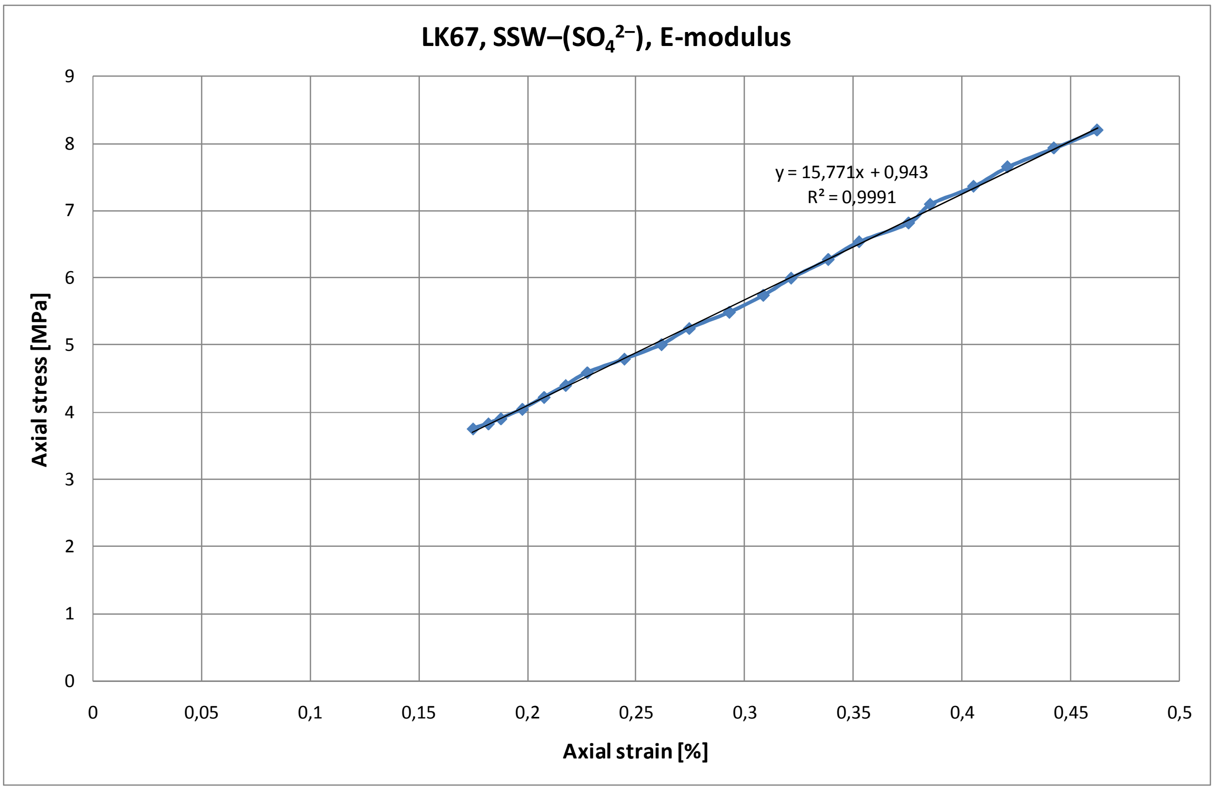

Figure A-12: *Section of the Axial stress versus axial strain plot for the 2.3 MPa deviatoric test performed on LK67 with SSW-($SO_4^{2-}$) flooding at ambient temperature used to estimate the Young's modulus*

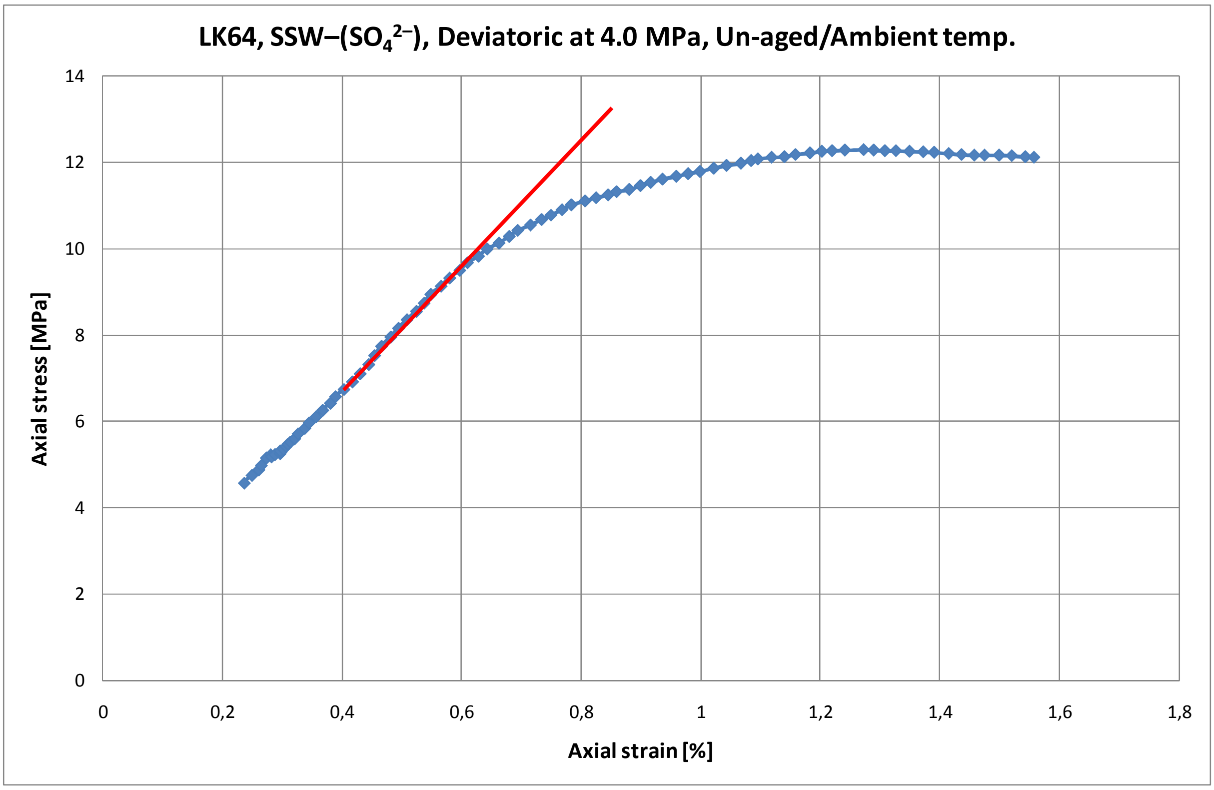

Figure A-13: *Axial stress versus axial strain plot for a 4.0 MPa deviatoric test performed on LK64 with SSW-($SO_4^{2-}$) flooding at ambient temperature*

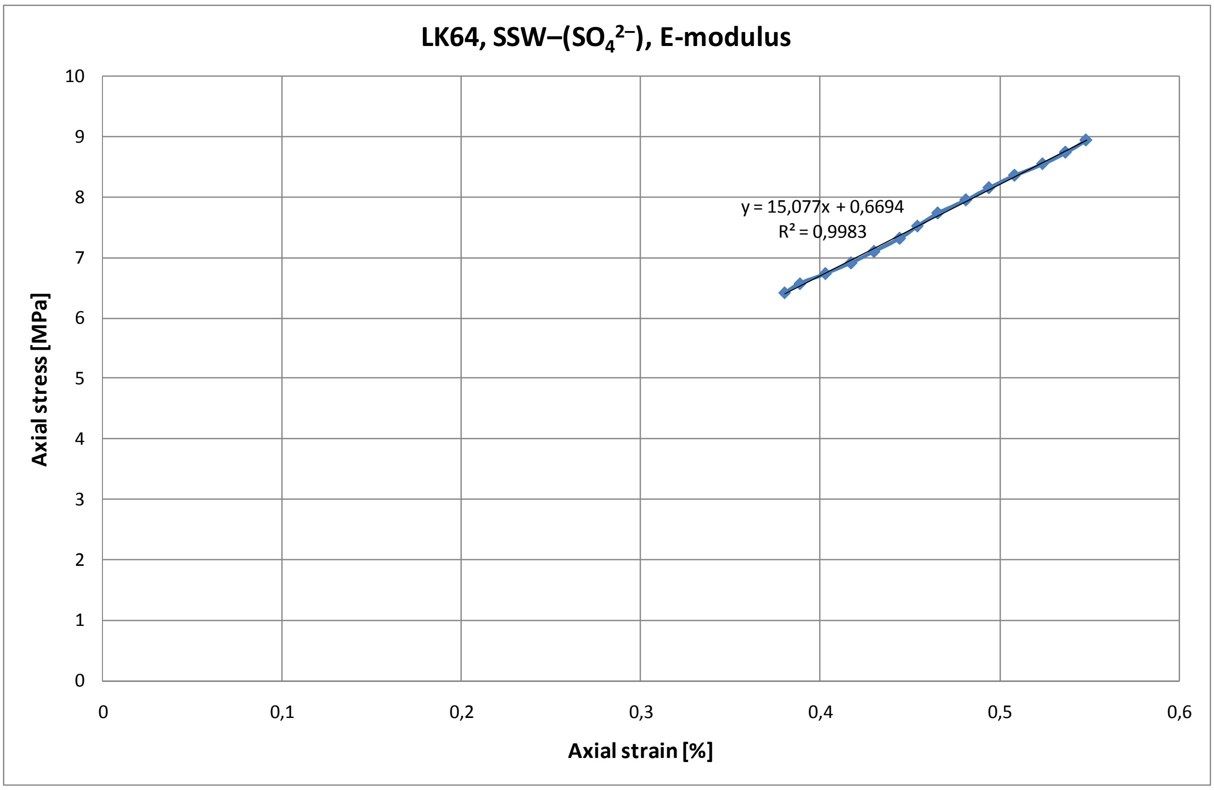

Figure A-14: *Section of the Axial stress versus axial strain plot for the 4.0 MPa deviatoric test performed on LK64 with SSW-($SO_4^{2-}$) flooding at ambient temperature used to estimate the Young's modulus*

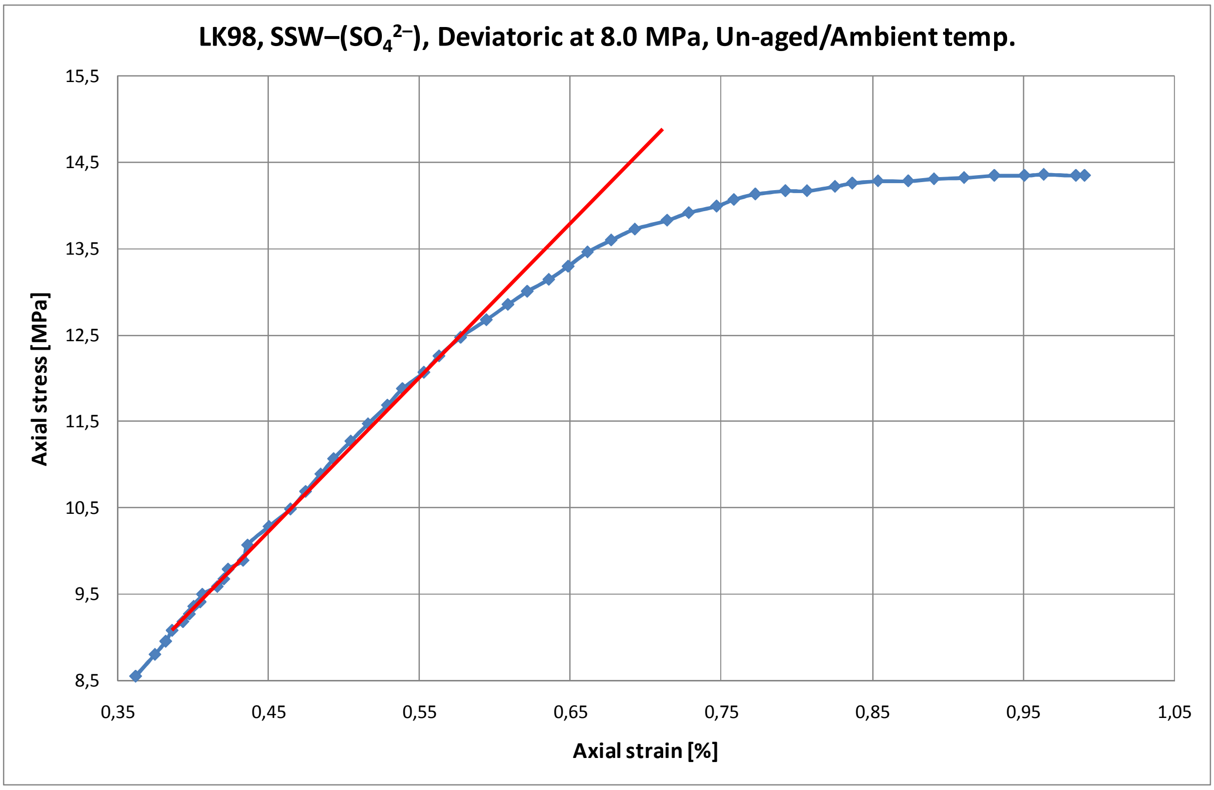

Figure A-15: *Axial stress versus axial strain plot for a 8.0 MPa deviatoric test performed on LK98 with SSW-($SO_4^{2-}$) flooding at ambient temperature*

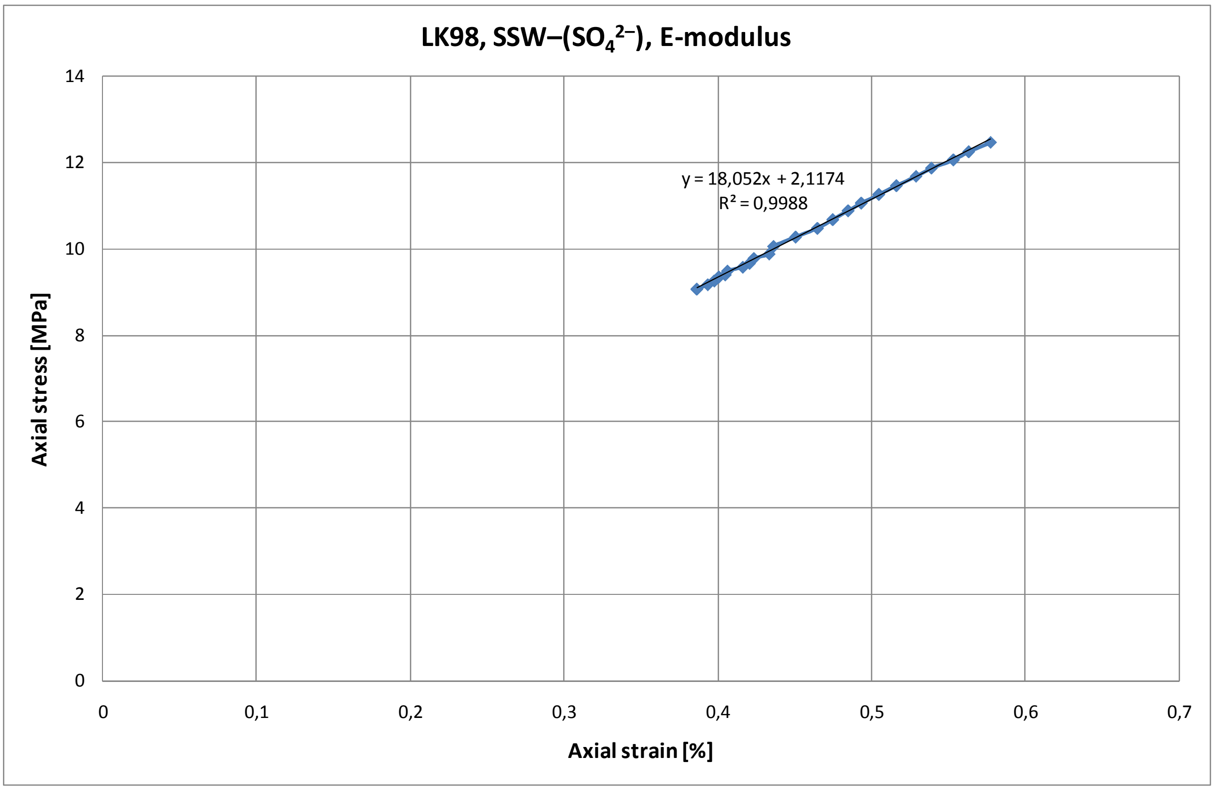

Figure A-16: *Section of the Axial stress versus axial strain plot for the 8.0 MPa deviatoric test performed on LK98 with SSW-($SO_4^{2-}$) flooding at ambient temperature used to estimate the Young's modulus*

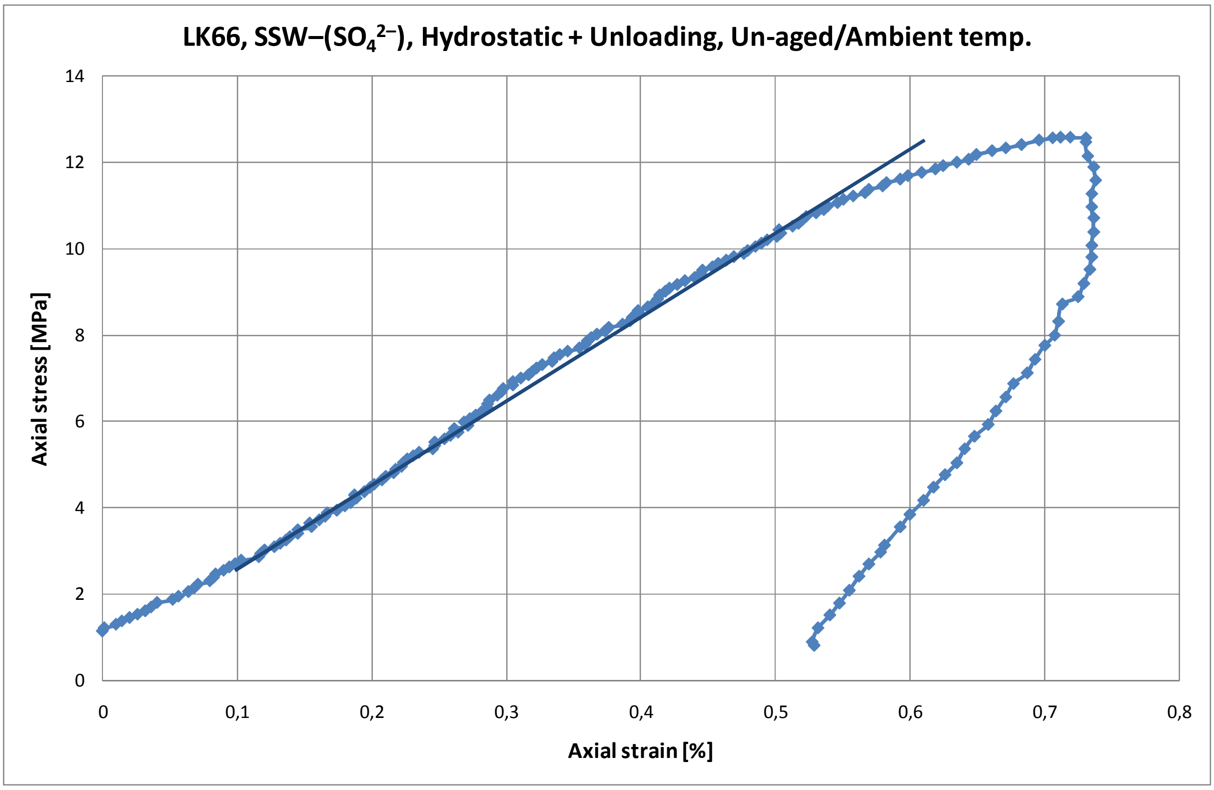

Figure A-17: *Axial stress versus axial strain plot for a hydrostatic test performed on LK66 with SSW-($SO_4^{2-}$) flooding at ambient temperature*

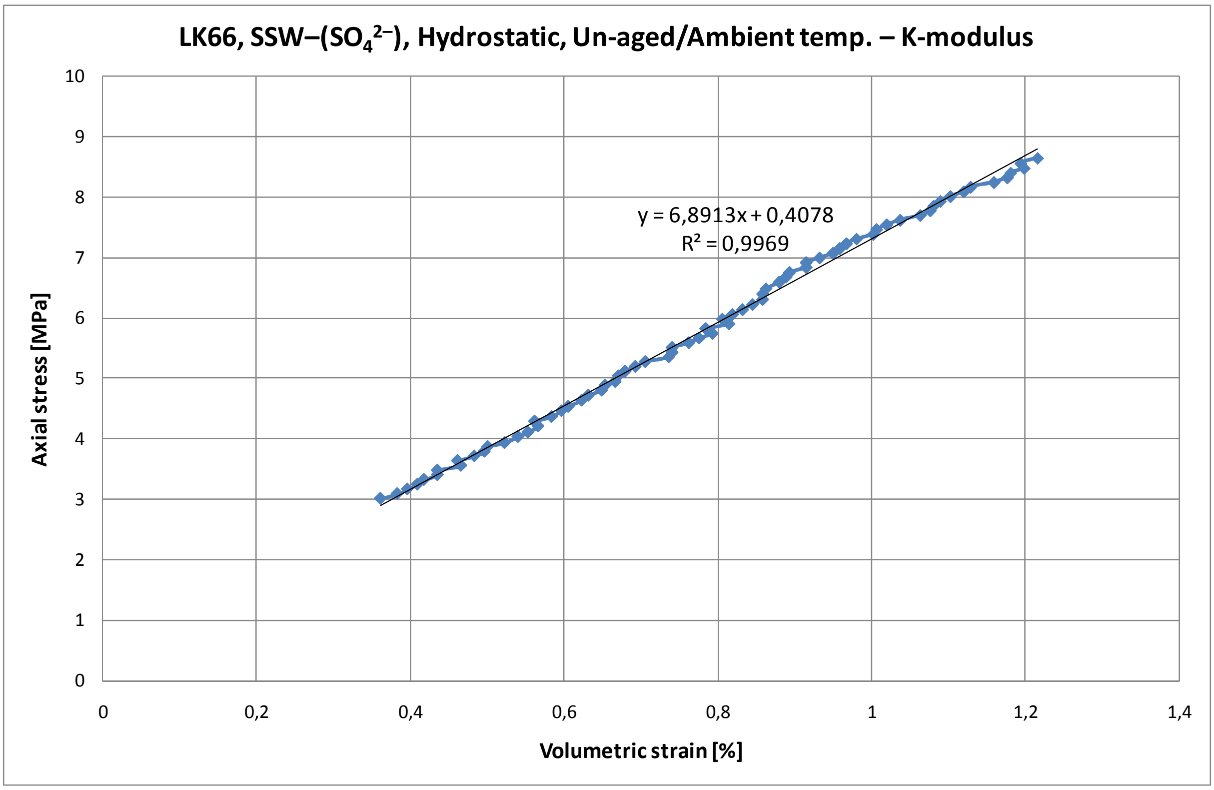

Figure A-18: *Section of the Axial stress versus Volumetric strain plot the hydrostatic test performed on LK66 with SSW-($SO_4^{2-}$) flooding at ambient temperature used to estimate the Bulk modulus.*

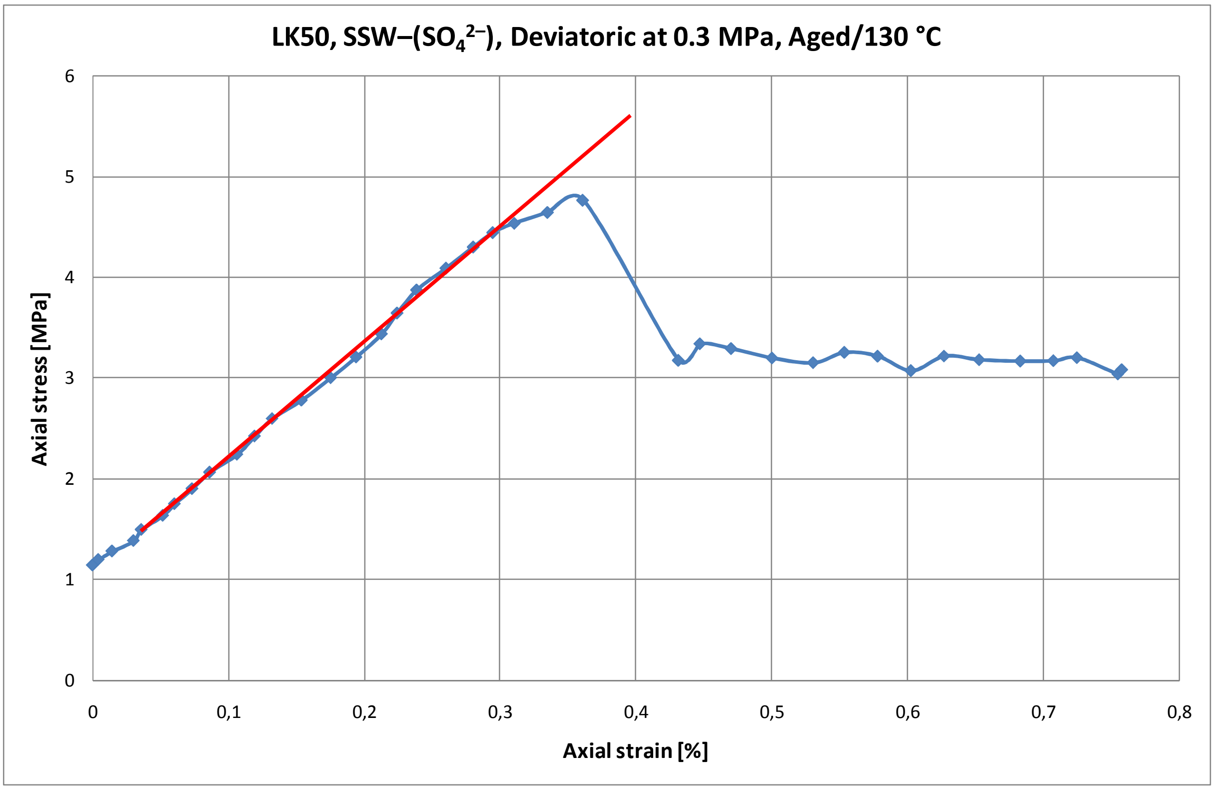

Figure A-19: *Axial stress versus axial strain plot for a 0.3 MPa deviatoric test performed on LK50 with SSW-($SO_4^{2-}$) flooding at 130 °C*

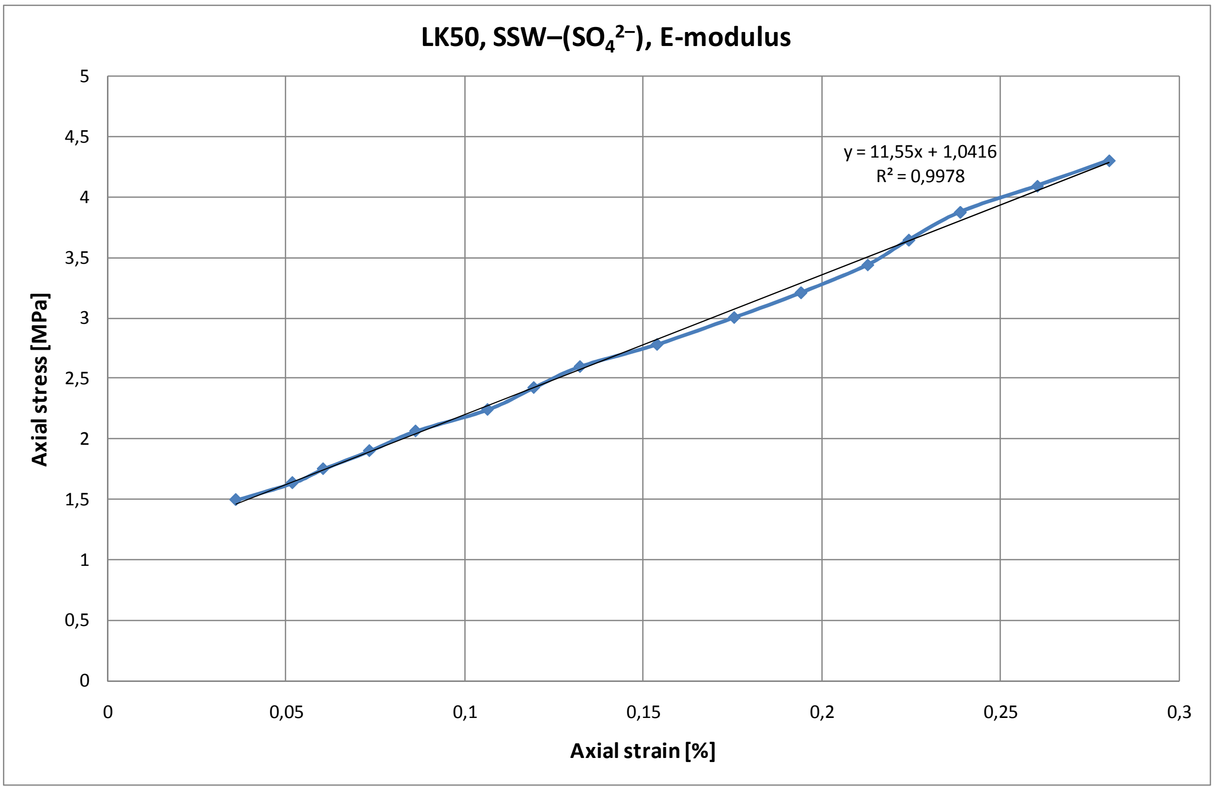

Figure A-20: *Section of the Axial stress versus axial strain plot for the 0.3 MPa deviatoric test performed on LK50 with SSW-($SO_4^{2-}$) flooding at 130 °C used to estimate the Young's modulus*

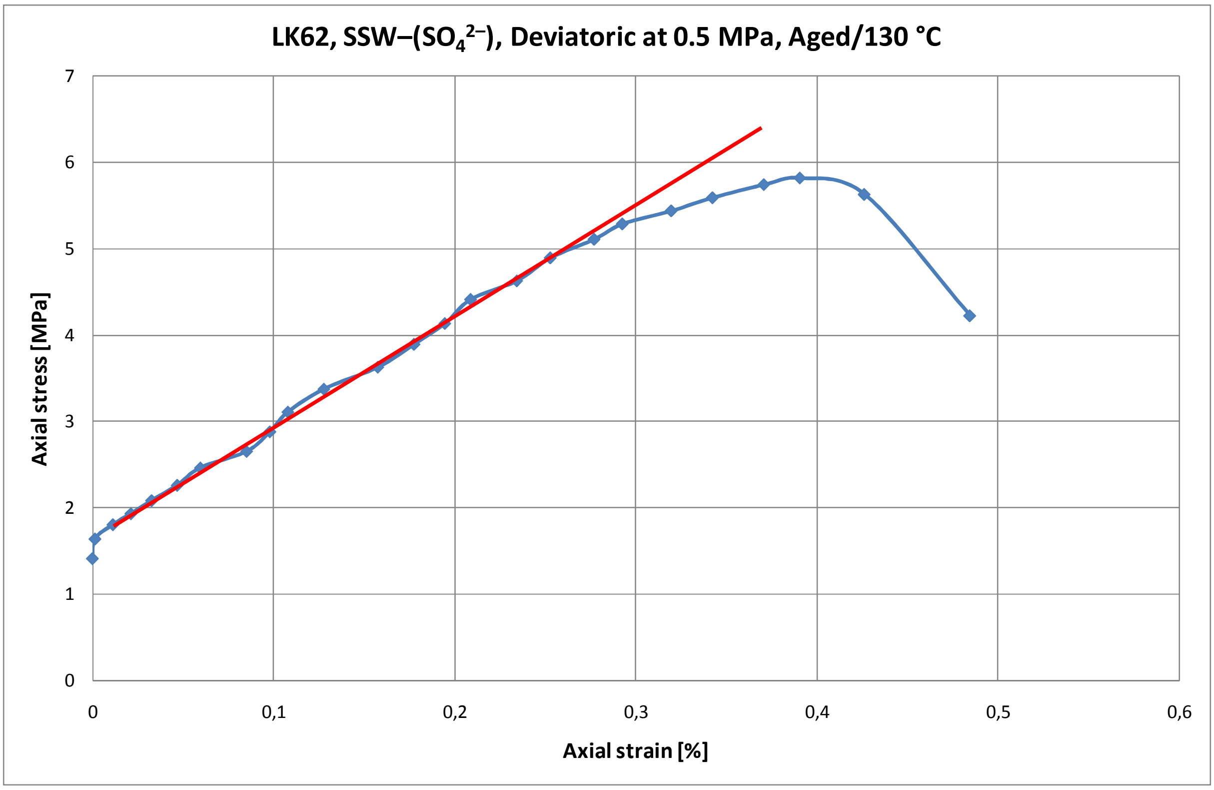

Figure A-21: *Axial stress versus axial strain plot for a 0.5 MPa deviatoric test performed on LK62 with SSW-($SO_4^{2-}$) flooding at 130 °C*

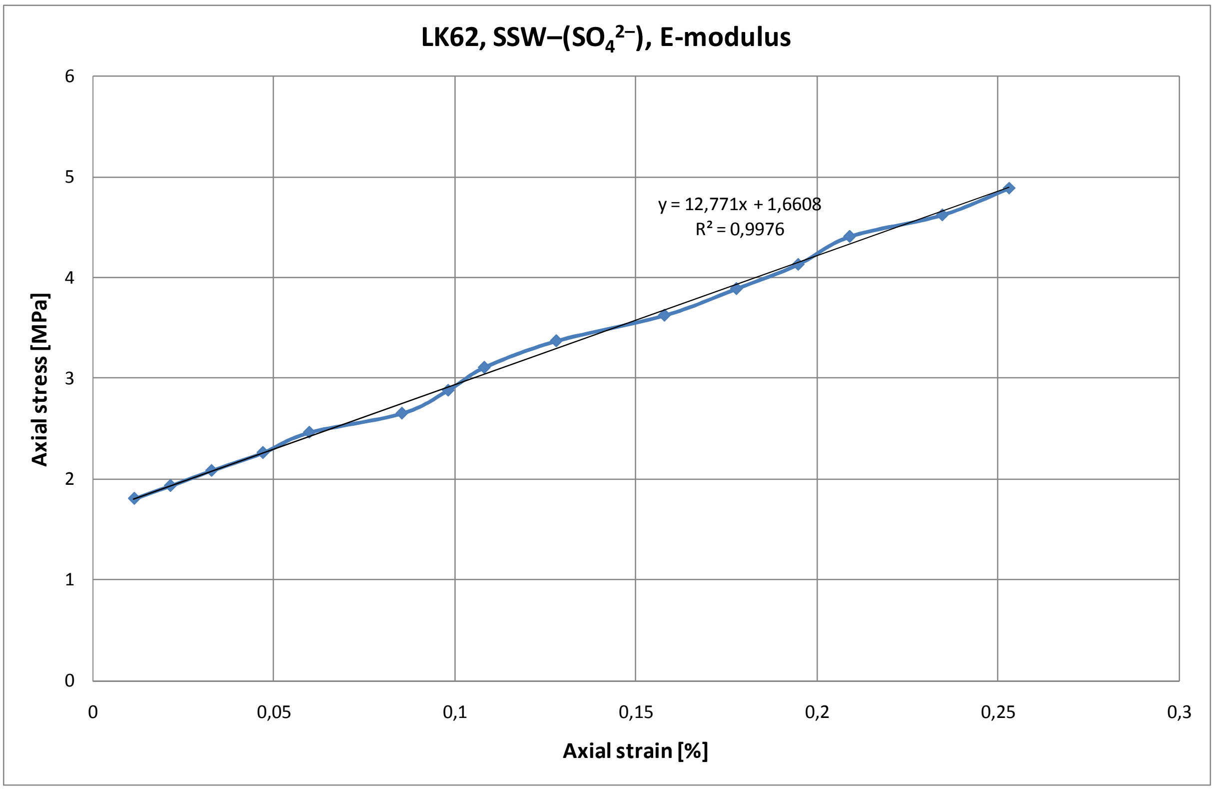

Figure A-22: *Section of the Axial stress versus axial strain plot for the 0.5 MPa deviatoric test performed on LK62 with SSW-($SO_4^{2-}$) flooding at 130 °C used to estimate the Young's modulus*

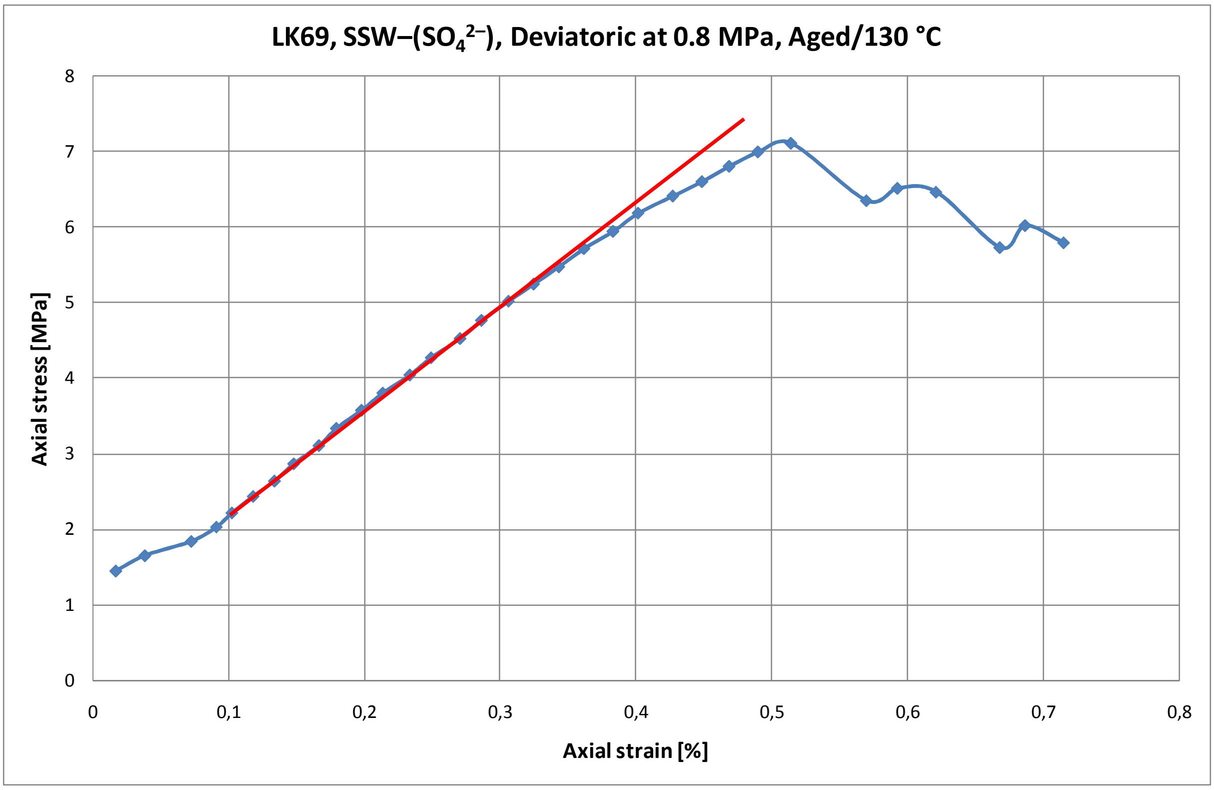

Figure A-23: *Axial stress versus axial strain plot for a 0.8 MPa deviatoric test performed on LK69 with SSW-($SO_4^{2-}$) flooding at 130 °C*

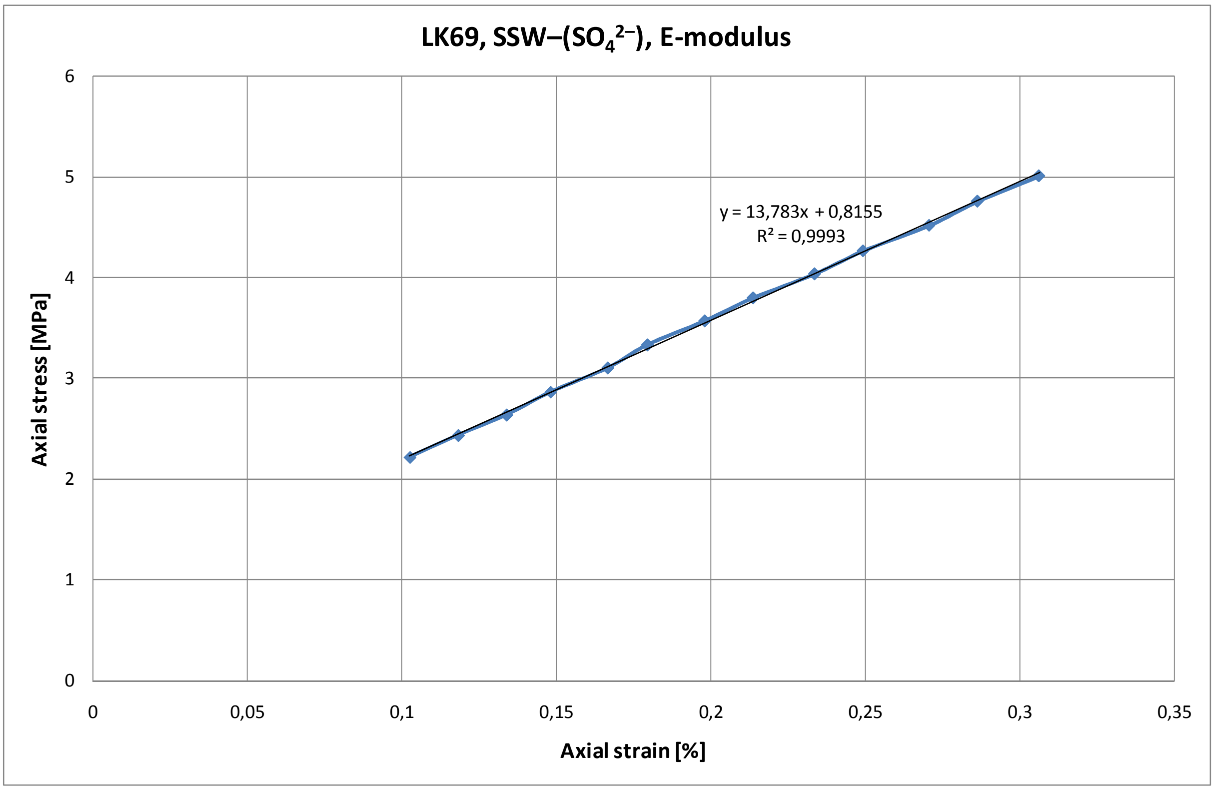

Figure A-24: *Section of the Axial stress versus axial strain plot for the 0.8 MPa deviatoric test performed on LK69 with SSW-($SO_4^{2-}$) flooding at 130 °C used to estimate the Young's modulus*

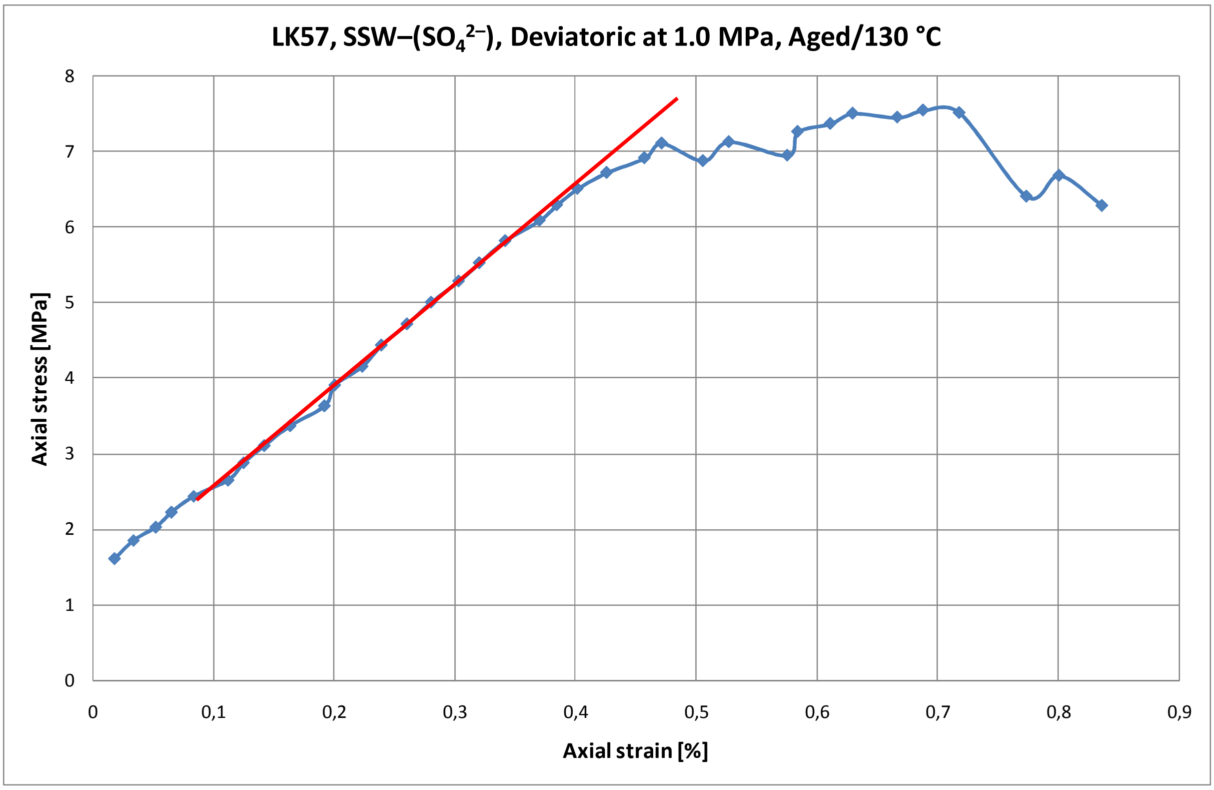

Figure A-25: *Axial stress versus axial strain plot for a 1.0 MPa deviatoric test performed on LK57 with SSW-($SO_4^{2-}$) flooding at 130 °C*

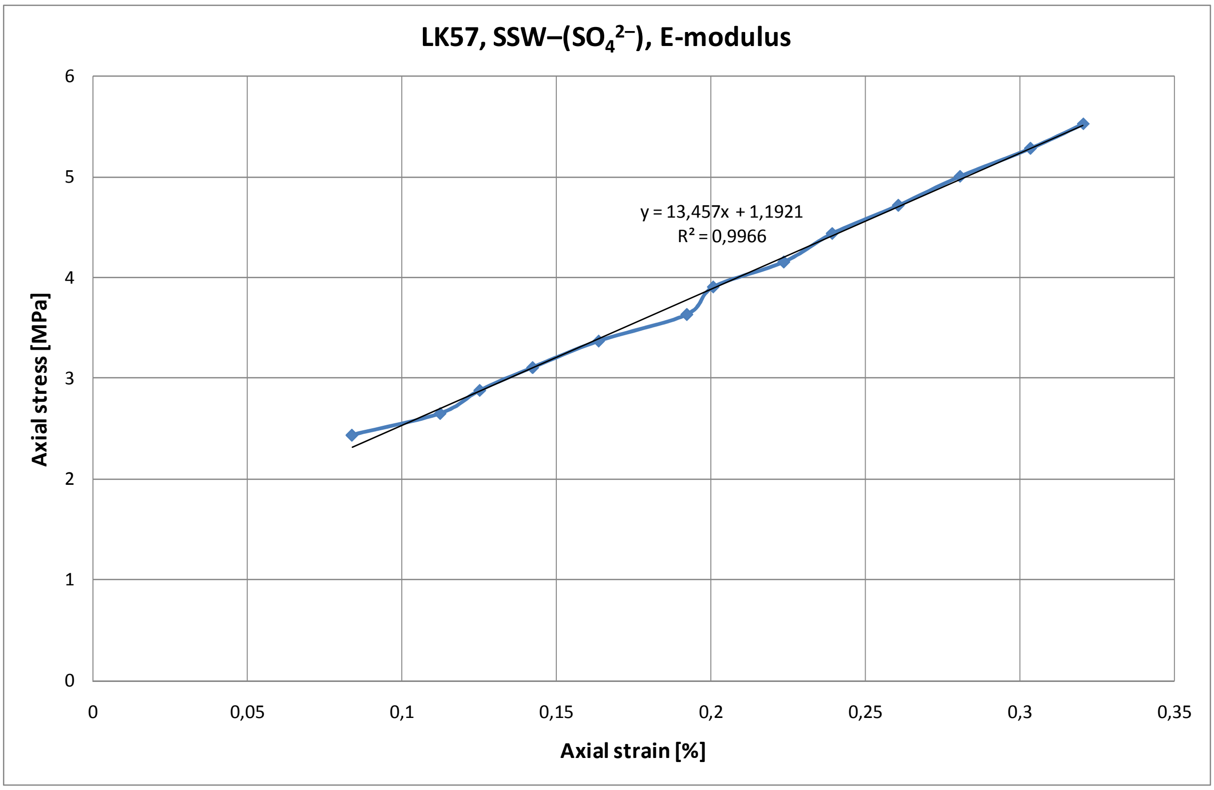

Figure A-26: *Section of the Axial stress versus axial strain plot for the 1.0 MPa deviatoric test performed on LK57 with SSW-($SO_4^{2-}$) flooding at 130 °C used to estimate the Young's modulus*

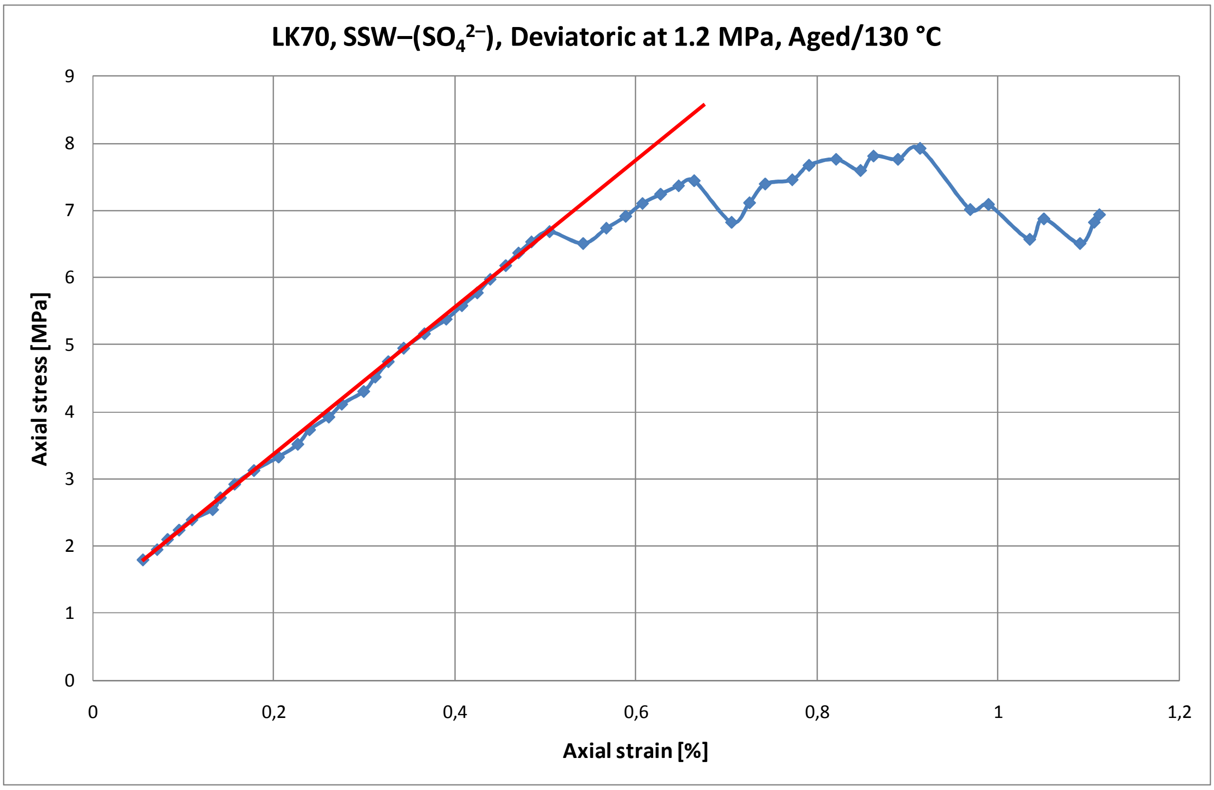

Figure A-27: *Axial stress versus axial strain plot for a 1.2 MPa deviatoric test performed on LK70 with SSW-($SO_4^{2-}$) flooding at 130 °C*

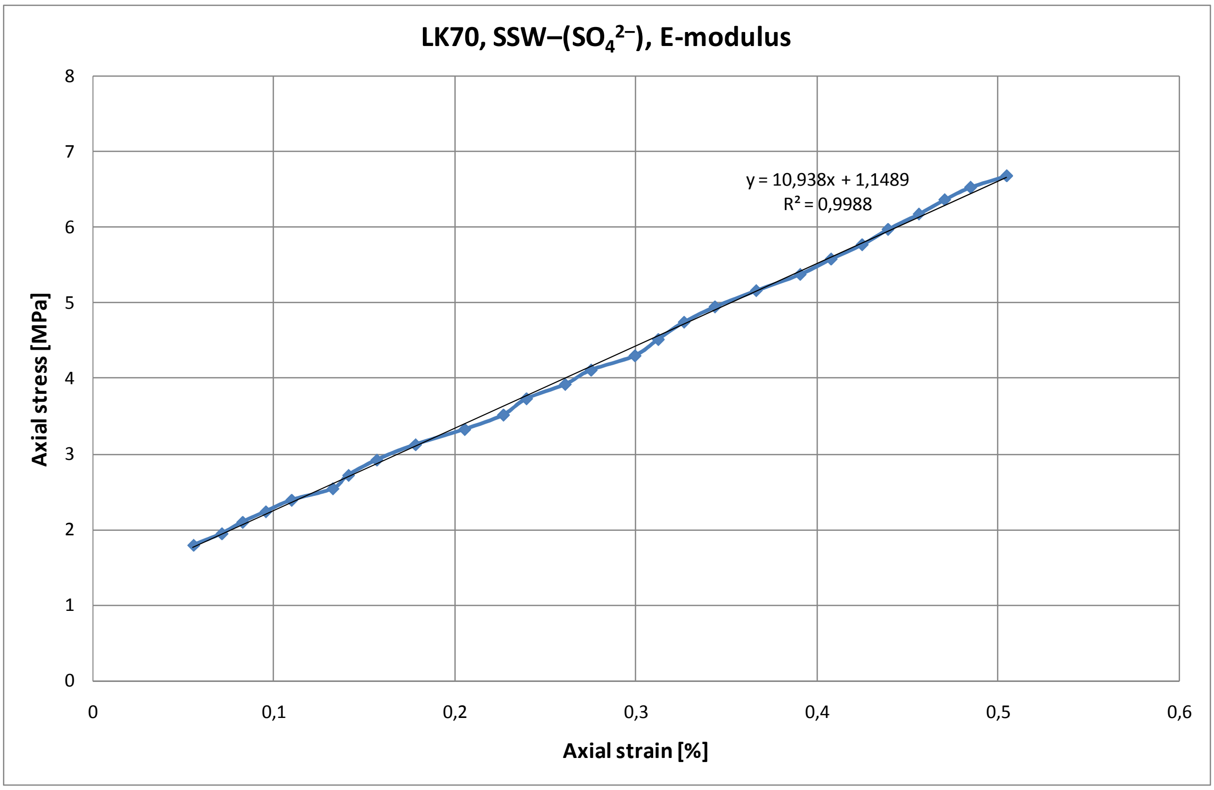

Figure A-28: *Section of the Axial stress versus axial strain plot for the 1.2 MPa deviatoric test performed on LK57 with SSW-($SO_4^{2-}$) flooding at 130 °C used to estimate the Young's modulus*

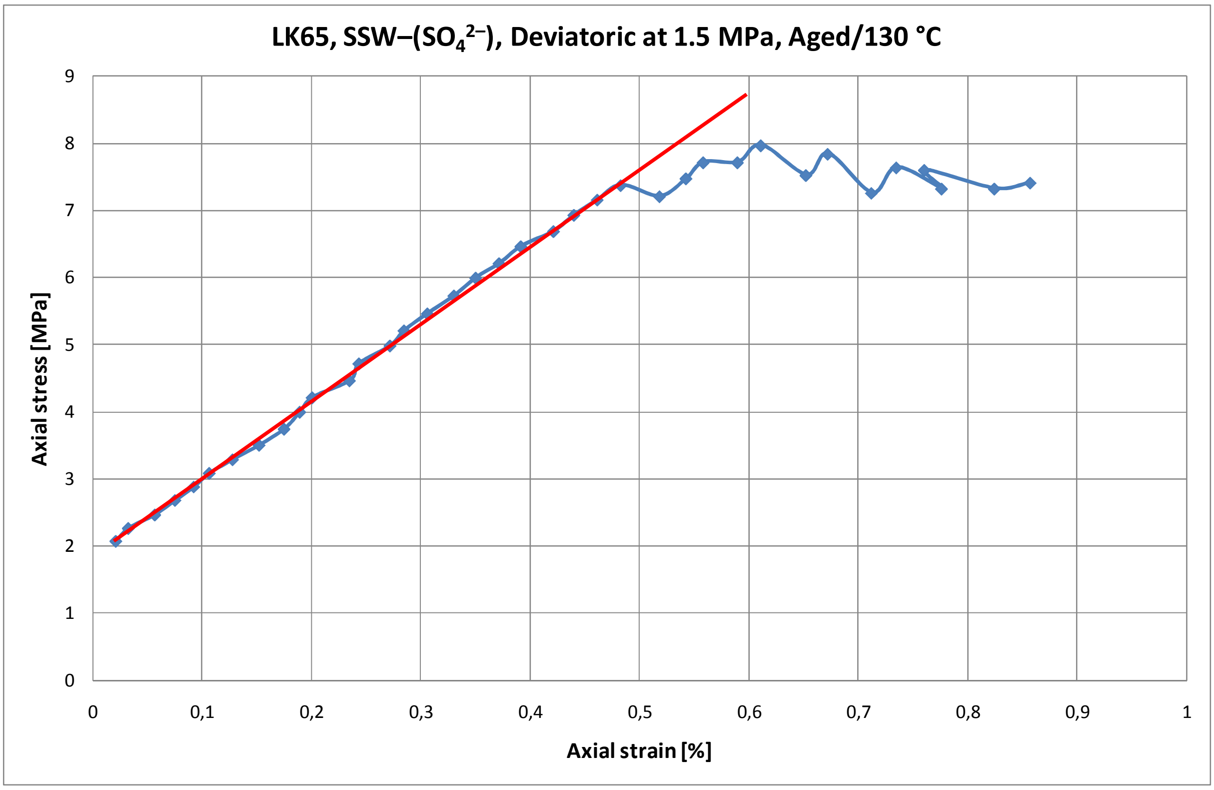

Figure A-29: *Axial stress versus axial strain plot for a 1.5 MPa deviatoric test performed on LK65 with SSW-($SO_4^{2-}$) flooding at 130 °C*

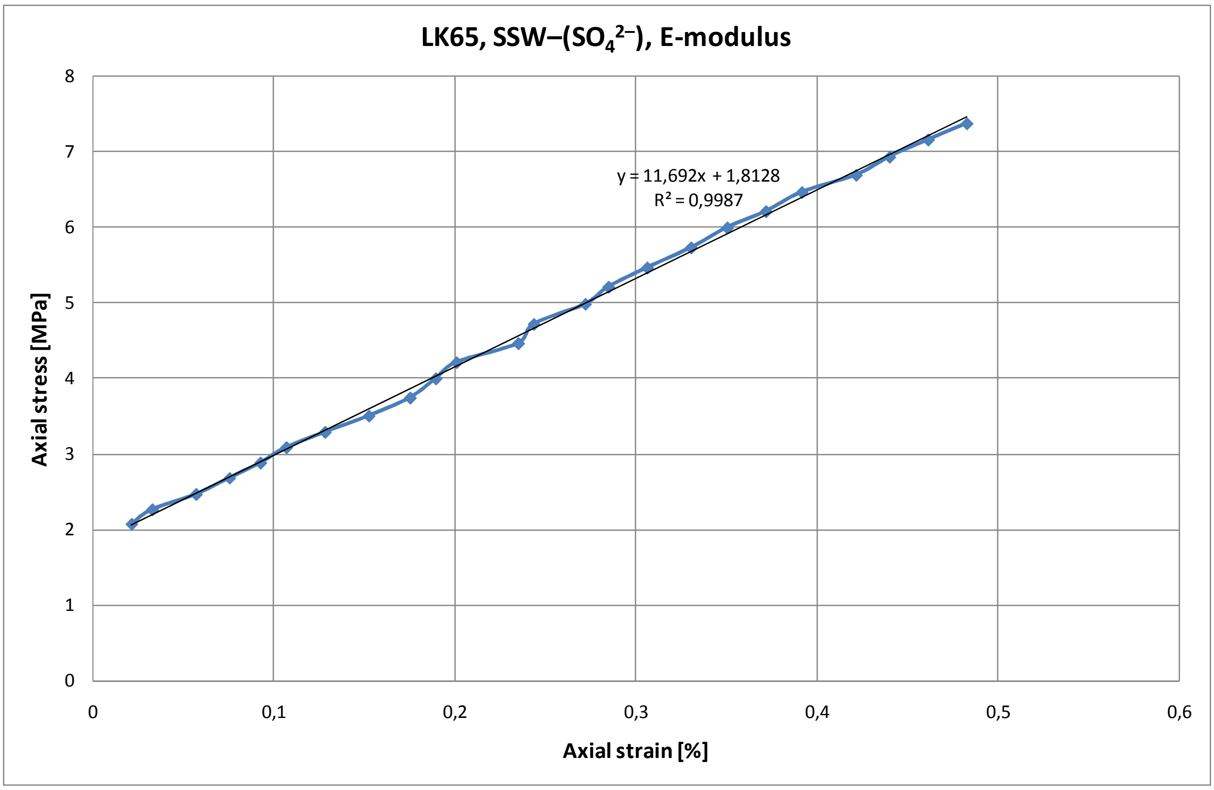

Figure A-30: *Section of the Axial stress versus axial strain plot for the 1.5 MPa deviatoric test performed on LK65 with SSW-($SO_4^{2-}$) flooding at 130 °C used to estimate the Young's modulus*

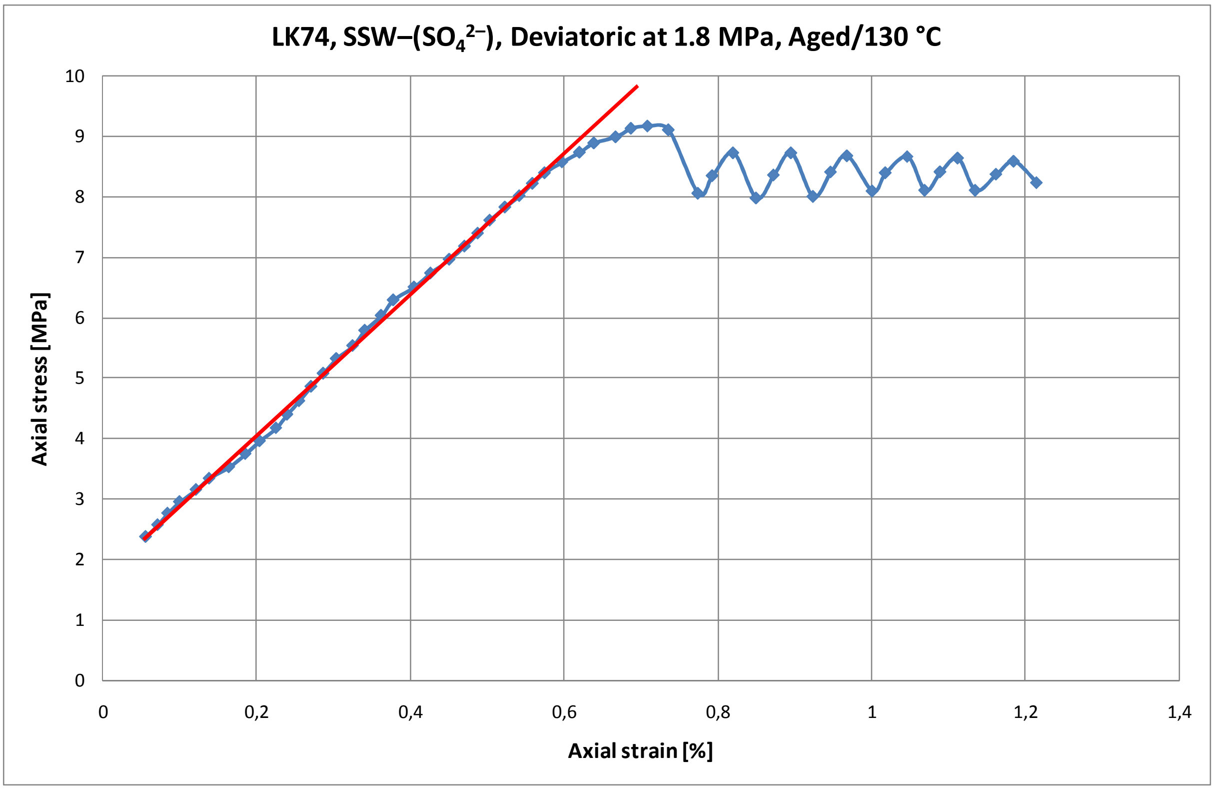

Figure A-31: *Axial stress versus axial strain plot for a 1.8 MPa deviatoric test performed on LK74 with SSW-($SO_4^{2-}$) flooding at 130 °C*

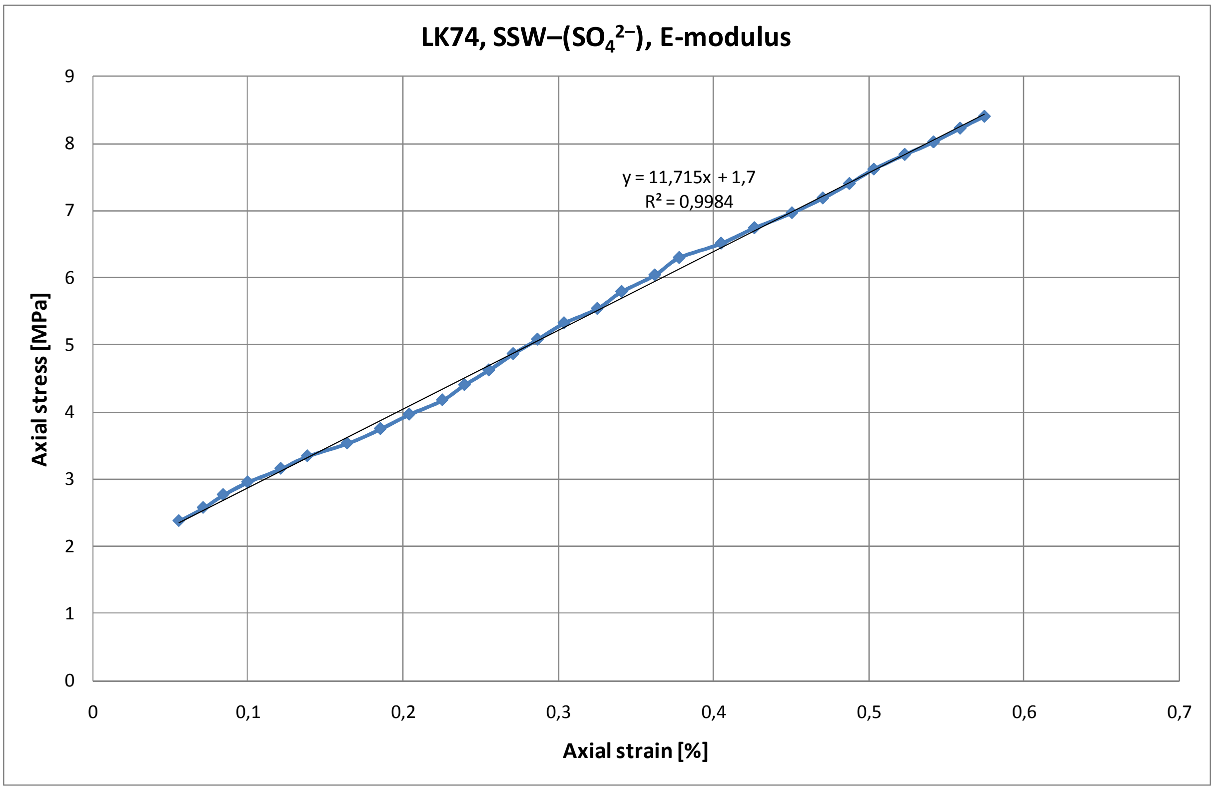

Figure A-32: *Section of the Axial stress versus axial strain plot for the 1.8 MPa deviatoric test performed on LK74 with SSW-($SO_4^{2-}$) flooding at 130 °C used to estimate the Young's modulus*

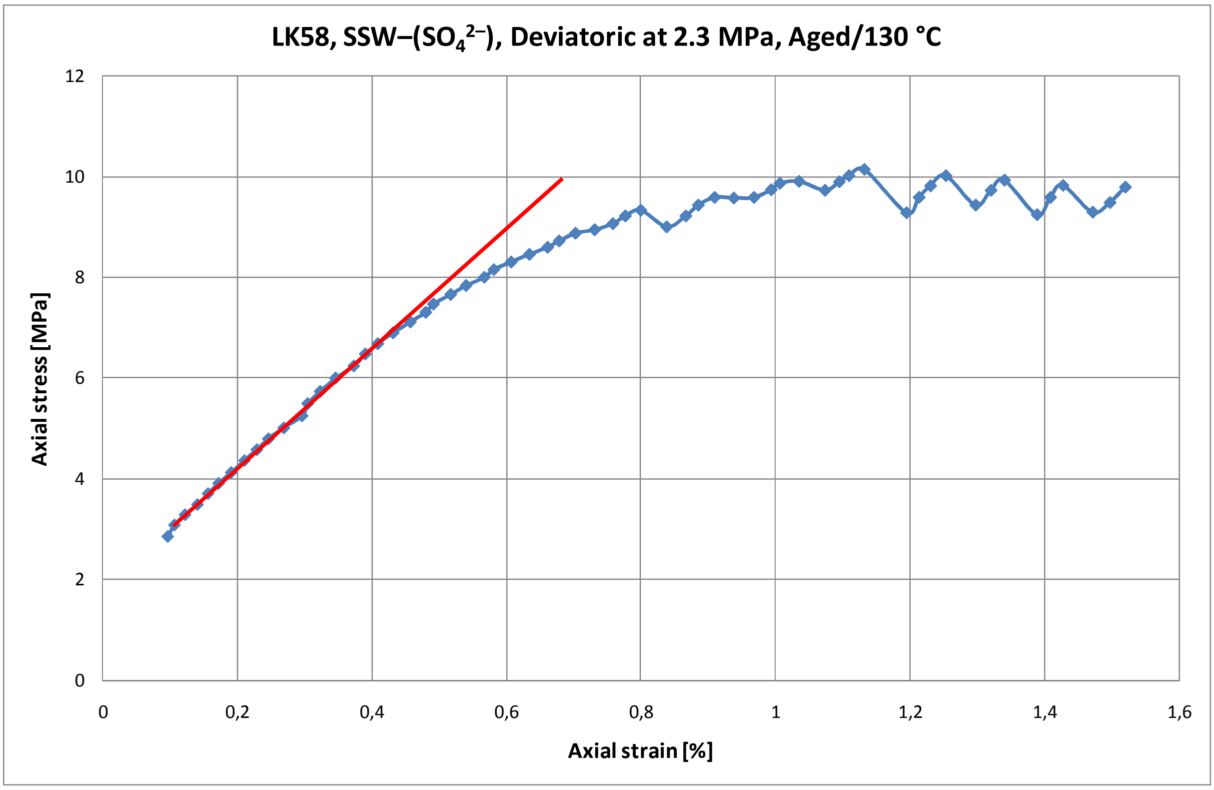

Figure A-33: *Axial stress versus axial strain plot for a 2.3 MPa deviatoric test performed on LK58 with SSW-($SO_4^{2-}$) flooding at 130 °C*

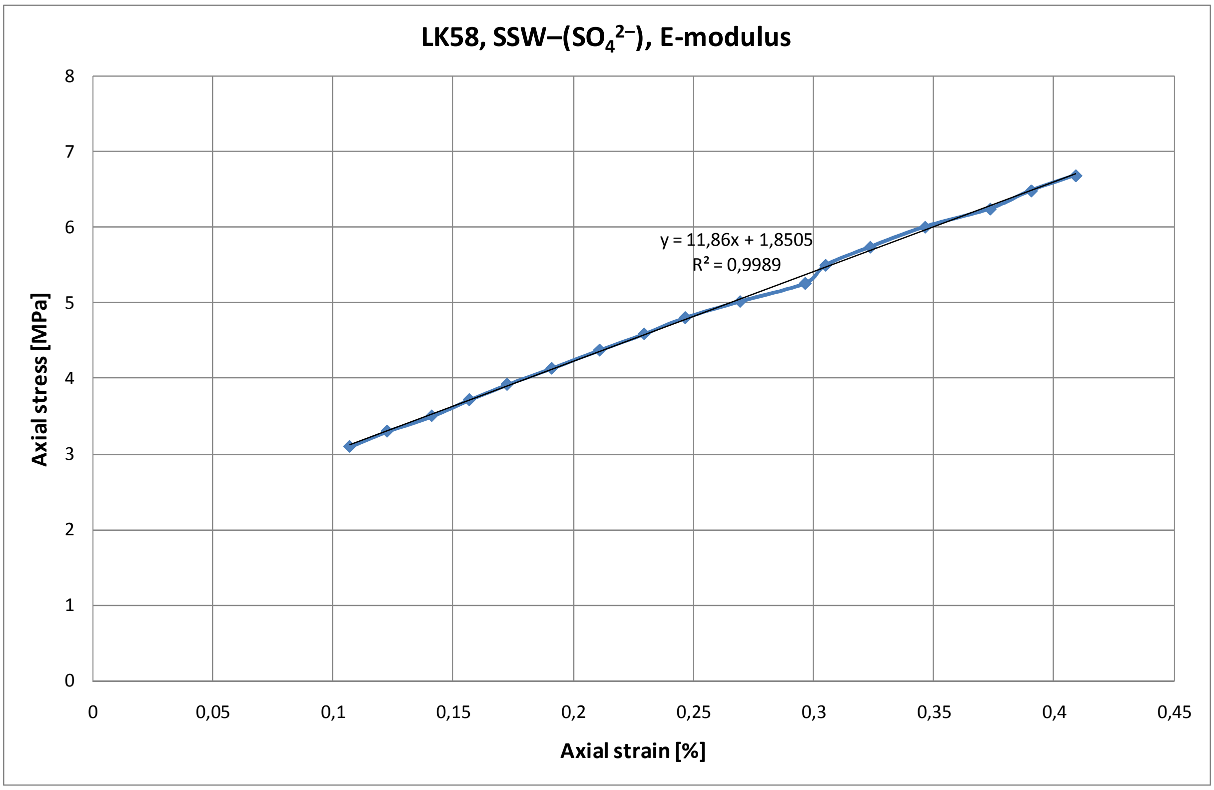

Figure A-34: *Section of the Axial stress versus axial strain plot for the 2.3 MPa deviatoric test performed on LK58 with SSW-($SO_4^{2-}$) flooding at 130 °C used to estimate the Young's modulus*

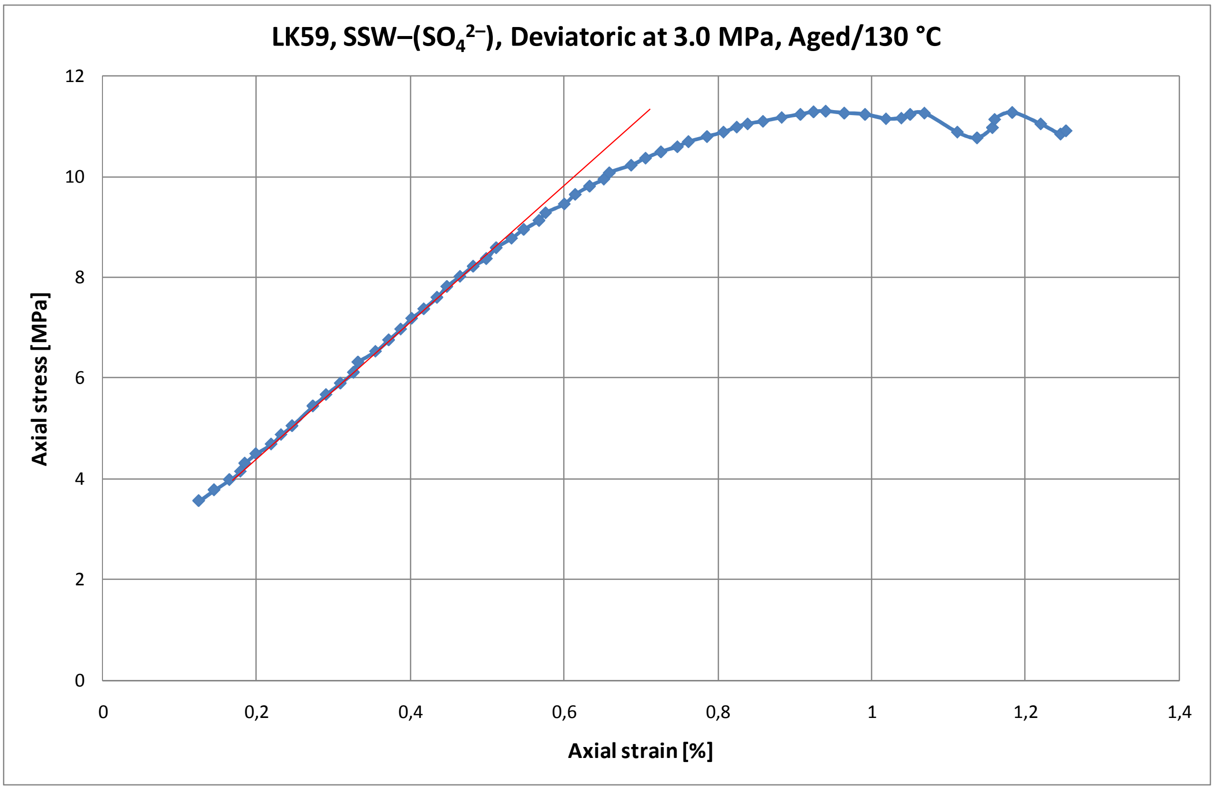

Figure A-35: *Axial stress versus axial strain plot for a 3.0 MPa deviatoric test performed on LK59 with SSW-($SO_4^{2-}$) flooding at 130 °C*

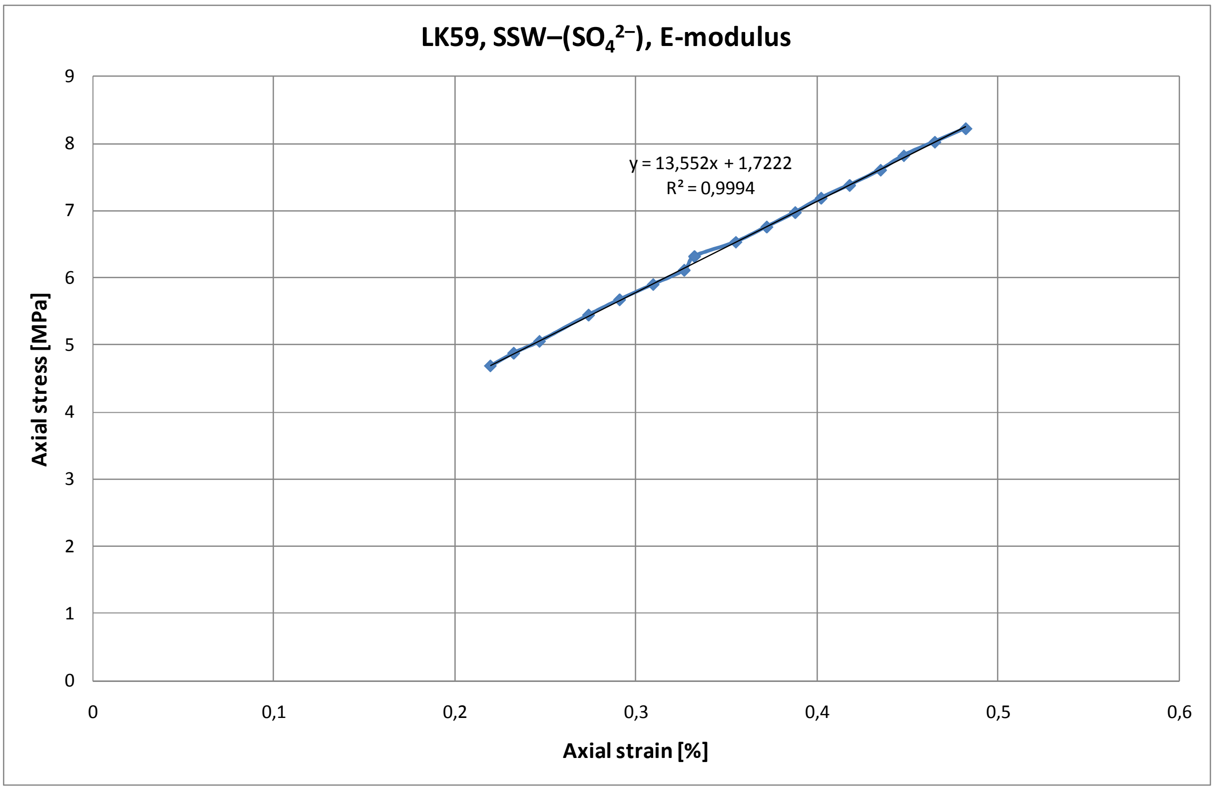

Figure A-36: *Section of the Axial stress versus axial strain plot for the 3.0 MPa deviatoric test performed on LK59 with SSW-($SO_4^{2-}$) flooding at 130 °C used to estimate the Young's modulus*

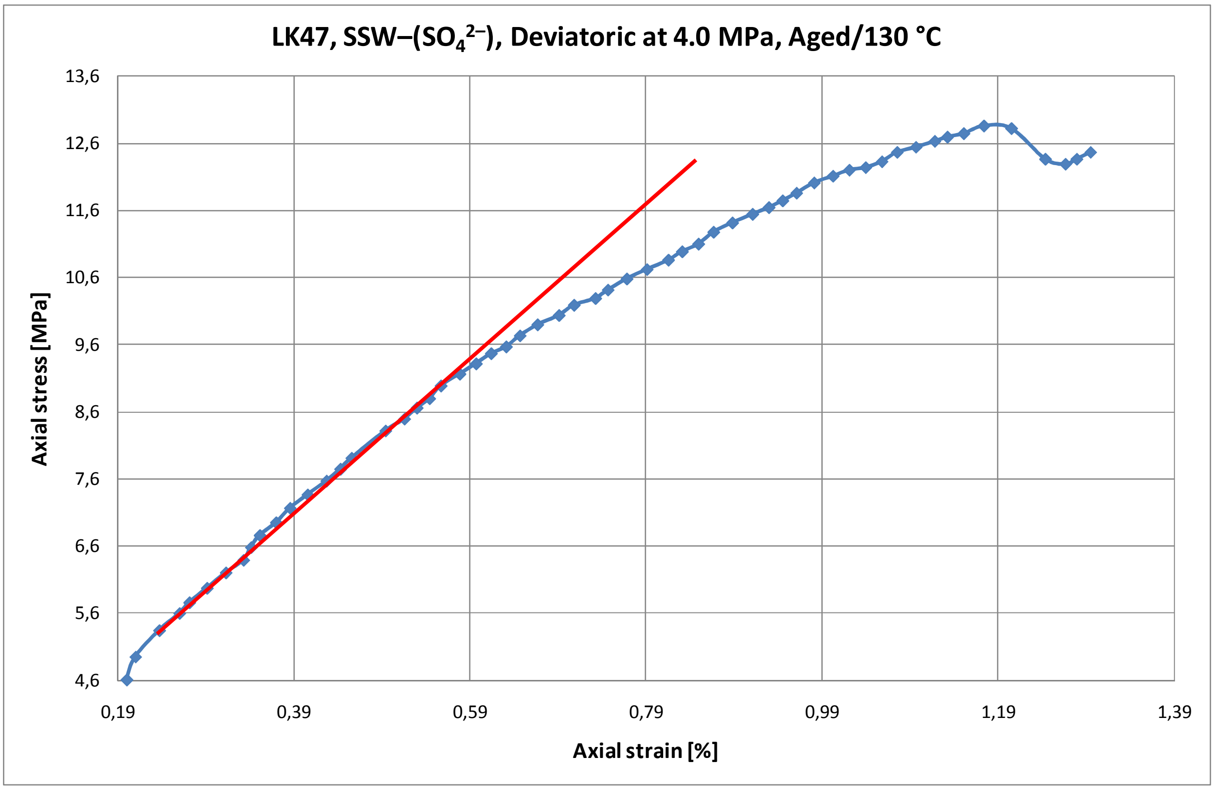

Figure A-37: *Axial stress versus axial strain plot for a 4.0 MPa deviatoric test performed on LK47 with SSW-($SO_4^{2-}$) flooding at 130 °C*

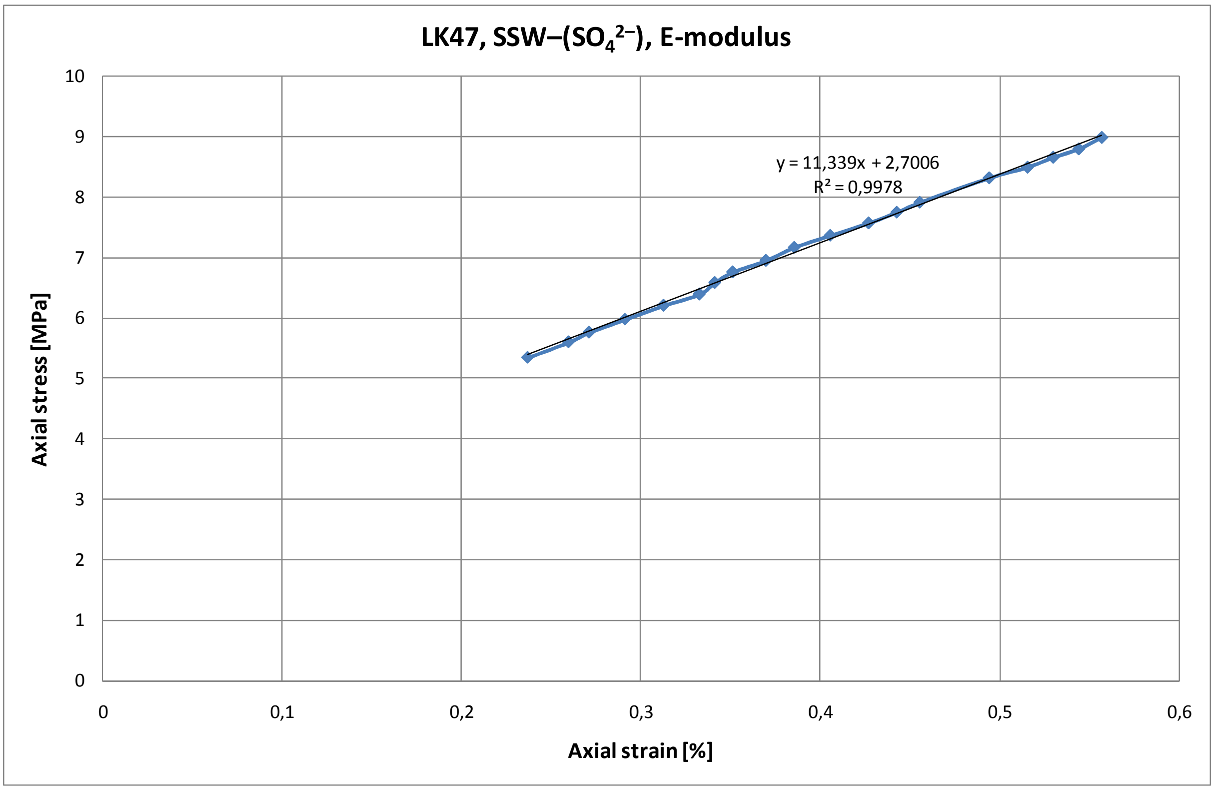

Figure A-38: *Section of the Axial stress versus axial strain plot for the 4.0 MPa deviatoric test performed on LK57 with SSW-($SO_4^{2-}$) flooding at 130 °C used to estimate the Young’s modulus*

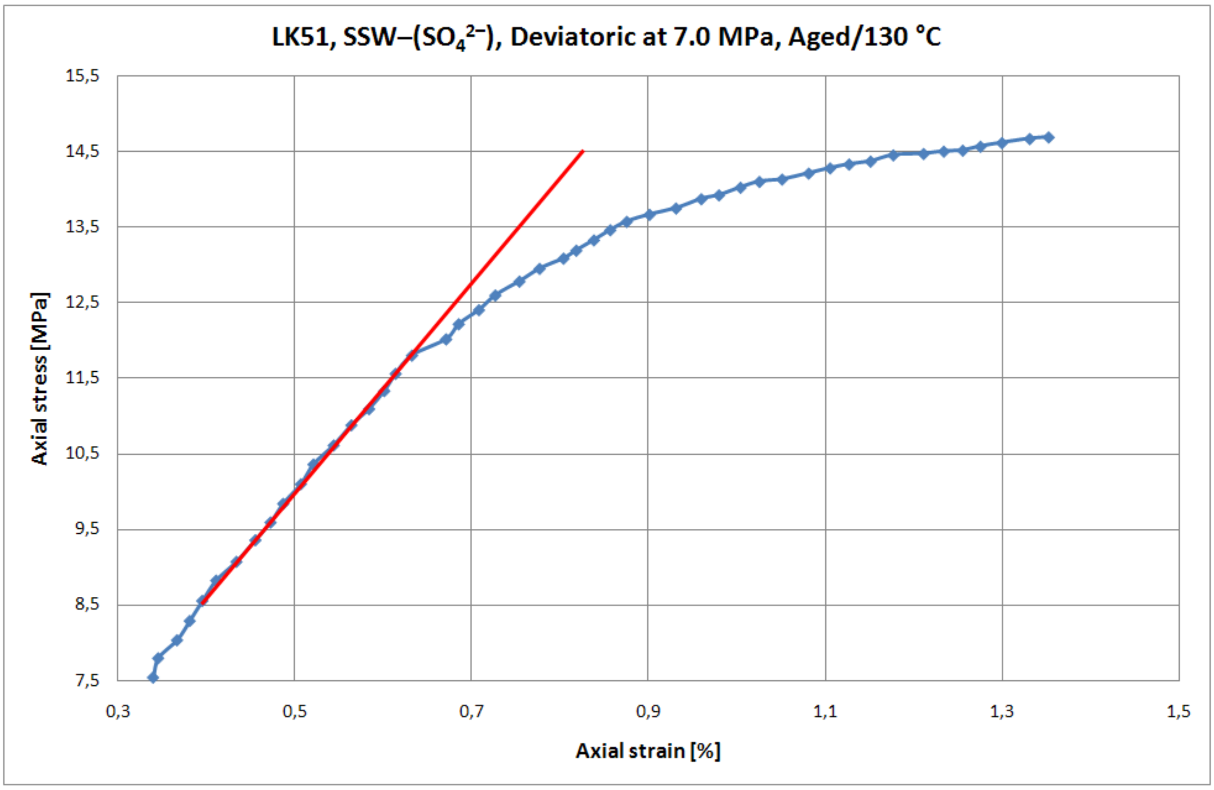

Figure A-39: *Axial stress versus axial strain plot for a 7.0 MPa deviatoric test performed on LK51 with SSW-($SO_4^{2-}$) flooding at 130 °C*

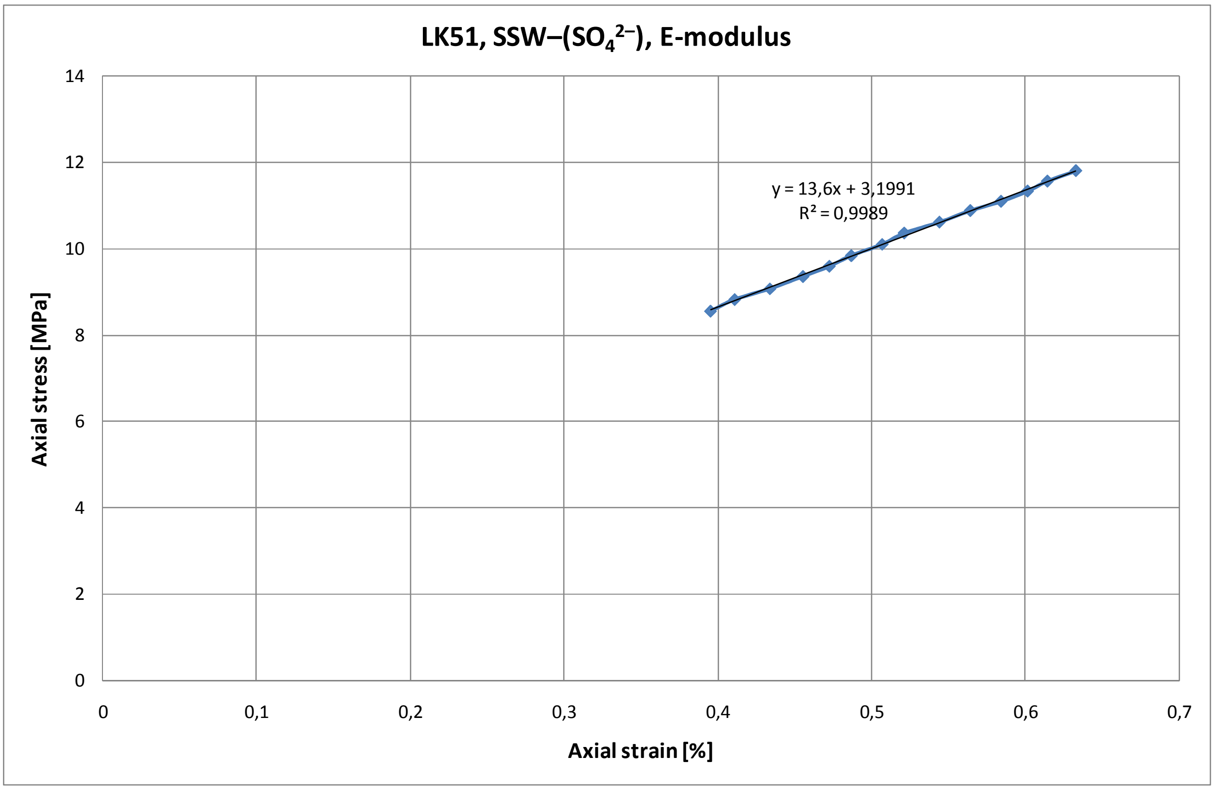

Figure A-40: *Section of the Axial stress versus axial strain plot for the 7.0 MPa deviatoric test performed on LK51 with SSW-($SO_4^{2-}$) flooding at 130 °C used to estimate the Young's modulus*

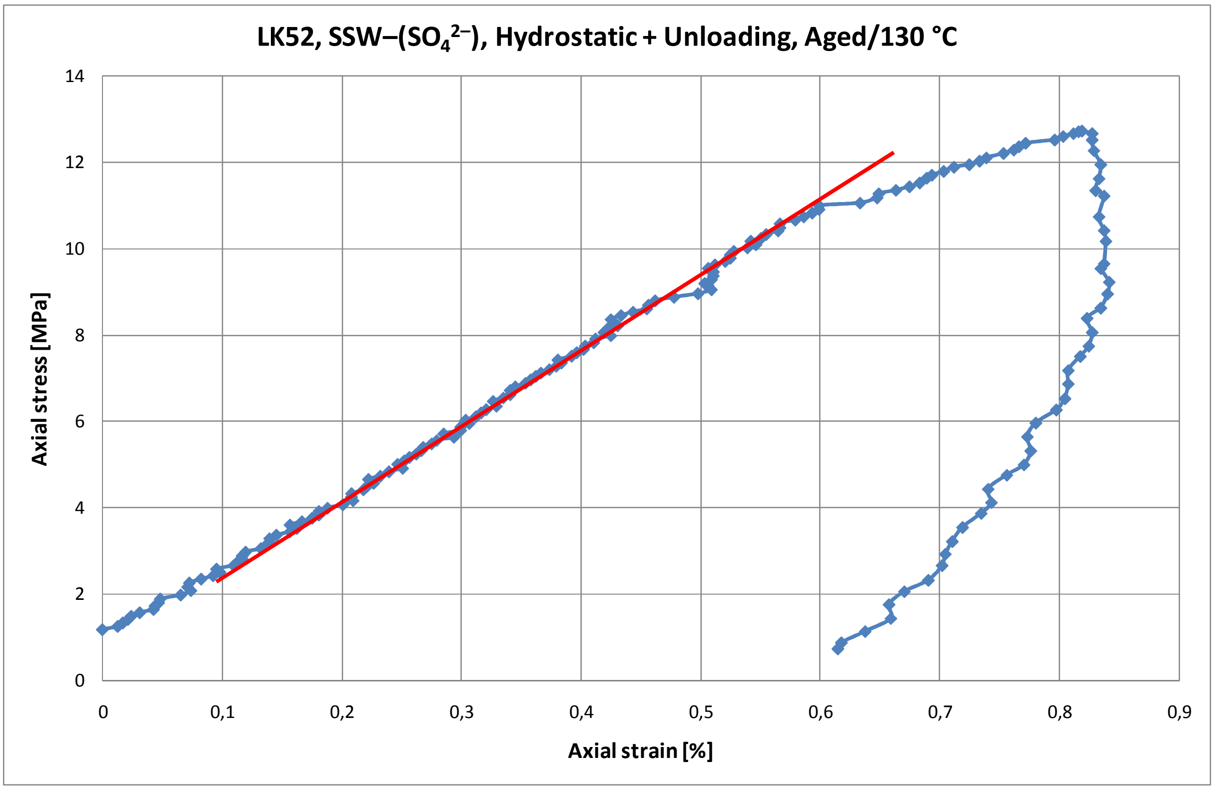

Figure A-41: *Axial stress versus axial strain plot for a hydrostatic test performed on LK52 with SSW-($SO_4^{2-}$) flooding at 130 °C*

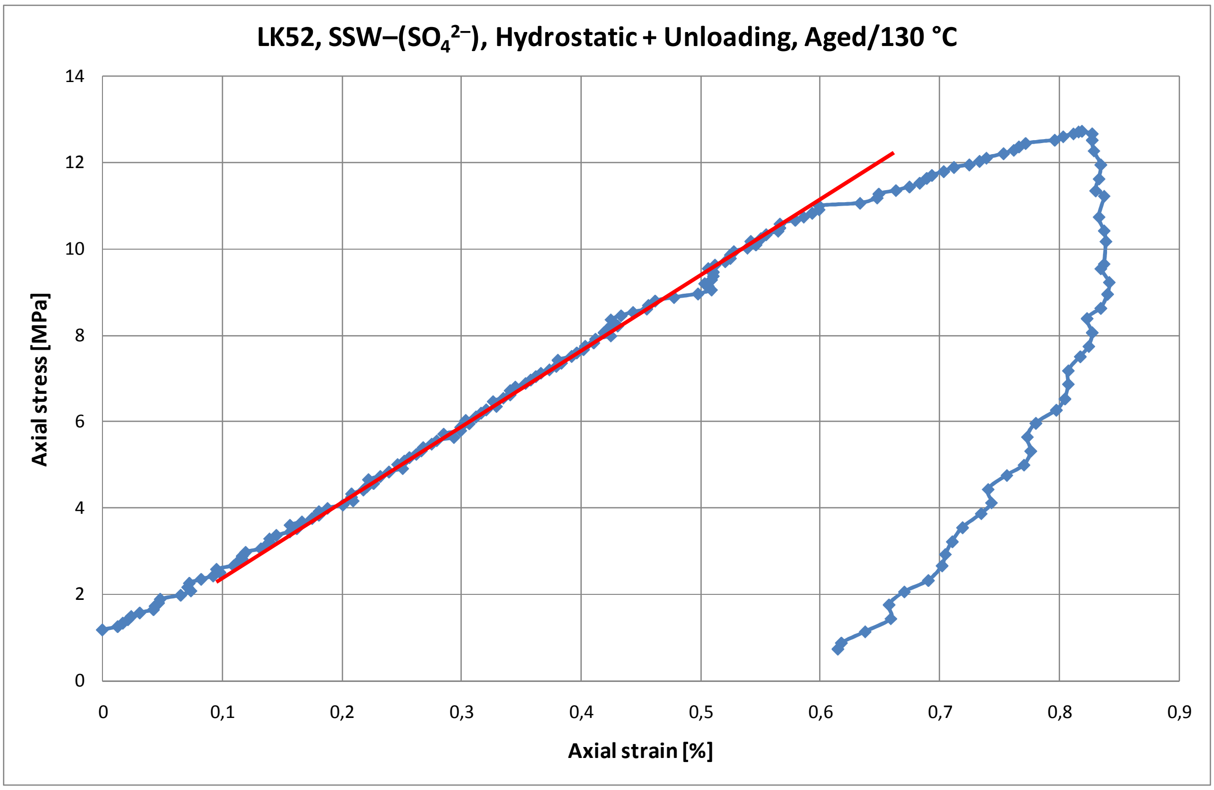

Figure A-18: *Section of the Axial stress versus Volumetric strain plot the hydrostatic test performed on LK52 with SSW-($SO_4^{2-}$) flooding at 130 °Cused to estimate the Bulk modulus.*

# Appendix B – Plots from tests using SSW

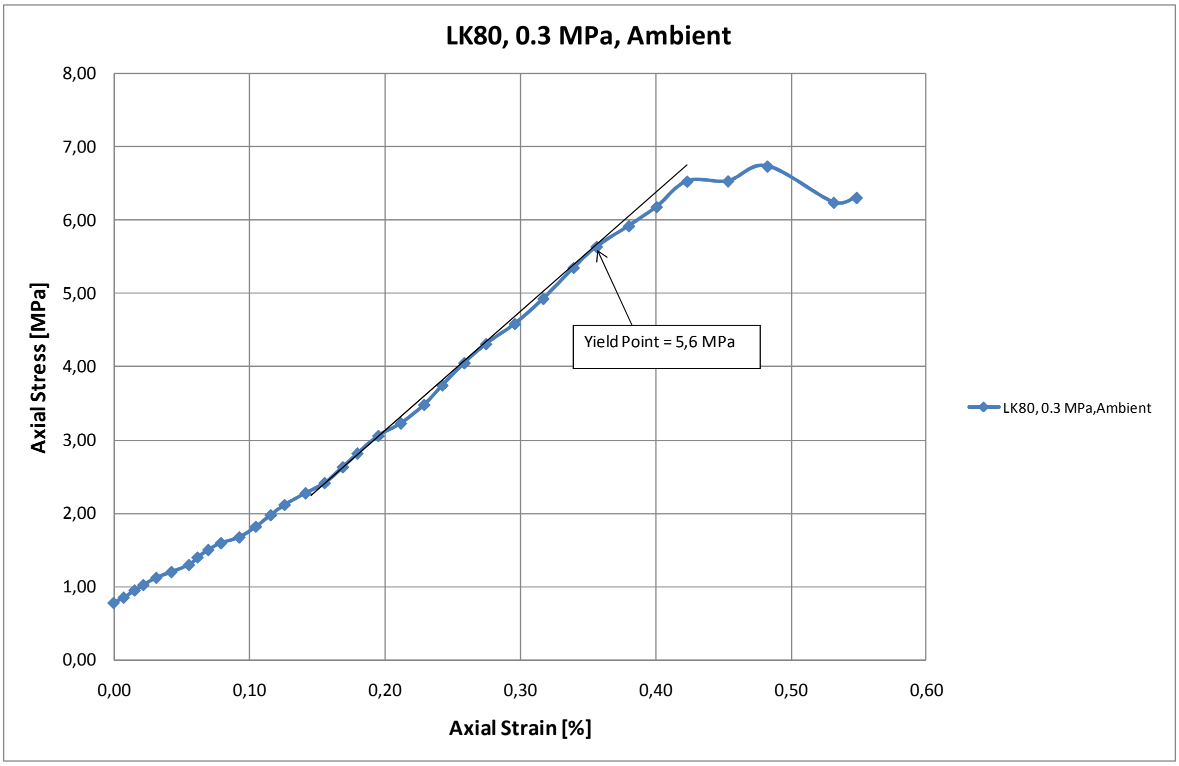

Figure B-1: *Axial stress versus axial strain plot for a 0.3 MPa deviatoric test performed on LK80 with SSW flooding at ambient temperature*

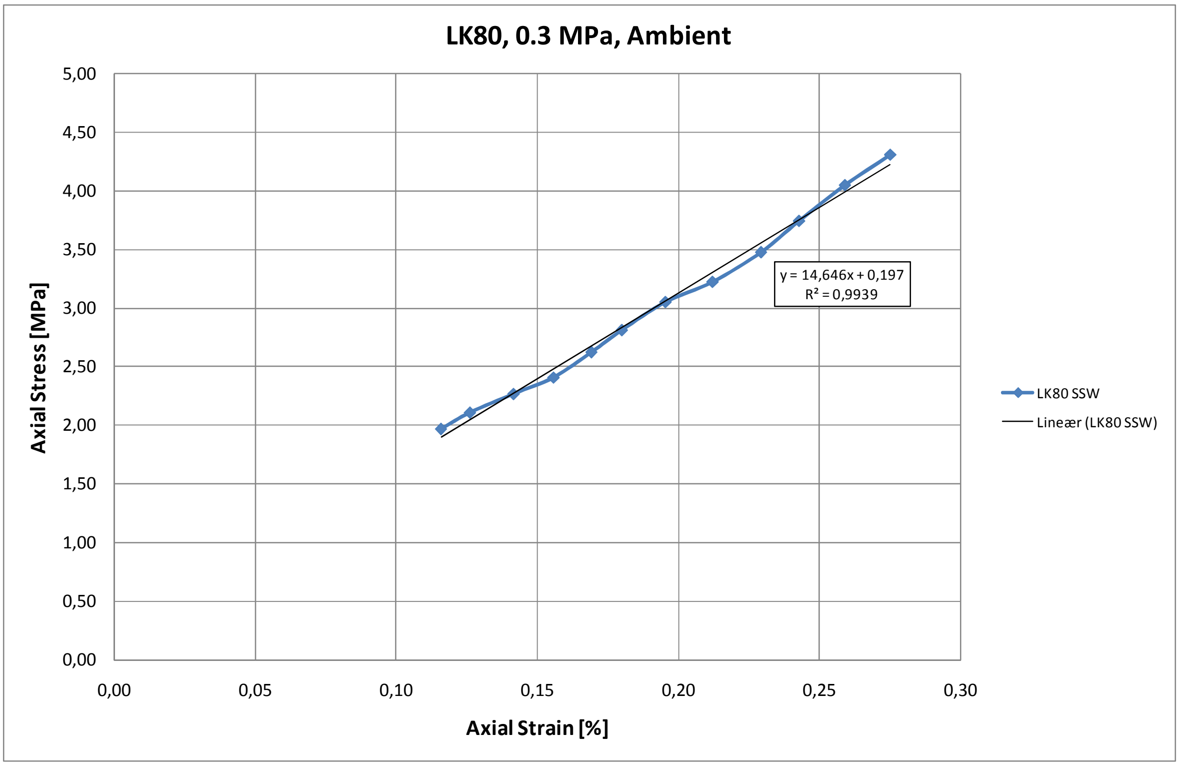

Figure B-2: *Section of the Axial stress versus axial strain plot for the 0.3 MPa deviatoric test performed on LK80 with SSW flooding at ambient temperature used to estimate the Young’s modulus.*

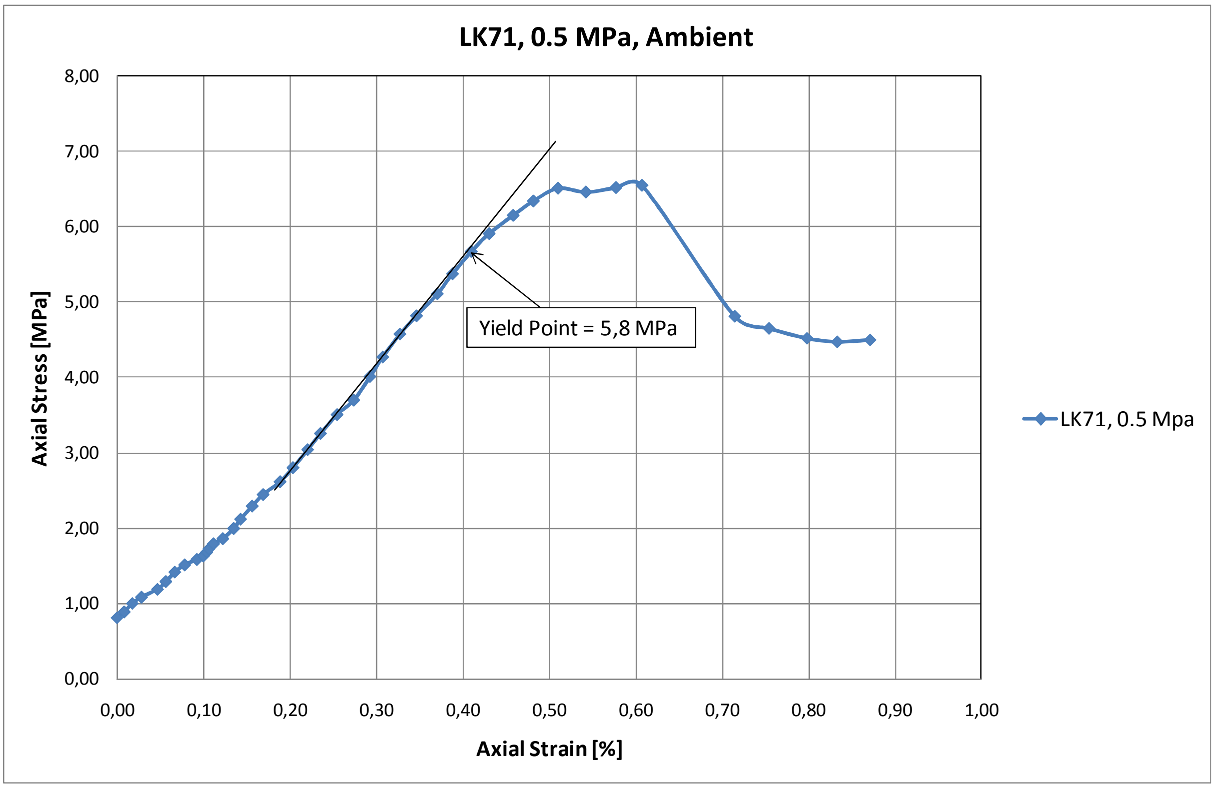

Figure B-3: *Axial stress versus axial strain plot for a 0.5 MPa deviatoric test performed on LK71 with SSW flooding at ambient temperature*

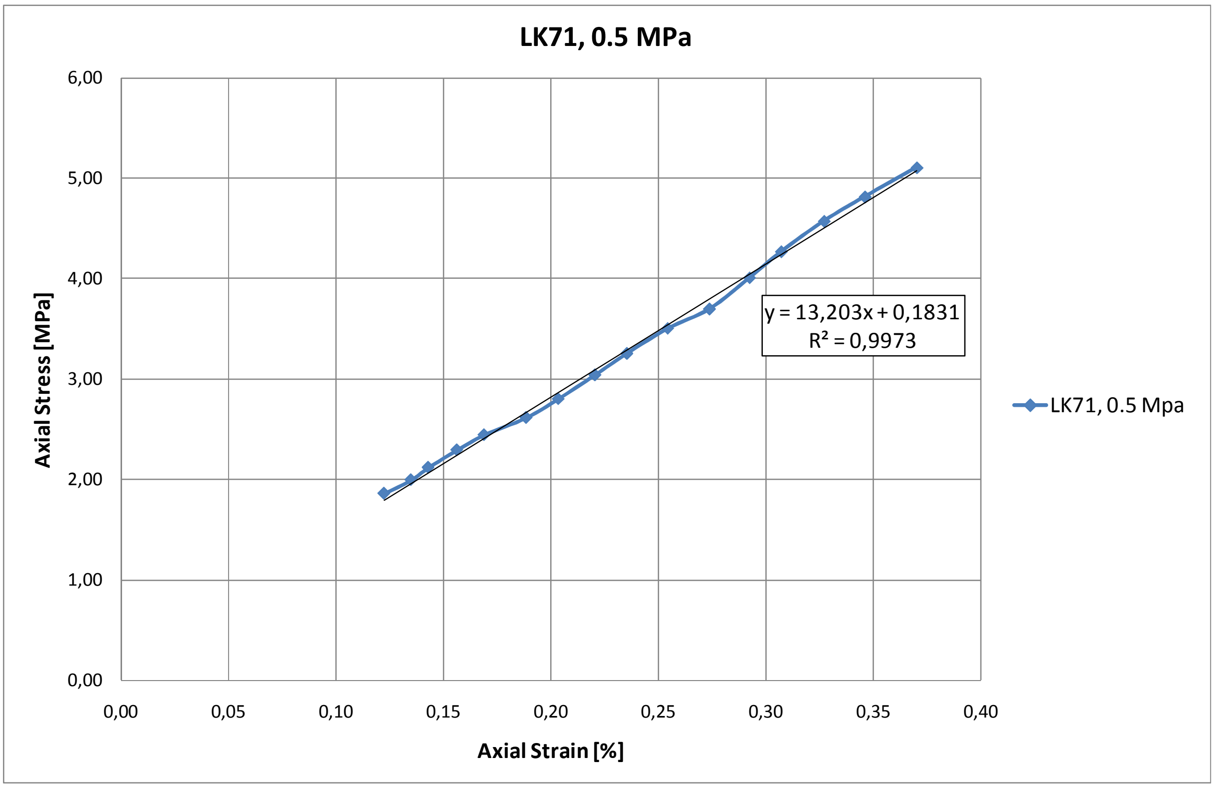

Figure B-4: *Section of the Axial stress versus axial strain plot for the 0.5 MPa deviatoric test performed on LK71 with SSW flooding at ambient temperature used to estimate the Young's modulus.*

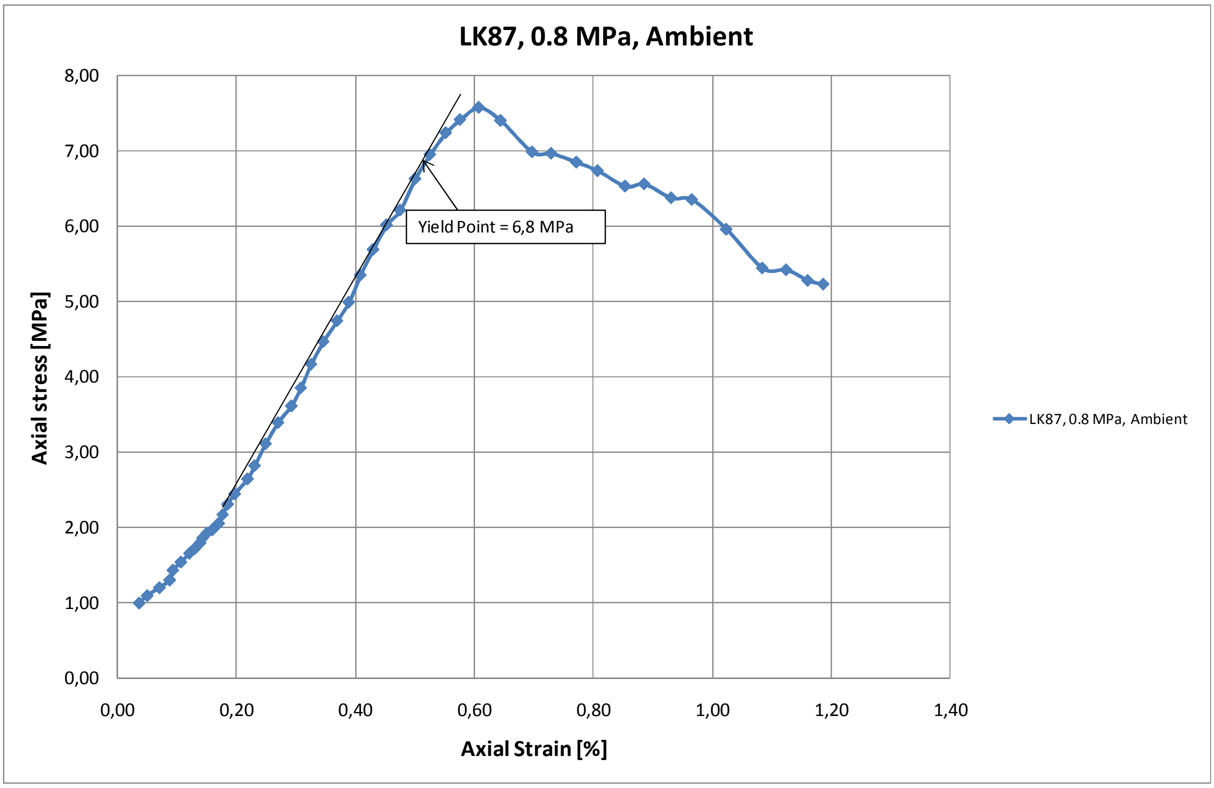

Figure B-5: *Axial stress versus axial strain plot for a 0.8 MPa deviatoric test performed on LK87 with SSW flooding at ambient temperature*

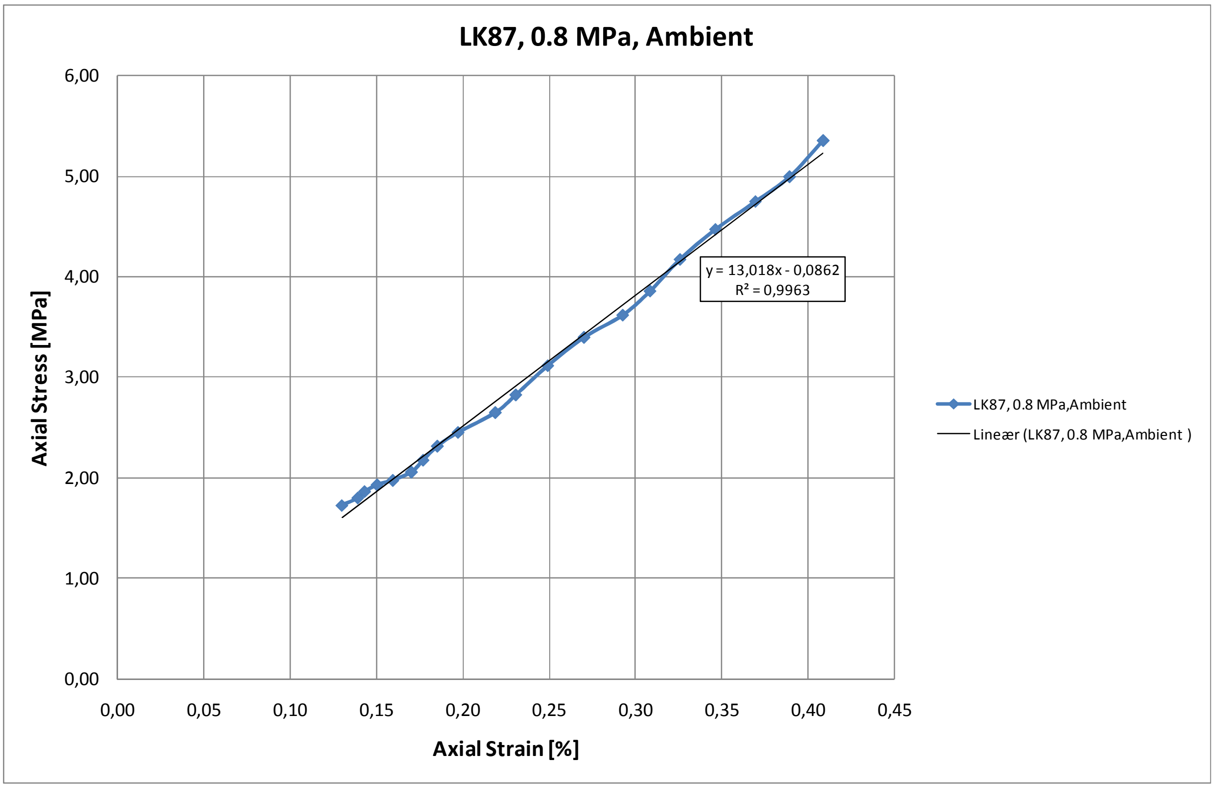

Figure B-6: *Section of the Axial stress versus axial strain plot for the 0.8 MPa deviatoric test performed on LK87 with SSW flooding at ambient temperature used to estimate the Young's modulus.*

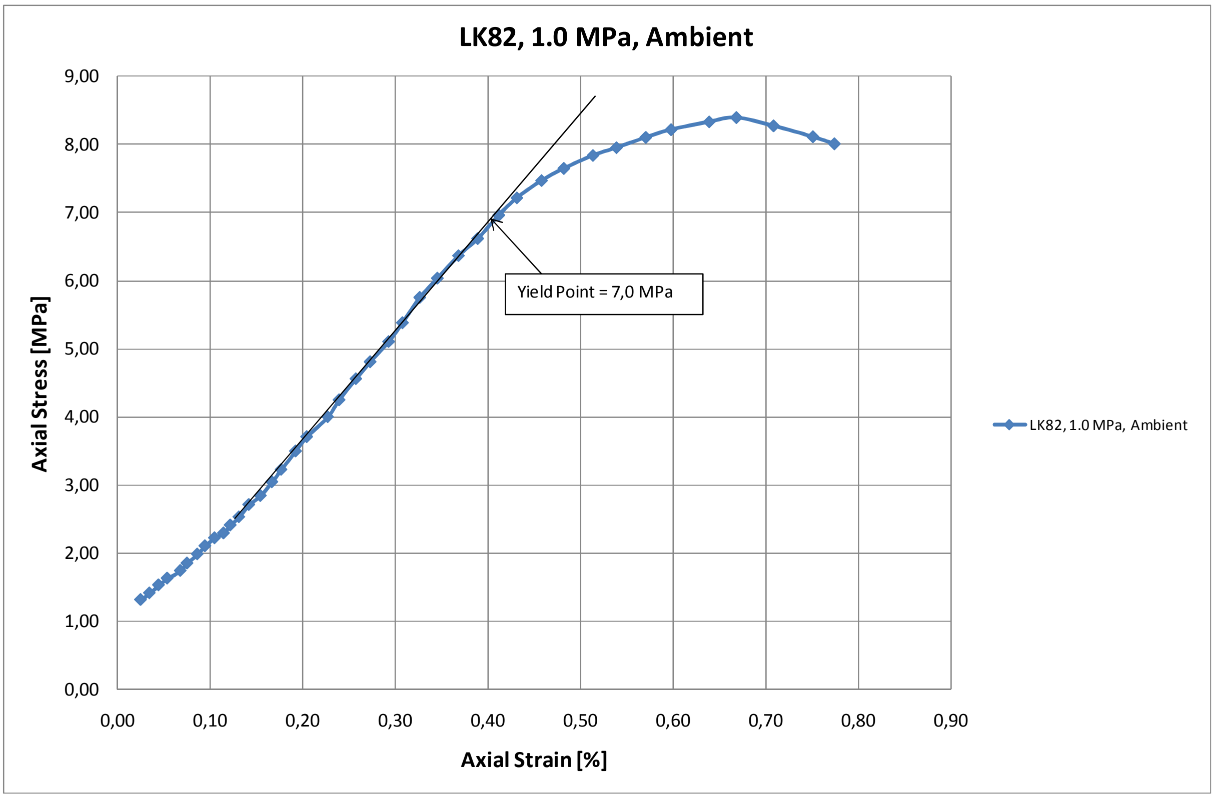

Figure B-7: *Axial stress versus axial strain plot for a 1.0 MPa deviatoric test performed on LK82 with SSW flooding at ambient temperature*

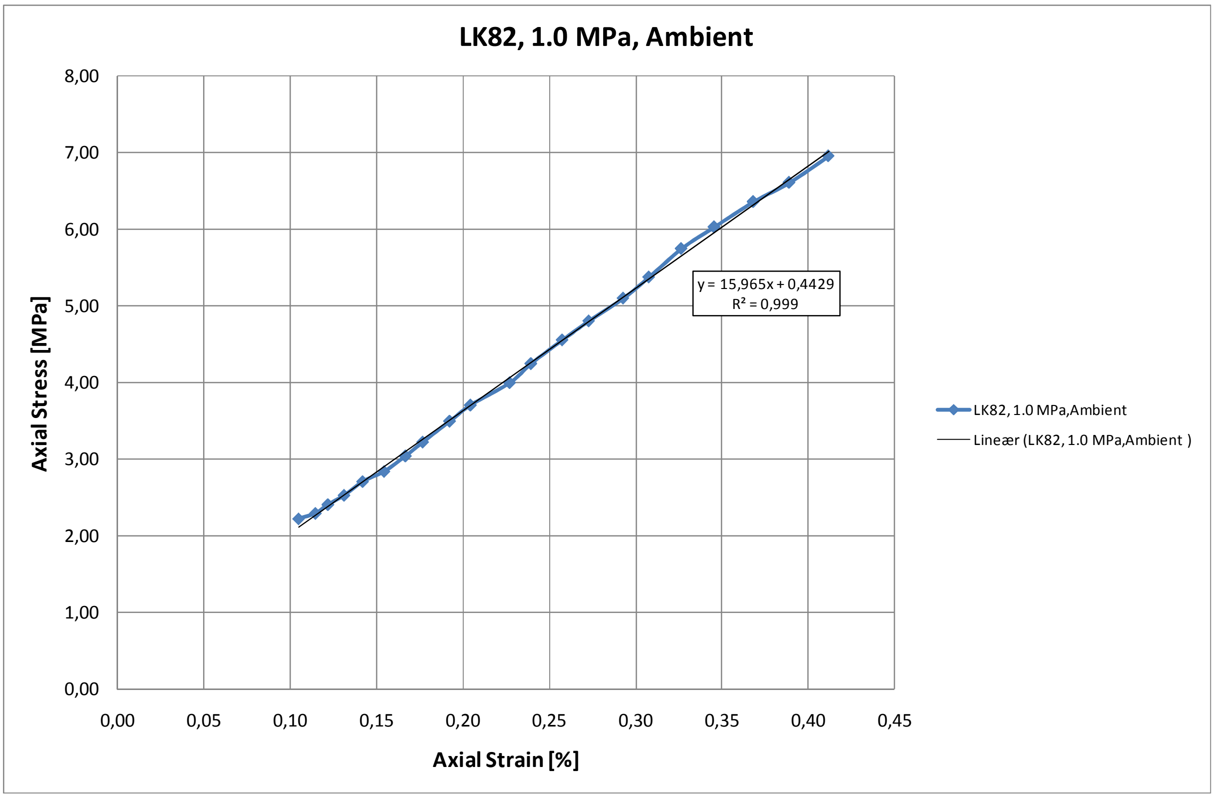

Figure B-8: *Section of the Axial stress versus axial strain plot for the 1.0 MPa deviatoric test performed on LK82 with SSW flooding at ambient temperature used to estimate the Young's modulus.*

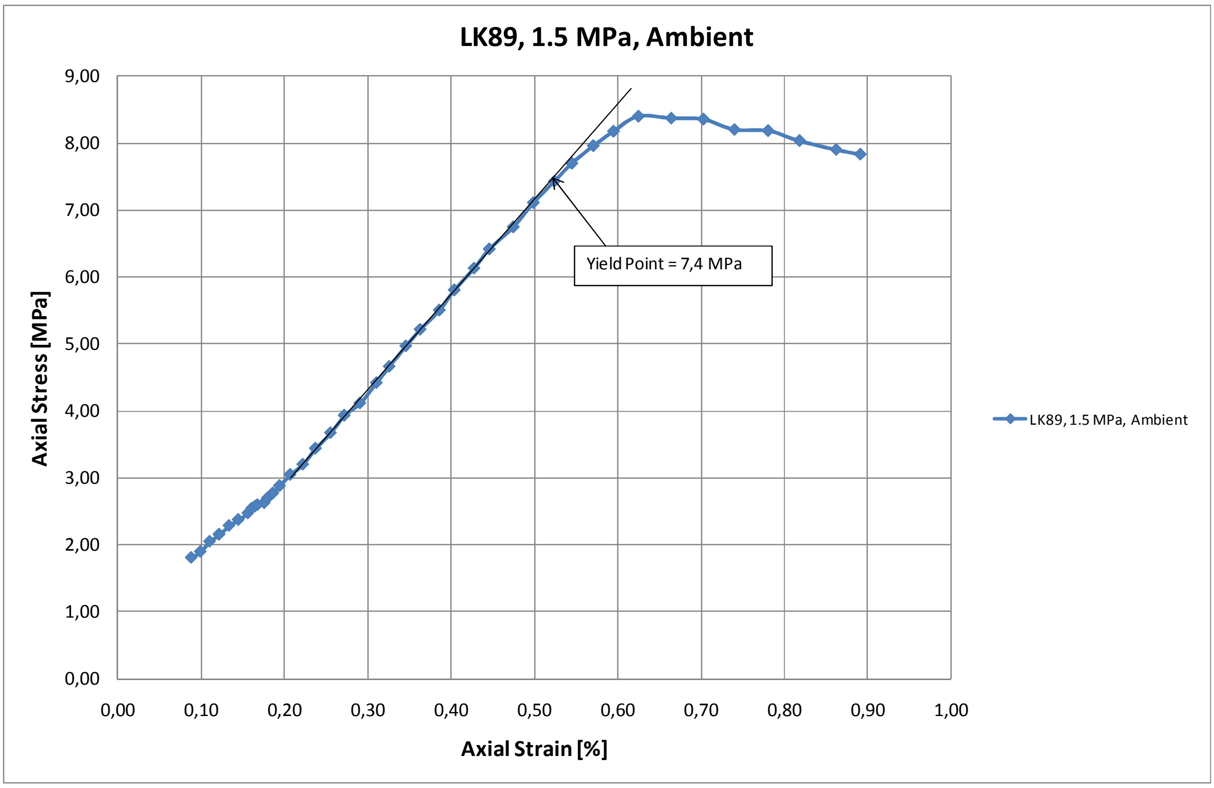

Figure B-9: *Axial stress versus axial strain plot for a 1.5 MPa deviatoric test performed on LK89 with SSW flooding at ambient temperature*

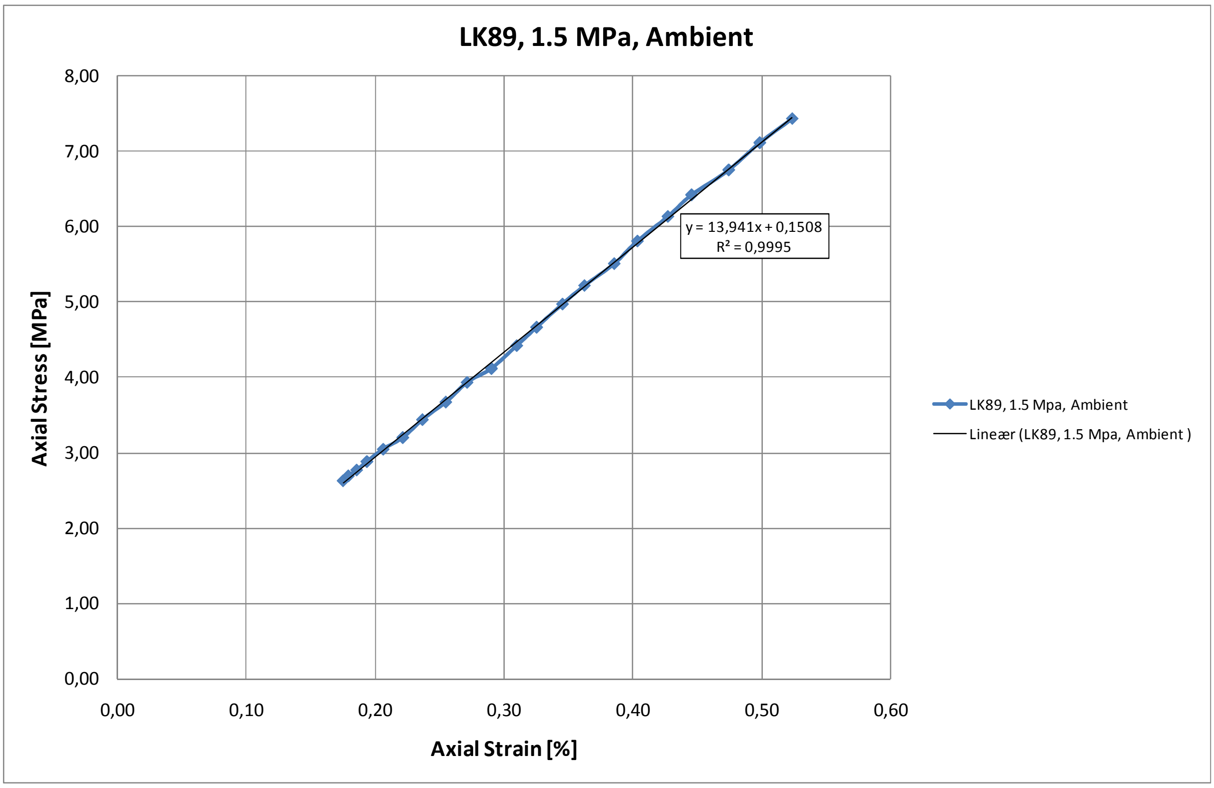

Figure B-10: *Section of the Axial stress versus axial strain plot for the 1.5 MPa deviatoric test performed on LK89 with SSW flooding at ambient temperature used to estimate the Young's modulus.*

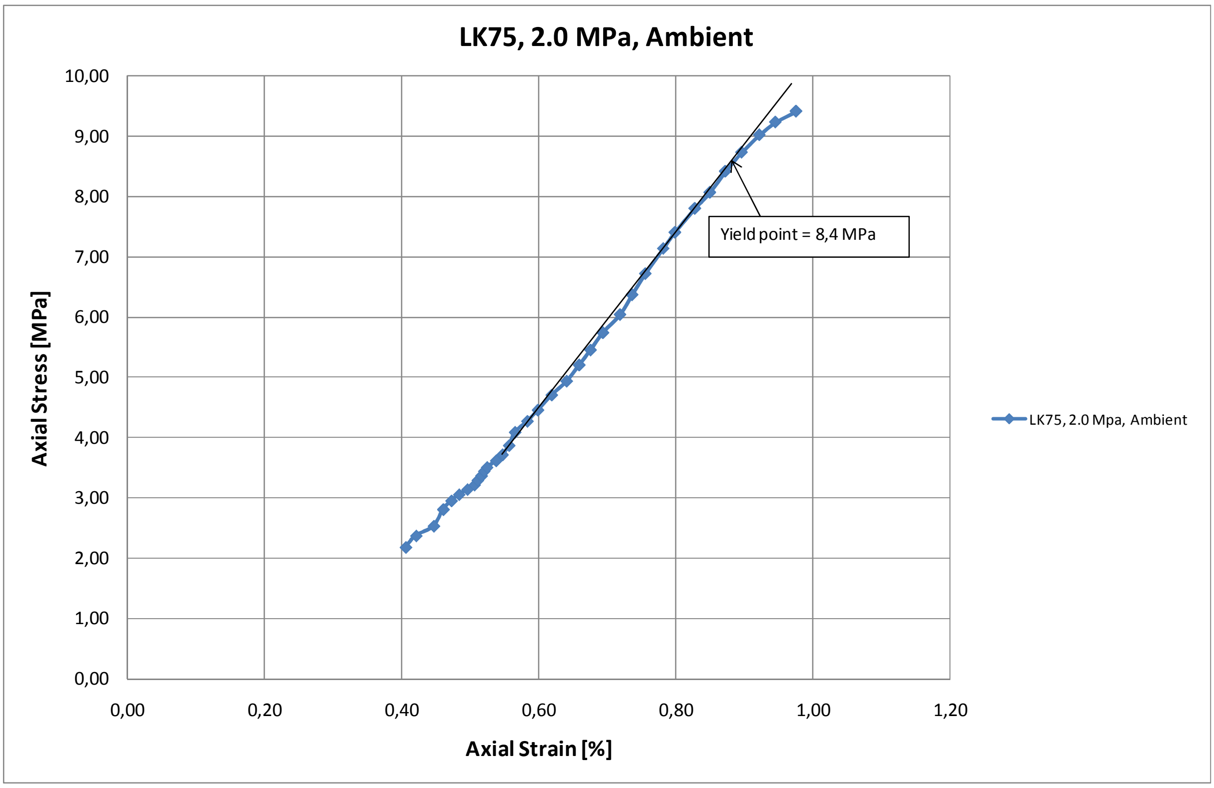

Figure B-11: *Axial stress versus axial strain plot for a 2.0 MPa deviatoric test performed on LK75 with SSW flooding at ambient temperature*

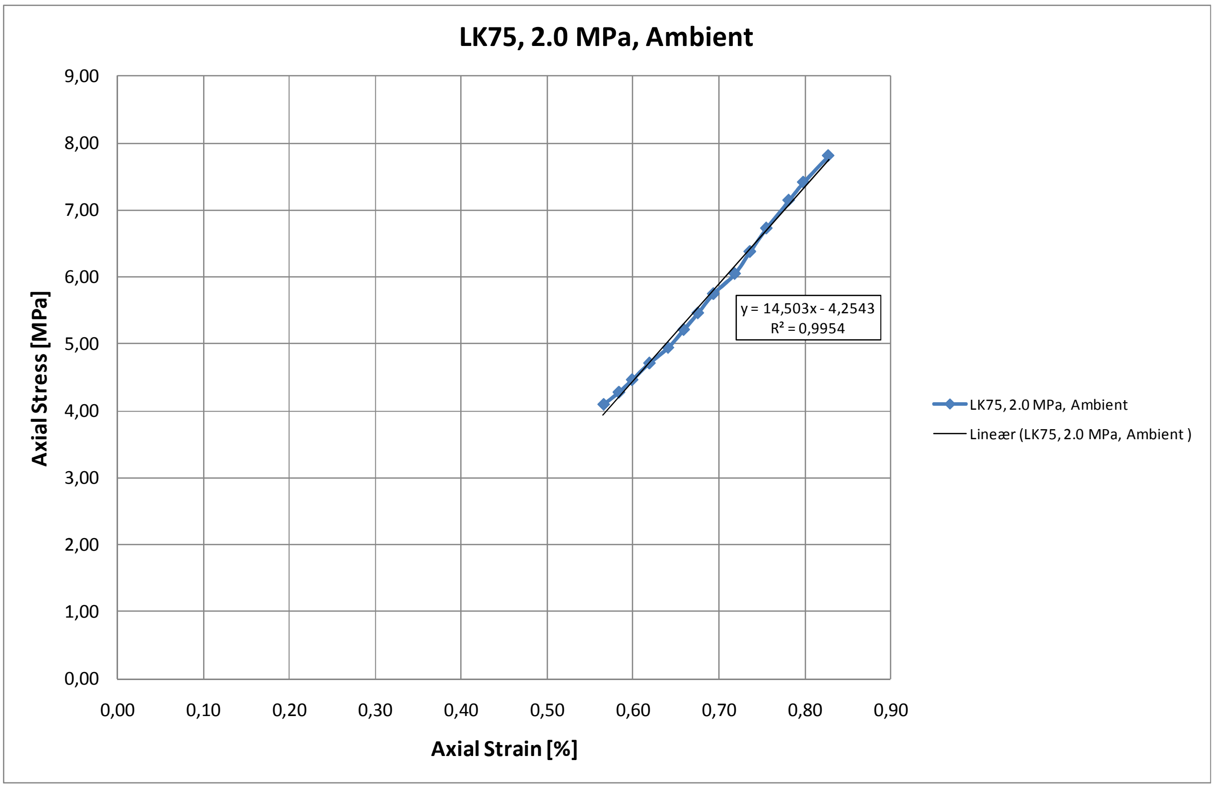

Figure B-12: *Section of the Axial stress versus Axial Strain plot for the 2.0 MPa deviatoric test performed on LK75 with SSW flooding at ambient temperature used to estimate the Young's modulus.*

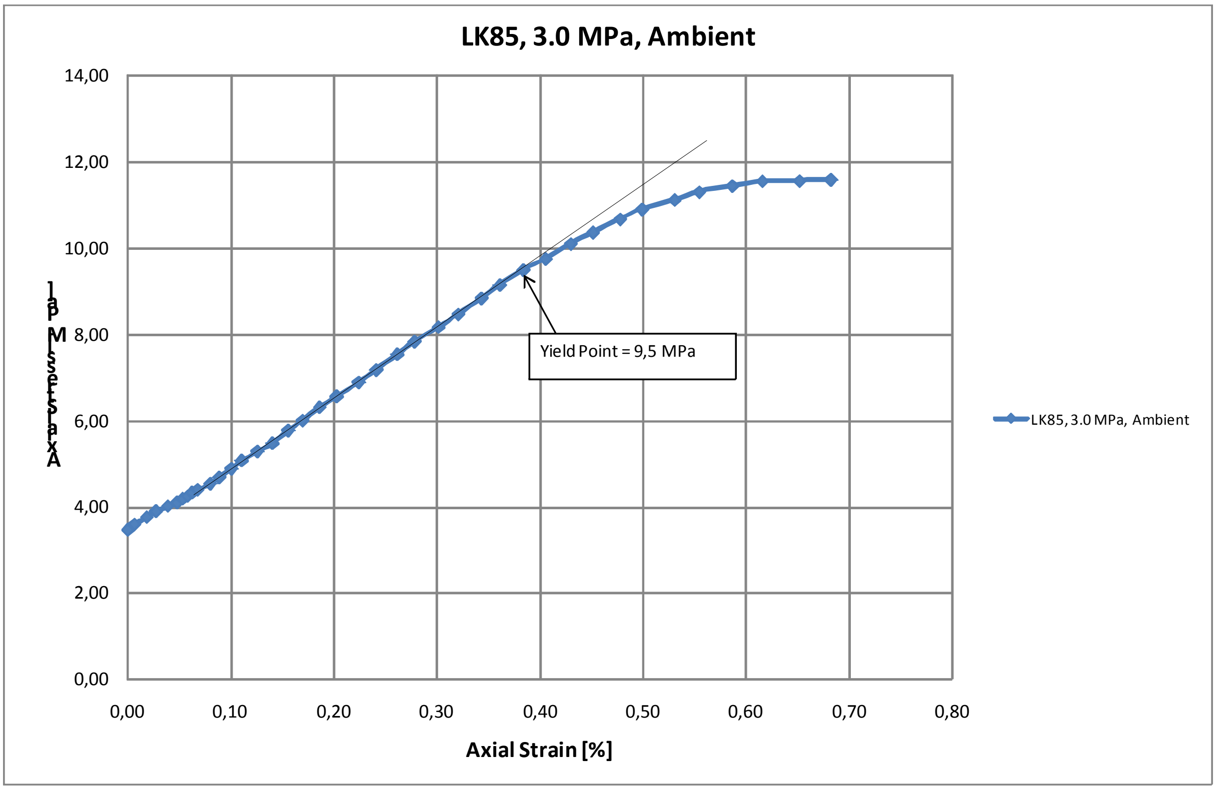

Figure B-13: *Axial stress versus axial strain plot for a 3.0 MPa deviatoric test performed on LK85 with SSW flooding at ambient temperature*

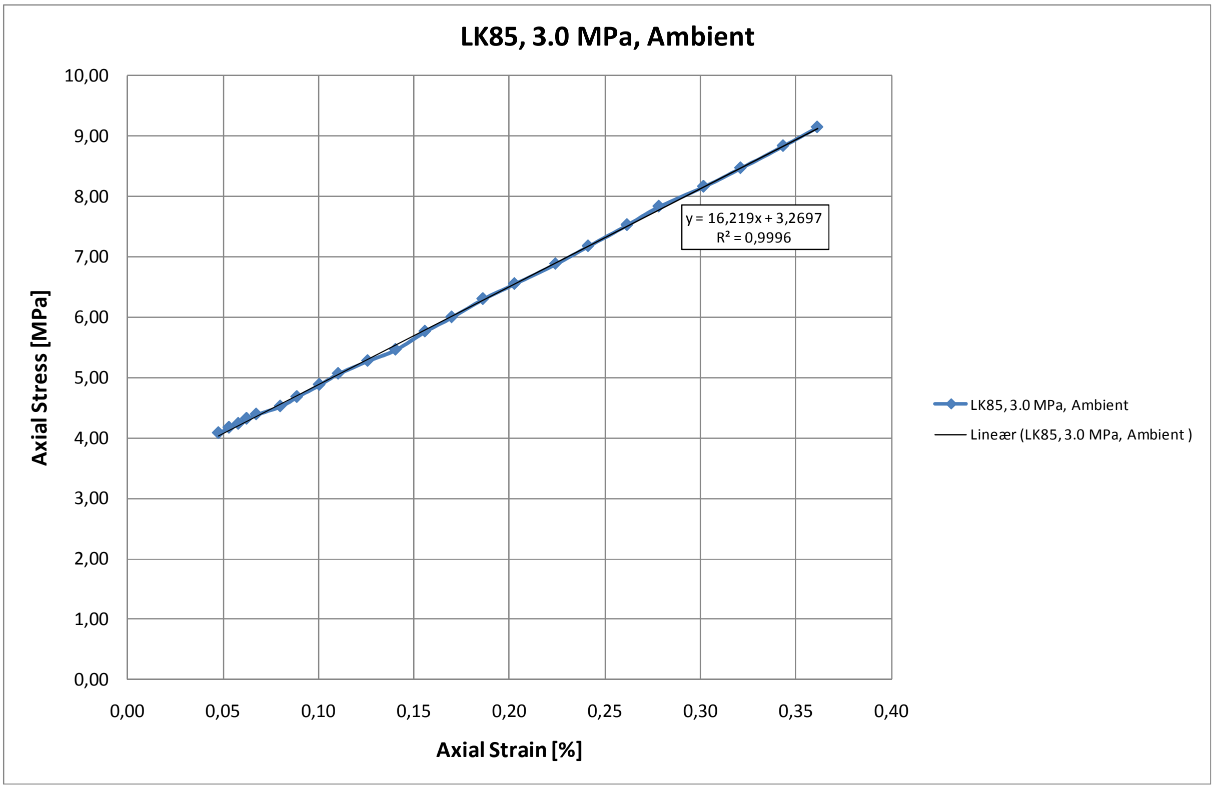

Figure B-14: *Section of the Axial stress versus axial strain plot for the 3.0 MPa deviatoric test performed on LK85 with SSW flooding at ambient temperature used to estimate the Young's modulus.*

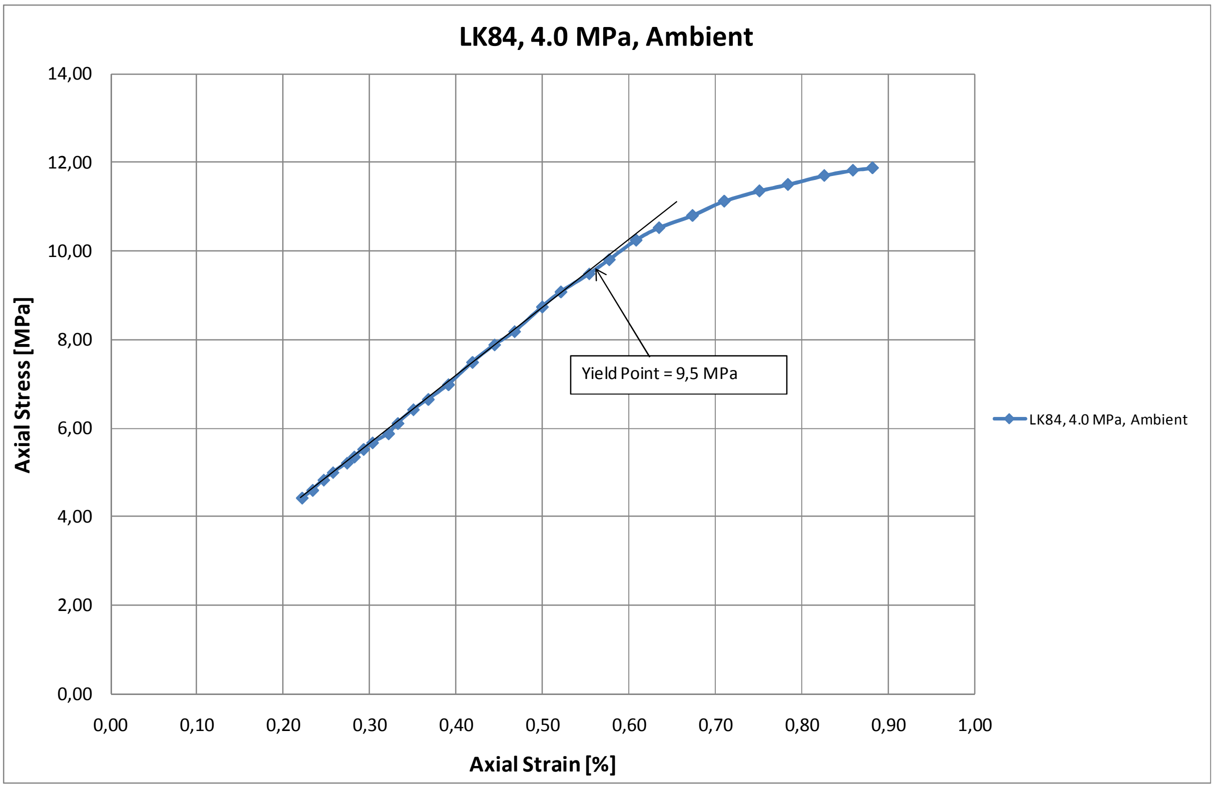

Figure B-15: *Axial stress versus axial strain plot for a 4.0 MPa deviatoric test performed on LK84 with SSW flooding at ambient temperature*

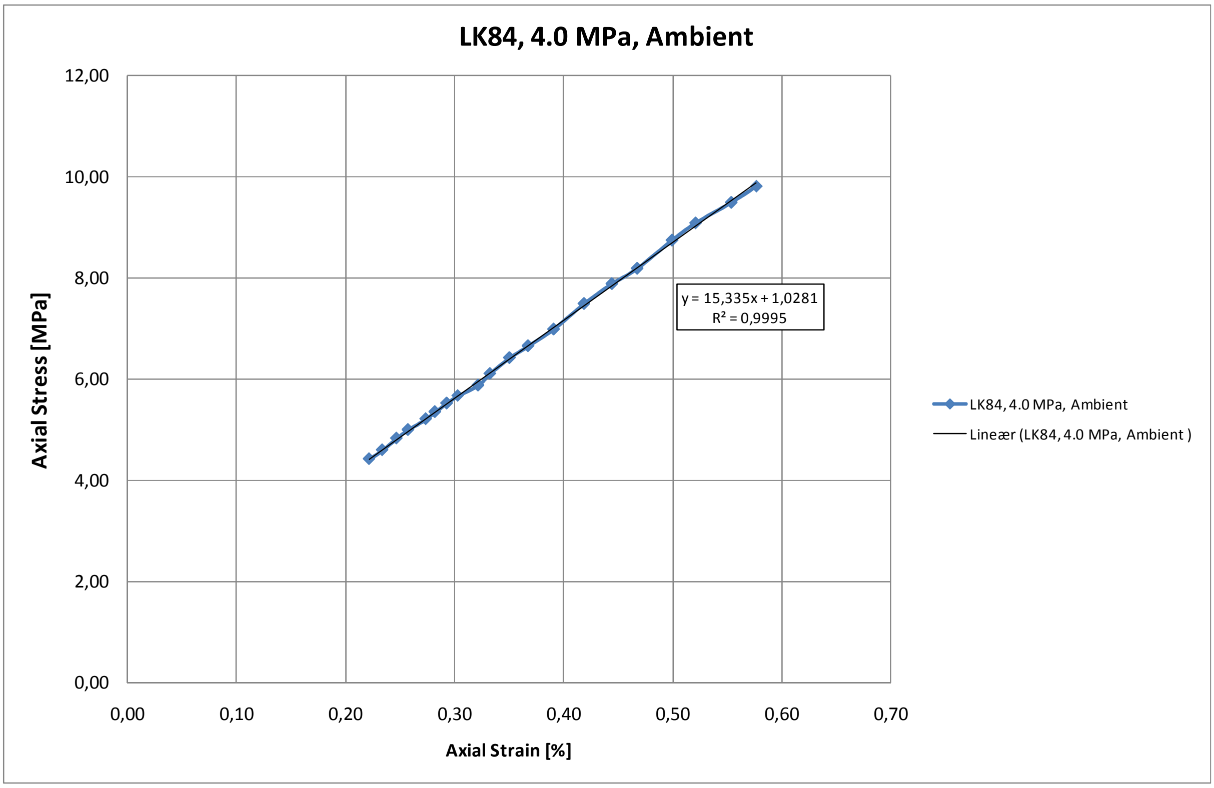

Figure B-16: *Section of the Axial stress versus axial strain plot for the 4.0 MPa deviatoric test performed on LK84 with SSW flooding at ambient temperature used to estimate the Young's modulus.*

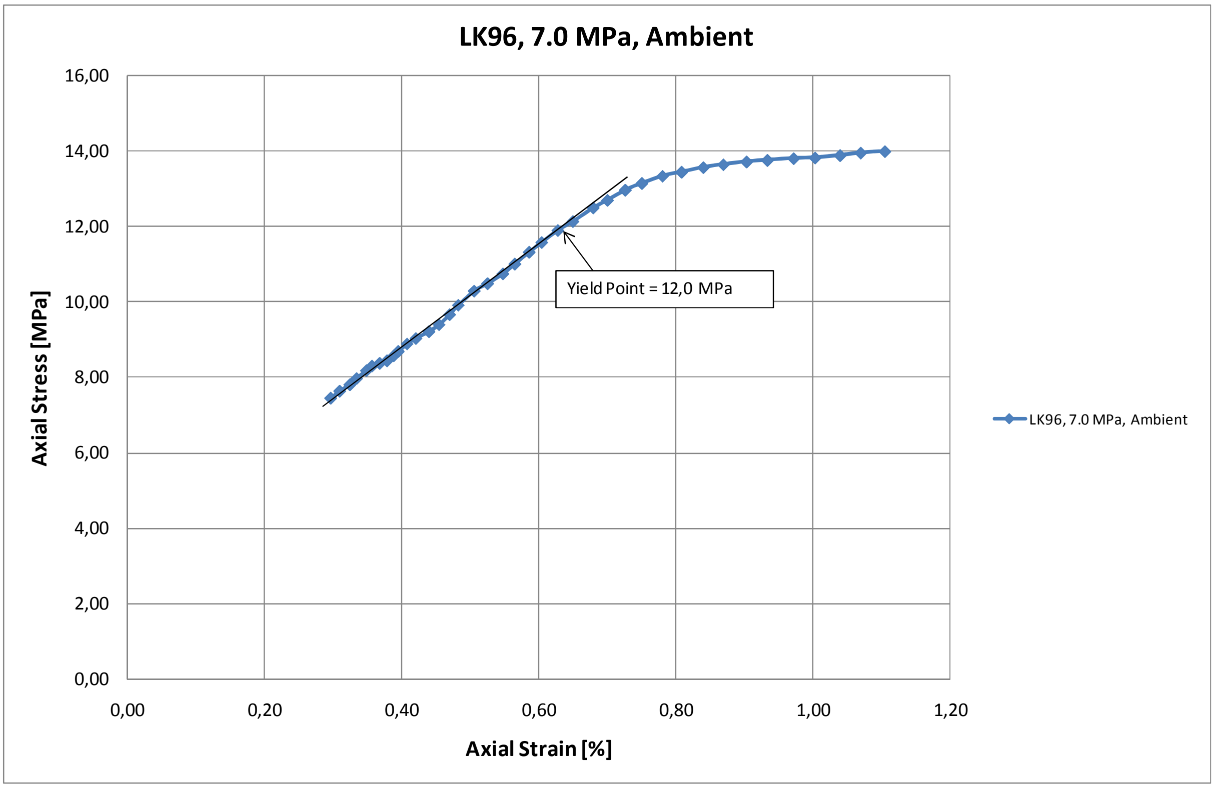

Figure B-17: *Axial stress versus axial strain plot for a 7.0 MPa deviatoric test performed on LK96 with SSW flooding at ambient temperature*

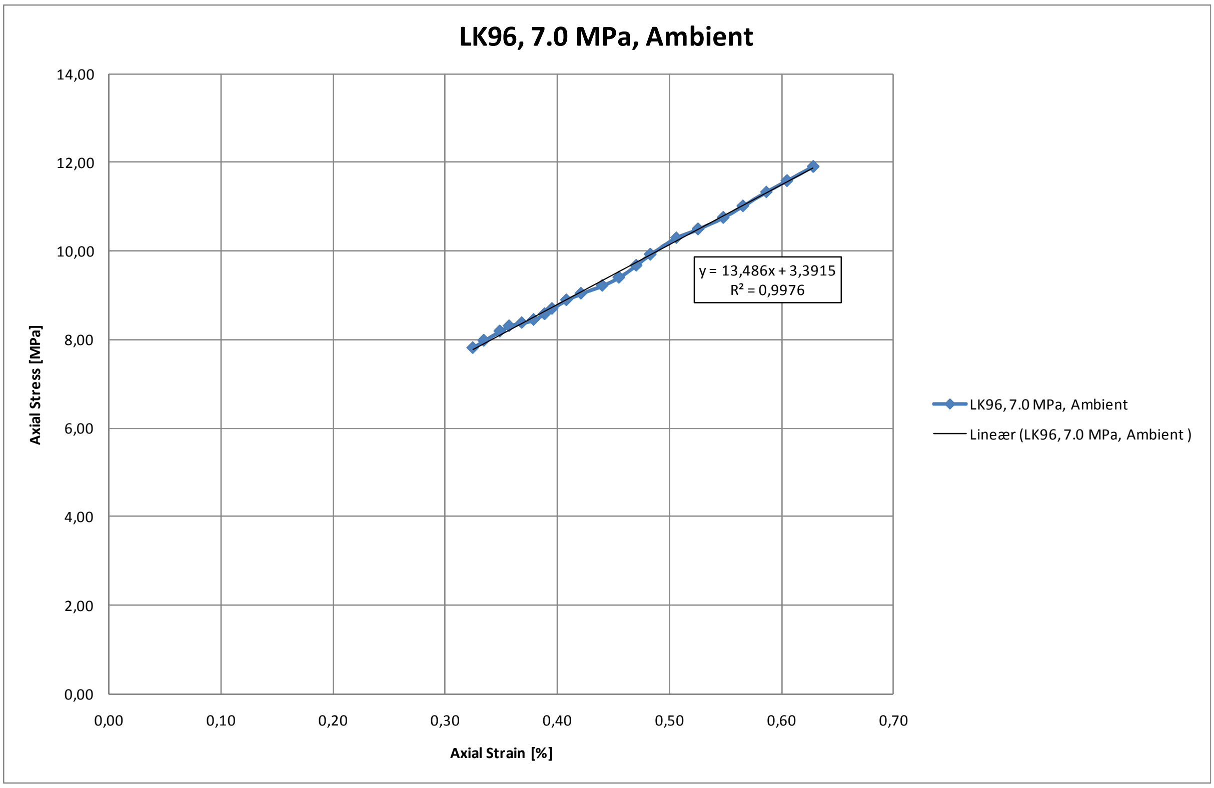

Figure B-18: *Section of the Axial stress versus axial strain plot for the 7.0 MPa deviatoric test performed on LK84 with SSW flooding at ambient temperature used to estimate the Young's modulus.*

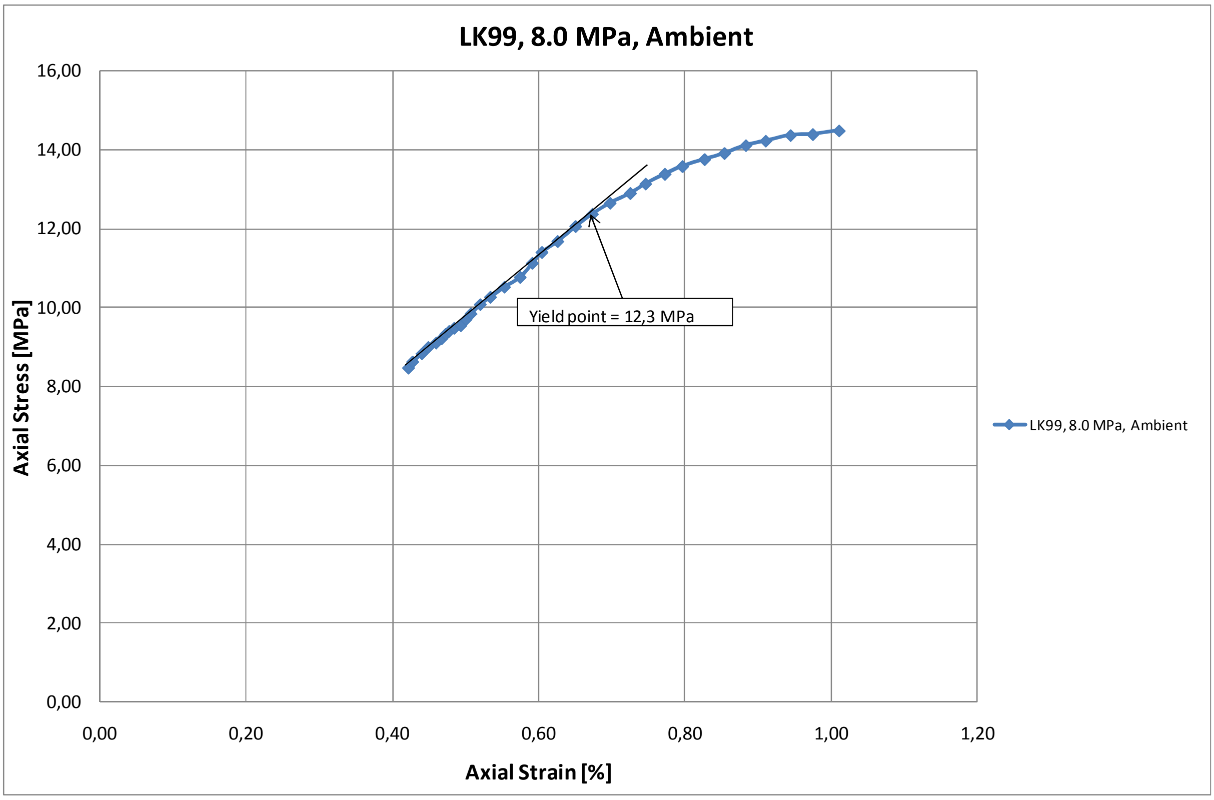

Figure B-19: *Axial stress versus axial strain plot for the 8.0 MPa deviatoric test performed on LK99 with SSW flooding at ambient temperature*

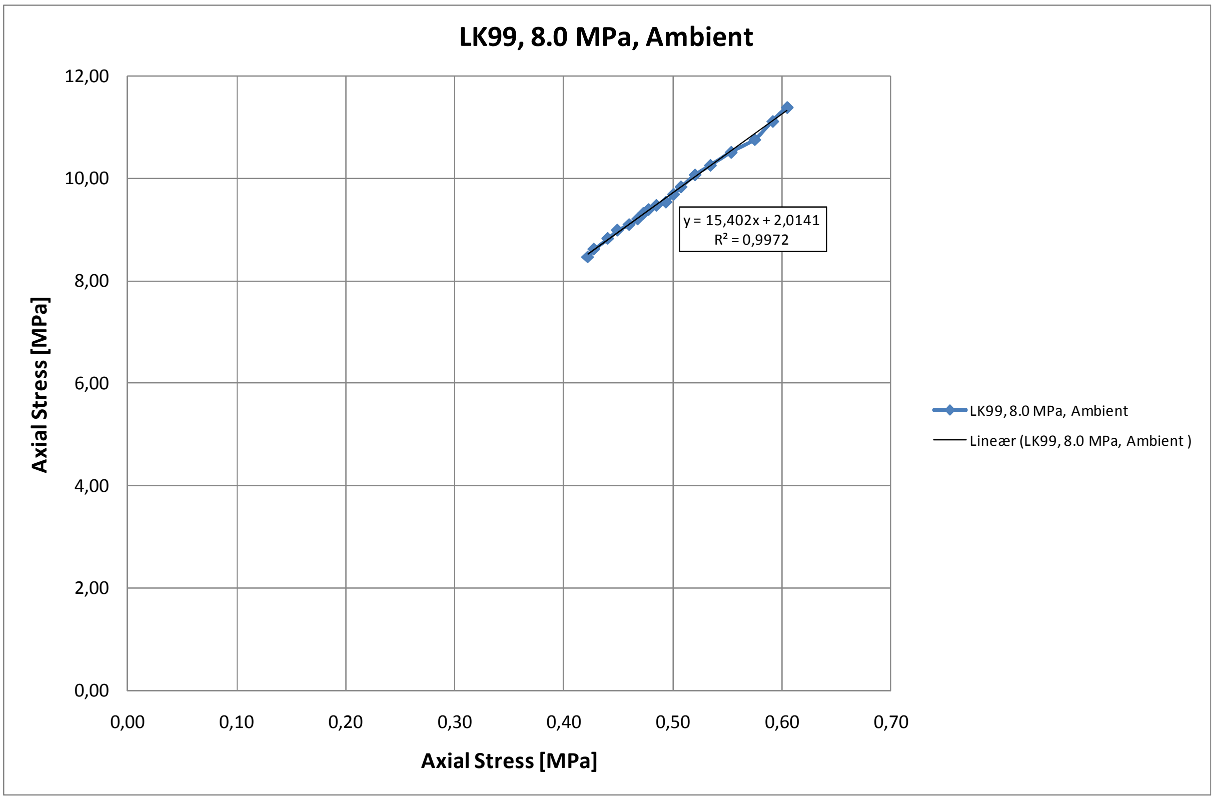

Figure B-20: *Section of the Axial stress versus axial strain plot for the 8.0 MPa deviatoric test performed on LK99 with SSW flooding at ambient temperature used to estimate the Young's modulus.*

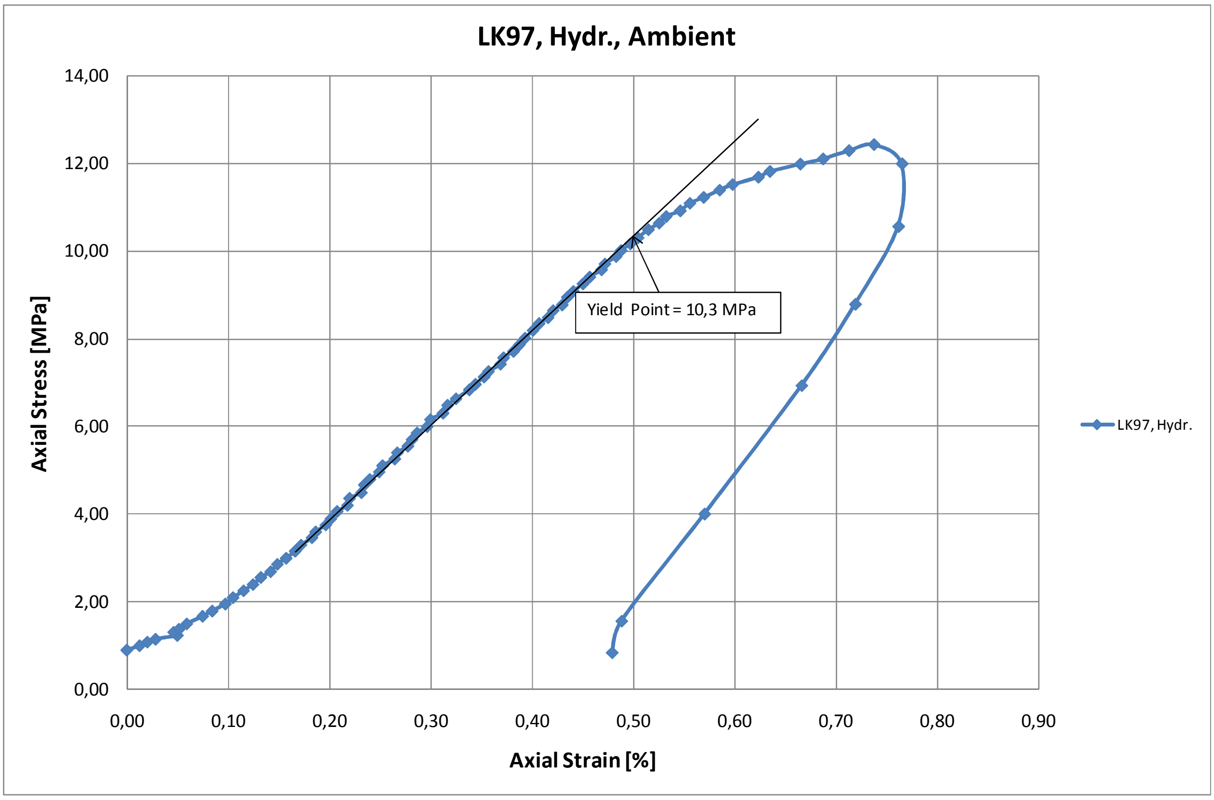

Figure B-21: *Axial stress versus axial strain plot for a hydrostatic test performed on LK97 with SSW flooding at ambient temperature*

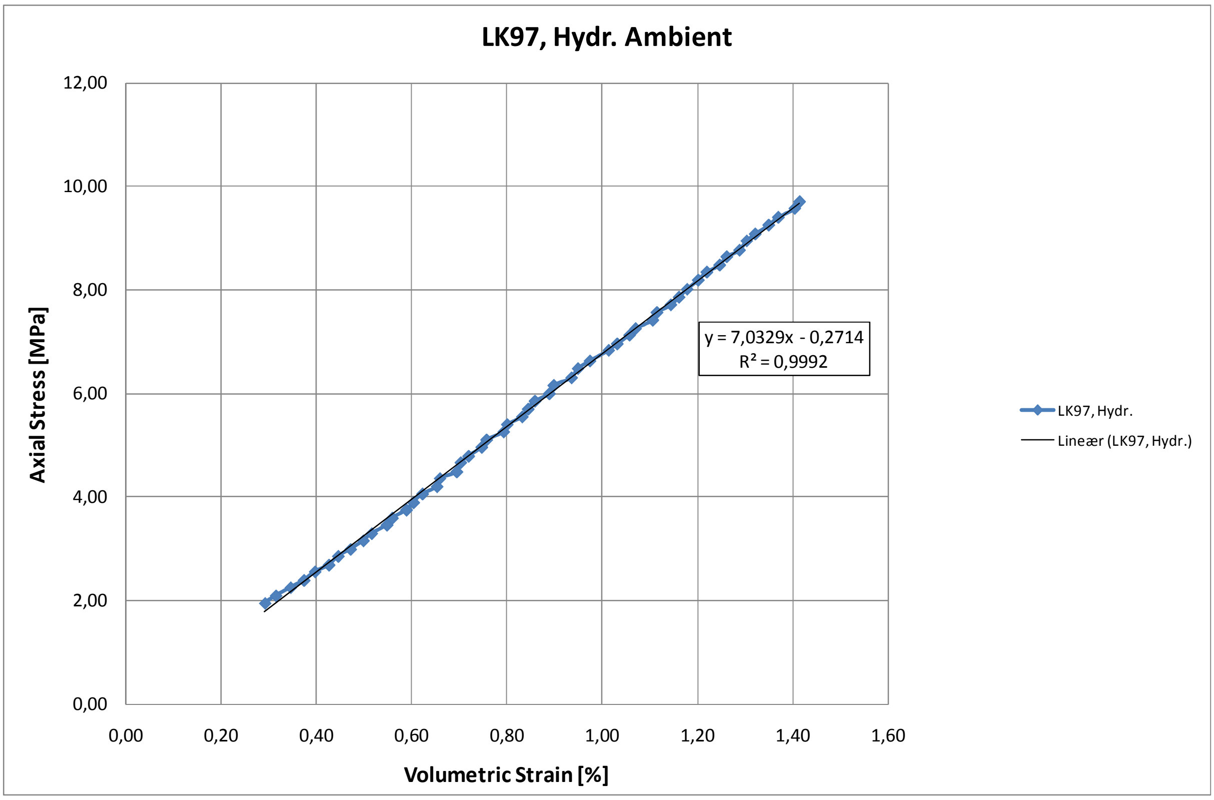

Figure B-22: *Section of the Axial stress versus Volumetric strain plot the hydrostatic test performed on LK97 with SSW flooding at ambient temperature used to estimate the Bulk modulus.*

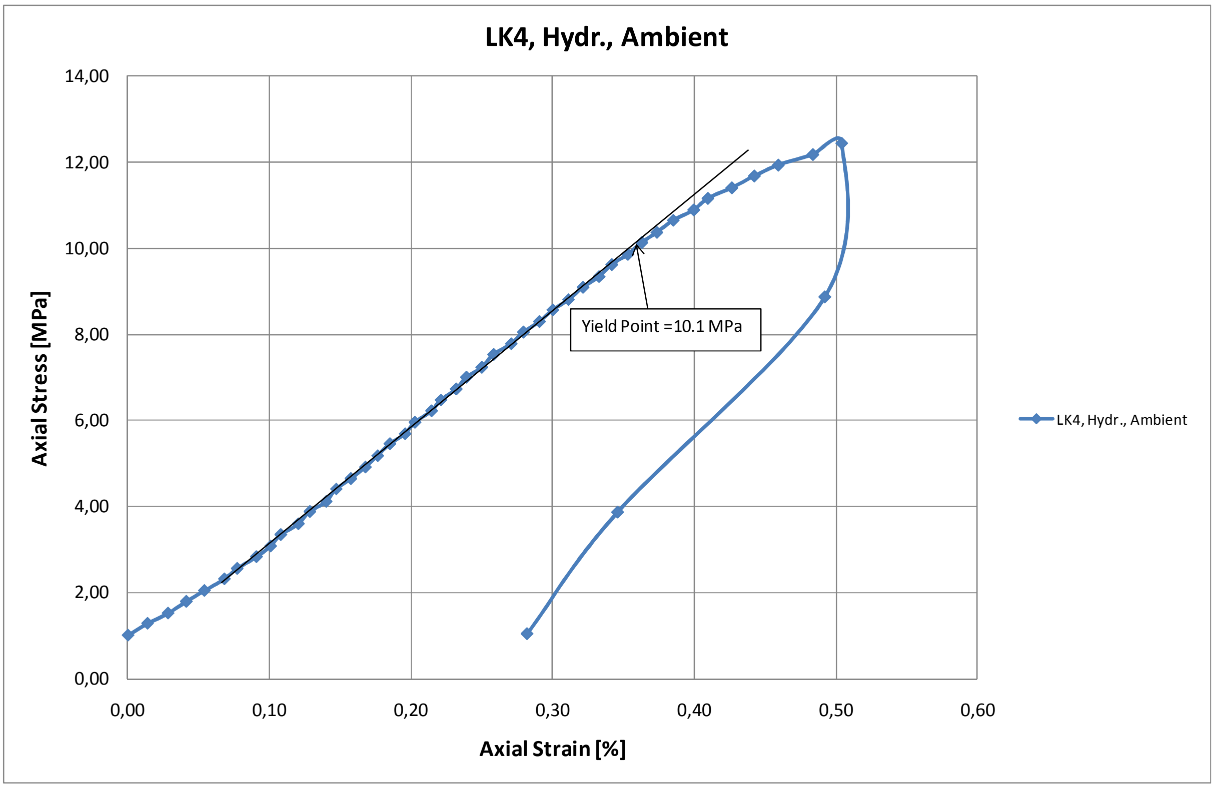

Figure B-23: *Axial stress versus axial strain plot for a hydrostatic test performed on LK4 with SSW flooding at ambient temperature*

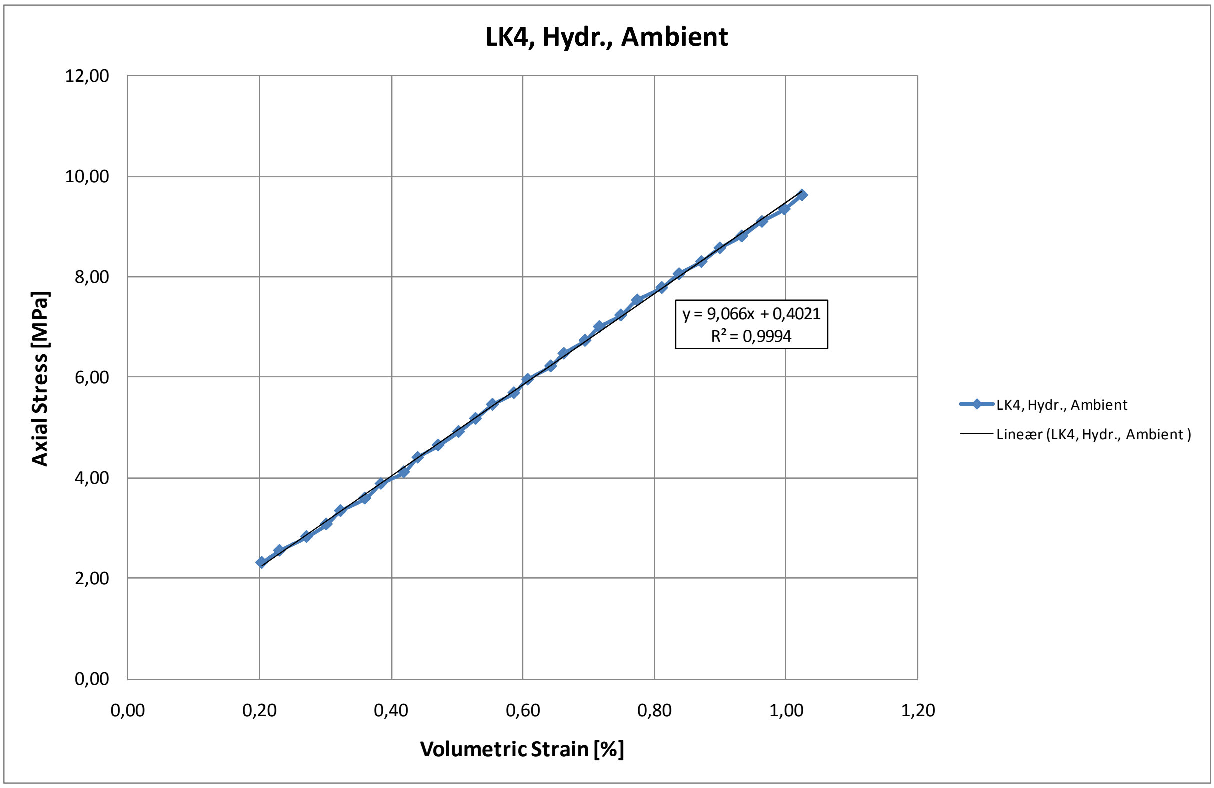

Figure B-24: *Section of the Axial stress versus Volumetric strain plot the hydrostatic test performed on LK4 with SSW flooding at ambient temperature used to estimate the Bulk modulus.*

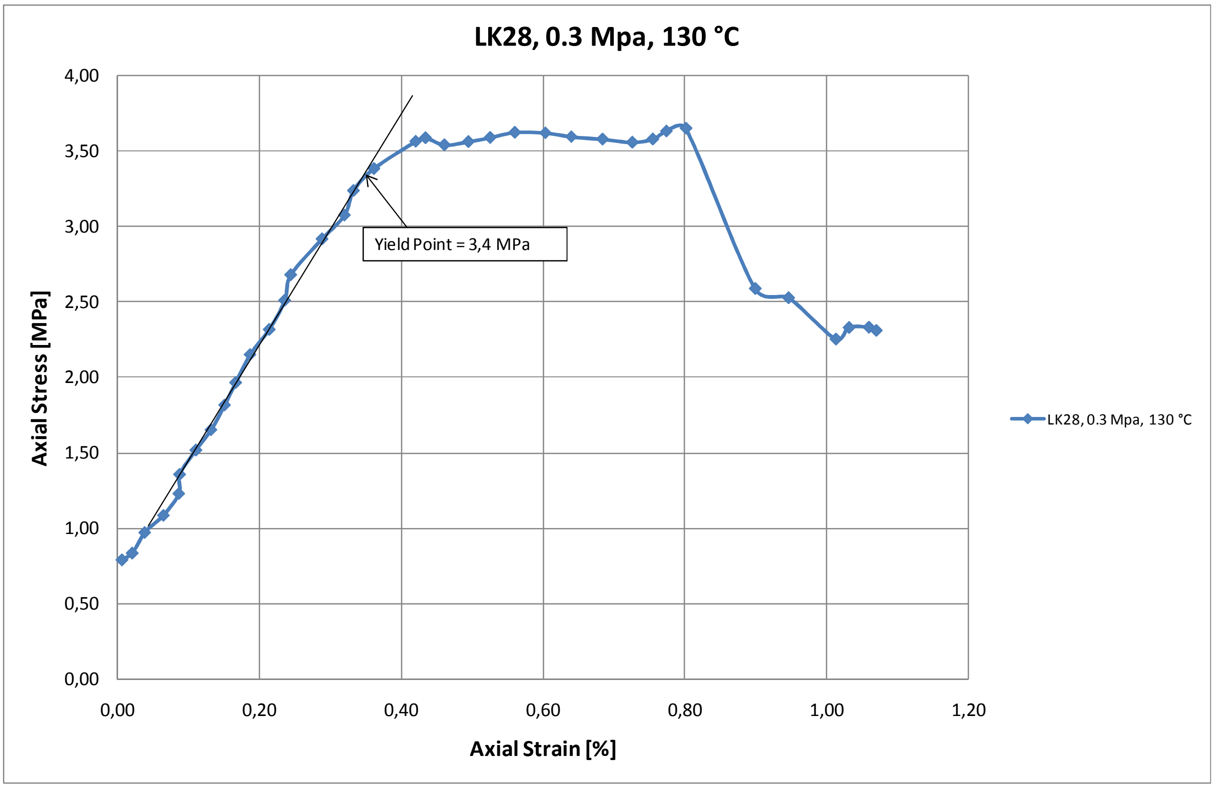

Figure B-25: *Axial stress versus axial strain plot for the 0.3 MPa deviatoric test performed on LK28 with SSW flooding at 130 °C*

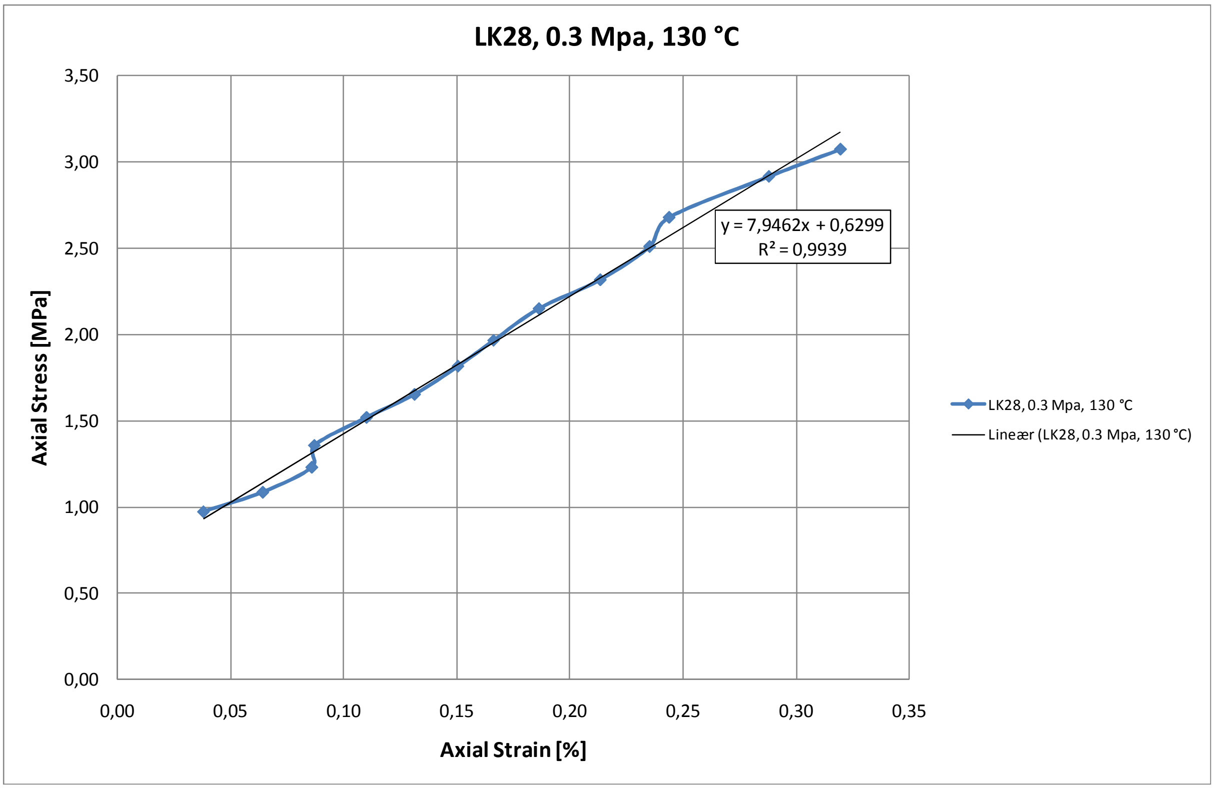

Figure B-26: *Section of the Axial stress versus axial strain plot for the 0.3 MPa deviatoric test performed on LK28 with SSW flooding at 130 °C used to estimate the Young's modulus.*

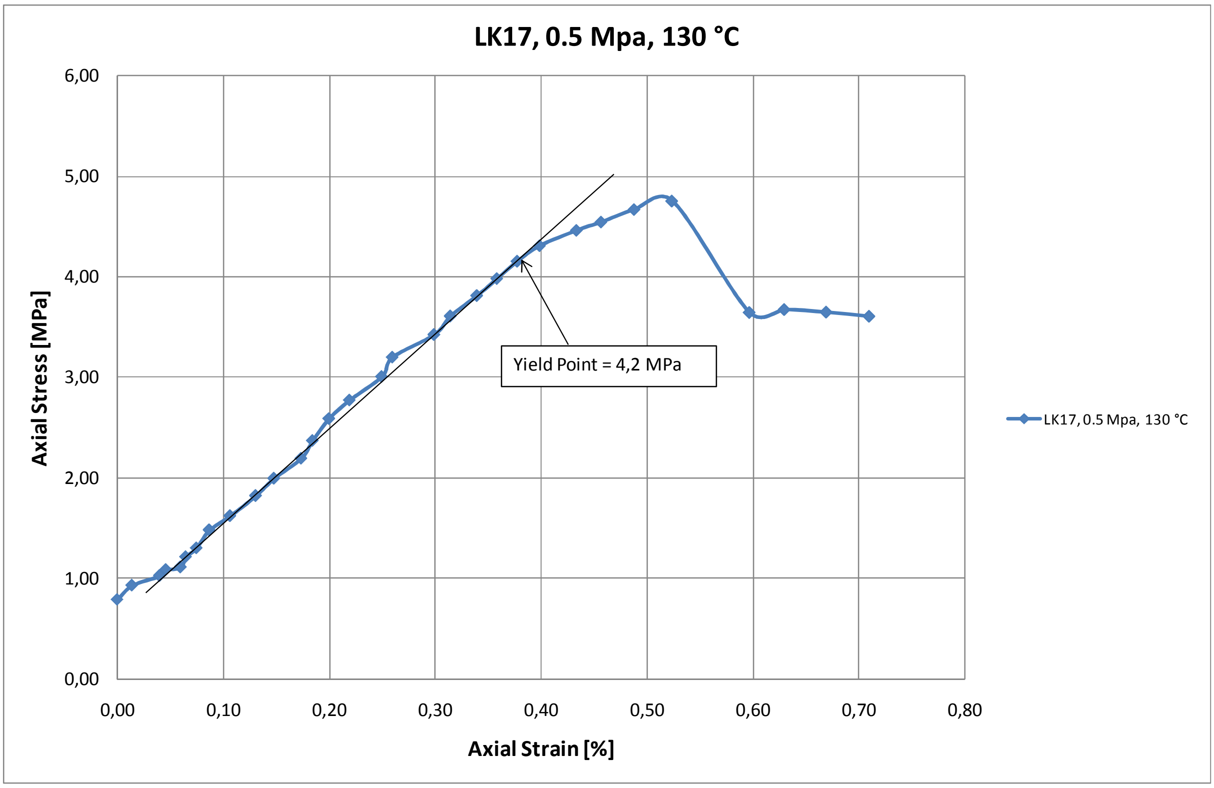

Figure B-27: *Axial stress versus axial strain plot for the 0.5 MPa deviatoric test performed on LK17 with SSW flooding at 130 °C*

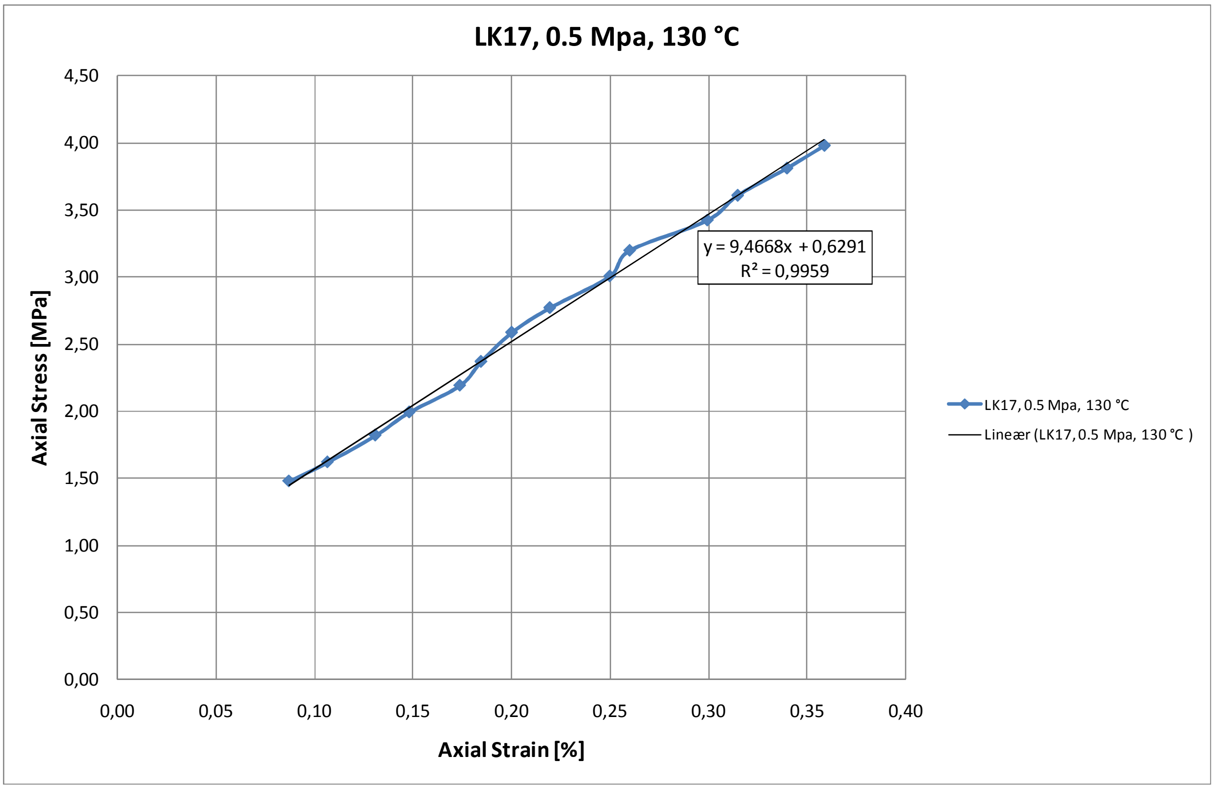

Figure B-28: *Section of the Axial stress versus axial strain plot for the 0.5 MPa deviatoric test performed on LK17 with SSW flooding at 130 °C used to estimate the Young's modulus.*

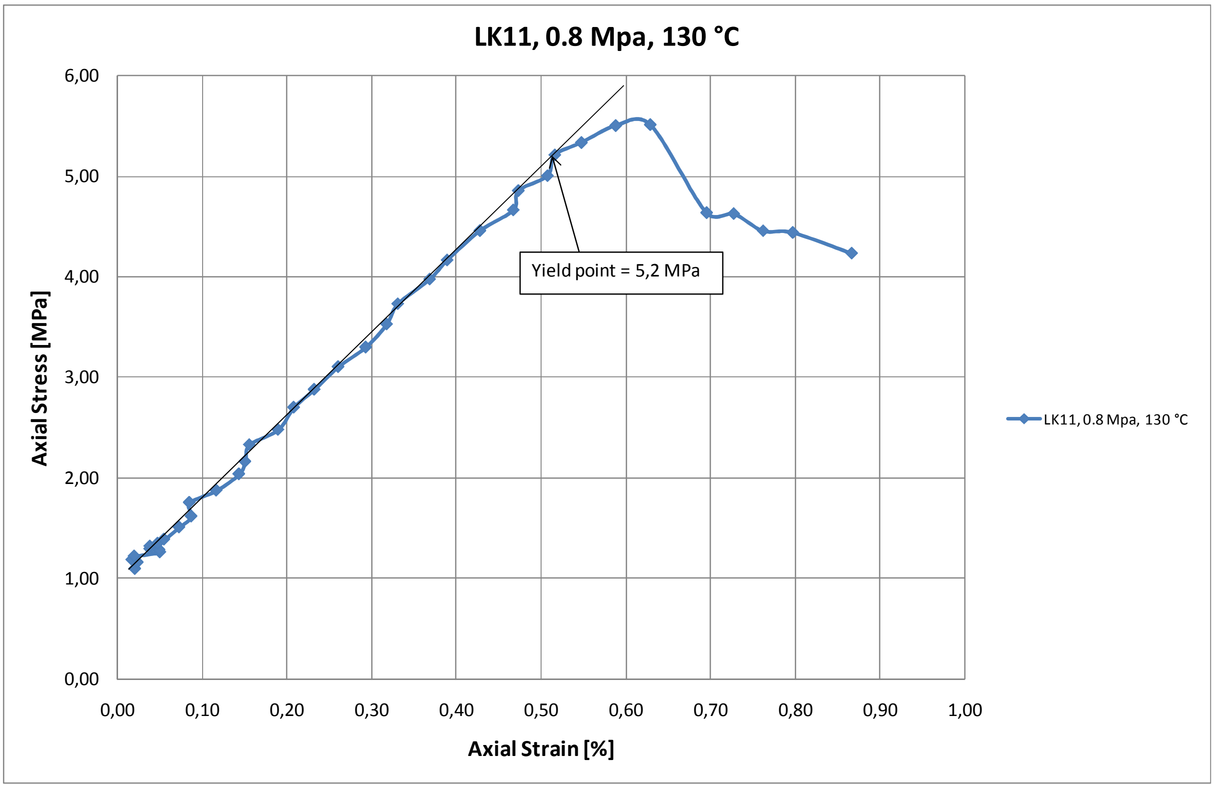

Figure B-29: *Axial stress versus axial strain plot for the 0.8 MPa deviatoric test performed on LK11 with SSW flooding at 130 °C*

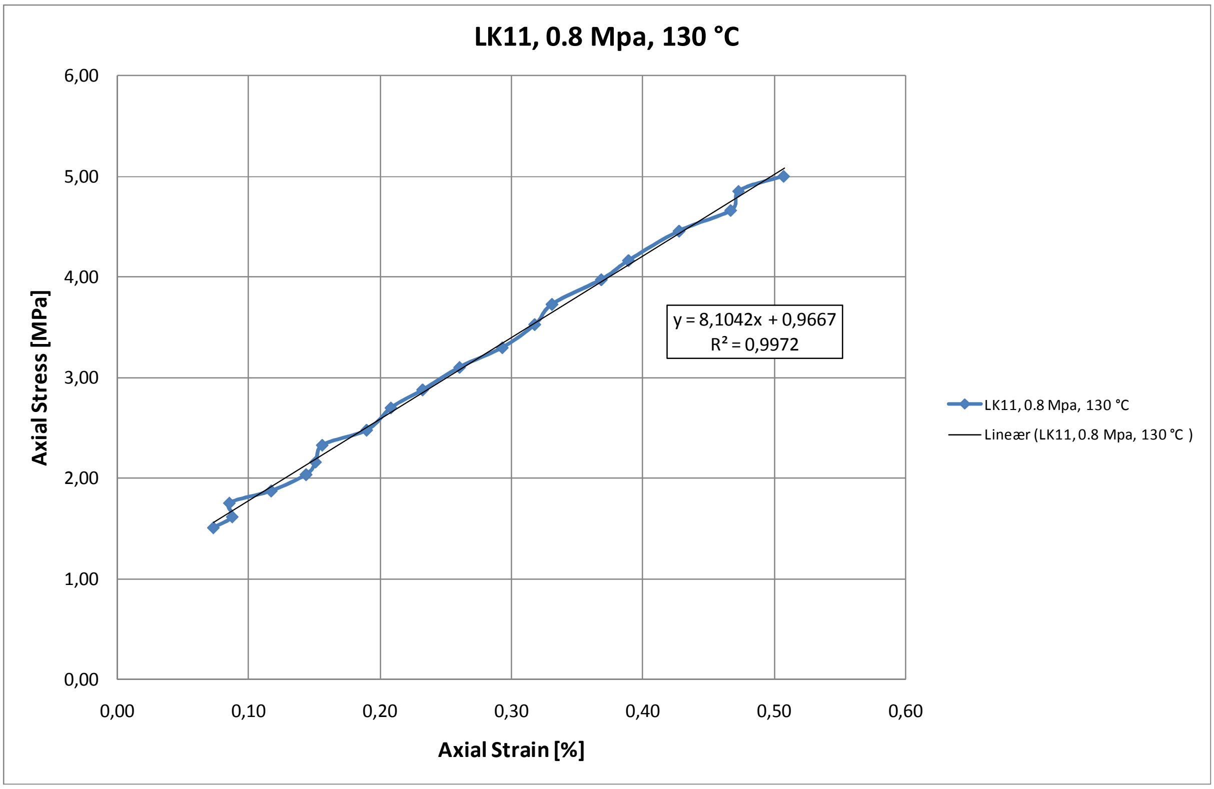

Figure B-30: *Section of the Axial stress versus axial strain plot for the 0.8 MPa deviatoric test performed on LK11 with SSW flooding at 130 °C used to estimate the Young's modulus.*

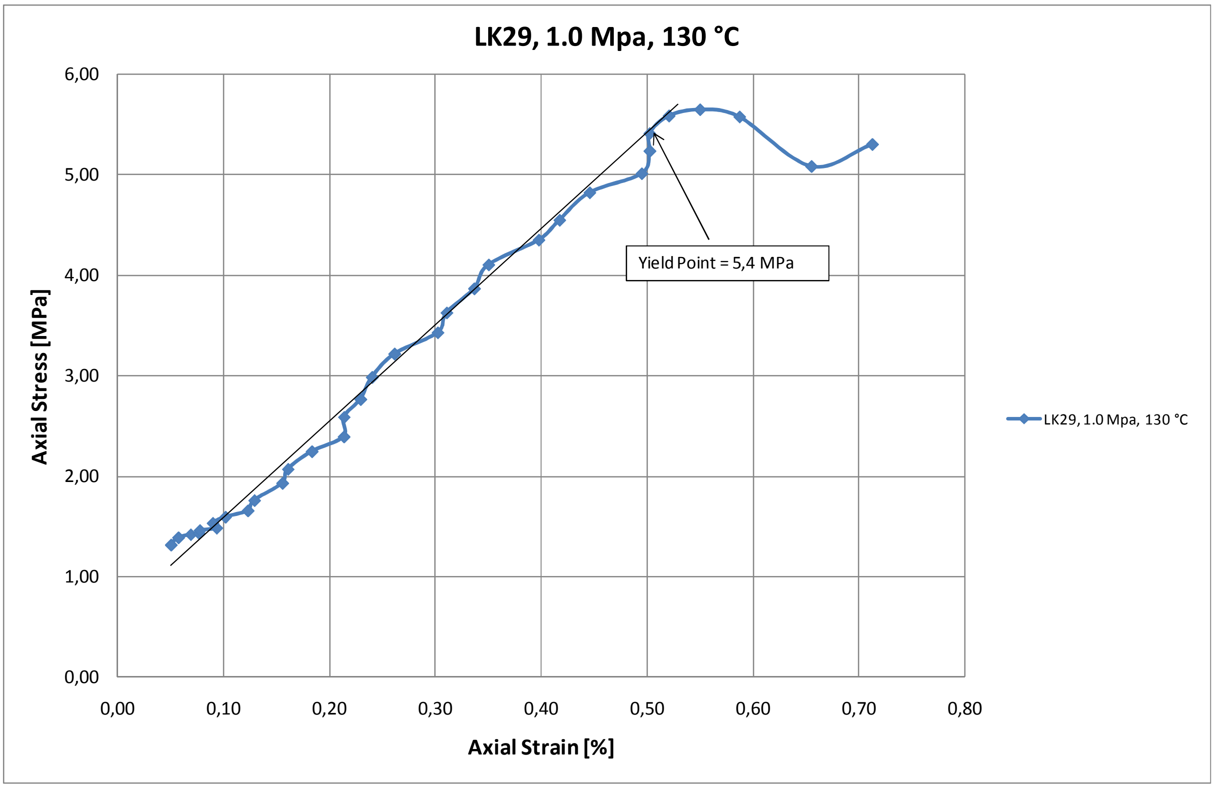

Figure B-31: *Axial stress versus axial strain plot for the 1.0 MPa deviatoric test performed on LK29 with SSW flooding at 130 °C*

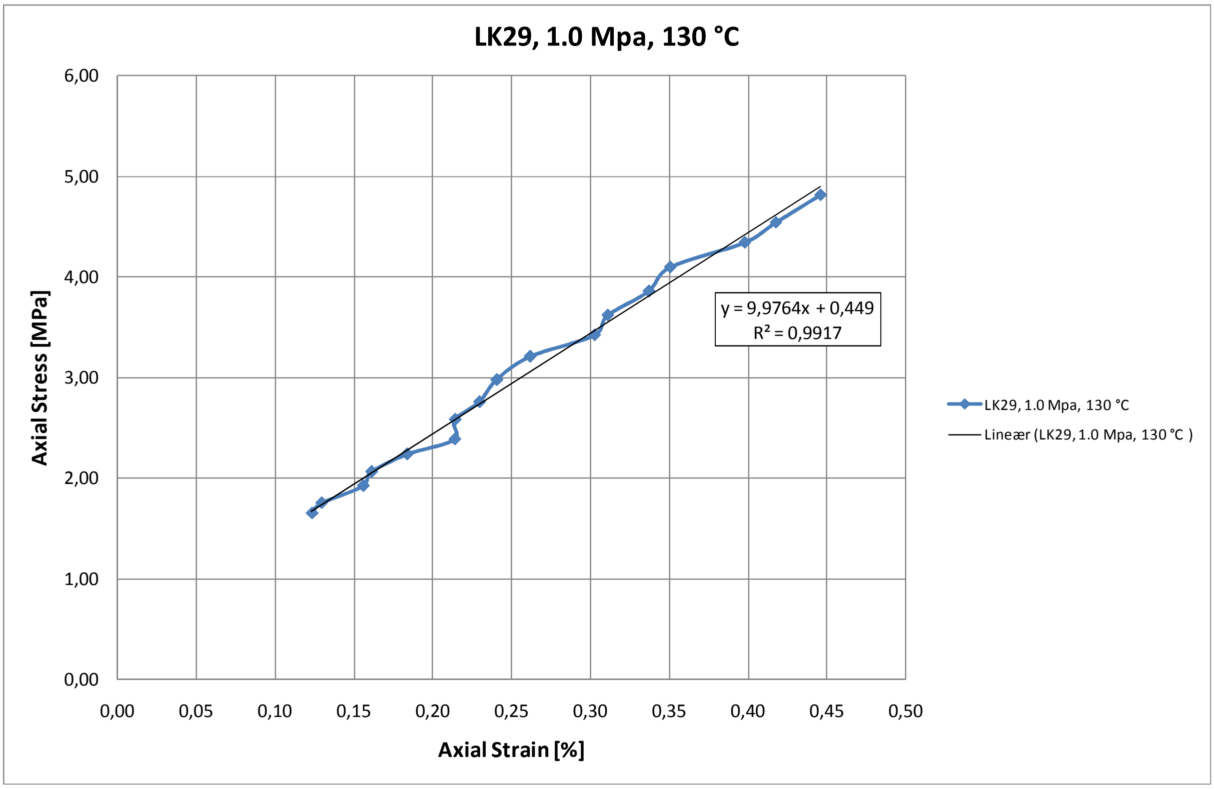

Figure B-32: *Section of the Axial stress versus axial strain plot for the 1.0 MPa deviatoric test performed on LK29 with SSW flooding at 130 °C used to estimate the Young's modulus.*

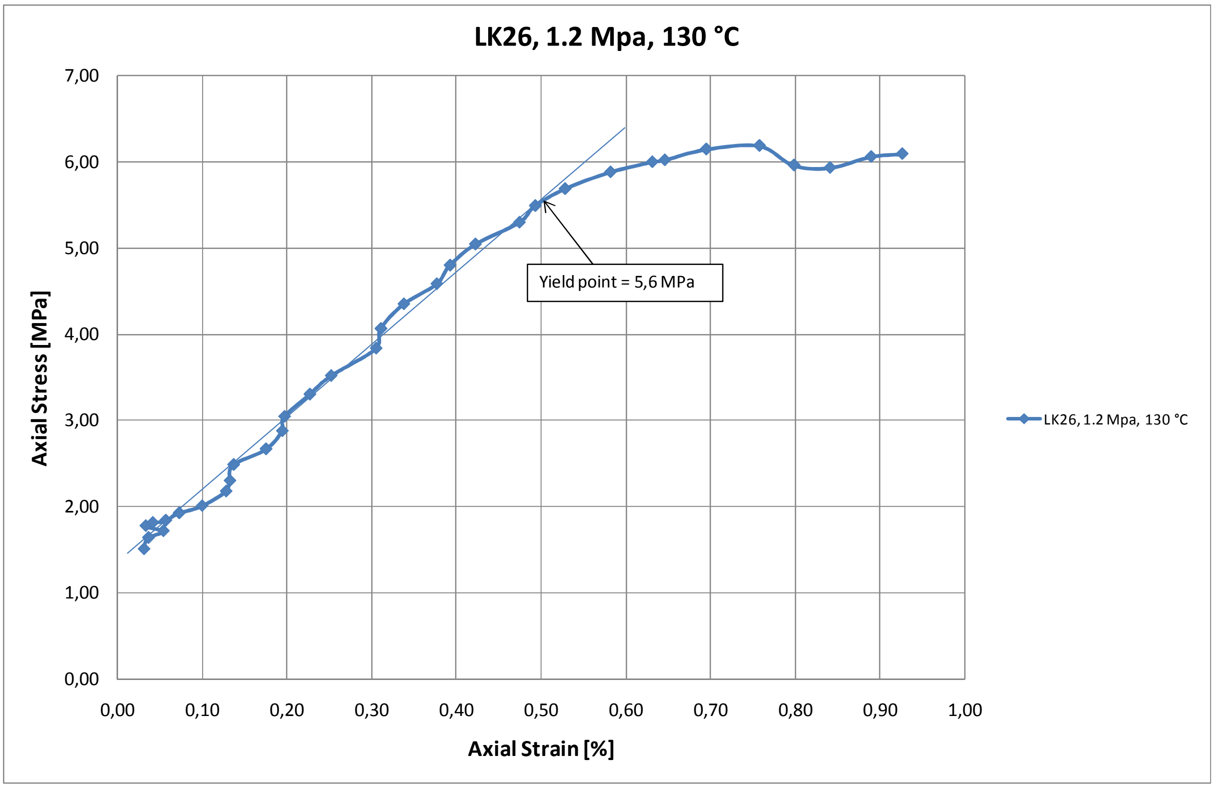

Figure B-33: *Axial stress versus axial strain plot for the 1.2 MPa deviatoric test performed on LK26 with SSW flooding at 130 °C*

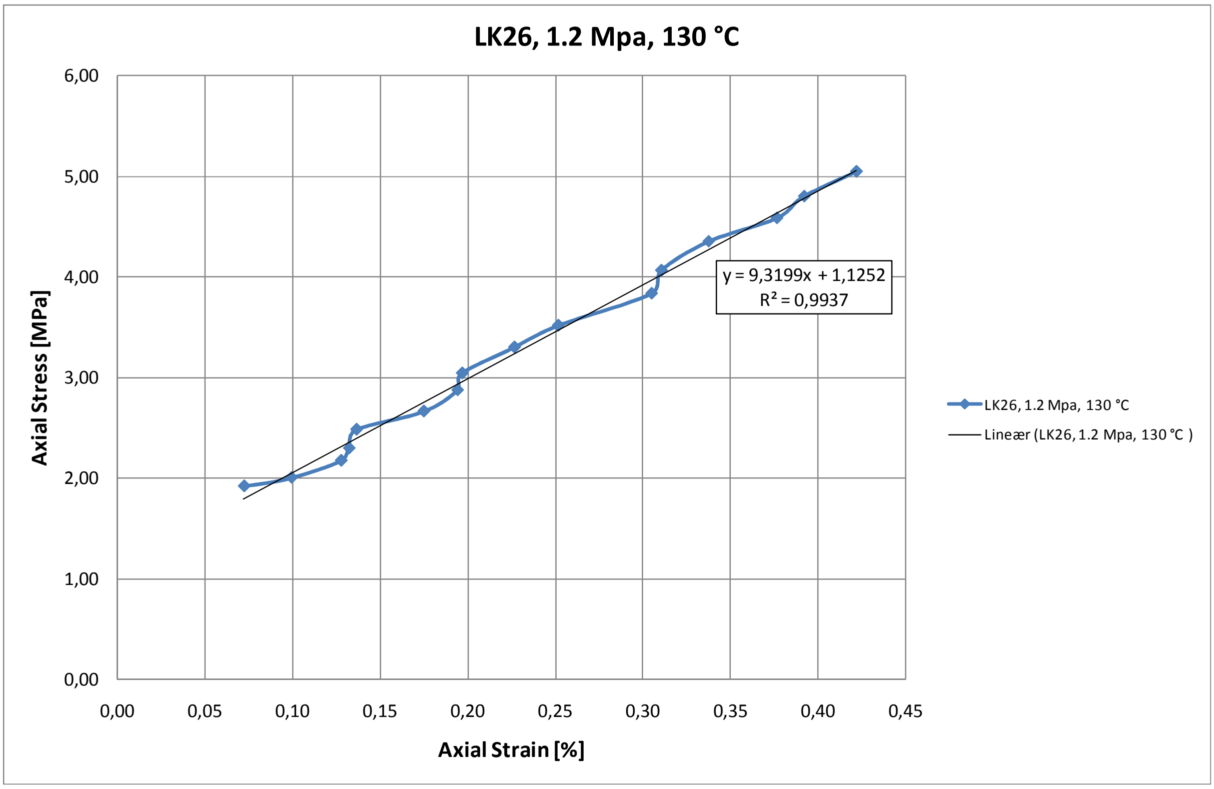

Figure B-34: *Section of the Axial stress versus axial strain plot for the 1.2 MPa deviatoric test performed on LK26 with SSW flooding at 130 °C used to estimate the Young’s modulus.*

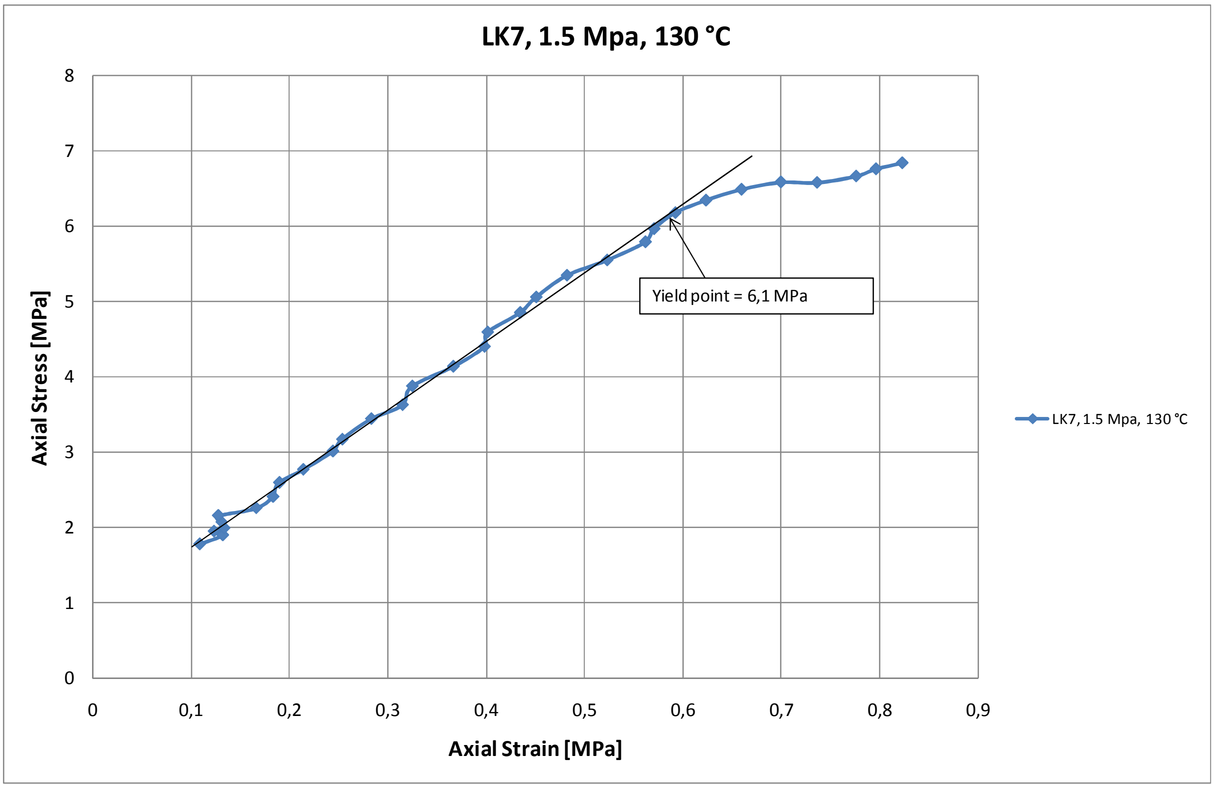

Figure B-35: *Axial stress versus axial strain plot for the 1.5 MPa deviatoric test performed on LK7 with SSW flooding at 130 °C*

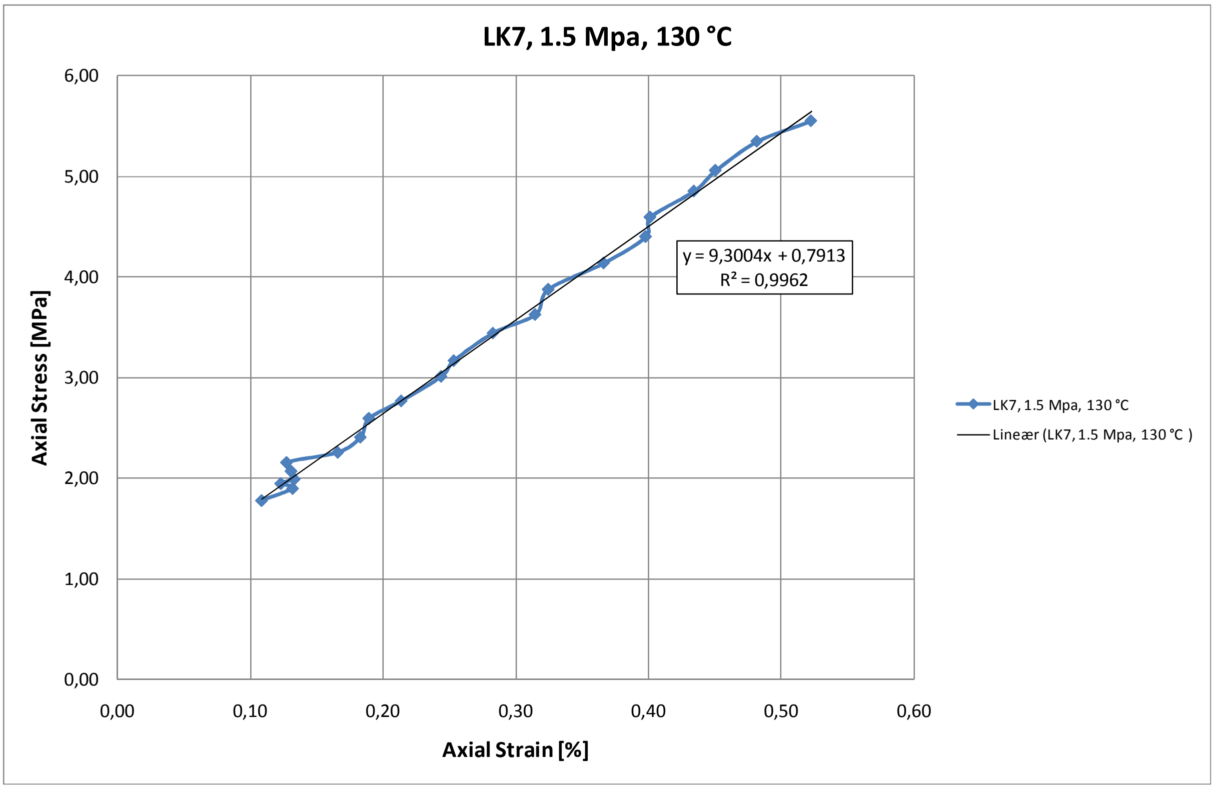

Figure B-36: *Section of the Axial stress versus axial strain plot for the 1.5 MPa deviatoric test performed on LK7 with SSW flooding at 130 °C used to estimate the Young's modulus.*

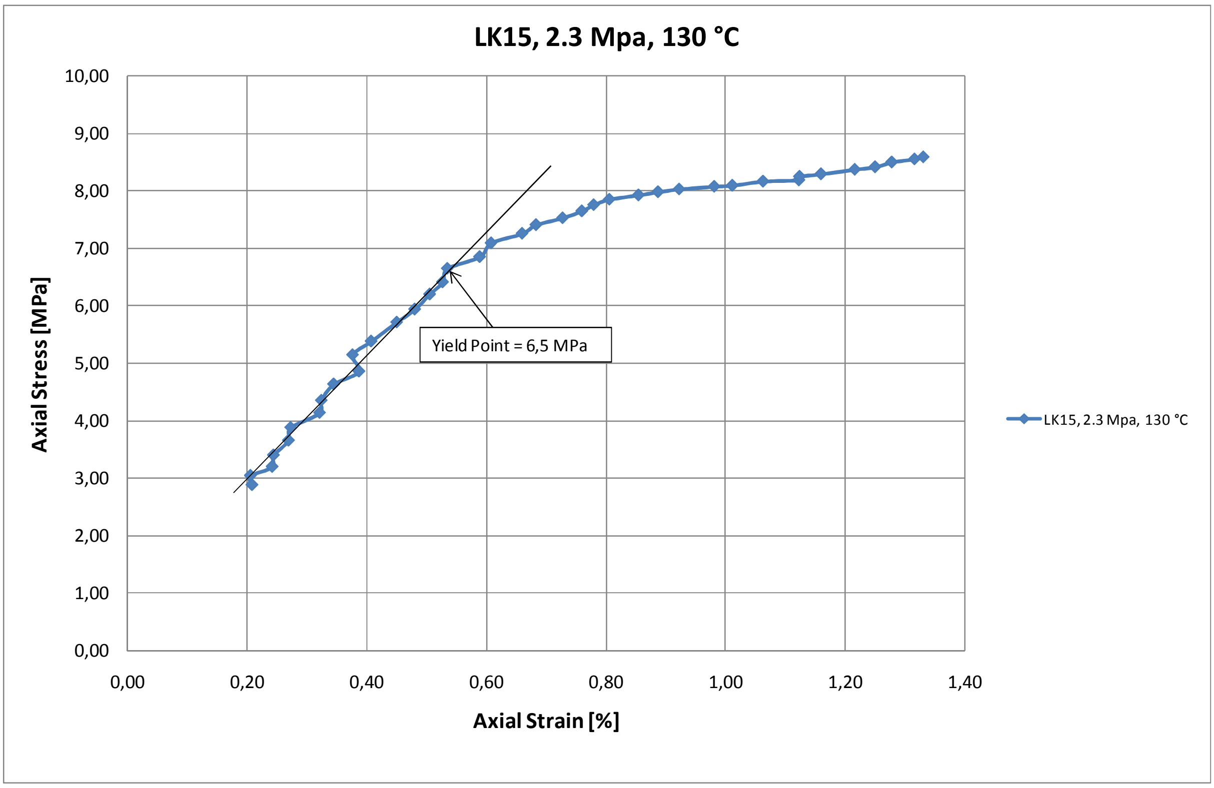

Figure B-37: *Axial stress versus axial strain plot for the 2.3 MPa deviatoric test performed on LK15 with SSW flooding at 130 °C*

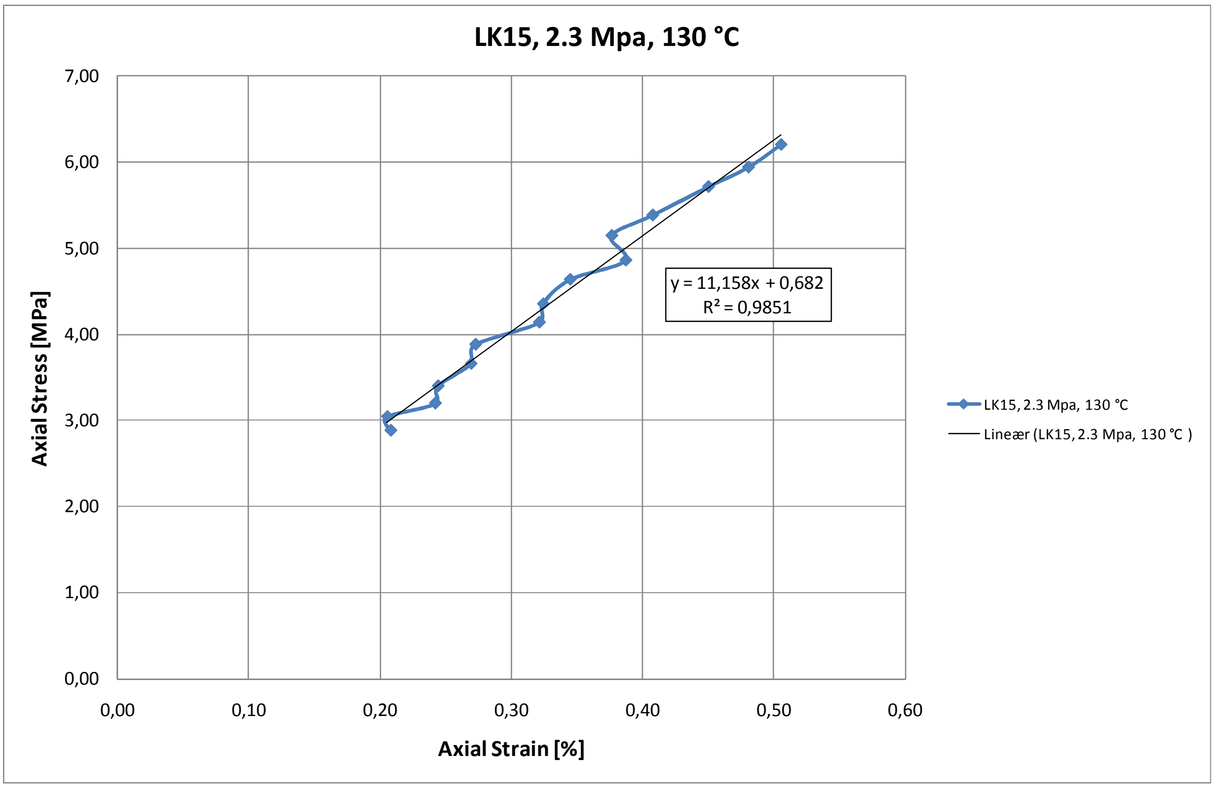

Figure B-38: *Section of the Axial stress versus axial strain plot for the 2.3 MPa deviatoric test performed on LK15 with SSW flooding at 130 °C used to estimate the Young's modulus.*

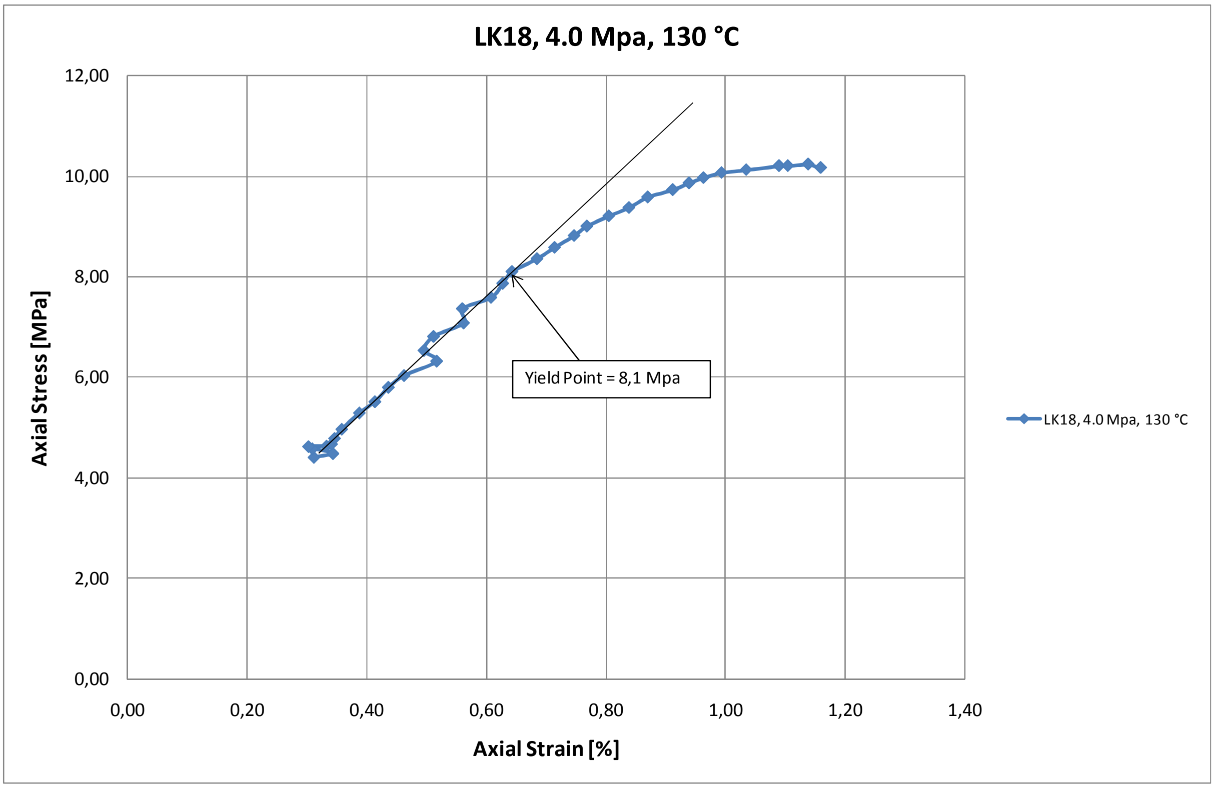

Figure B-39: *Axial stress versus axial strain plot for the 4.0 MPa deviatoric test performed on LK18 with SSW flooding at 130 °C*

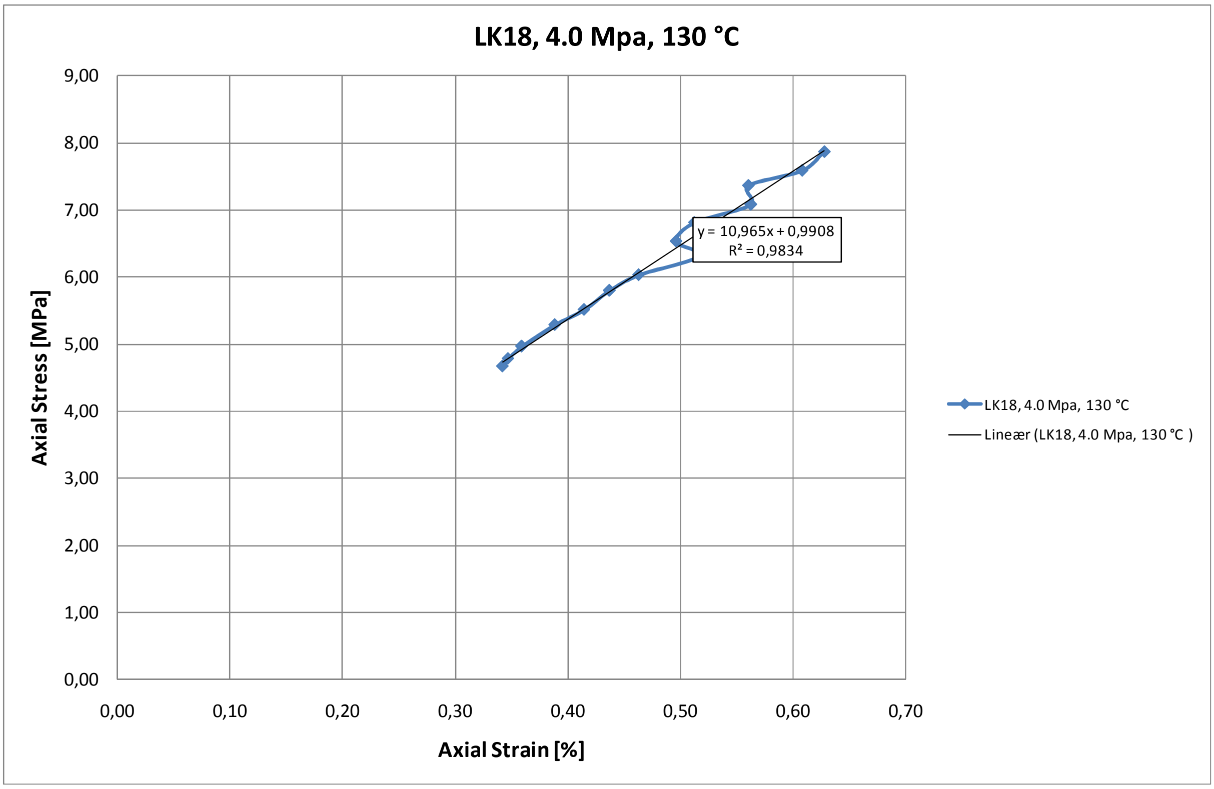

Figure B-40: *Section of the Axial stress versus axial strain plot for the 4.0 MPa deviatoric test performed on LK18 with SSW flooding at 130 °C used to estimate the Young's modulus.*

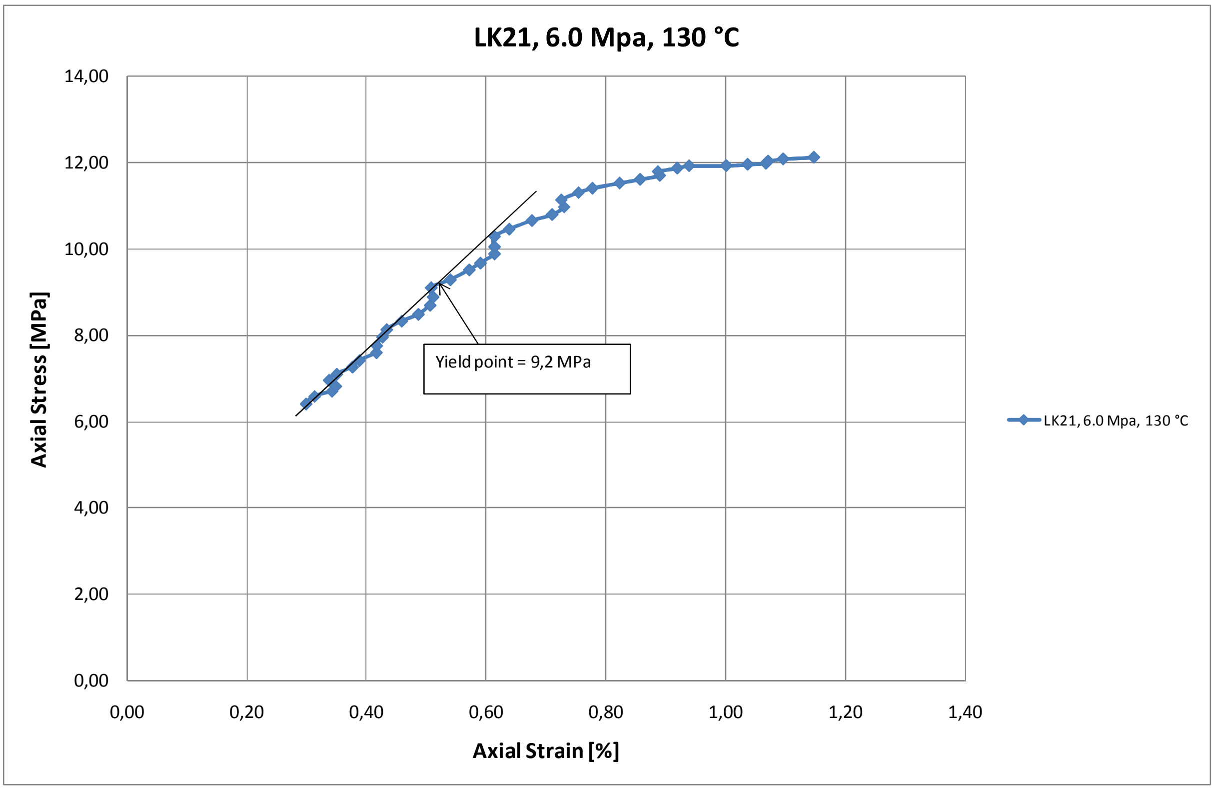

Figure B-41: *Axial stress versus axial strain plot for the 6.0 MPa deviatoric test performed on LK21 with SSW flooding at 130 °C*

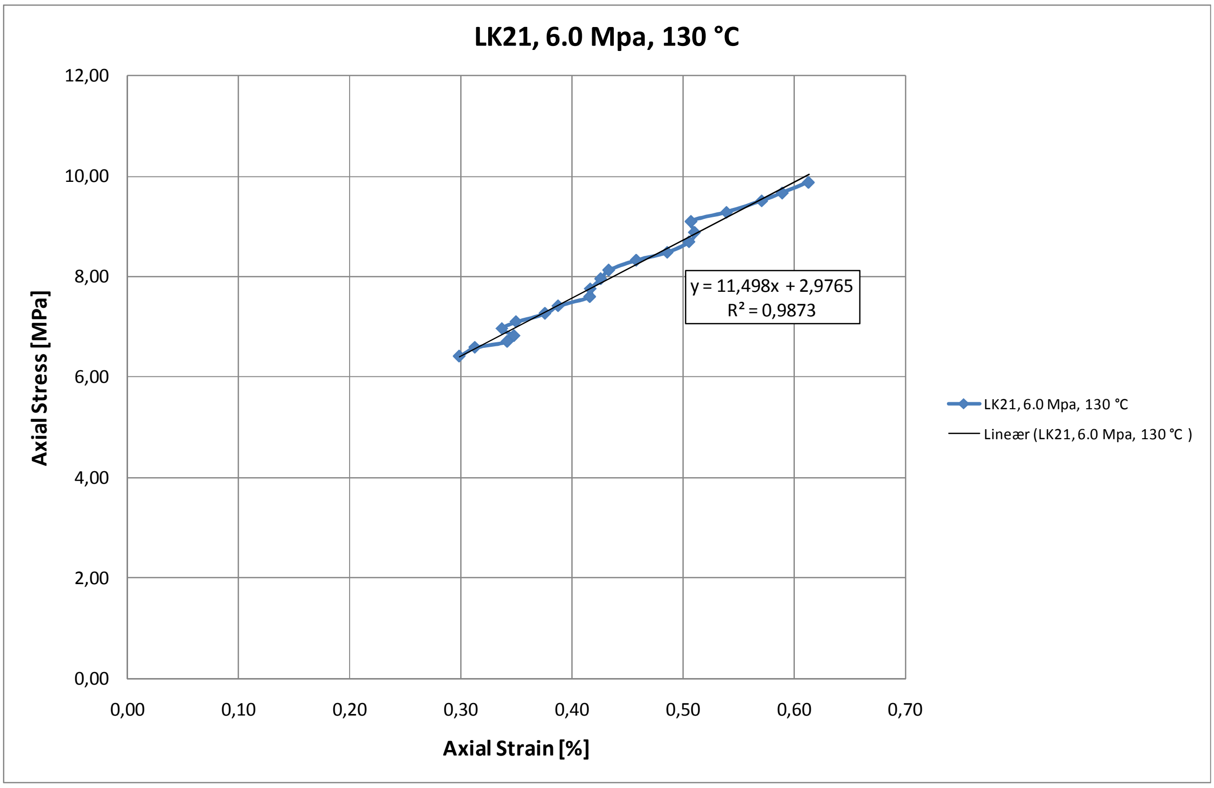

Figure B-42: *Section of the Axial stress versus axial strain plot for the 6.0 MPa deviatoric test performed on LK21 with SSW flooding at 130 °C used to estimate the Young's modulus.*

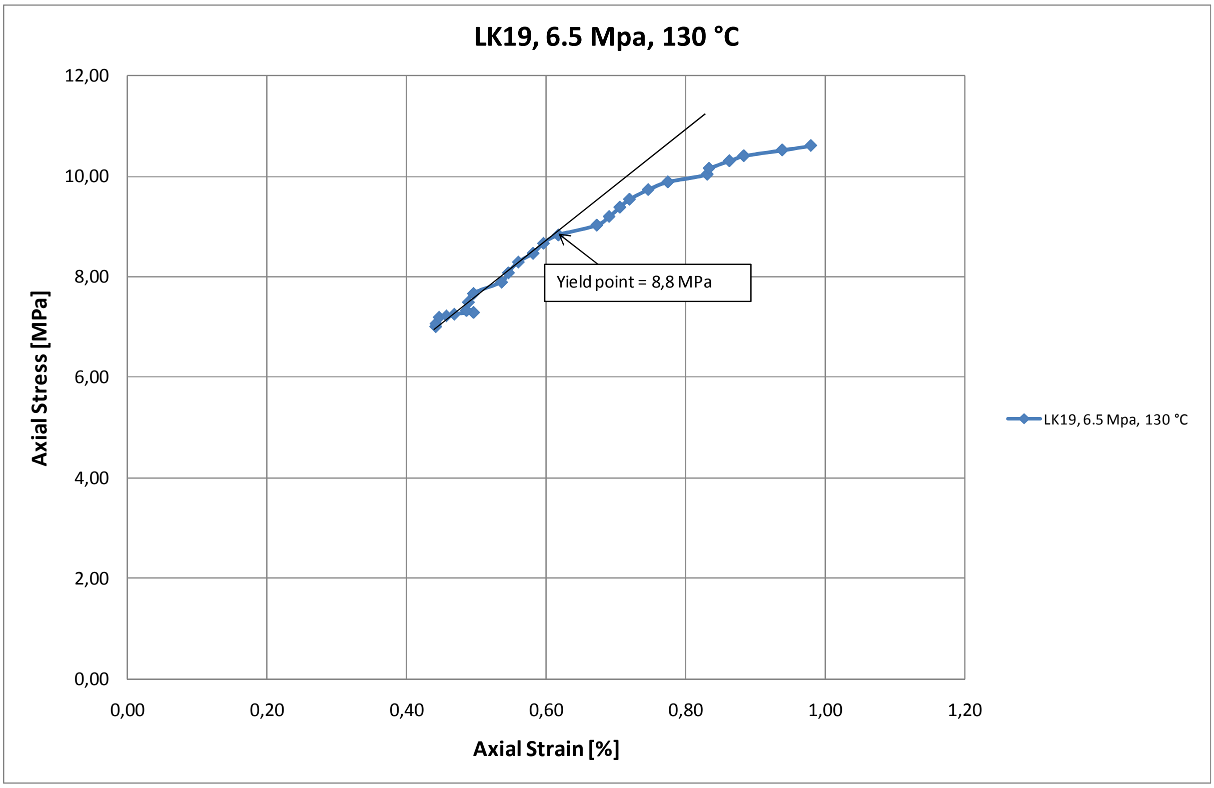

Figure B-43: *Axial stress versus axial strain plot for the 6.5 MPa deviatoric test performed on LK19 with SSW flooding at 130 °C*

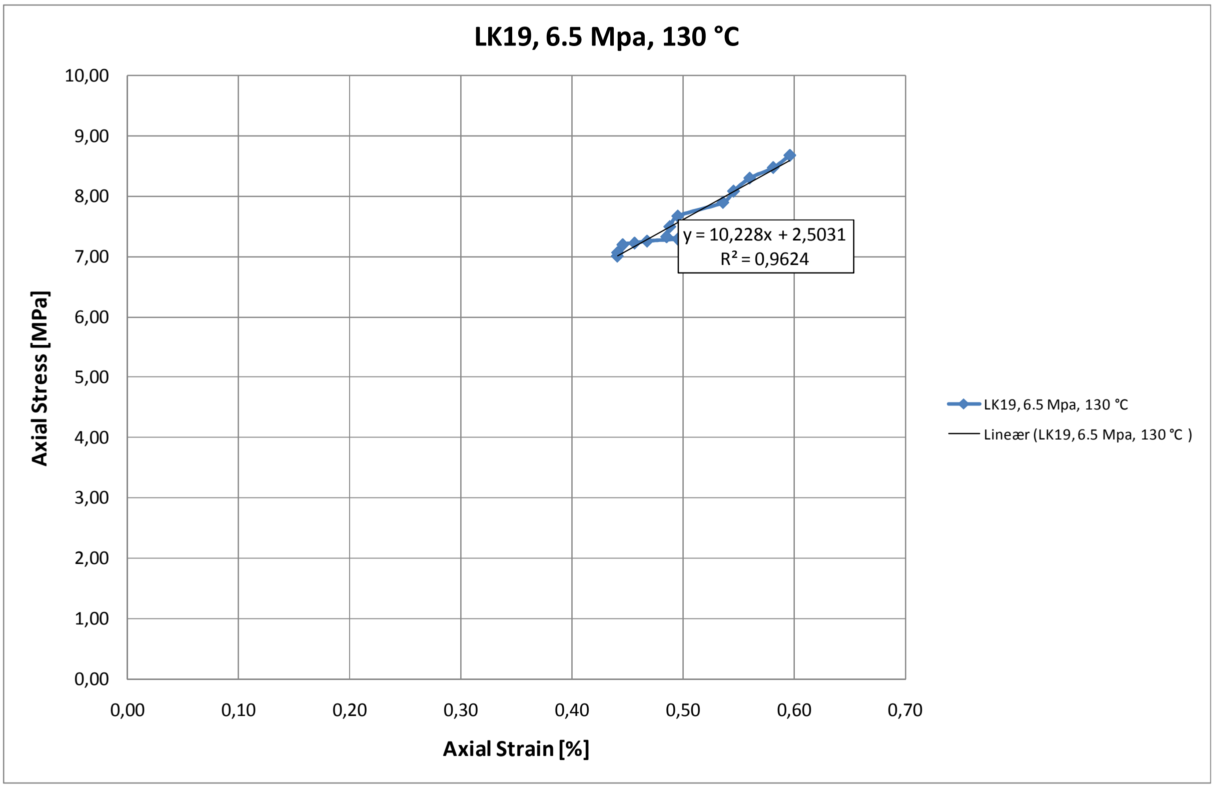

Figure B-44: *Section of the Axial stress versus axial strain plot for the 6.5 MPa deviatoric test performed on LK19 with SSW flooding at 130 °C used to estimate the Young's modulus.*

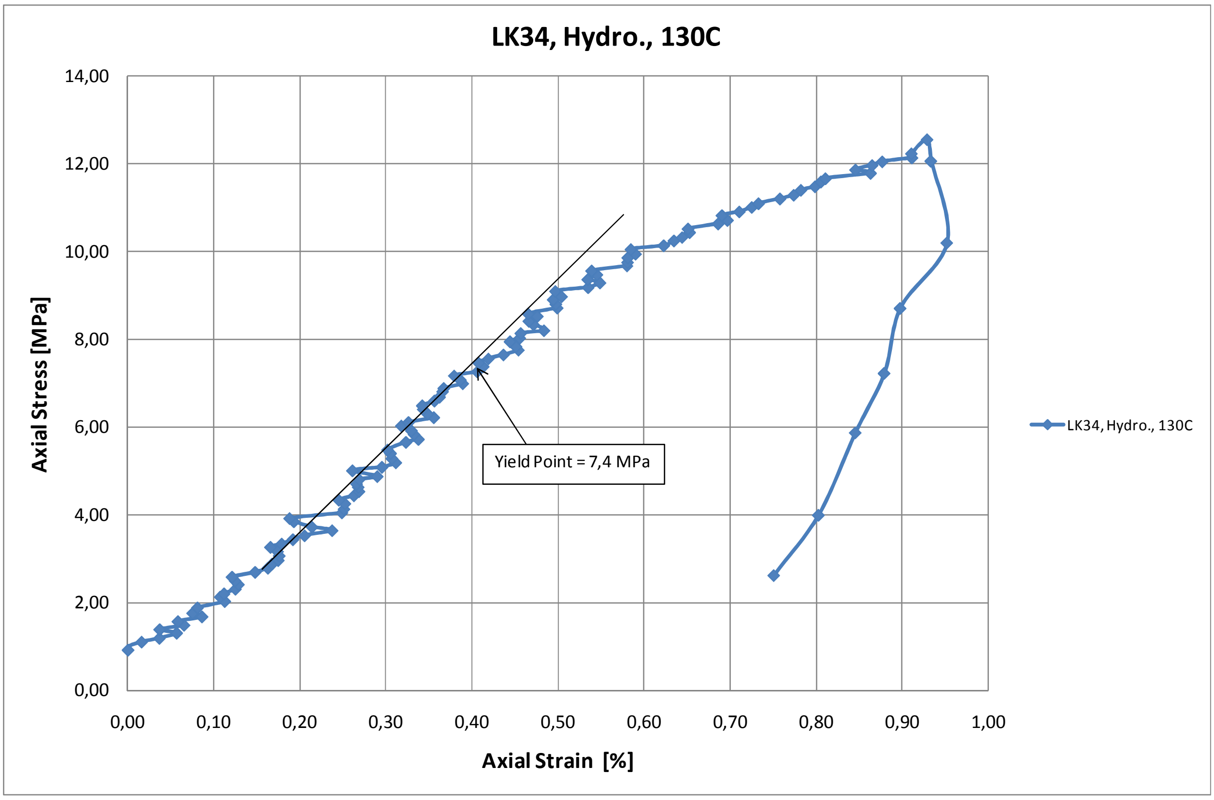

Figure B-45: *Axial stress versus axial strain plot for a hydrostatic test performed on LK34 with SSW flooding at ambient 130 °C*

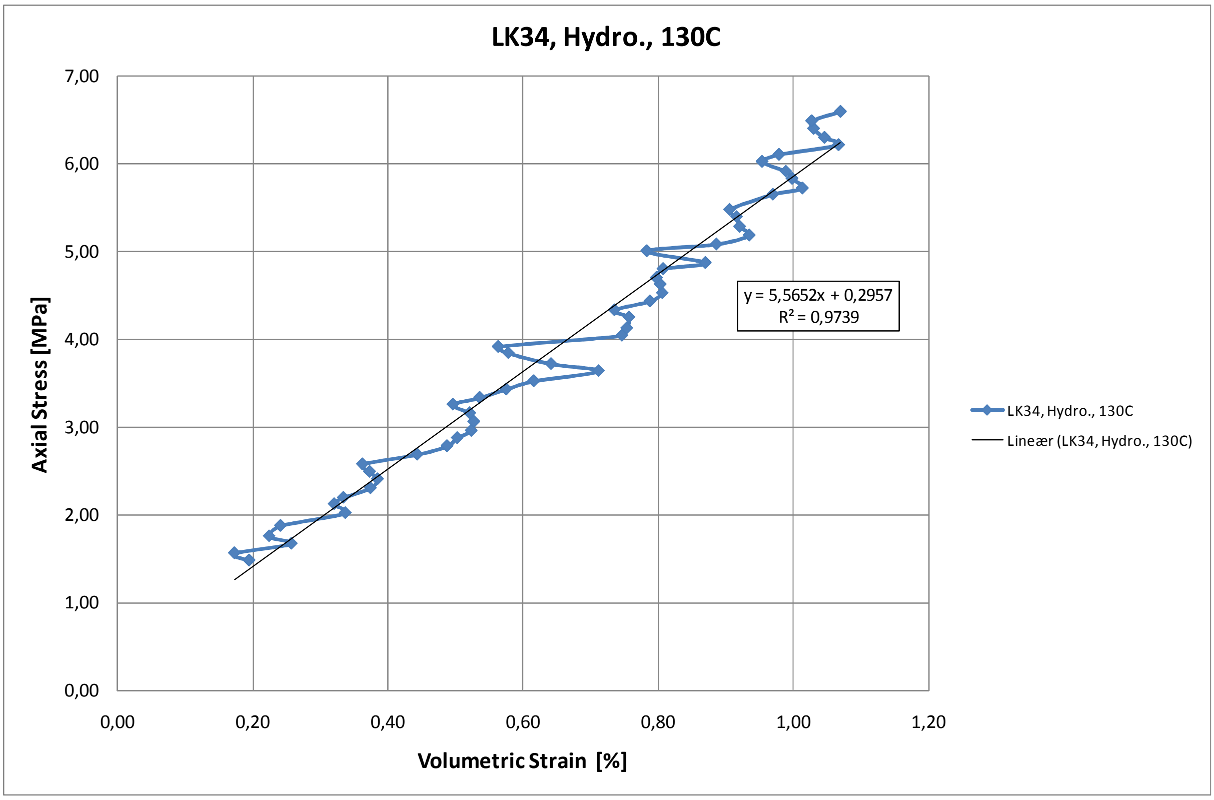

Figure B-46: *Section of the Axial stress versus Volumetric strain plot the hydrostatic test performed on LK34 with SSW flooding at 130 °C used to estimate the Bulk modulus*

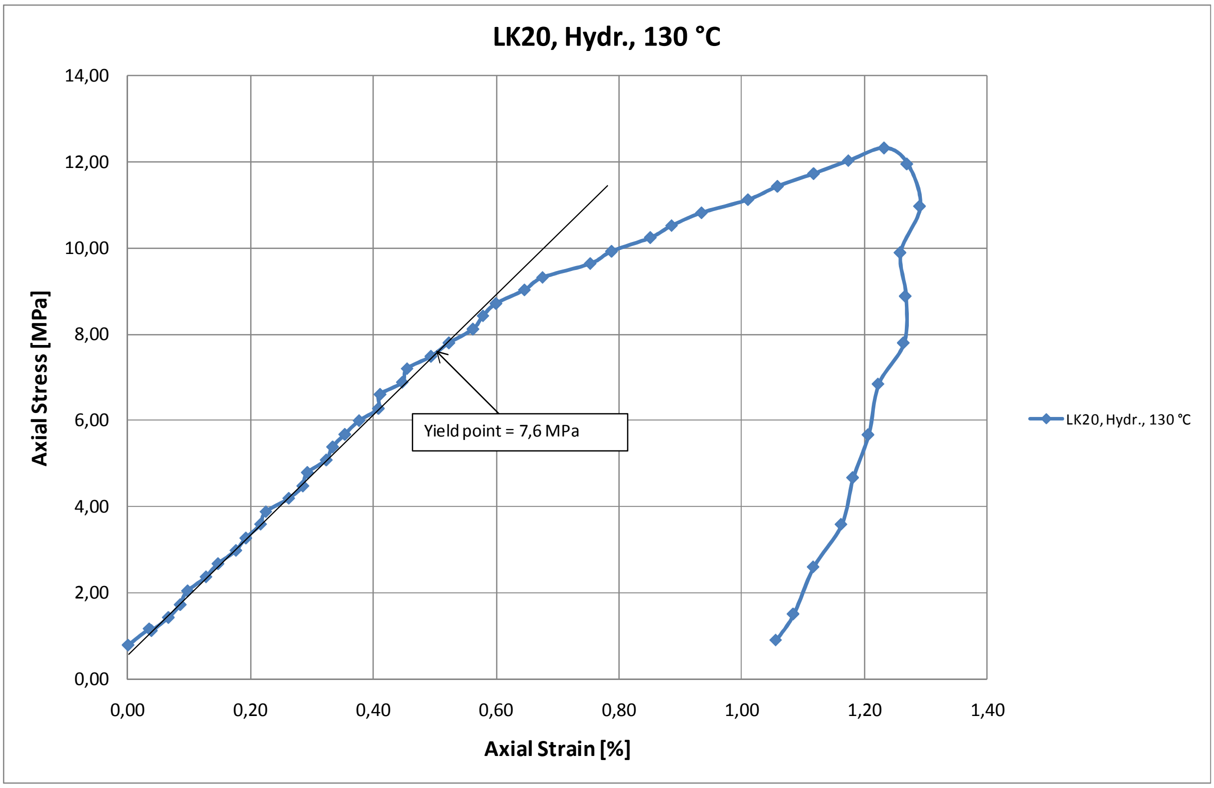

Figure B-47: *Axial stress versus axial strain plot for a hydrostatic test performed on LK20 with SSW flooding at ambient 130 °C*

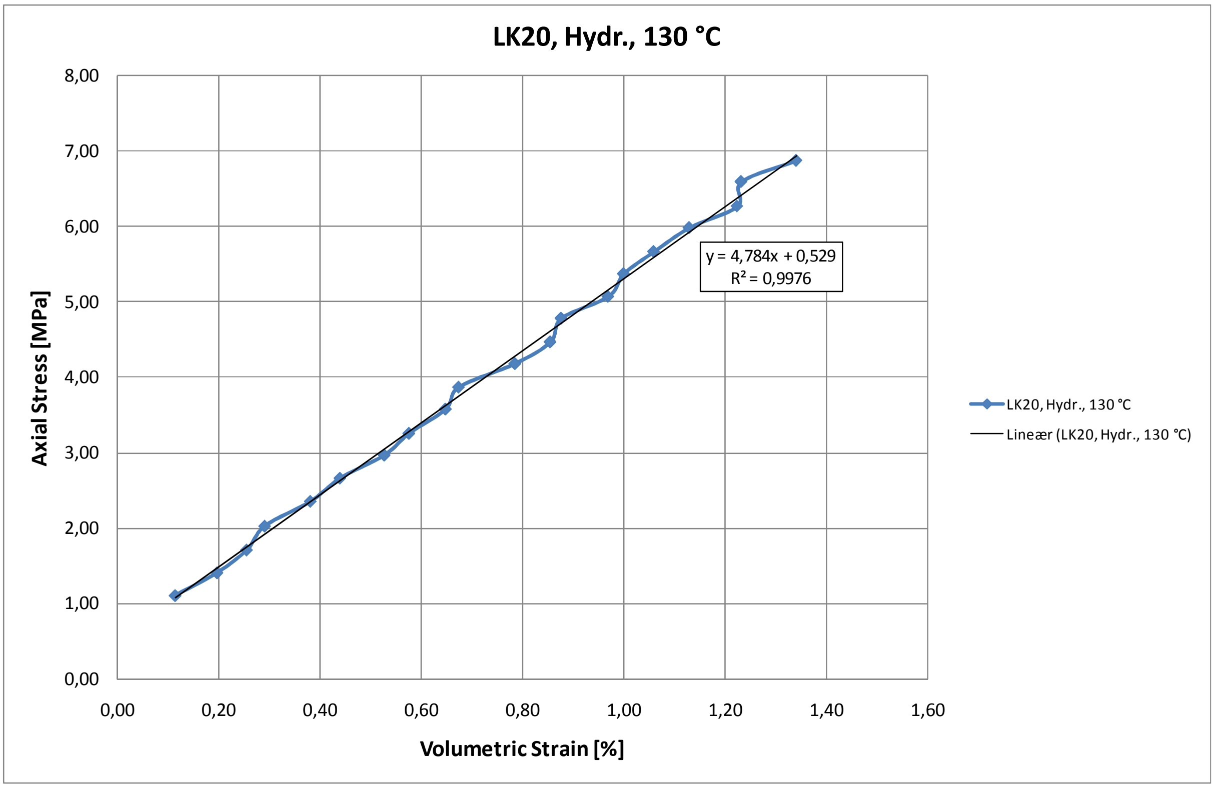

Figure B-48: *Section of the Axial stress versus Volumetric strain plot the hydrostatic test performed on LK20 with SSW flooding at 130 °C used to estimate the Bulk modulus*